Kinetic and Spectroscopic Investigation of Structural Influences on Hydrogen-atom Transfer Reactivity of N5-Ligated Oxomanganese(IV) Complexes

By

Allyssa A. Massie

Submitted to the graduate degree program in Chemistry and the Graduate Faculty of the University of Kansas in partial fulfillment of the requirements for the degree of Doctor of Philosophy.

_____

Chairperson: Dr. Timothy A. Jackson

_____

Dr. Mikhail V. Barybin

_____

Dr. James D. Blakemore

_____

Dr. Marco Caricato

_____

Dr. Alan M. Allgeier

Date Defended: May 4, 2018

The Dissertation Committee for Allyssa A. Massie
certifies that this is the approved version of the following dissertation:

Kinetic and Spectroscopic Investigation of Structural Influences on Hydrogen-atom Transfer Reactivity of N5-Ligated Oxomanganese(IV) Complexes

_____
Chairperson: Dr. Timothy A. Jackson

Date approved: May 7, 2018

Abstract

High valent iron- and manganese-oxo intermediates perform important hydrogen-atom transfer (HAT) reactions in both biological and synthetic systems. There has been extensive characterization of HAT reactivity of enzymatic and synthetic oxoiron(IV) species, and these complexes have been shown to cleave a wide range of C-H bonds. Although there is no evidence for this type of reactivity by manganese enzymes in nature, several synthetic oxomanganese(IV) species are also capable of activating C-H bonds. However, whereas oxoiron(IV) species have been extensively characterized, the factors that influence HAT reactivity of oxomanganese(IV) species is poorly understood. In an effort to further understand the structure-reactivity relationship of oxomanganese(IV) species, a series of novel oxomanganese(IV) species with subtle perturbations to the equatorial ligand field of the neutral, pentadentate supporting ligand were prepared. Extensive spectroscopic studies, including structural characterization by X-ray absorption spectroscopy (XAS), revealed very minor geometric and electronic structure changes.

Kinetic studies of C-H bond containing substrates offered insight into the effects of the ligand perturbations on the reactivity of these oxomanganese(IV) species. Electron donation from the supporting ligand decreases the rate of C-H activation. Conversely, weakening the ligand field through the use of a bulkier ligand dramatically speeds up HAT reactivity, allowing for the reaction with the strong C-H bonds of cyclohexane at rates exceeding that of oxoiron(IV) species with similar ligands. Further, it was discovered that the reaction with cyclohexane could be carried out catalytically in the presence of excess oxidant. The products of catalytic cyclohexane oxidation, cyclohexanol and cyclohexanone, provided evidence of the ability of this oxomanganese(IV) species to perform substrate hydroxylation.

Lastly, peroxomanganese(III) species are proposed to be important intermediates in many biological systems. However, in both biological and synthetic systems, the factors that determine the cleavage of the O-O versus Mn-O bonds are not well understood. A novel peroxomanganese(III) species was prepared using electrochemically generated superoxide. The electrochemical reduction of this species was probed to further understand the effects of supporting ligand, which has an amide group *trans* to the peroxo.

Acknowledgements

First and foremost, I must thank my research advisor, Professor Tim Jackson. I cannot imagine being as successful as I have been in any other research group. Not only do I appreciate what a great mentor you have been, but also all of the things you have taught me in both research and class settings. I did not initially consider your group because I saw the prefix “bio” before inorganic and I assumed I would hate it. Boy was I wrong! Your infinite knowledge and enthusiasm of the bioinorganic field has always kept me striving to learn more. I am also very grateful for the opportunity you gave me to work with Dr. Elodie Anxolabéhère-Mallart, to whom I am also grateful. I hope to bring the different mentoring styles as well as the different things I have learned from both of you to any future mentoring experiences I will have.

I need to thank all of my committee members. Professor Misha Barybin, I appreciate that I have gotten to work so closely to you and your group. You have been a great person to talk to, and I really appreciate all the help you were able to give me during my recent post-doc search. Professor Marco Caricato, Professor James Blakemore, and Dr. Alan Allgeier, thank you all for agreeing to serve on my dissertation committee. I hope you enjoy the extra amount of time you will be spending reading about manganese.

There have been many others who have helped me be successful during my time at KU. Dr. Justin Douglas, thank you for teaching me so much and trusting me with the the EPR. Also, thank you so much for your patience when my EPR samples broke and when I had no clue what I was doing. Thank you Lawrence Seib for all of the help with mass spectrometry and general friendliness. Also, thank you to Dr. Victor Day for all of the help with crystal structures, even when I e-mail you two years later asking for specific details. Your work has been incredibly useful to my Ph. D. work.

I owe a lot of gratitude to many of the past and present Jackson group members. Domenick, thank you for leaving me with a great project and a solid foundation of skills with which to further it. Thank you Gayan for always being there to answer my question and being so helpful and inspirational in my post-doc search. Thank you Hannah for all of the walks to Wescoe to get our caffeine fix and general grad school guidance. Josh, you have been a great friend and I am glad to always have been able to count on you.

Melissa, I was selfishly so glad when I found out you were switching into our group. You have been a great lab-mate and friend. You taking me for walks has been one of the only things keeping me sane in grad school. I wish you and Josh the best of luck being the senior students when I am gone! Aruna, I am glad you have been trustworthy enough to take over most of my lab responsibilities. Yuri, you have been such a fun person to work with. I hope you continue to grow into a great chemist. Jaycee and Liz, I am glad you two join the group and I wish you tons of success. To the undergrads I have been fortunate enough to mentor, Louisa, Nicci, and Ellie- I am so glad I had to opportunity to work with you. It is exciting to see all of the success you have had and I look forward to all of your future success. Shannon, although I never directly worked with you, I am so thankful that you have been part of the group. Your constant curiosity and pursuit of understanding are inspirational. I also appreciate your friendship and I look forward to hearing about all of your future endeavors (and successes!). Anna, you always have the best stories to tell and you have made the lab a fun place. Andrew, we joined the Jackson lab at the same time and now we will be graduating together. It's been a fun time and I wish you the best.

The members of the Barybin group, Nate, Jason, and Mason, have also been very important to my time as a graduate student. Not only were you all around to help me open gas tanks when I was too weak and to answer my synthesis questions, but you have all been good friends. Many other KU chemistry graduate students have also been important to my time in grad school.

Of course I need to thank my family. Although you do not always understand why I am so stressed and crazy, you have always supported me. Thank you for raising me to appreciate education and always have a passion for going above and beyond and learning more.

Lastly, I must thank Derek, my lab-mate and partner. You have somehow managed to stick with me. I am glad we have got to share the grad school experience, even despite its ups and downs. I am so happy I have found someone to eat schnitzel and pork knuckle with during my post-doc adventures and hopefully beyond that! I am excited to see where life takes us, both as scientists and as partners. Thank you for being there for me and pushing me to be my best in everything.

Table of Contents

Abbreviations and Acronyms

Abs	absorption
BDE	bond dissociation enthalpy
BDFE	bond dissociation free energy
DFT	density functional theory
DHA	9,10-dihydroanthracene
DCM	dichloromethane
DMF	dimethylformamide
DPM	diphenylmethane
CASSCF	complete active space self-consistent field
COSMO	conductor-like screening model
CV	cyclic voltammetry
EPR	electron paramagnetic resonance
ESI-MS	electrospray ionization mass spectrometry
EtBn	ethylbenzene
EXAFS	extended X-ray absorption fine structure
GC-MS	gas-chromatography mass spectrometry
HAT	hydrogen atom transfer
IR	infrared
KIE	kinetic isotope effect
*m*CPBA	*m*-chloroperoxybenzoic acid
MCD	magnetic circular dichroism
MeCN	acetonitrile
MnSOD	manganese superoxide dismutase
MO	molecular orbital
NEVPT2	second-order-*N*-electron valence state perturbation theory
NMR	nuclear magnetic resonance
OEC	oxygen evolving center
PhIO	iodosobenzene
SOD	superoxide dismutase
SSRL	Stanford Synchrotron Radiation Lightsource

TD-DFT	time dependent density functional theory
TFE	2,2,2-trifluoroethanol
THF	tetrahydrofuran
Tol	toluene
TON	turn over number
TPM	triphenylmethane
UV	ultraviolet
XANES	X-ray absorption near-edge structure
XAS	X-ray absorption spectroscopy
XRD	X-ray diffraction
ZFS	zero field splitting

Chapter 1. Oxo and Peroxo-manganese Intermediates of Relevance to Biology and Catalysis

1.1 Introduction

The use of synthetic transition metal complexes to perform the oxidation of C-H bonds is widespread.[1-3] In nature, hydrogen atom transfer (HAT) reactions involving C-H bond cleavage are often performed by high-valent iron enzymes. In heme enzymes, like cytochrome P450, it has been shown that Compound I, an oxoiron(IV) species coupled to a porphyrin radical, is responsible for the oxidation of strong C-H bonds under ambient conditions.[4-5] Oxoiron(IV) species in several non-heme iron enzymes have also been shown to abstract hydrogen atoms from C-H bonds to give halogenation, hydroxylation, or desaturation products.[6-7] In non-heme enzyme systems, oxoiron(IV) species are found to have a *S*=2 (quintet) ground state. Because of the biological relevance, a wide variety of oxoiron(IV) model complexes have been prepared and extensively characterized.[8-9] Over 60 oxoiron(IV) model complexes have been isolated and their reactivity towards C-H bond-containing substrates has been broadly investigated.[8] However, most early synthetic models exhibited a *S*=1 (triplet) ground state. Further, while still quite reactive towards C-H bonds, many model systems react far more slowly than their related enzymes. Whether or not this is a consequence of the different spin state of their synthetic oxoiron(IV) complexes (*S*=1) is uncertain.

Analogous to oxoiron(IV) species, synthetic oxomanganese(IV) species have shown the ability to perform hydrogen atom transfer (HAT) reactions with C-H bonds of various strengths. However, in stark contrast to the over 60 examples of oxoiron(IV) complexes, there are only around 10 reported oxomanganese(IV) complexes that have been isolated and characterized. This work looks to investigate the effects of electronic structure on HAT reactivity of oxomanganese(IV) species using synthetic, kinetic, and spectroscopic methods.

1.2 Inspiration from Nature: Hydrogen-atom Transfer by Oxoiron(IV) Species

Our current understanding of the HAT reactivity of synthetic oxoiron(IV) species has developed from a variety of experimental and theoretical approaches taken by a number of different research groups. The first strategy was to create *S*=2 oxoiron(IV) species by changing the geometry from *pseudo*-octahedral to trigonal-bipyramidal

(Scheme 1.1).[8] A representative example of a trigonal-bipyramidal *S*=2 complex is $[Fe^{IV}(O)(TMG_3tren)]^{2+}$ (Figure 1.1).[10] The use of bulky ligands enforces the trigonal-bipyramidal geometry.[10] This *S*=2 complex was expected to perform C-H oxidation much faster than the synthetic *S*=1 oxoiron(IV) species. However, a comparison study showed that $[Fe^{IV}(O)(TMG_3tren)]^{2+}$ reacted with the small, weak C-H bond containing substrate, 1,4-cyclohexadiene, at nearly the same rate the *S*=1 $[Fe^{IV}(O)(N4py)]^{2+}$ complex (Figure 1.1).[10] When reacting with a larger substrate, 9,10-dihydroanthracene, $[Fe^{IV}(O)(N4py)]^{2+}$ actually reacts much more rapidly $[Fe^{IV}(O)(TMG_3tren)]^{2+}$, likely due to the steric encumbrance of the bulky TMG_3tren ligand in the latter complex (Figure 1.1).[10] Efforts to produce *S*=2 trigonal-bipyramidal oxoiron(IV) complexes have largely been hampered by instability and steric constraints of the bulky ligands.[8]

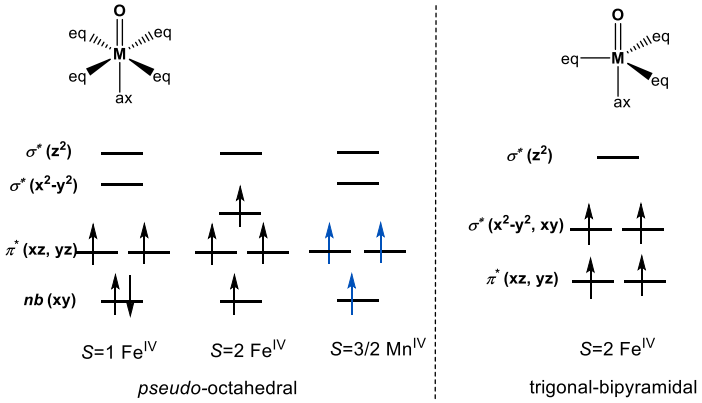

Scheme 1.1. Expected d-orbital splitting patterns for oxoiron(IV) (black) and oxomanganese(IV) species for *pseudo*-octahedral (right) and trigonal bipyramidal (left) geometries.

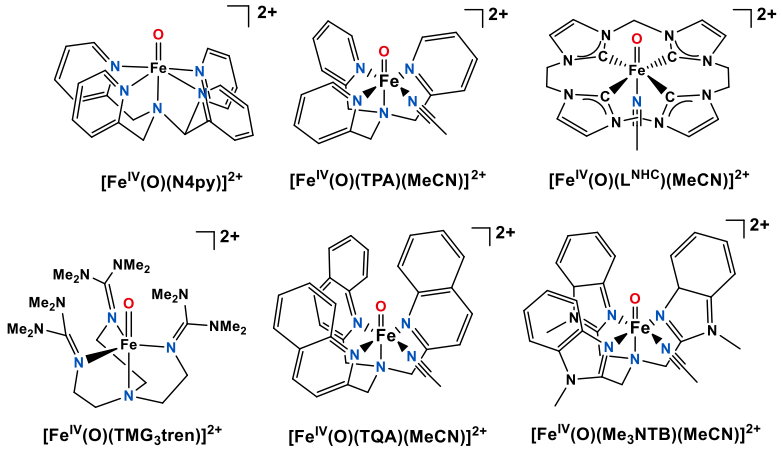

Figure 1.1. Molecular structures of several oxoiron(IV) species.

Another approach to isolating a *S*=2 oxoiron(IV) species was to modulate the ligand field of the *pseudo*-octahedral supporting ligand. Weak-field ligands (or sterically-encumbered) ligands can lower the energy of the σ^* $d_{x^2-y^2}$ orbital, thus allowing for the promotion of one of the usually paired (for *S*=1) d_{xy} electrons into the $d_{x^2-y^2}$ orbital (Scheme 1.1). This perturbation was first achieved by replacing the pyridines of the *S*=1 complex $[Fe^{IV}(O)(TPA)(MeCN)]^{2+}$ with quinoline groups to create $[Fe^{IV}(O)(TPA)(MeCN)]^{2+}$ (Figure 1.1).[11] The weakened equatorial field resulted in an *S*=2 ground state for $[Fe^{IV}(O)(TPA)(MeCN)]^{2+}$.[11] The rate of reaction with cyclohexane of $[Fe^{IV}(O)(TPA)(MeCN)]^{2+}$ at -40 ºC is 3-4 orders of magnitude faster than that of $[Fe^{IV}(O)(N4py)]^{2+}$ at room temperature.[11-12] More impressively, the rate of cyclohexane oxidation by of $[Fe^{IV}(O)(TPA)(MeCN)]^{2+}$ is comparable to the rate of taurine oxidation by the oxoiron(IV) intermediate of the nonheme iron enzyme TauD.[11, 13]

While efforts to characterize *S*=2 oxoiron(IV) species led to very reactive intermediates, it is still important to understand why many *S*=1 species also show impressive reactivity. To explain the slower, but still significant reactivity of many *S*=1 oxoiron(IV) species, a two-state reactivity (TSR) model was proposed. In this mode, complexes with an *S*=1 ground state access a low-lying *S*=2 excited state that provides a lower transition barrier for HAT.[14-16] This model is supported by the observation of very large kinetic isotope effects (KIE) in substrate oxidation, which is predicted by theory for *S*=2 ground or excited state reactivity pathways.[17] A prime example of a highly reactive oxoiron(IV) species with a *S*=1 ground state is $[Fe^{IV}(O)(Me_3NTB)(MeCN)]^{2+}$ (Figure 1.1).[18] The reactivity of $[Fe^{IV}(O)(Me_3NTB)(MeCN)]^{2+}$ towards cyclohexane is nearly as fast as that of $[Fe^{IV}(O)(TPA)(MeCN)]^{2+}$ despite the difference in ground states (*S*=1 versus *S*=2, respectively.[11, 18] The rapid reactivity of $[Fe^{IV}(O)(Me_3NTB)(MeCN)]^{2+}$ was attributed to a theoretically-determined very-low lying *S*=2 excited state.[18]

However, a recent study using a very unique, strong sigma-donating ligand, L^{NHC}, allowed for the formation of $[Fe^{IV}(O)(L^{NHC})(MeCN)]^{2+}$ (Figure 1.1).[19-21] This ligand causes the σ^* $d_{x^2-y^2}$ orbital to be strongly destabilized due to the strong sigma-bonding interactions with the tetracarbene ligand. The d-orbital splitting of this complex is similar to that of the *pseudo*-octahedral d-orbital splitting (Scheme 1.1, left) except for the $d_{x^2-y^2}$ orbital, which

is now much higher in energy than the d_{z^2} orbital.[20] This unusual electronic structure confines the oxoiron(IV) species to the triplet pathway, due to the large gap between the empty and full d-orbitals.[21] Interestingly, the *S*=1 $[Fe^{IV}(O)(L^{NHC})(MeCN)]^{2+}$ is more reactive in HAT reactions than an analogous *S*=1 complex, for which an *S*=2 excited state is proposed to be involved in HAT reactions.[21]

Throughout these representative studies, as well as many others, significant insight has come from looking at the effects of electronic structure on oxoiron(IV) HAT reactivity. Although there are still open questions, mainly regarding the TSR model, many general trends in reactivity have been elucidated.

1.3 Significance of Hydrogen-atom Transfer by Oxomanganese(IV) Species

The influences of electronic structure on HAT reactivity of oxomanganese(IV) is more poorly understood relative to oxoiron(IV) species, where some general trends regarding HAT reactivity have been noted. The few examples of non-porphyrin oxomanganese(IV) species that perform HAT can be seen in Figure 1.2. The only other examples missing from Figure 1.2 are two oxomanganese(IV) species supported by isomeric bispidine ligands and those that will be discussed later within this body of work.[22] This limited set of complexes features very diverse ligands, which give rise to differences in coordination number, complex charges, and Mn^{IV} geometry. Further, comparison of reactivity (Table 1.1) is complicated by the use of different solvents, temperatures, and C-H bond containing substrates. One particular substrate, 9,10-dihydroanthracene (DHA), which has fairly weak C-H bonds (BDE 76 kcal mol^{-1}), provides a good point of comparison of reactivity between these complexes and has been used as a probe of reactivity for most of these complexes.[23]

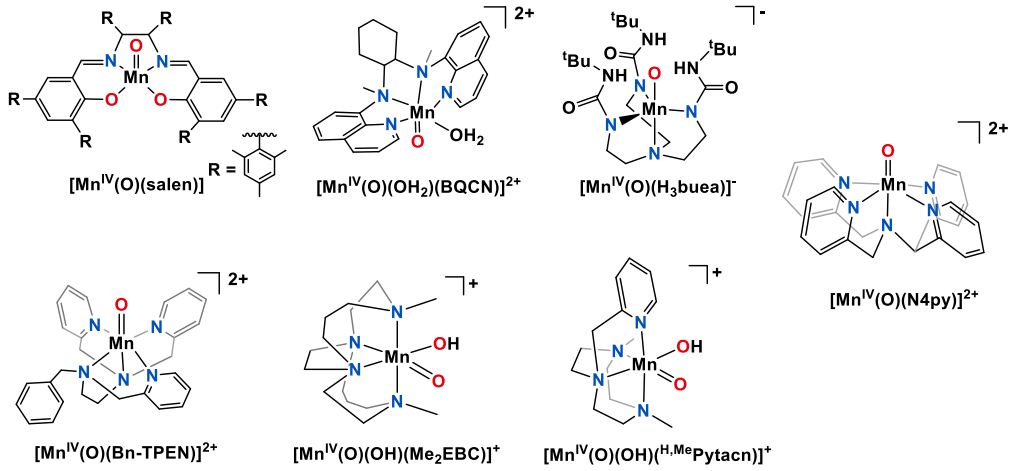

Figure 1.2. Molecular structures of oxomanganese(IV) that have been shown to perform HAT reactions. Structures are inferred from a variety of spectroscopic techniques and in some cases, DFT computations as no XRD structures currently exist for oxomanganese(IV) species.

Table 1.1 Second order rate constants for the reaction with DHA and reduction potentials for several oxomanganese(IV) species.

Complex	k_2 (DHA) (M^{-1} s^{-1})	Temp. (K)	Reduction Potential (mV)[a]	Ref
$[Mn^{IV}(O)(N4py)]^{2+}$	3.6	298	750	24
$[Mn^{IV}(O)(OH_2)(BQCN)]^{2+}$	0.12	273	N/R[b]	25
$[Mn^{IV}(O)(H_3buea)]^{-}$	0.10	293	-570	26
$[Mn^{IV}(O)(OH)(Me_2EBC)]^{+}$	0.060	288	515	27
$[Mn^{IV}(O)(OH)(^{H,Me}Pytacn)]^{+}$	0.026	298	160	28
$[Mn^{IV}(O)(Bn\text{-}TPEN)]^{2+}$	N/R[b]	298	780	29
$[Mn^{IV}(O)(salen)]$	0.00011[c]	203	N/R[b]	30

[a] mV versus Saturated Calomel Electrode (SCE) [b] Not reported [c] k_{obs} with 100 equivalents of DHA.

One of the earliest reported oxomanganese(IV) species, $[Mn^{IV}(O)(salen)]$ (Figure 1.2), is supported by a dianionic tetradentate ligand and can be formed from the oxidation of Mn^{III} starting material by either *m*-chloroperoxybenzoic acid (*m*-CPBA) or ozone.[30-31] $[Mn^{IV}(O)(salen)]$ shows very rapid reactivity (> 100 M^{-1} s^{-1}) with the O-H bonds of substituted phenols that have a bond dissociation enthalpy (BDE) of 81- 85 kcal mol^{-1}.[31] However, when reacted with the much weaker C-H bond of 1,4-cyclohexadiene (76 kcal mol^{-1}), the second order rate, k_2, was only 0.023 M^{-1} s^{-1}, despite the much weaker bond.[31] With the slightly stronger C-H bonds of DHA, $[Mn^{IV}(O)(salen)]$ exhibited an observed rate constant of 0.00011 s^{-1} when reacted with 100 eqivalents of DHA.[30] However, these

reactivity studies were performed at -70 ºC, which is probably why these rates seem so low. The use of low temperature makes comparing the reactivity of these complexes to the others quite difficult.

Two different oxomanganese(IV) complexes feature an hydroxo moiety alongside the terminal oxo unit, $[Mn^{IV}(O)(OH)(Me_2EBC)]^+$ and $[Mn^{IV}(O)(OH)(^{H,Me}Pytacn)]^+$ (Figure 1.2).[27-28, 32-35] Both complexes were prepared by a deprotonation of a dihydroxomanganse(IV) species.[28, 32] These complexes offer a comparison for the reactivity of the hydroxo and the oxo moieties. Although these complexes show only modest HAT rates (Table 1.1), they both show that the terminal oxo performs HAT reactions faster than the corresponding di-hydroxo species (rate enhancements ~ XXfold).[27-28] A similar complex, $[Mn^{IV}(O)(OH_2)(BQCN)]^{2+}$(Figure 1.2), is prepared using water as an oxygen source and cerium(IV) ammonium nitrate (CAN) as a one-electron oxidant.[25] $[Mn^{IV}(O)(OH_2)(BQCN)]^{2+}$, however features water as a ligand in the sixth coordination site instead of the anionic hydroxo ligand. It must be noted that the formulation of the sixth ligand as water comes only from ambiguous mass spectrometry data that suggest either a dihydroxo species or an oxo species with a water bound. Their formulation of an oxomanganese(IV) species is further supported by Mn-O vibrational data, but it remains that the exact identity of the sixth ligand is unclear. Although this complex is investigated at a lower temperature than either $[Mn^{IV}(O)(OH)(Me_2EBC)]^+$ or $[Mn^{IV}(O)(OH)(^{H,Me}Pytacn)]^+$, it still reacts more rapidly with DHA (Table 1.1).

The trigonal bipyramidal oxomanganese(IV) species $[Mn^{IV}(O)(H_3buea)]^-$ (Figure 1.2), is the only example that features both a tri-anionic supporting ligand and a Mn^{IV} center in a trigonal bipyramidal environment.[36] This oxomanganese(IV) species is prepared by treating the oxomanganese(III) starting material with the one-electron oxidant ferrocenium tetrafluoroborate.[36] As shown in Table 1.1, $[Mn^{IV}(O)(H_3buea)]^-$ shows moderate reactivity with DHA even though this complex has a very negative reduction potential.[26] It has been postulated that $[Mn^{IV}(O)(H_3buea)]^-$ is able to oxidize substrate C-H bonds due to the basicity of the terminal oxo ligand.[26] $[Mn^{IV}(O)(H_3buea)]^-$ and $[Mn^{IV}(O)(OH)(Me_2EBC)]^+$ represent the only examples where the basicity of the oxo ligand has been determined.[26]

Lastly, the bulk of this work will focus on oxomanganese(IV) species supported by neutral, pentadentate ligands, such as those seen in $[Mn^{IV}(O)(Bn\text{-}TPEN)]^{2+}$ and $[Mn^{IV}(O)(N4py)]^{2+}$ (Figure 1.2).[24, 37-38] Although the reactivity of $[Mn^{IV}(O)(Bn\text{-}TPEN)]^{2+}$ towards DHA is unknown, reactivity with another substrate, ethlybenzene, allows for a comparison with the reactivity of $[Mn^{IV}(O)(N4py)]^{2+}$. For ethylbenzene, the k_2 is 2.7 x 10^{-2} and 2.7 x 10^{-3} M^{-1} s^{-1} for $[Mn^{IV}(O)(Bn\text{-}TPEN)]^{2+}$ and $[Mn^{IV}(O)(N4py)]^{2+}$, respectively.[24, 38] In general, it can be seen that these two oxomanganese(IV) species react much more quickly than the other complexes. The reactivity of $[Mn^{IV}(O)(Bn\text{-}TPEN)]^{2+}$ and $[Mn^{IV}(O)(N4py)]^{2+}$ is substantially higher than other oxomanganese(IV) species, and approaches the rates observed for oxoiron(IV) reactivity. The basis for the enhanced reactivity of $[Mn^{IV}(O)(Bn\text{-}TPEN)]^{2+}$ and $[Mn^{IV}(O)(N4py)]^{2+}$ is currently unclear. Both thermodynamic[24] and excited-state reactivity[39] arguments have been offered to explain the reactivity.[40] This work focuses on $[Mn^{IV}(O)(N4py)]^{2+}$ because it shows rapid reactivity with a wide range of C-H bonds as well having a ligand framework that is amenable to systematic perturbations, which allow for further insight into electronic structure effects on HAT reactivity.

We postulated that the high reactivity of $[Mn^{IV}(O)(N4py)]^{2+}$ is caused by its high $Mn^{III/IV}$ reduction potential (+800 mV versus SCE). In comparison, $[Mn^{IV}(O)(OH)(^{H,Me}Pytacn)]^{+}$ reacts 100-times more slowly with DHA than $[Mn^{IV}(O)(N4py)]^{2+}$ and has a much lower $Mn^{III/IV}$ reduction potential (+50 mV versus SCE).[28] However, the thermodynamic driving force for a HAT reaction depends on both the $Mn^{III/IV}$ reduction potential and the basicity of the Mn^{III}-hydroxo product. The importance of basicity is highlighted by comparison with $[Mn^{IV}(O)(H_3buea)]^{-}$ which has an exceptionally low $Mn^{III/IV}$ potential of -570 mV versus SCE but shows a DHA oxidation rate only slightly less than that of $[Mn^{IV}(O)(N4py)]^{2+}$.[26] Thus, a proper understanding of reactivity requires knowledge of the basicity of the Mn^{III}-hydroxo product complexes, which, at present, is lacking for the majority of these species.

An alternative description of the enhanced HAT reactivity of $[Mn^{IV}(O)(N4py)]^{2+}$ was offered by Nam and Shaik.[39] Their DFT calculations suggested a two-state reactivity model, where a ^4E excited state offers a lower-energy transition state for HAT than the

$^4B_1$ ground state (Figure 1.3). Because the ^4E excited state differs from the $^4B_1$ ground-state by an $e(d_{xz},d_{yz})\rightarrow b_1(d_{x^2-y^2})$ excitation (*i.e.*, a Mn^{IV}-based *d-d* transition), we set-out to identify the ^4E excited state using magnetic circular dichroism (MCD) spectroscopy. Excited states with actual, or near, orbital degeneracy, such as the ^4E state in question, appear in an MCD spectrum as a pseudo-*A* term; a derivative-shaped signal whose intensity increases at low temperature. Electronic absorption and MCD data collected for $[Mn^{IV}(O)(N4py)]^{2+}$ show that the near-IR absorption band at 10 500 cm^{-1} appears as a pseudo-*A* term in the corresponding MCD spectrum (Figure 1.4), allowing us to assign this near-IR feature as the $^4B_1\rightarrow{}^4E(e(d_{xz},d_{yz})\rightarrow b_1(d_{x^2-y^2}))$ transition.[41] Electronic structure calculations and a graphical analysis of the pseudo-*A* term sign lent further support to the assignment.

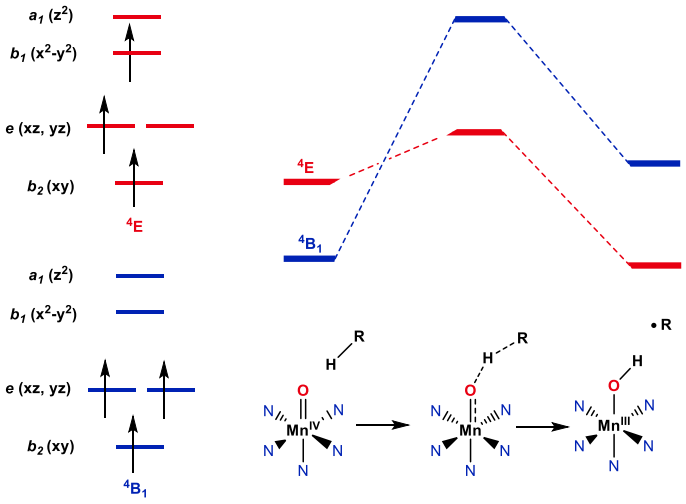

Figure 1.3 Electron configurations for $^4B_1$ and ^4E states (left) and qualitative HAT reaction coordinate based on DFT computations from ref.[39] (right).

The work described in chapter 2 describes our approach at probing the effects of systematically tuning the energy of the ^4E excited state.[42] The synthesis and characterization of novel oxomanganese(IV) species based on the N4py ligand scaffold allows for a detailed investigation of the effects of electronic structure on HAT reactivity. Although still not as widely studied as oxoiron(IV) species, oxomanganese(IV) species have been shown to perform HAT reactions, albeit at a slower rate. A further understanding of the reactivity differences between oxoiron(IV) and oxomanganese(IV) species can help shed light on the synthetic usefulness of both species.

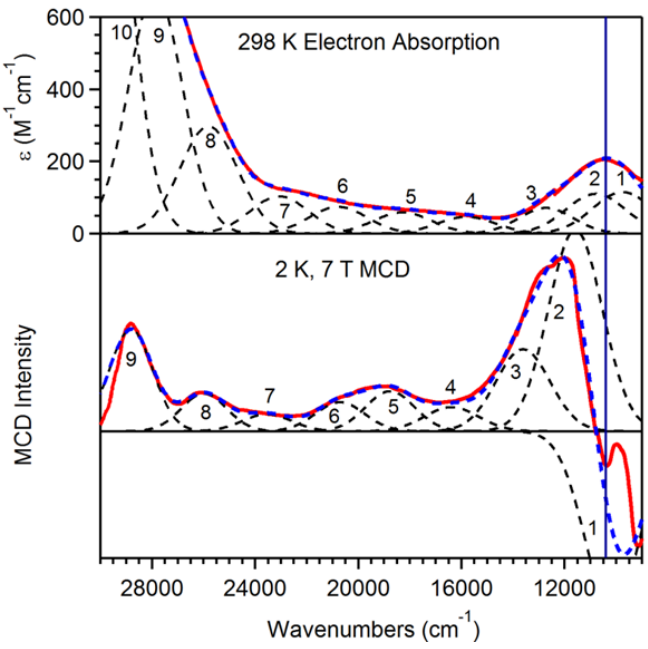

Figure 1.4. Electronic absorption (top) and MCD (bottom) spectra of $[Mn^{IV}(O)(N4py)]^{2+}$. Individual Gaussian curves (dashed black traces) and their sums (dashed blue traces) are displayed. The vertical line at 10 500 cm^{-1} shows correspondence between the near-IR absorption maxima and the center of the MCD pseudo-A term.

1.4 Spectroscopic Techniques for Characterization of Manganese Intermediates

Unlike oxoiron(IV) species, for which many complexes have been structurally characterized by X-ray diffraction (XRD), there have been no crystal structures reported for oxomanganese(IV) species. However, a wide range of spectroscopic methods, often supported by theoretical calculations, have been employed to understand the structures of these intermediates. One of the most useful spectroscopic technique is UV-visible spectroscopy. *Pseudo*-octahedral oxomanganese(IV) species are characterized by a broad, lower-intensity feature in the near-IR region of the UV-visible spectra. For example, the $[Mn^{IV}(O)(N4py)]^{2+}$ complex shows a weak absorption band at 950 nm, whereas the trigonal-bipyramidal $[Mn^{IV}(O)(H_3buea)]^-$ has a less broad absorption band that occurs at a higher energy (635 nm).[24, 36, 43] Magnetic circular dichroism (MCD) spectroscopy, supported by time-dependent (TD) DFT and CASSCF/NEVPT2 computations, led to the assignment this feature as a $^4B_1 \rightarrow {}^4E$ transition, corresponding to a one-electron excitation from the Mn^{IV} $e(d_{xz},d_{yz})$ to the $b_1(d_{x^2-y^2})$ orbital (bands 1 and 2 in Figure 1.4).[41] The energy

of this transition is expected to shift with the energy of the x^2-y^2 d orbital. Many of these complexes have also been characterized by electrospray ionization mass spectrometry (ESI-MS). [24, 30, 42-43]

Table 1.2 λ_{max} and extinction coefficient data for selected oxomanganese(IV) species.

Complex	λ_{max} (nm)	ε (M^{-1} cm^{-1})	Temp. (K)	Ref
$[Mn^{IV}(O)(N4py)]^{2+}$	950	250	298	24, 43
$[Mn^{IV}(O)(OH_2)(BQCN)]^{2+}$	630	400	273	25
$[Mn^{IV}(O)(H_3buea)]^{-}$	635	2000[a]	293	26
$[Mn^{IV}(O)(OH)(Me_2EBC)]^{+}$	870	150	288	34
$[Mn^{IV}(O)(OH)(^{H,Me}Pytacn)]^{+}$	825	190[a]	298	28
$[Mn^{IV}(O)(Bn\text{-}TPEN)]^{2+}$	1040	220	298	29

[a] Estimated from reported electronic absorption spectra and concentration.

Due to the *S*=3/2 ground states of all known oxomanganese(IV) centers, the characterization of these complexes by ^{1}H nuclear magnetic resonance (NMR) is hindered by rapid spin relaxation. Instead, characterization of the electronic ground states of oxomanganese(IV) species is done using electron paramagnetic resonance (EPR) spectroscopy. EPR is useful tool for probing the environment of a paramagnetic center through its interaction with an applied magnetic field.[44] The orientation of unpaired electrons in a magnetic field give rise to two (or more) energetically different spin sublevels (m_s states), which show a differential population at low temperatures. The transition to the less-populated energy state(s) (resonance) is achieved through application of electromagnetic radiation. Often, the magnetic field is varied, and the field strength at which a resonance signal appears is characteristic of different metals, spin states, and even geometry around the metal center. Further information can also be gained from the interaction of the unpaired electron(s) with nearby atomic nuclei with a non-zero nuclear spin (hyperfine coupling). From this information, once can gain insight into the number of unpaired electrons, oxidation state, and in ideal cases, information about the coordination sphere. All of the complexes shown in Figure 1.2 have been characterized by EPR spectroscopy. [24-25, 28, 30, 36, 38, 43, 45] EPR has been used to characterize all of these complexes as *S*=3/2 ground state.

Structural information on many of these complexes comes from X-ray absorption spectroscopy (XAS). For manganese species, Mn K-edge XAS can be used to determine

metal-ligand bond distances without the need for crystalline material. However, this technique requires the use of high-intensity, tunable X-rays that come from synchrotron radiation. K-edge XAS spectra are characterized by two regions. The first is the X-ray absorption near edge structure (XANES), which is within about 10 eV of the K-edge. The XANES regions consists of the K-edge absorption feature and pre-edge features. The energy of the K-edge absorption comes from the metal 1s-to-4p transition, and is sensitive to the metal its oxidation state. The pre-edge features come from the 1s-to-3d transitions that have a low XAS intensity because this is a parity-forbidden transition. However, metal 3d-4p mixing due to low symmetry and/ or metal-ligand covalency provides intensity to pre-edge features.[46] The second region of the XAS spectra is the extended X-ray absorption fine structure (EXAFS), which is beyond the K-edge. The EXAFS region consists of the physical interaction of the photodissociated 1s electron with electron density surrounding the metal atom. The photoelectron scattering influences the absorption coefficient of the X-ray photon, giving rise to modulations in the EXAFS signal as a function of the kinetic energy of the photoelectron. A careful analysis of EXAFS data provides information about the coordination sphere of the metal complex, including information on the coordination number, and the identity of scattering atoms. Several of the complexes listed in Figure 1.2 have been characterized by XAS.[24, 30, 38, 43, 47] The analysis of the EXAFS region to provide structural information is often strengthened by the use of density functional theory (DFT) calculations, which typically provides Mn-ligand bond distances in good agreement those obtained from fitting EXAFS data. Thus, although no crystal structure information is available for oxomanganese(IV) complexes, there are still a wide range of spectroscopic techniques that can provide valuable information on the geometric and electronic structures of these complexes.

1.5 Electrochemical Generation of Peroxomanganese(III) Species

The study of peroxomanganese(III) species takes more direct inspiration from nature. Several manganese enzymes react with dioxygen and its reduced species ($O_2^{\bullet-}$, H_2O_2, H_2O) for a wide range of biological functions.[48-49] Peroxomanganese(III) species are often invoked as important intermediates in many of these enzymes. This is bolstered by the structural characterization of a peroxomanganese(III) adduct of Mn superoxide dismutase (MnSOD) adduct, which was formed by soaking cryotrapped MnSOD with peroxide.[50] The proposed mechanism of MnSOD requires acid to cleave the Mn-O bond of the peroxomanganese intermediate to give H_2O_2 and a Mn^{III} center.[49] In contrast, synthetic Mn/H_2O_2 catalysts feature Mn-peroxo intermediates that are postulated to undergo O–O bond cleavage to yield high-valent Mn-oxo species.[51-52] This variation in reactivity has fostered interest in identifying factors controlling O–O versus Mn–O bond cleavage for Mn-peroxo adducts.[53]

A wide range of synthetic peroxomanganese(III) complexes have been characterized by many groups. Several mononuclear peroxomanganese(III) species have demonstrated the ability to act as nucleophiles to perform the deformylation of aldehydes.[54-61] However, there is less understanding about the factors that influence the cleavage of either the Mn-O or O-O bond.[40, 53, 59, 62-65] There are often difficulties involved in forming peroxomanganese(III) intermediate, including formation only in low yield, high reactivity of intermediates, or unwanted side products. These problems limit the reactivity studies of peroxomanganese(III) species.

The formation of peroxomanganese(III) species from electrochemically generated superoxide avoids many of the side products and allows for the formed peroxomanganese(III) species to be further probed with cyclic voltammetry (CV).[63, 66] The electrochemical generation of superoxide allowed for the formation and characterization of a peroxomanganese(III) species, $[Mn^{III}L(O_2)]$, supported by an N_4O^- ligand, L (LH= *N*-(2-hydroxybenzyl)-*N,N'*-bis[2-*N*-methylimidazolyl)methyl]ethane-1,2-diamine) (Figure 1.5).[63] In the presence of a strong acid, $HClO_4$, $[Mn^{III}L(O_2)]$ shows evidence for the cleavage of the Mn-O bond with the release of H_2O_2. However, in the presence of a weak acid, H_2O, there is a cleavage of the O-O bond in a concerted dissociative two-electron transfer. While $[Mn^{III}L(O_2)]$ offers very interesting insights into the factors that influence

O-O versus Mn-O cleavage, the redox active phenolate-containing ligand complicates mechanistic studies. Additionally, the Mn-based products of the bond cleavage events, in particular the O-O bond cleavage are very unstable, leaving them uncharacterized.

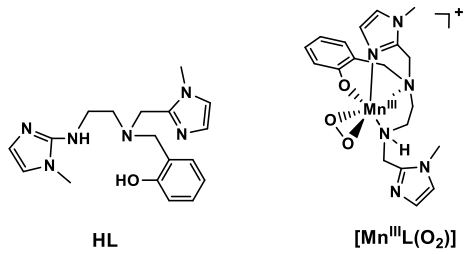

Figure 1.5. Molecular structures of protonated ligand, HL, and superoxide generated $[Mn^{III}L(O_2)]$.

Additional evidence of O–O bond activation of a Mn^{III}-peroxo species came from studies of $[Mn^{III}(O_2)(\kappa^4\text{-N4py})]^+$ (N4py=*N*,*N*-bis(2-pyridylmethyl)-*N*-bis(2-pyridyl)methylamine; Scheme 1.2).[64] Spectroscopic and computational methods were used to demonstrate that $[Mn^{III}(O_2)(\kappa^4\text{-N4py})]^+$ featured a side-on (η^2) peroxo with N4py bound in an unusual tetradentate fashion, giving a six-coordinate Mn^{III} center.[67] The $[Mn^{III}(O_2)(\kappa^4\text{-N4py})]^+$ complex was unique among Mn^{III}-peroxo adducts known to date, as it could only be generated upon reaction of the Mn^{II} compound with O_2^-.[64, 66-67] Commonly, Mn^{III}-peroxo species can be accessed by oxidation with either O_2^- or H_2O_2 and base. Treatment of $[Mn^{II}(N4py)(OTf)]^+$ with H_2O_2 led to the formation of the oxo-bridged dimer $[Mn^{III}Mn^{IV}(\mu\text{-}O)_2(\kappa^4\text{-N4py})_2]^{3+}$ (Scheme 1.2). Crystallographic characterization of $[Mn^{III}Mn^{IV}(\mu\text{-}O)_2(\kappa^4\text{-N4py})_2]^{3+}$ confirmed the tetradentate binding mode of the N4py ligand.[64] $[Mn^{III}Mn^{IV}(\mu\text{-}O)_2(\kappa^4\text{-N4py})_2]^{3+}$ also forms when the $[Mn^{III}(O_2)(\kappa^4\text{-N4py})]^+$ complex reacts with $[Mn^{II}(N4py)(OTf)]^+$, implying O–O bond activation assuming that the oxo bridges in the resulting $[Mn^{III}Mn^{IV}(\mu\text{-}O)_2(\kappa^4\text{-N4py})_2]^{3+}$ complex originate from the peroxo unit of $[Mn^{III}(O_2)(\kappa^4\text{-N4py})]^+$ (Scheme 1.2).

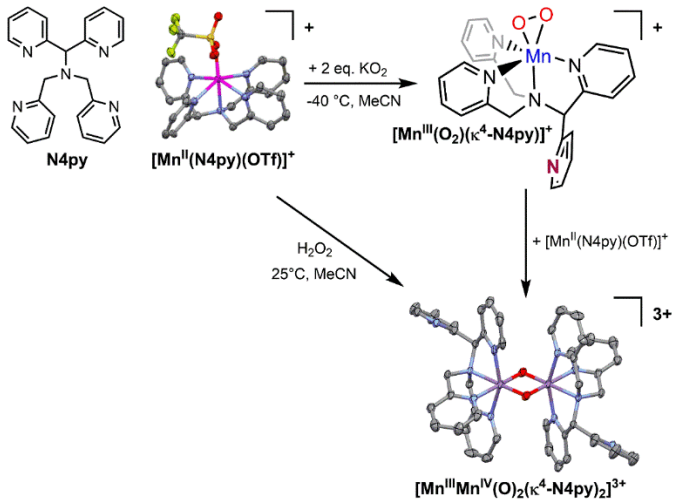

Scheme 1.2 Reactions of $[Mn^{II}(N4py)(OTf)]^{+}$ upon treatment with KO_2 and H_2O_2.

Although the observations for $[Mn^{III}(O_2)(\kappa^4\text{-N4py})]^{+}$ suggest O–O bond activation to generate a high-valent species, the resulting $[Mn^{III}Mn^{IV}(\mu\text{-}O)_2(\kappa^4\text{-N4py})]^{3+}$ complex is very stable and not particularly reactive towards C–H bonds. In contrast, our lab[24] and Nam and co-workers[43] separately reported the mononuclear Mn^{IV}-oxo analogue, $[Mn^{IV}(O)(N4py)]^{2+}$ that is reactive towards C–H bonds. Unlike the $[Mn^{III}(O_2)(\kappa^4\text{-N4py})]^{+}$ complex, $[Mn^{IV}(O)(N4py)]^{2+}$ presumably features the N4py ligand bound in a pentadentate fashion. Thus, conversion of $[Mn^{III}(O_2)(\kappa^4\text{-N4py})]^{+}$ to $[Mn^{IV}(O)(N4py)]^{2+}$ would require re-coordination of the dangling pyridine ligand. Ligand rearrangement was seen to be a problem with $[Mn^{III}L(O_2)]$ as well.[63] The relatively few examples of peroxomanganese(III) systems that show O-O bond activation reveals a considerable gap in knowledge. Further insight into the activation of dioxygen by peroxomanganese(III) species could provide a unique way to access reactive, high valent oxomanganese species using fairly benign oxidants such as dioxygen, superoxide, or hydrogen peroxide.

1.6 Notes and References

1. Gunay, A.; Theopold, K. H., C-H Bond Activations by Metal Oxo Compounds. *Chem. Rev.* **2010,** *110*, 1060.

2. Liu, W.; Ackermann, L., Manganese-Catalyzed C–H Activation. *ACS Catalysis* **2016,** *6* (6), 3743-3752.

3. Shang, R.; Ilies, L.; Nakamura, E., Iron-Catalyzed C–H Bond Activation. *Chem. Rev.* **2017,** *117* (13), 9086-9139.

4. Rittle, J.; Green, M. T., Cytochrome P450 Compound I: Capture, Characterization, and C-H Bond Activation Kinetics. *Science* **2010,** *330* (6006), 933-937.

5. Huang, X.; Groves, J. T., Oxygen Activation and Radical Transformations in Heme Proteins and Metalloporphyrins. *Chem. Rev.* **2017**.

6. Wong, S. D.; Srnec, M.; Matthews, M. L.; Liu, L. V.; Kwak, Y.; Park, K.; Bell Iii, C. B.; Alp, E. E.; Zhao, J.; Yoda, Y.; Kitao, S.; Seto, M.; Krebs, C.; Bollinger, J. M.; Solomon, E. I., Elucidation of the Fe(iv)=O intermediate in the catalytic cycle of the halogenase SyrB2. *Nature* **2013,** *499*, 320.

7. Srnec, M.; Wong, S. D.; Matthews, M. L.; Krebs, C.; Bollinger, J. M.; Solomon, E. I., Electronic Structure of the Ferryl Intermediate in the α-Ketoglutarate Dependent Non-Heme Iron Halogenase SyrB2: Contributions to H Atom Abstraction Reactivity. *J. Am. Chem. Soc* **2016,** *138* (15), 5110-5122.

8. Puri, M.; Que, L., Toward the Synthesis of More Reactive S = 2 Non-Heme Oxoiron(IV) Complexes. *Acc. Chem. Rev.* **2015,** *48* (8), 2443-2452.

9. Nam, W., Synthetic Mononuclear Nonheme Iron–Oxygen Intermediates. *Acc. Chem. Res.* **2015,** *48* (8), 2415-2423.

10. England, J.; Martinho, M.; Farquhar, E. R.; Frisch, J. R.; Bominaar, E. L.; Münck, E.; Que, L., A Synthetic High-Spin Oxoiron(IV) Complex: Generation, Spectroscopic Characterization, and Reactivity. *Angewandte Chemie International Edition* **2009,** *48* (20), 3622-3626.

11. Biswas, A. N.; Puri, M.; Meier, K. K.; Oloo, W. N.; Rohde, G. T.; Bominaar, E. L.; Münck, E.; Que Jr., L., Modeling TauD-J: A High-Spin Nonheme Oxoiron(IV) Complex with High Reactivity toward C–H Bonds. *J. Am. Chem. Soc* **2015,** *137* (7), 2428-2431.

12. Kaizer, J.; Klinker, E. J.; Oh, N. Y.; Rohde, J.-U.; Song, W. J.; Stubna, A.; Kim, J.; Münck, E.; Nam, W.; Que Jr., L., Nonheme FeIVO Complexes That Can Oxidize the C−H Bonds of Cyclohexane at Room Temperature. *J. Am. Chem. Soc* **2004,** *126* (2), 472-473.

13. Price, J. C.; Barr, E. W.; Glass, T. E.; Krebs, C.; Bollinger, J. M., Evidence for Hydrogen Abstraction from C1 of Taurine by the High-Spin Fe(IV) Intermediate Detected during Oxygen Activation by Taurine:α-Ketoglutarate Dioxygenase (TauD). *J. Am. Chem. Soc* **2003,** *125* (43), 13008-13009.

14. Shaik, S.; Hirao, H.; Kumar, D., Reactivity of High-Valent Iron–Oxo Species in Enzymes and Synthetic Reagents: A Tale of Many States. *Acc. Chem. Res.* **2007,** *40* (7), 532-542.

15. Cho, K.-B.; Hirao, H.; Shaik, S.; Nam, W., To rebound or dissociate? This is the mechanistic question in C-H hydroxylation by heme and nonheme metal-oxo complexes. *Chem. Soc. Rev.* **2016,** *45* (5), 1197-1210.

16. Mandal, D.; Shaik, S., Interplay of Tunneling, Two-State Reactivity, and Bell–Evans–Polanyi Effects in C–H Activation by Nonheme Fe(IV)O Oxidants. *J. Am. Chem. Soc* **2016,** *138* (7), 2094-2097.

17. Klinker, E. J.; Shaik, S.; Hirao, H.; Que, L., A Two-State Reactivity Model Explains Unusual Kinetic Isotope Effect Patterns in C□H Bond Cleavage by Nonheme Oxoiron(IV) Complexes. *Angewandte Chemie International Edition* **2009,** *48* (7), 1291-1295.

18. Seo, M. S.; Kim, N. H.; Cho, K.-B.; So, J. E.; Park, S. K.; Clemancey, M.; Garcia-Serres, R.; Latour, J.-M.; Shaik, S.; Nam, W., A mononuclear nonheme iron(iv)-oxo complex which is more reactive than cytochrome P450 model compound I. *Chemical Science* **2011,** *2* (6), 1039-1045.

19. Meyer, S.; Klawitter, I.; Demeshko, S.; Bill, E.; Meyer, F., A Tetracarbene–Oxoiron(IV) Complex. *Angewandte Chemie International Edition* **2013,** *52* (3), 901-905.

20. Ye, S.; Kupper, C.; Meyer, S.; Andris, E.; Navrátil, R.; Krahe, O.; Mondal, B.; Atanasov, M.; Bill, E.; Roithová, J.; Meyer, F.; Neese, F., Magnetic Circular Dichroism Evidence for an Unusual Electronic Structure of a Tetracarbene–Oxoiron(IV) Complex. *Journal of the American Chemical Society* **2016,** *138* (43), 14312-14325.

21. Kupper, C.; Mondal, B.; Serrano-Plana, J.; Klawitter, I.; Neese, F.; Costas, M.; Ye, S.; Meyer, F., Nonclassical Single-State Reactivity of an Oxo-Iron(IV) Complex Confined to Triplet Pathways. *Journal of the American Chemical Society* **2017,** *139* (26), 8939-8949.

22. Comba, P.; Maurer, M.; Vadivelu, P., Oxidation of Cyclohexane by High-Valent Iron Bispidine Complexes: Tetradentate versus Pentadentate Ligands. *Inorg. Chem.* **2009,** *48* (21), 10389-10396.

23. Warren, J. J.; Tronic, T. A.; Mayer, J. M., Thermochemistry of Proton-Coupled Electron Transfer Reagents and its Implications. *Chem. Rev.* **2010,** *110* (12), 6961-7001.

24. Leto, D. F.; Ingram, R.; Day, V. W.; Jackson, T. A., Spectroscopic properties and reactivity of a mononuclear oxomanganese(iv) complex. *Chem. Commun.* **2013,** *49* (47), 5378-5380.

25. Sawant, S. C.; Wu, X.; Cho, J.; Cho, K.-B.; Kim, S. H.; Seo, M. S.; Lee, Y.-M.; Kubo, M.; Ogura, T.; Shaik, S.; Nam, W., Water as an Oxygen Source: Synthesis, Characterization, and Reactivity Studies of a Mononuclear Nonheme Manganese(IV) Oxo Complex. *Angew. Chem., Int. Ed. Engl.* **2010,** *49* (44), 8190-8194.

26. Parsell, T. H.; Yang, M.-Y.; Borovik, A. S., C−H Bond Cleavage with Reductants: Re-Investigating the Reactivity of Monomeric MnIII/IV−Oxo Complexes and the Role of Oxo Ligand Basicity. *J. Am. Chem. Soc* **2009,** *131* (8), 2762-2763.

27. Yin, G.; Danby, A. M.; Kitko, D.; Carter, J. D.; Scheper, W. M.; Busch, D. H., Understanding the Selectivity of a Moderate Oxidation Catalyst: Hydrogen Abstraction by a Fully Characterized, Activated Catalyst, the Robust Dihydroxo Manganese(IV) Complex of a Bridged Cyclam. *J. Am. Chem. Soc* **2007,** *129* (6), 1512-1513.

28. Garcia-Bosch, I.; Company, A.; Cady, C. W.; Styring, S.; Browne, W. R.; Ribas, X.; Costas, M., Evidence for a Precursor Complex in C□H Hydrogen Atom Transfer Reactions Mediated by a Manganese(IV) Oxo Complex. *Angew. Chem., Int. Ed. Engl.* **2011,** *123* (25), 5766-5771.

29. Yoon, H.; Morimoto, Y.; Lee, Y.-M.; Nam, W.; Fukuzumi, S., Electron-transfer properties of a nonheme manganese(iv)-oxo complex acting as a stronger one-electron oxidant than the iron(iv)-oxo analogue. *Chem. Commun.* **2012,** *48* (91), 11187-11189.

30. Kurahashi, T.; Kikuchi, A.; Tosha, T.; Shiro, Y.; Kitagawa, T.; Fujii, H., Transient Intermediates from Mn(salen) with Sterically Hindered Mesityl Groups: Interconversion between MnIV-Phenolate and MnIII-Phenoxyl Radicals as an Origin for Unique Reactivity. *Inorg. Chem.* **2008,** *47* (5), 1674-1686.

31. Kurahashi, T.; Kikuchi, A.; Shiro, Y.; Hada, M.; Fujii, H., Unique Properties and Reactivity of High-Valent Manganese−Oxo versus Manganese−Hydroxo in the Salen Platform. *Inorg. Chem.* **2010,** *49* (14), 6664-6672.

32. Yin, G.; McCormick, J. M.; Buchalova, M.; Danby, A. M.; Rodgers, K.; Day, V. W.; Smith, K.; Perkins, C. M.; Kitko, D.; Carter, J. D.; Scheper, W. M.; Busch, D. H., Synthesis, Characterization, and Solution Properties of a Novel Cross-Bridged Cyclam Manganese(IV) Complex Having Two Terminal Hydroxo Ligands. *Inorg. Chem.* **2006,** *45* (20), 8052-8061.

33. Yin, G.; Danby, A. M.; Kitko, D.; Carter, J. D.; Scheper, W. M.; Busch, D. H., Oxidative Reactivity Difference among the Metal Oxo and Metal Hydroxo Moieties: pH Dependent Hydrogen Abstraction by a Manganese(IV) Complex Having Two Hydroxide Ligands. *J. Am. Chem. Soc* **2008,** *130* (48), 16245-16253.

34. Chattopadhyay, S.; Geiger, R. A.; Yin, G.; Busch, D. H.; Jackson, T. A., Oxo- and Hydroxo-Manganese(IV) Species: A Comparative Spectroscopic and Computational Study. *Inorg. Chem.* **2010,** *49*, 7530-7535.

35. Shi, S., Wang, Y., Xu, A., Wang, H., Zhu, D., Roy, S.B., Jackson, T.A., Busch, D.H., Yin, G., Distinct Reactivity Differences of Metal Oxo and Its Corresponding Hydroxo Moieties in Oxidations: Implications from a Manganese(IV) Complex Having Dihydroxide Ligand. *Angew. Chem. Int. Ed.* **2011,** *50*, 7321-7324.

36. Parsell, T. H.; Behan, R. K.; Green, M. T.; Hendrich, M. P.; Borovik, A. S., Preparation and Properties of a Monomeric MnIV-Oxo Complex. *J. Am. Chem. Soc* **2006,** *128* (27), 8728-8729.

37. Chen, J.; Cho, K.-B.; Lee, Y.-M.; Kwon, Y. H.; Nam, W., Mononuclear nonheme iron(iv)-oxo and manganese(iv)-oxo complexes in oxidation reactions: experimental results prove theoretical prediction. *Chem. Commun.* **2015,** *51* (66), 13094-7.

38. Wu, X.; Seo, M. S.; Davis, K. M.; Lee, Y.-M.; Chen, J.; Cho, K.-B.; Pushkar, Y. N.; Nam, W., A Highly Reactive Mononuclear Non-Heme Manganese(IV)–Oxo Complex That Can Activate the Strong C–H Bonds of Alkanes. *J. Am. Chem. Soc* **2011,** *133* (50), 20088-20091.

39. Cho, K.-B.; Shaik, S.; Nam, W., Theoretical Investigations into C–H Bond Activation Reaction by Nonheme MnIVO Complexes: Multistate Reactivity with No Oxygen Rebound. *J. Phys. Chem. Lett.* **2012,** *3* (19), 2851-2856.

40. Rice, D. B.; Massie, A. A.; Jackson, T. A., Manganese–Oxygen Intermediates in O–O Bond Activation and Hydrogen-Atom Transfer Reactions. *Acc. Chem. Res.* **2017,** *50* (11), 2706-2717.

41. Leto, D. F.; Massie, A. A.; Rice, D. B.; Jackson, T. A., Spectroscopic and Computational Investigations of a Mononuclear Manganese(IV)-Oxo Complex Reveal

Electronic Structure Contributions to Reactivity. *J. Am. Chem. Soc* **2016,** *138* (47), 15413-15424.

42. Massie, A. A.; Denler, M. C.; Cardoso, L. T.; Walker, A. N.; Hossain, M. K.; Day, V. W.; Nordlander, E.; Jackson, T. A., Equatorial Ligand Perturbations Influence the Reactivity of Manganese(IV)-Oxo Complexes. *Angew. Chem., Int. Ed. Engl.* **2017,** *56* (15), 4178-4182.

43. Chen, J.; Lee, Y.-M.; Davis, K. M.; Wu, X.; Seo, M. S.; Cho, K.-B.; Yoon, H.; Park, Y. J.; Fukuzumi, S.; Pushkar, Y. N.; Nam, W., A Mononuclear Non-Heme Manganese(IV)–Oxo Complex Binding Redox-Inactive Metal Ions. *J. Am. Chem. Soc* **2013,** *135* (17), 6388-6391.

44. Que, L., Physical Methods in Bioinorganic Chemistry: Spectroscopy and Magnetism. University Science Books: 2000.

45. Leto, D. F.; Massie, A. A.; Colmer, H. E.; Jackson, T. A., X-Band Electron Paramagnetic Resonance Comparison of Mononuclear MnIV-oxo and MnIV-hydroxo Complexes and Quantum Chemical Investigation of MnIV Zero-Field Splitting. *Inorg. Chem.* **2016,** *55* (7), 3272-3282.

46. Westre, T. E.; Kennepohl, P.; DeWitt, J. G.; Hedman, B.; Hodgson, K. O.; Solomon, E. I., A Multiplet Analysis of Fe K-Edge 1s → 3d Pre-Edge Features of Iron Complexes. *Journal of the American Chemical Society* **1997,** *119* (27), 6297-6314.

47. Leto, D. F.; Jackson, T. A., Mn K-Edge X-ray Absorption Studies of Oxo- and Hydroxomanganese(IV) Complexes: Experimental and Theoretical Insights into Pre-Edge Properties. *Inorg. Chem.* **2014,** *53*, 6179-6194.

48. Pecoraro, V. L.; Baldwin, M. J.; Gelasco, A., Interaction of Manganese with Dioxygen and Its Reduced Derivatives. *Chem. Rev.* **1994,** *94* (3), 807-826.

49. Sheng, Y.; Abreu, I. A.; Cabelli, D. E.; Maroney, M. J.; Miller, A.-F.; Teixeira, M.; Valentine, J. S., Superoxide Dismutases and Superoxide Reductases. *Chem. Rev.* **2014,** *114* (7), 3854-3918.

50. Porta, J.; Vahedi-Faridi, A.; Borgstahl, G. E. O., Structural Analysis of Peroxide-Soaked MnSOD Crystals Reveals Side-On Binding of Peroxide to Active-Site Manganese. *J. Mol. Biol.* **2010,** *399* (3), 377-384.

51. Ottenbacher, R. V.; Samsonenko, D. G.; Talsi, E. P.; Bryliakov, K. P., Enantioselective Epoxidations of Olefins with Various Oxidants on Bioinspired Mn

Complexes: Evidence for Different Mechanisms and Chiral Additive Amplification. *ACS Catalysis* **2016,** *6* (2), 979-988.

52. Codola, Z.; Lloret-Fillol, J.; Costas, M., Aminopyridine Iron and Manganese Complexes as Molecular Catalysts for Challenging Oxidative Transformations. In *Progress in Inorganic Chemistry: Volume 59*, John Wiley & Sons, Inc.: 2014; pp 447-532.

53. Leto, D. F.; Jackson, T. A., Peroxomanganese complexes as an aid to understanding redox-active manganese enzymes. *J. Biol. Inorg. Chem.* **2014,** *19*, 1-15.

54. Geiger, R. A.; Chattopadhyay, S.; Day, V. W.; Jackson, T. A., Nucleophilic reactivity of a series of peroxomanganese(iii) complexes supported by tetradentate aminopyridyl ligands. *Dalton Transactions* **2011,** *40* (8), 1707-1715.

55. Annaraj, J.; Cho, J.; Lee, Y.-M.; Kim, S. Y.; Latifi, R.; de Visser, S. P.; Nam, W., Structural Characterization and Remarkable Axial Ligand Effect on the Nucleophilic Reactivity of a Nonheme Manganese(III)-Peroxo Complex. *Angew. Chem. Int. Ed.* **2009,** *48* (23), 4150-4153.

56. Kang, H.; Cho, J.; Cho, K.-B.; Nomura, T.; Ogura, T.; Nam, W., Mononuclear Manganese–Peroxo and Bis(μ-oxo)dimanganese Complexes Bearing a Common N-Methylated Macrocyclic Ligand. *Chem. Eur* **2013,** *19* (14119-14125).

57. Seo, M. S.; Kim, J. Y.; Annaraj, J.; Kim, Y.; Lee, Y.-M.; Kim, S.-J.; Kim, J.; Nam, W., $[Mn(tmc)(O_2)]^+$: A Side-On Peroxide Manganese(III) Complex Bearing a Non-heme Ligand. *Angewandte Chemie International Edition* **2007,** *46*, 377-380.

58. Shook, R. L.; Gunderson, W. A.; Greaves, J.; Ziller, J. W.; Hendrich, M. P.; Borovik, A. S., A Monomeric Mn^{III}-Peroxo Complex Derived Directly from Dioxygen. *Journal of the American Chemical Society* **2008,** *130* (28), 8888-8889.

59. Shook, R. L.; Peterson, S. M.; Greaves, J.; Moore, C.; Rheingold, A. L.; Borovik, A. S., Catalytic Reduction of Dioxygen to Water with a Monomeric Manganese Complex at Room Temperature. *Journal of the American Chemical Society* **2011,** *133* (15), 5810-5817.

60. Shook, R. L.; Borovik, A. S., Role of the Secondary Coordination Sphere in Metal-Mediated Dioxygen Activation. *Inorg. Chem.* **2010,** *49* (8), 3646-3660.

61. Barman, P.; Upadhyay, P.; Faponle, A. S.; Kumar, J.; Nag, S. S.; Kumar, D.; Sastri, C. V.; Visser, S. P. d., Deformylation Reaction by a Nonheme Manganese(III)–Peroxo Complex via Initial Hydrogen-Atom Abstraction. *Angewandte Chemie* **2016,** *128* (37), 11257-11261.

62. Colmer, H. E.; Howcroft, A. W.; Jackson, T. A., Formation, Characterization, and O–O Bond Activation of a Peroxomanganese(III) Complex Supported by a Cross-Clamped Cyclam Ligand. *Inorg. Chem.* **2016,** *55* (5), 2055-2069.

63. Ching, H. Y. V.; Anxolabéhère-Mallart, E.; Colmer, H. E.; Costentin, C.; Dorlet, P.; Jackson, T. A.; Policar, C.; Robert, M., Electrochemical Formation and Reactivity of a Manganese Peroxo Complex: Acid Driven H2O2 Generation vs. O-O Bond Cleavage. *Chemical Science* **2014,** *5* (2304-2310).

64. Leto, D. F.; Chattopadhyay, S.; Day, V. W.; Jackson, T. A., Reaction landscape of a pentadentate N5-ligated MnII complex with O2˙− and H2O2 includes conversion of a peroxomanganese(III) adduct to a bis(μ-oxo)-dimanganese(III,IV) species. *Dalton Trans.* **2013,** *42*, 13014.

65. Groni, S.; Dorlet, P.; Blain, G.; Bourcier, S.; Guillot, R.; Anxolabéhère-Mallart, E., Reactivity of an Aminopyridine $[LMn^{II}]^{2+}$ Complex with H_2O_2. Detection of Intermediates at Low Temperature. *Inorg. Chem.* **2008,** *47* (8), 3166-3172.

66. El Ghachtouli, S.; Vincent Ching, H. Y.; Lassalle-Kaiser, B.; Guillot, R.; Leto, D. F.; Chattopadhyay, S.; Jackson, T. A.; Dorlet, P.; Anxolabehere-Mallart, E., Electrochemical formation of MnIII-peroxo complexes supported by pentadentate amino pyridine and imidazole ligands. *Chemical Communications* **2013,** *49* (50), 5696-5698.

67. Geiger, R. A.; Leto, D. F.; Chattopadhyay, S.; Dorlet, P.; Anxolabéhère-Mallart, E.; Jackson, T. A., Geometric and Electronic Structures of Peroxomanganese(III) Complexes Supported by Pentadentate Amino-Pyridine and -Imidazole Ligands. *Inorg. Chem.* **2011,** *50* (20), 10190-10203.

Chapter 2. Equatorial Ligand Perturbations Influence the Reactivity of Oxomanganese(IV) Species

This work has been reproduced from: Massie, A. A.; Denler, M. C.; Cardoso, L. T.; Walker, A. N.; Hossain, M. K.; Day, V. W.; Nordlander, E.; Jackson, T. A. *Angew. Chem., Int. Ed. Engl.* **2017**, *56*, 4178, with permission from John Wiley and Sons.

2.1 Introduction

Oxidation reactions by earth-abundant metals often require hydrogen-atom transfer (HAT) or oxygen-atom transfer (OAT) steps by high-valent metal-oxo species.[1-4] Prototypic biological examples involve Fe^{IV}-oxo centers, which have been extensively investigated.[5-7] There is interest to expand understanding of high-valent metal-oxo species beyond iron to access the potential of other earth-abundant metals in catalytic oxidations. Advances in Mn catalysis for C-H bond functionalization and alkene epoxidation have been described, with Mn^{V}- and Mn^{IV}-oxo intermediates proposed.[8-14] These intermediates show varied reactivity, the basis of which is poorly understood. Some Mn^{IV}-oxo centers react slowly with highly activated C-H bonds,[15-16] while other species attack the strong C-H bonds of cyclohexane.[17] Large variations in supporting ligands and reaction media make it challenging to rationalize reactivity trends.

On the basis of density functional theory (DFT) studies, Nam and Shaik have attributed the enhanced reactivity of $[Mn^{IV}(O)(N4py)]^{2+}$ and $[Mn^{IV}(O)(BnTPEN)]^{2+}$ [17-19] to a ^4E excited state, which offers a lower barrier for HAT and OAT than the $^4B_1$ ground-state (Figure 2.1).[20-21] This model was also applied to the olefin epoxidation activity of $[Mn^{IV}(O)(N4py)]^{2+}$.[22] We recently identified the ^4E excited state of $[Mn^{IV}(O)(N4py)]^{2+}$ using magnetic circular dichroism spectroscopy.[23] This state arises from a Mn^{IV} $e(d_{xz}, d_{yz}) \rightarrow b_1(d_{x^2-y^2})$ one-electron excitation and gives rise to a weak electronic absorption band at 10 500 cm^{-1}. As the Mn^{IV} $b_1(d_{x^2-y^2})$ acceptor MO is Mn-N4py σ- antibonding, the ^4E energy, and hence HAT and OAT reactivity, should be sensitive to perturbations in the equatorial ligand field. In this study, we test this model using new Mn^{IV}-oxo complexes supported by electron-rich ^{DMM}N4py[24] and sterically encumbered 2pyN2Q[25] (Figure 2.2). These derivatives modulate the equatorial ligand field of the Mn^{IV} center, influencing the ^4E energy, and leading to large rate variations.

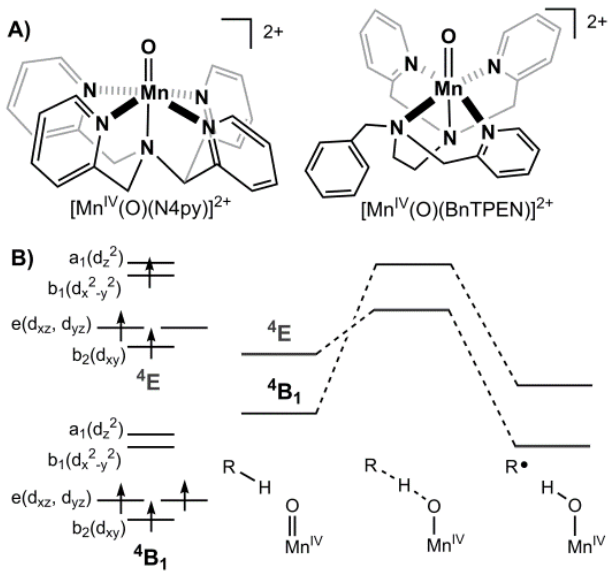

Figure 2.1 A) Structures of $[Mn^{IV}(O)(N4py)]^{2+}$ and $[Mn^{IV}(O)(BnTPEN)]^{2+}$.

B) Computed electronic configurations and reaction coordinates for HAT by $^4B1$ and ^4E states.[21]

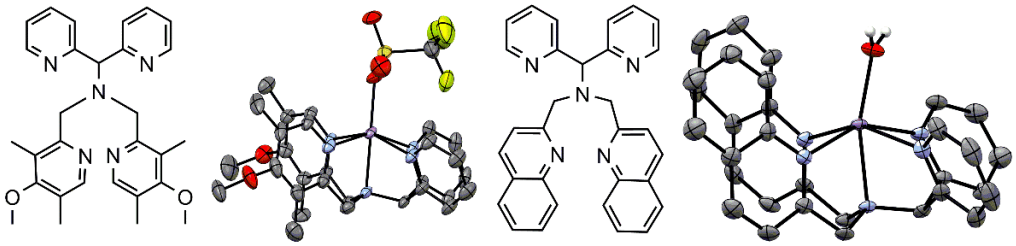

Figure 2.2 ^{DMM}N4py and 2pyN2Q ligands and X-ray structures of cationic portions of $[Mn^{II}(^{DMM}N4py)(OTf)]^+$ and $[Mn^{II}(2pyN2Q)(OH_2)]^{2+}$.

2.2 Experimental and Computational Methods

2.2.1 Materials

Chemicals and solvents were purchased from commercial vendors and were ACS reagent-grade quality or better. $Mn^{II}(OTf)_2$•$2CH_3CN$ was generated according to a reported procedure.[26] Chemicals and solvents were used as received, with the exception of 9,10-dihydroanthracene (DHA) and xanthene, which were recrystallized from ethanol.[27] For O_2-free reactions, solvents were dried according to published procedures and degassed using the freeze-pump-thaw method.[27] $H_2{}^{18}O$ (97% ^{18}O) was purchased from

Cambridge Isotope Laboratories, Inc. (Andover, MA, USA). d_4-DHA was prepared following a previously reported procedure.[28] Iodosylbenzene was purchased commercially or prepared from iodosobenzene diacetate following a published procedure.[29]

Electronic absorption spectra for formation and kinetic reactions were obtained on a Varian Cary 50 Bio or an Agilent 8453 spectrophotometer. Both instruments were interfaced with a Unisoku cryostat (USP-203-A) that can maintain temperatures between 150 and 373 K. Near-IR absorption data were collected on a Shimadzu UV-3600 UV-vis-NIR spectrophotometer. Electrospray-ionization mass spectrometry experiments were performed using an LCT Primers Mircomass electrospray time-of-flight instrument. NMR data were collected on a Bruker AVIIIHD 400 MHz NMR instrument. For the 2pyN2Q ligand, the ESI mass spectrum was recorded on a Waters QTOF XEVO-G2 spectrometer. The sample was injected as an MeCN solution. The results are denoted as cationic mass peaks; unit is the mass/charge ratio. The ^{1}H and ^{13}C NMR spectra of the 2pyN2Q ligand were recorded on a Varian Inova 500 MHz spectrometer using deuterated chloroform as solvent, and referenced to the residual signal of the solvent.

2.2.2 Synthesis and Characterization

Synthesis of Ligands and Mn^{II} Complexes. The N4py ligand, $[Mn^{II}(N4py)(OTf)](OTf)$, and $[Mn^{IV}(O)(N4py)]^{2+}$ were prepared following previously described methods.[19, 30-32] The ^{DMM}N4py ligand (^{DMM}N4py = *N*,*N*-bis(4-methoxy-3,5-dimethyl-2-pyridylmethyl)-*N*-bis(2-pyridyl)methylamine) was synthesized based on a modified version of the synthesis for N4py,[30-31] which is similar to a previously reported procedure.[24] 2-chloromethyl-4-methoxy-3,5-dimethylpyridine hydrochloride (0.99 g, 4.45 mmol) was added to 2 mL of 5 M NaOH on ice. To this solution were added 2 mL H_2O and 4 mL acetone, which facilitated dissolution of the pyridine salt. This bright pink solution was added to bis(2-pyridyl)methylamine (0.35 g, 1.9 mmol) in 2 mL of 5 M NaOH. The resulting solution was stirred vigorously for 48 hours, during which time the solution turned from pink to reddish-orange. To isolate the free ligand, 2.5 M NaOH and CH_2Cl_2 were added to the reaction mixture until the colored solution went into the CH_2Cl_2 layer.

The solution was extracted 3 times with CH_2Cl_2. The CH_2Cl_2 fractions were collected and dried with Na_2SO_4 and filtered to remove solid Na_2SO_4. Solvent was removed by rotary evaporation, resulting in a reddish-brown oil. The oil was further purified using column chromatography (basic alumina). Initially, pure CH_2Cl_2 was used, and elution was achieved with a methanol gradient increased to a maximum of 10%. The ^{1}H NMR spectrum of the dried, pure ligand was consistent with previous reports.[24] (In an initial synthesis, the ^{DMM}N4py ligand was isolated as the perchloride salt, by addition of perchloric acid to the ligand. This introduced the perchlorate observed in one of the X-ray diffraction structures of the metal salt (*vide infra*). However, the perchlorate precipitation was not optimal and was omitted in later syntheses.)

The pentadentate *N*5 donor ligand 2pyN2Q (2pyN2Q = bis(2-pyridyl)-*N*,*N*-bis(2 quinolylmethyl)methanamine)[25] was prepared by adaptation of a published procedure for a similar ligand.[33] Two equivalents of 2-(chloromethyl)quinoline hydrochloride (1.20 g, 5.64 mmol) was dissolved in 4 ml of a 5 M NaOH solution with vigorous stirring for 10 min and one equivalent of bis(2-pyridyl)methylamine (0.52 g, 2.82 mmol) in 2 ml of 5 M NaOH was added to the solution. The reaction mixture was allowed to stir for three days at room temperature. The prolonged stirring resulted in the formation of a light brown sticky insoluble solid. To this solid, HPF_6 was added dropwise to precipitate a greenish solid, which was recrystallized from hot water. After recrystallization, 5 M NaOH was added to basify the reaction mixture (until pH > 12). The product was extracted with dichloromethane (3×30 ml) and dried over Na_2SO_4. Evaporation of the solvent led to the desired ligand **2pyN2Q** as a pale greenish solid. Yield: 0.896 g (68%). The spectroscopic data matched with previously published data [ref 10]. ^{1}H NMR (500 MHz, $CDCl_3$) δ 8.59 (d, J = 4.3 Hz, 2H, py-H), 8.05 (d, J = 8.5 Hz, 2H, Qn-H), 8.01 (d, J = 8.5 Hz, 2H, Qn-H), 7.80 (d, J = 8.4 Hz, 2H, Qn-H), 7.75 – 7.71 (m, 4H, py-H, Qn-H), 7.70 – 7.62 (m, 4H, py-H, Qn-H), 7.45 (ddd, J = 8.2, 6.9, 1.1 Hz, 2H, Qn-H), 7.15 (ddd, J = 7.2, 4.7, 1.1 Hz, 2H, py-H), 5.47 (s, 1H, NCH), 4.24 (s, 4H, CH_2Qn). ^{13}C NMR (126 MHz, $CDCl_3$) δ 160.42, 159.72, 149.29, 147.44, 136.32, 136.21, 129.25, 128.92, 127.38, 127.21, 126.01, 124.32, 122.18, 121.19 (Ar-C), 72.10 (CH), 58.23 (CH_2). HRMS (in CH_3CN): *m/z* 468.2185 [**2pyN2Q**+H]$^+$, 490.2008 [**2pyN2Q**+Na]$^+$.

The [Mn^{II}(^{DMM}N4py)(OTf)](OTf) and [Mn^{II}(2pyN2Q)(OTf)](OTf) complexes were prepared using the same procedure reported for [Mn^{II}(N4py)(OTf)](OTf).[32] Under an argon atmosphere, a 1:1 molar ratio of ligand and $Mn^{II}(OTf)_2$•$2CH_3CN$ were combined in acetonitrile and stirred overnight. The resulting solution was filtered through a membrane filter and collected in a Schlenk flask, where solvent was removed under reduced pressure. The resulting oil was dissolved in acetonitrile and solid was isolated by layering with diethyl ether. The crude metal salt was isolated as a solid precipitate, washed with diethyl ether, and dried under vacuum. Further purification by layering or vapor diffusion (diethyl ether and acetonitrile) was necessary to obtain pure samples of [Mn^{II}(^{DMM}N4py)(OTf)](OTf) and [Mn^{II}(2pyN2Q)(OTf)](OTf) suitable for further studies.

Crystals of [Mn^{II}(^{DMM}N4py)(OTf)](OTf) suitable for characterization by X-ray diffraction were obtained by vapor diffusion of diethyl ether into an acetonitrile solution of [Mn^{II}(^{DMM}N4py)(OTf)](OTf). Elemental Analysis [Mn^{II}(^{DMM}N4py)(OTf)](OTf) $C_{31}H_{33}F_6MnN_5O_8S_2$ calc (%): C 44.50, H 3.98 5, N 8.37; Found (%); C 44.26, H 3.73, N 8.32. ESI-MS data are as follows: [Mn^{II}(^{DMM}N4py)](Cl)$^+$ *m/z* = 573.1677 (calc. 573.1698). In the mass spectrometer the triflate ion was displaced by a chloride. The effective magnetic moment (μ_{eff}) was found to be 5.95 μ_b, which is in good agreement with the expected μ_{eff} of 5.92 μ_b for high-spin Mn^{II} centers.

Crystals of [Mn^{II}(2pyN2Q)(OTf)](OTf) suitable for characterization by X-ray diffraction were obtained by two methods. In the first method, vapor diffusion of diethyl ether into an acetonitrile solution of [Mn^{II}(2pyN2Q)(OTf)](OTf) at 233 K yielded crystals of [Mn^{II}(2pyN2Q)(OTf)](OTf). These crystals were heavily twinned and resulted in a structure with low precision (*vide infra*). In the second method, vapor diffusion of pentane into a tetrahydrofuran solution of Mn^{II}-2pyN2Q salt yielded crystals of [Mn^{II}(2pyN2Q)(OH_2)]$(OTf)_2(OH_2)_2$. These crystals allowed for the determination of a higher precision structure. Elemental Analysis [Mn^{II}(2pyN2Q)(OTf)](OTf)•H_2O $C_{33}H_{27}F_6MnN_5O_7S_2$ calc (%): C 47.26, H 3.25, N 8.35; Found (%); C 47.27, H 3.13, N 8.19. ESI-MS data are as follows: [Mn^{II}(2pyN2Q)](Cl)$^+$ *m/z* = 557.1157 (calc. 557.1173). The triflate ion was displaced by a chloride in the mass spectrometer. The effective magnetic moment (μ_{eff}) was found to be 5.94 μ_b, in good agreement with the expected μ_{eff}

of 5.92 μ_b for high-spin Mn^{II} centers. Crystallographic details are discussed in Appendix A2.1

Synthesis and Characterization of Mn^{IV}-oxo Complexes. Preparation of $[Mn^{IV}(O)(^{DMM}N4py)]^{2+}$ and $[Mn^{IV}(O)(2pyN2Q)]^{2+}$ followed that previously described for $[Mn^{IV}(O)(N4py)]^{2+}$, with only minor modification.[19] In a typical procedure, a solution of the appropriate Mn^{II} salt was dissolved in 1 mL 2,2,2-trifluoroethanol (TFE), transferred to a cuvet, and placed in a temperature-controlled cryostat (298 K). Iodosylbenzene, dissolved in 1 mL TFE, was added to the solution of the Mn^{II} complex. Formation of the oxomanganese(IV) species was monitored by electronic absorption spectroscopy (Figure A2.3). In typical preparations, the total Mn concentration in the final solution was 1 or 2 mM, unless otherwise noted. The use of TFE as solvent, or co-solvent, is required to form the Mn^{IV}-oxo complexes in high yields. Corresponding reactions in CH_3CN provide no evidence of Mn^{IV}-oxo formation. The use of TFE to facilitate Mn^{IV}-oxo formation PhIO oxidation of Mn^{II} precursors has been reported previously by Nam and co-workers,[17-18] and this phenomenon could relate to observations that fluoroalcohols stabilize hypervalent iodine species.[34]

The formation of $[Mn^{IV}(O)(^{DMM}N4py)]^{2+}$ was optimized by treating $[Mn^{II}(^{DMM}N4py)(OTf)](OTf)$ with 1.2 equivalents of iodosylbenzene (PhIO) in TFE at 298 K. The formation of the green solution of $[Mn^{IV}(O)(^{DMM}N4py)]^{2+}$ was complete in roughly 15 minutes. Solutions of $[Mn^{IV}(O)(^{DMM}N4py)]^{2+}$ showed a broad electronic absorption band at 920 nm (ε = 290 M^{-1} cm^{-1}). The extinction coefficient was determined assuming maximum formation under these conditions. Formation of $[Mn^{IV}(O)(^{DMM}N4py)]^{2+}$ in 1:1 (volume:volume) CF_3CH_2OH:CH_2Cl_2 did not impact the yield or stability of $[Mn^{IV}(O)(^{DMM}N4py)]^{2+}$. Under an air atmosphere, $[Mn^{IV}(O)(^{DMM}N4py)]^{2+}$ has a half-life of 6.2 hours at 298 K. We note that $[Mn^{IV}(O)(N4py)]^{2+}$ displayed a longer half-life under air than under argon (2 hr. vs. 30 min.).[18-19] Presumably, the decay of the Mn^{IV}-oxo generates radicals that hasten further decay. The presence of dioxygen traps some of the radicals, increasing the half-life of the Mn^{IV}-oxo.

A similar procedure was used to generate $[Mn^{IV}(O)(2pyN2Q)]^{2+}$; however, in this case maximum formation required the addition of 10 equivalents of PhIO and formation was complete within 90 seconds, as assessed by the appearance of a broad electronic absorption band in the near-IR region (Figure A2.3). For reactivity studies performed using the Agilent or Cary UV-vis instruments, the signal at 1080 nm was monitored to assess maximum formation (λ = 161 M^{-1} cm^{-1}). Additional characterization $[Mn^{IV}(O)(2pyN2Q)]^{2+}$ using a Shimadzu UV-3600 spectrometer established the actual λ_{max} at 1180 nm (ε = 179 M^{-1} cm^{-1}, determined assuming maximum formation). Of the Mn^{IV}-oxo complexes considered in this study, $[Mn^{IV}(O)(2pyN2Q)]^{2+}$ is the least stable, with a half-life of only 12 minutes at 298 K under an air atmosphere. (The analogous Fe^{IV}-oxo complex of **2PyN2Q** exhibits a similar short half-life of 20 minutes at ambient temperature.[35])

Electrospray-Ionization Mass Spectrometry (ESI-MS) Characterization of Mn^{IV}-oxo Complexes. For characterization by ESI-MS, a 2 mM sample of $[Mn^{IV}(O)(^{DMM}N4py)]^{2+}$ was prepared in 2 mL TFE. Formation was monitored by electronic absorption spectroscopy. At maximum formation of the Mn^{IV}-oxo species, 50 µL of the $[Mn^{IV}(O)(^{DMM}N4py)]^{2+}$ solution was added to 2 mL CH_3OH precooled to 233 K. The sample was then injected into the ESI-MS instrument. To generate the ^{18}O-labeled sample, 15 µL $H_2{}^{18}O$ was added to 0.4 mL of the TFE solution of $[Mn^{IV}(O)(^{DMM}N4py)]^{2+}$ and allowed to stir for 5 minutes. No evidence of decay of $[Mn^{IV}(O)(^{DMM}N4py)]^{2+}$ was observed by electronic absorption spectroscopy during this time period. The ESI-MS sample was generated by adding 50 µL of the ^{18}O labeled $[Mn^{IV}(O)(^{DMM}N4py)]^{2+}$ solution to 2 mL CH_3OH precooled to 233 K. $[Mn^{IV}(O)(^{DMM}N4py)]^{2+}$ is significantly less stable in CH_3OH than in pure TFE, so the dominant peaks in the mass spectra come from Mn^{II} decay products (Figure A2.4).

ESI-MS data for samples of $[Mn^{IV}(O)(2pyN2Q)]^{2+}$, prepared in a similar manner as $[Mn^{IV}(O)(^{DMM}N4py)]^{2+}$, are shown in Figure A2.5. The only modification in preparation of the $[Mn^{IV}(O)(2pyN2Q)]^{2+}$ samples is that the reaction solution was cooled to 273 K and diluted into CH_3CN rather than CH_3OH. Because of the low stability of

$[Mn^{IV}(O)(2pyN2Q)]^{2+}$ in CH_3CN, the Mn^{III} decay product, $[Mn^{III}(2pyN2Q)(OCH_2CF_3)_2]^{+}$, is the dominant feature in the ESI-MS spectra (Figure A2.5).

X-Band EPR Characterization of Mn^{IV}-oxo Complexes. A 5 mM solution of $[Mn^{IV}(O)(^{DMM}N4py)]^{2+}$ was prepared by dissolving 12.5 mg $[Mn^{II}(^{DMM}N4py)(OTf)](OTf)$ in 0.5 mL TFE. To this solution were added 4.0 mg PhIO in 2.5 mL TFE, giving a final volume of 3 mL. Formation of $[Mn^{IV}(O)(^{DMM}N4py)]^{2+}$ was monitored by electronic absorption spectroscopy. At maximum formation, 250 µL of $[Mn^{IV}(O)(^{DMM}N4py)]^{2+}$ was transferred into a 4 mm quartz EPR tube and flash frozen in liquid nitrogen. Due to the short-lived nature of $[Mn^{IV}(O)(2pyN2Q)]^{2+}$, EPR samples of this complex were prepared in the EPR tube. Solutions of 4.1 mg $[Mn^{II}(2pyN2Q)(OTf)](OTf)$ in 0.5 mL TFE and 11.0 mg PhIO in 0.5 mL TFE were prepared, and 75 µL of each solution were combined in an EPR tube and agitated to promote mixing for 1 minute. The sample was flash frozen in liquid nitrogen.

EPR spectra were collected at 5 K on a 9 GHz Bruker EMXPlus spectrometer with an Oxford ESR900 continuous-flow liquid helium cryostat controlled by an Oxford ITC503 temperature system. Perpendicular mode data were collected in a dual mode Bruker ER4116DM cavity. Recording conditions for $[Mn^{IV}(O)(^{DMM}N4py)]^{2+}$ were 9.636 GHz microwave frequency, 2.0 mW microwave power, 6 G modulating amplitude, 100 kHz modulation frequency, and 40.96 ms time constant. Data collected for $[Mn^{IV}(O)(2pyN2Q)]^{2+}$ used the same parameters, except the microwave frequency, which was 9.643 GHz.

Mn K-edge X-ray Absorption (XAS) Experiments. A 15 mM sample of $[Mn^{IV}(O)(^{DMM}N4py)]^{2+}$ was prepared by dissolving 25.1 mg $[Mn^{II}(^{DMM}N4py)(OTf)](OTf)$ in 1 mL TFE. This was combined with a solution of 7.9 mg PhIO in 1 mL TFE and stirred for 15 minutes. Excess PhIO was removed by filtering the solution through a 0.45 µm membrane directly into a UV-Vis cuvette. When the formation of $[Mn^{IV}(O)(^{DMM}N4py)]^{2+}$ was complete, as assessed by electronic absorption spectroscopy, approximately 200 µL of the reaction solution were transferred to an XAS sample holder and then immediately flash frozen in liquid nitrogen. A 30 mM sample of $[Mn^{IV}(O)(2pyN2Q)]^{2+}$, was prepared by

dissolving 24.6 mg [Mn^{II}(2pyN2Q)(OTf)](OTf) in 0.2 mL TFE and cooling the solution to 233 K. A solution of 49.5 mg PhIO in 1.3 mL TFE was also cooled to 233 K. These solutions were combined and Mn^{IV}-oxo formation was monitored by electronic absorption spectroscopy at 273 K. At maximum formation of $[Mn^{IV}(O)(2pyN2Q)]^{2+}$**,** 200 µL of the solution was transferred to a pre-cooled XAS sample holder and flash frozen in liquid nitrogen.

XAS data of the frozen samples were collected at beamline 2-2 at Stanford Synchrotron Radiation Lightsource (SSRL). Mn K-edge X-ray absorption spectra were collected over the energy range of 6.3 to 7.25 keV (Si(111) monochromator) at 15 K. XAS spectra were obtained as fluorescence excitation spectra using a 13-element Ge array. For reference, spectra of a manganese foil were collected with each scan. An internal calibration was performed where the zero crossing of the second derivative of the K-edge energy of the foil was assigned to 6539.0 eV. A comparison of sequential XAS scans revealed no evidence for photoreduction under these experimental conditions.

Data reduction and processing for $[Mn^{IV}(O)(^{DMM}N4py)]^{2+}$ and $[Mn^{IV}(O)(2pyN2Q)]^{2+}$, as well as a re-analysis (for comparative purposes) of $[Mn^{IV}(O)(N4py)]^{2+}$, were performed done using Athena software.[36] Fitting of the pre-edge area was performed with the Fityk curve fitting software.[37] The background was fit using a pseudo-Voigt function and then subtracted from the fit of the pre-edge feature. The area reported represents the area of the fit pre-edge peak minus the area of the background. These fits can be seen in Figure A2.6.

2.2.3 Electronic Structure Computations

All electronic structure calculations were performed using *ORCA* version 3.0.1.[38-39] Geometry optimizations, without any symmetry constraints, were carried out at the spin unrestricted level, using the TPSS functional[40] and SVP basis sets for C and H and the larger TZVP basis sets for Mn, O, and N.[41-42] These optimizations utilized the resolution of identity (RI) approximation,[43] along with SV/J and TZV/J auxiliary basis sets. TD-DFT calculations used the same basis sets employed for the geometry optimizations, but were performed with the B3LYP/G functional,[44-46] the RIJCOSX approximation,[47] and the

COSMO solvation model.[48-49] The TD-DFT methodology has been described elsewhere.[50-54] To generate electronic absorption spectra from the TD-DFT results, each electronic transition was modeled as a Gaussian band with a full-width-at-half-maximum ($v_{1/2}$) of 2 500 cm^{-1}. The calculated transition oscillator strength (f) was related to the extinction coefficient (ε_{max}) using the following relation: $f = (4.61 \times 10^{-9})(\varepsilon_{max} v_{1/2})$. Isosurface plots of Kohn-Sham orbitals were generated using gOpenMol.[55-56] DFT calculated coordinates can be found in Appendix A2.3.

2.2.4 Mn^{IV}-oxo Reactivity towards C-H Bonds

The reactivity of $[Mn^{IV}(O)(^{DMM}N4py)]^{2+}$ and $[Mn^{IV}(O)(2pyN2Q)]^{2+}$ towards C-H bonds was determined through kinetic investigations involving a variety of substrates. The general procedure for these reactions involved treating the freshly prepared Mn^{IV}-oxo complex (2 mM) with a molar excess of substrate (>10 equivalents) at 298 K. A representative reaction with $[Mn^{IV}(O)(^{DMM}N4py)]^{2+}$ is: 3.5 mg $[Mn^{II}(^{DMM}N4py)(OTf)](OTf)$ were dissolved in 1 mL deoxygenated CH_2Cl_2 and combined with 1.1 mg PhIO (1.2 equivalents) in 1 mL deoxygenated TFE in a UV-Vis cuvette and sealed under an Ar atmosphere. The reaction mixture was then placed into a temperature-controlled cryostat and formation of $[Mn^{IV}(O)(^{DMM}N4py)]^{2+}$ was monitored by UV-Vis spectroscopy. At maximum formation, an appropriate amount of substrate was added in 100 µL CH_2Cl_2. The decay of the $[Mn^{IV}(O)(^{DMM}N4py)]^{2+}$ peak at 940 nm was monitored and fit to obtain first order rate constants, k_{obs}. Under these reaction conditions, rates were observed to be first-order for five half-lives. For each substrate, k_{obs} values were determined at four substrate concentrations (xanthene: 20 – 80 mM; dihydroanthracene: 20 – 50 mM; diphenylmethane: 194 – 461 mM; ethylbenzene: 389 – 890 mM). Plots of k_{obs} versus the substrate concentration yielded second-order rate constants (k_2; $M^{-1}s^{-1}$) from the slope of the linear correlation (Figures A2.7-A2.8). For all substrates, the intercept at concentration = 0 mM deviated slightly from $k_2 = 0$ $M^{-1}s^{-1}$; however, the observed deviation in k_2 is within one standard deviation, except for reaction with xanthene. These reactions were more rapid and showed larger error. To compare rates for multiple substrates, k_2 was divided by the number of equivalent C-H bonds in each substrate to obtain the corrected second-order rate constant, k_2'. To facilitate solubility of the larger amounts of substrate required

to react with the slower $[Mn^{IV}(O)(^{DMM}N4py)]^{2+}$ oxidant, kinetic studies were performed in a 1:1 (volume:volume) mixture of TFE:CH_2Cl_2. Previous kinetic studies of $[Mn^{IV}(O)(N4py)]^{2+}$ showed that the use of 1:1 TFE:CH_2Cl_2 cause only minor differences in rate when compared to reactions in pure TFE.[19]

Kinetic investigations involving $[Mn^{IV}(O)(2pyN2Q)]^{2+}$ (2 mM final concentration, 1 mM for dihydroanthracene reactions) were performed in a similar fashion. In a typical experiment, 3.4 mg $[Mn^{II}(2pyN2Q)(OTf)](OTf)$ in 1 mL TFE was combined with 9.2 mg PhIO (10 equivalents) in 1 mL TFE in a UV-Vis cuvette, and formation of $[Mn^{IV}(O)(2pyN2Q)]^{2+}$ was monitored by electronic absorption spectroscopy. All experiments were performed at 298 K. An excess of substrate (100 µL in TFE or CH_2Cl_2) was added, and the decay of the near-IR feature at 1080 nm was monitored to determine k_{obs} values. Second-order rate constants were obtained as previously described for $[Mn^{IV}(O)(^{DMM}N4py)]^{2+}$ (Figure A2.7). These reactions used varied concentrations of dihydroanthracene (10 – 40 mM), diphenylmethane (20 – 80 mM), ethylbenzene (95 – 380 mM), and toluene (196 – 904 mM). For reactions of $[Mn^{IV}(O)(2pyN2Q)]^{2+}$ with dihydroanthracene (DHA), toluene, and ethylbenene, the intercept at concentration = 0 mM deviated from $k_2 = 0\ M^{-1}s^{-1}$; however, the observed intercept was in agreement with the self-decay rate of $[Mn^{IV}(O)(2pyN2Q)]^{2+}$ for all substrates except DHA.

For the determination of the kinetic isotope effect (KIE) of $[Mn^{IV}(O)(^{DMM}N4py)]^{2+}$, the same procedure described for the kinetic study of DHA was followed, but with the use of d_4-DHA as substrate. A linear relationship between the observed rate (k_{obs}) and the d_4-DHA concentration gave a second-order rate constant of 0.0337 $M^{-1}\ s^{-1}$. By comparing this with the k_2 for DHA oxdiation (0.343 $M^{-1}\ s^{-1}$), we determined a KIE of 10.2. For the KIE determination of $[Mn^{IV}(O)(2pyN2Q)]^{2+}$, we compared the k_{obs} for the reaction of $[Mn^{IV}(O)(2pyN2Q)]^{2+}$ with 10 equivalents DHA (0.65 s^{-1}) or d_4-DHA (0.126 s^{-1}) to obtain a KIE of 5.3. The second-order rate constant for the reaction of $[Mn^{IV}(O)(2pyN2Q)]^{2+}$ with d_4-DHA was not determined because of the limited solubility of the substrate in the required solvent mixture.

Analysis of organic and Mn products. Anthracene quantification was performed for the reaction of $[Mn^{IV}(O)(^{DMM}N4py)]^{2+}$ (2 mM) with 10 equivalents of DHA. Following the reaction, anthracene was extracted from the reaction mixture using cyclohexane, and the anthracene concentration was determined using the absorbance at 356 nm and the known extinction coefficient.[57] Anthracene quantification was also performed using an extinction coefficient of anthracene in 10:11 volume:volume TFE:CH_2Cl_2 (which was the final solvent mixture used in these reactions). Both methods established 0.5 equivalents anthracene produced per equivalent $[Mn^{IV}(O)(^{DMM}N4py)]^{2+}$. This ratio was previously observed for $[Mn^{IV}(O)(N4py)]^{2+}$.[19] Iodometric titrations were performed to assess the Mn oxidation state following DHA oxidation by $[Mn^{IV}(O)(^{DMM}N4py)]^{2+}$. This yielded an average Mn oxidation state of 2.8±0.1, in good agreement with that observed previously for the reaction of $[Mn^{IV}(O)(N4py)]^{2+}$ with DHA.[19] Similar product analyses were carried out for the other C-H bond oxidation reactions by $[Mn^{IV}(O)(^{DMM}N4py)]^{2+}$. Oxidation of xanthene, diphenylmethane, and ethylbenzene yielded xanthone, benzophenone, and acetophenone, respectively, although the oxidation of ethylbenzene also yielded other unidentified products. In these cases, product analysis was performed after the reaction of $[Mn^{IV}(O)(^{DMM}N4py)]^{2+}$ with each substrate. After the reaction was completed, as verified by electronic absorption, solvent was removed *in vacuo*. Organic products were isolated by rinsing the dried material with 1 mL diethyl ether five times. Diethyl ether was then removed *in vacuo* and products were verified by ^1H NMR experiments in $CDCl_3$. After the diethyl ether rinse, the remaining Mn complex was analyzed by iodometric titration.[58] Iodometric titrations of solutions following the reaction yielded average Mn oxidation states of 2.8±0.2, 2.9±0.1, and 3.0±0.1 for the reactions with xanthene, diphenylmethane, and ethylbenzene, respectively. Thus, we presume the over-oxidation of substrate results from radical trapping by dioxygen.

Quantification of anthracene production by DHA oxidation by $[Mn^{IV}(O)(2pyN2Q)]^{2+}$ was complicated by the excess PhIO (10 equivalents relative to $[Mn^{IV}(O)(2pyN2Q)]^{2+}$) used to generate the Mn^{IV}-oxo. Specifically, the anthracene signal at 356 nm continued to grow, albeit at a far reduced rate, even after disappearance of the near-IR absorption signal associated with $[Mn^{IV}(O)(2pyN2Q)]^{2+}$. This behavior could be caused by reformation of $[Mn^{IV}(O)(2pyN2Q)]^{2+}$ due to the presence of excess PhIO in solution.

Alternatively, a Mn^{III} species, formed from the reaction of $[Mn^{IV}(O)(2pyN2Q)]^{2+}$ with DHA, could also react with DHA to slowly form anthracene. EPR spectra of solutions of following reaction of $[Mn^{IV}(O)(2pyN2Q)]^{2+}$ with DHA showed weak signals associated with $[Mn^{IV}(O)(2pyN2Q)]^{2+}$, consistent with some re-formation of the Mn^{IV}-oxo by the excess PhIO. Because of this, we did not attempt detailed product analysis of Mn content following reaction of $[Mn^{IV}(O)(2pyN2Q)]^{2+}$ with substrates.

Substrate bond dissociate energies for hydrocarbon substrates were xanthene BDE = 75 kcal mol^{-1}; 9,10-dihydroanthrace BDE = 78 kcal mol^{-1}, diphenylmethane BDE = 82 kcal mol^{-1}, ethylbenzene BDE = 85 kcal mol^{-1}, and toluene 88 kcal mol^{-1}.[59]

2.2.5 Mn^{IV}-oxo Cyclic Voltammetry Data

Cyclic voltammetry (CV) was used to probe the electrochemical properties of both $[Mn^{IV}(O)(^{DMM}N4py)]^{2+}$ and $[Mn^{IV}(O)(2pyN2Q)]^{2+}$. A glassy carbon working electrode, a platinum auxiliary electrode, and a Ag/AgCl quasi-reference electrode were used with an external ferrocene/ferrocenium potential used as an external reference. Cyclic voltammograms were recorded on an Epsilon potentiostat. These experiments used 2 mM Mn^{IV}-oxo complex in TFE with 0.1 M Bu_4NPF_6 electrolyte at 298 K. The CV trace for $[Mn^{IV}(O)(^{DMM}N4py)]^{2+}$ exhibited an irreversible one-electron oxidation process at 0.06 V vs. Cp_2Fe/Cp_2Fe^+ (0.61 V vs. SCE), which we attribute to the $Mn^{III}(O)/Mn^{IV}(O)$ couple (Figure A2.9). Increasing scan rate up to 1000 mV s^{-1} did not make this process appear reversible. The CV trace of $[Mn^{IV}(O)(^{DMM}N4py)]^{2+}$ also exhibits a reversible process at 1.30 V vs. Cp_2Fe/Cp_2Fe^+ (1.83 V vs. SCE). This wave could be due to a Mn^{IV}/Mn^{V} couple,[60] or to ligand oxidation. The nature of this redox process will be the subject of future investigation. $[Mn^{IV}(O)(2pyN2Q)]^{2+}$ exhibits a partially reversible one-electron process centered at 0.48 V vs. Cp_2Fe/Cp_2Fe^+ (1.01 V vs. SCE).

2.3 Results and Analysis

X-ray structures of $[Mn^{II}(^{DMM}N4py)(OTf)](OTf)$ (Figure 2.3) and $[Mn^{II}(2pyN2Q)(OH_2)](OTf)_2$ (Figure 2.4) each show a Mn^{II} center in a distorted octahedral geometry. The average Mn^{II}-$N_{equatorial}$ bond lengths of $[Mn^{II}(^{DMM}N4py)(OTf)](OTf)$ are

contracted relative to [Mn^{II}(N4py)(OTf)](OTf) (2.246 and 2.263 Å, respectively), while the [Mn^{II}(2pyN2Q)(OH_2)]($OTf)_2$ structure shows Mn^{II}-$N_{equatorial}$ elongations (2.279 Å). The axial H_2O ligand in [Mn^{II}(2pyN2Q)(OH_2)]($OTf)_2$ is tilted from the bulky quinolone moieties, giving an N_{axial}-Mn-O angle of 164° (Table A2.5). Overall, the structural variations suggest the ^{DMM}N4py and 2pyN2Q ligands strengthen and weaken the equatorial field, respectively, relative to N4py, with the 2pyN2Q ligand also influencing the axial position.

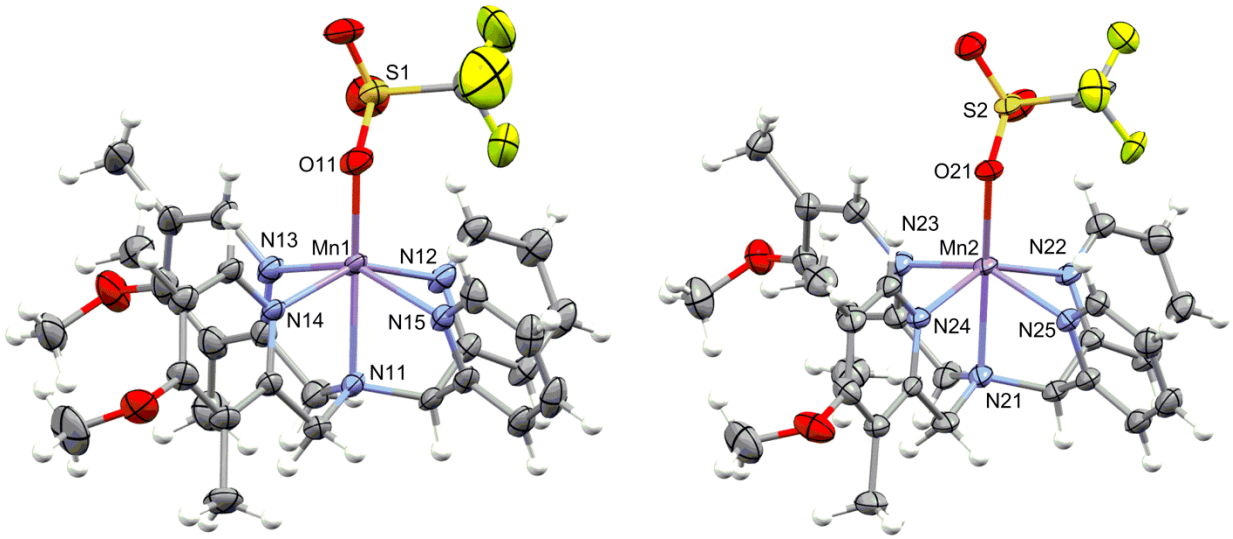

Figure 2.3. Molecular structures of [Mn^{II}(^{DMM}N4py)(OTf)]$^+$ cations found in the asymmetric unit of [Mn^{II}(^{DMM}N4py)(OTf)](OTf).

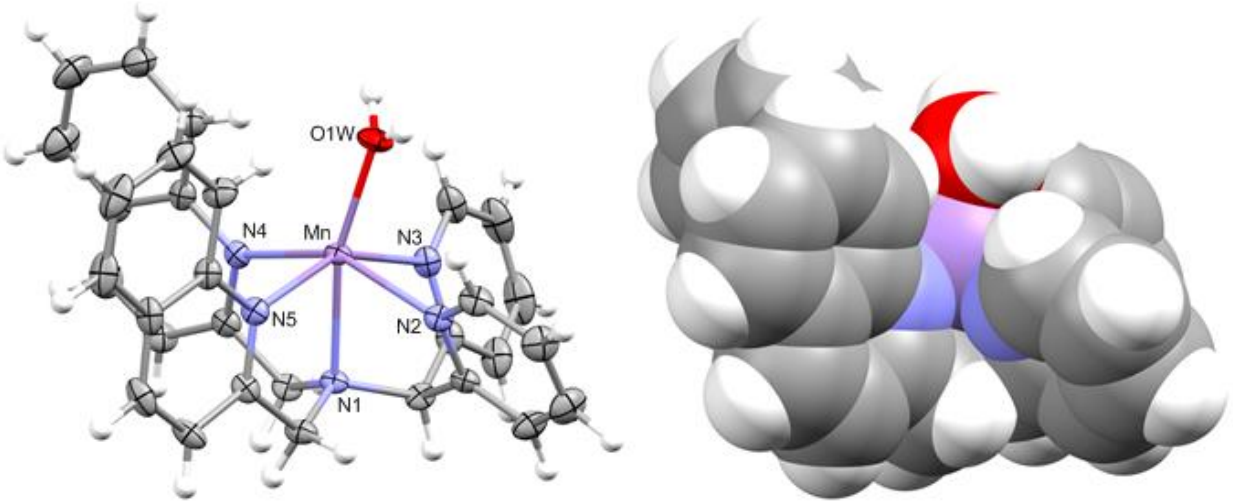

Figure 2.4. Molecular structure of [Mn^{II}(2pyN2Q)(OH_2)]$^{2+}$ cation found in the asymmetric unit of [Mn^{II}(2pyN2Q)(OH_2)]($OTf)_2$(OH_2) and corresponding space-filling diagram. The space-filling diagram highlights the steric influence of the quinoline donors on the axial water ligand.

The addition of excess iodosylbenzene (PhIO) to solutions of $[Mn^{II}(^{DMM}N4py)(OTf)](OTf)$ and $[Mn^{II}(2pyN2Q)(OTf)](OTf)$ in 2,2,2-trifluoroethanol (TFE) leads to the formation of new chromophores ($[Mn^{IV}(O)(^{DMM}N4py)]^{2+}$ and $[Mn^{IV}(O)(2pyN2Q)]^{2+}$) with near-IR absorption bands typical of Mn^{IV}-oxo species (Figures 2.5 and A2.3). The near-IR maxima of $[Mn^{IV}(O)(^{DMM}N4py)]^{2+}$ and $[Mn^{IV}(O)(2pyN2Q)]^{2+}$ are, respectively, blue- and red-shifted relative to $[Mn^{IV}(O)(N4py)]^{2+}$, with λ_{max} values at 10 870 and 8 475 cm^{-1} (ε = 290 and 179 $M^{-1}cm^{-1}$). Maximum formation of $[Mn^{IV}(O)(^{DMM}N4py)]^{2+}$ was achieved using 1.2 equivalents PhIO. This species is more stable than $[Mn^{IV}(O)(N4py)]^{2+}$, with a half-life ($t_{1/2}$) of 6 hr. at 298 K. In contrast, maximum formation of $[Mn^{IV}(O)(2pyN2Q)]^{2+}$ required 10 equivalents PhIO, and this species showed a $t_{1/2}$ of only 12 min. at 298 K. Both Mn^{IV}-oxo complexes fail to form when TFE is not a solvent or co-solvent. The ability of TFE to stabilize Mn^{IV}-oxo complexes was originally reported by Nam and co-workers.[17-18]

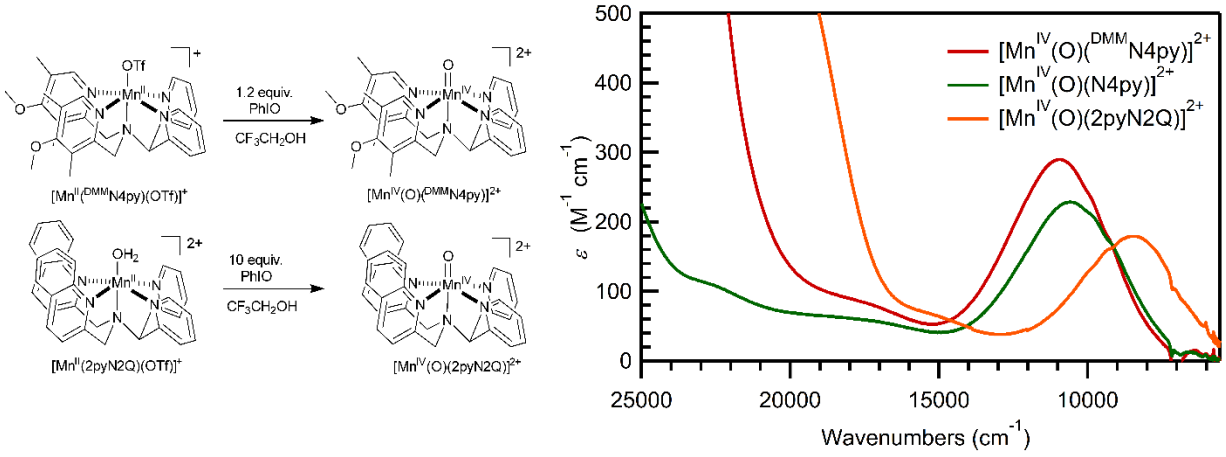

Figure 2.5. Formation reactions for Mn^{IV}-oxo species and electronic absorption spectra of $[Mn^{IV}(O)(^{DMM}N4py)]^{2+}$, $[Mn^{IV}(O)(2pyN2Q)]^{2+}$, and $[Mn^{IV}(O)(N4py)]^{2+}$.

ESI-MS experiments, performed for TFE solutions of $[Mn^{IV}(O)(^{DMM}N4py)]^{2+}$ and $[Mn^{IV}(O)(2pyN2Q)]^{2+}$ diluted in MeCN or MeOH, show ion peaks at *m/z* 277.10 and 269.07 (Figures A2.4 and A2.5), as expected for the corresponding Mn^{IV}-oxo adducts. Samples of $[Mn^{IV}(O)(^{DMM}N4py)]^{2+}$ and $[Mn^{IV}(O)(2pyN2Q)]^{2+}$ incubated with $H_2{}^{18}O$ showed new peaks at *m/z* 278.10 and 270.07. These new peaks indicate water exchange to form Mn^{IV}-^{18}O adducts.

The Mn^{IV} oxidation states in $[Mn^{IV}(O)(^{DMM}N4py)]^{2+}$ and $[Mn^{IV}(O)(2pyN2Q)]^{2+}$ were further established through EPR and Mn K-edge X-ray absorption (XAS) experiments. Mn K-edge for the Mn^{IV}-oxo complexes are compared in Figure 2.6. For these data, the post-edge line was normalized to 1, whereas data previously reported for $[Mn^{IV}(O)(N4py)]^{2+}$ were normalized to the most intense fluorescence feature.[61] EPR spectra of both $[Mn^{IV}(O)(^{DMM}N4py)]^{2+}$ and $[Mn^{IV}(O)(2pyN2Q)]^{2+}$ show a broad, derivative signal from 100 - 250 mT (Figure 2.7). The positive component at g_{eff} = 5.79 (~160 mT) shows a six-line hyperfine splitting (Table 2.1). These EPR features are typical of mononuclear, S = 3/2 Mn^{IV} centers,[62-63] and are very similar to those observed for $[Mn^{IV}(O)(N4py)]^{2+}$.[19] Weak multiline signals (g_{eff} = 2.0) in the EPR spectrum of $[Mn^{IV}(O)(2pyN2Q)]^{2+}$ are due to a small amount of dinuclear decay product.

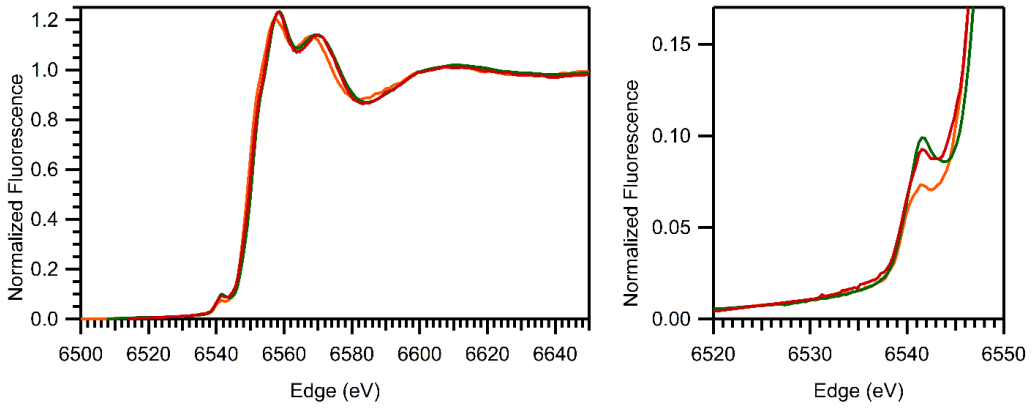

Figure 2.6. Comparison of normalized XAS edge energies (left) of $[Mn^{IV}(O)(N4py)]^{2+}$ (green), $[Mn^{IV}(O)(^{DMM}N4py)]^{2+}$ (red), and $[Mn^{IV}(O)(2pyN2Q)]^{2+}$ (orange). Comparison of normalized pre-edge features (right).

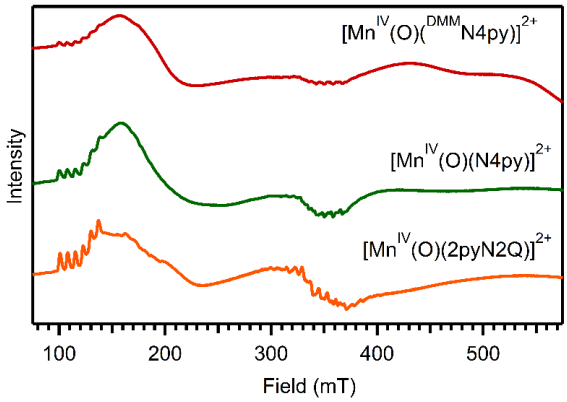

Figure 2.7. Perpendicular-mode X-band EPR spectra of $[Mn^{IV}(O)(^{DMM}N4py)]^{2+}$, $[Mn^{IV}(O)(2pyN2Q)]^{2+}$, and $[Mn^{IV}(O)(N4py)]^{2+}$.

Table 2.1. Spectroscopic properties of MnIV-oxo complexes.

Complex	λ_{max} (cm^{-1})	g_{eff}	a (mT)	edge (eV)	pre-edge (eV)	pre-edge area
$[Mn^{IV}(O)(^{DMM}N4py)]^{2+}$	10 870	5.79	77	6550.3	6541.3	19.6
$[Mn^{IV}(O)(N4py)]^{2+}$ [a]	10 530	5.76	76	6550.8	6541.6	18.9
$[Mn^{IV}(O)(2pyN2Q)]^{2+}$	8 475	5.79	72	6549.2	6541.2	17.0

[a] From references 19 and 18.

$[Mn^{IV}(O)(^{DMM}N4py)]^{2+}$ and $[Mn^{IV}(O)(2pyN2Q)]^{2+}$ exhibit XAS edge and pre-edge energies very close to those of $[Mn^{IV}(O)(N4py)]^{2+}$ (Table 2.1 and Figure 2.6), reinforcing the Mn^{IV} assignment. In addition, pre-edge peak areas of these complexes (~17-20 units) are in the range observed for tetragonal Mn^{IV}-oxo species.[61] The lower pre-edge area of $[Mn^{IV}(O)(2pyN2Q)]^{2+}$ is consistent with some fraction of Mn present as decay product. Unfortunately, EXAFS experiments were hampered by low XAS signal intensity, which is not unusual for samples in halogenated solvents.

In the absence of experimental structural information for $[Mn^{IV}(O)(^{DMM}N4py)]^{2+}$ and $[Mn^{IV}(O)(2pyN2Q)]^{2+}$, we turned to DFT computations. The DFT-derived structures show Mn=O distances of 1.678 Å (Figure 2.8), in accordance with the large pre-edge areas of these complexes (Table 2.1). The oxo ligand of $[Mn^{IV}(O)(2pyN2Q)]^{2+}$ is distorted away from the quinoline donors (Figure 2.9), leading to an N_{axial}-Mn-O bond angle of 170.6°. No such distortion is observed for $[Mn^{IV}(O)(^{DMM}N4py)]^{2+}$, where the corresponding angle is 179.8°. The average, calculated Mn^{II}-$N_{equatorial}$ distances are notably longer for $[Mn^{IV}(O)(2pyN2Q)]^{2+}$ than $[Mn^{IV}(O)(^{DMM}N4py)]^{2+}$ (2.054 *vs.* 2.015 Å, respectively).

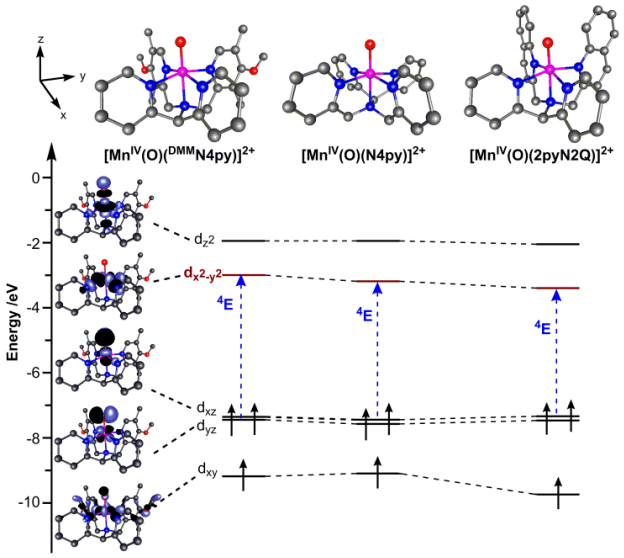

Figure 2.8. Structures of Mn^{IV}-oxo complexes from DFT computations and energy-level diagram using the α-spin Kohn-Sham MOs. Surface contour plots for the MOs of $[Mn^{IV}(O)(^{DMM}N4py)]^{2+}$ are included.

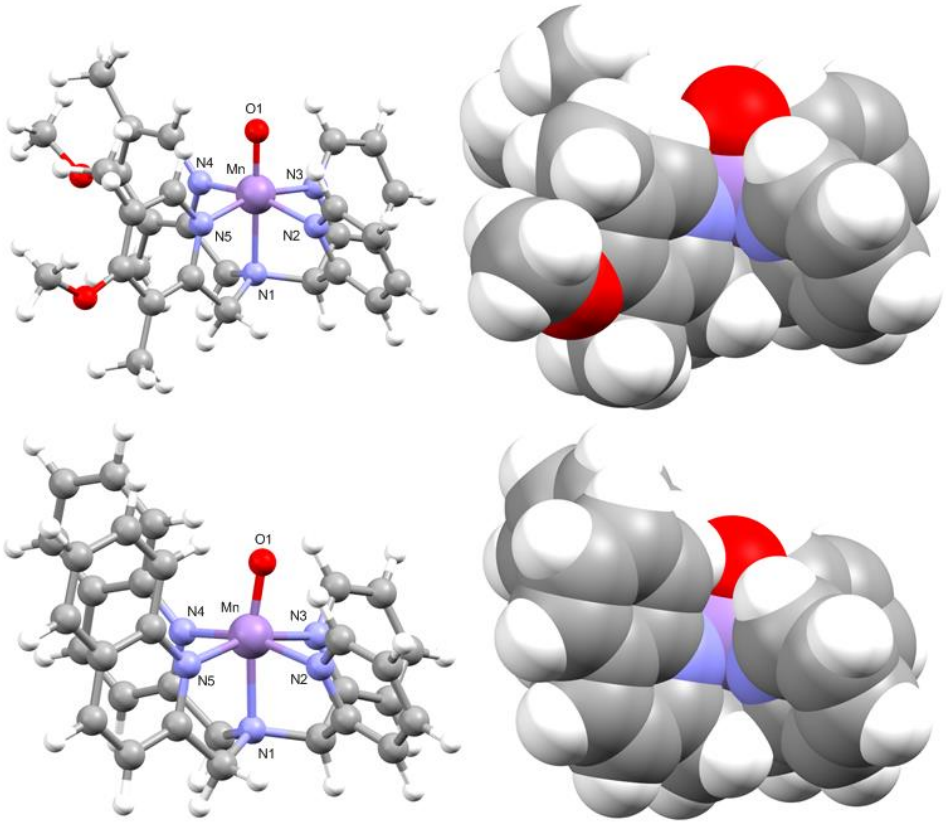

Figure 2.9. Molecular structures, including spacefilling models, of $[Mn^{IV}(O)(^{DMM}N4py)]^{2+}$ (top) and $[Mn^{IV}(O)(2pyN2Q)]^{2+}$ (bottom) from DFT geometry optimizations.

TD-DFT calculations for $[Mn^{IV}(O)(^{DMM}N4py)]^{2+}$ and $[Mn^{IV}(O)(2pyN2Q)]^{2+}$ predict near-IR absorption bands with energies in reasonable agreement with experiment (Figure 2.10). For each complex, these bands arise from the ^4E excited state. Inspection of Kohn-Sham MO energy-level diagrams reveals that the energy of the ^4E state largely reflects the position of the $b_1(d_{x^2-y^2})$ acceptor MO (Figure 2.8). The weaker equatorial field of $[Mn^{IV}(O)(2pyN2Q)]^{2+}$ causes the $b_1(d_{x^2-y^2})$ MO of this complex to lie 4 840 cm^{-1} below that of $[Mn^{IV}(O)(^{DMM}N4py)]^{2+}$ (Tables A2.9 and A2.10). The $e(d_{xz}, d_{yz})$ MO energies show a smaller variation of 1600 cm^{-1}. Thus, these ligand derivatives have achieved the intended goal of modulating the ^4E energy.

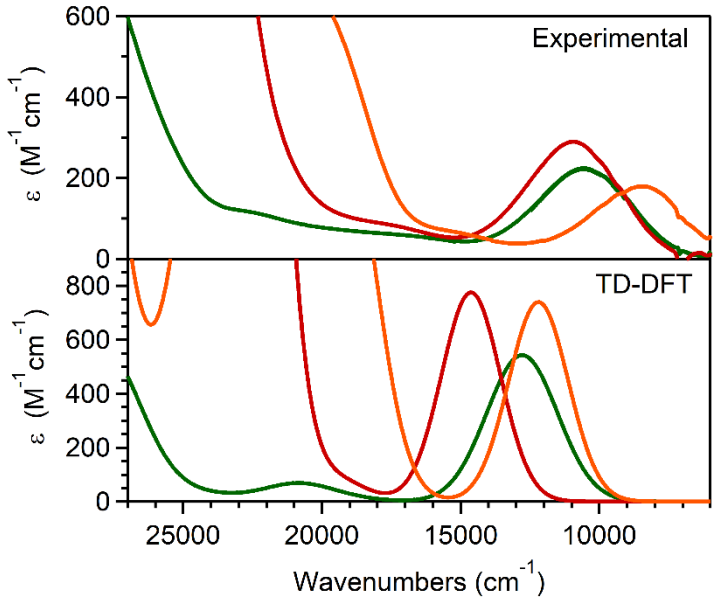

Figure 2.10. Experimental (top) and TD-DFT-computed (bottom) absorption spectra of $[Mn^{IV}(O)(^{DMM}N4py)]^{2+}$ (red), $[Mn^{IV}(O)(2pyN2Q)]^{2+}$ (green) and $[Mn^{IV}(O)(N4py)]^{2+}$ (orange).

To assess the impact of ligand perturbations on HAT reactions, $[Mn^{IV}(O)(^{DMM}N4py)]^{2+}$ and $[Mn^{IV}(O)(2pyN2Q)]^{2+}$ were treated with alkanes with C-H bond strengths ranging from 75 to 88 kcal/mol. Reactions with >10 equivalents substrate showed first-order decay of the near-IR absorption signals associated with the Mn^{IV}-oxo complexes to at least four half-lives and permitted determination of second-order rate constants, k_2 (Figure 2.11 and Supporting Information). The values of k_2', the rate constant corrected for the number of reactive C-H bonds, reveal an order of reactivity of $[Mn^{IV}(O)(2pyN2Q)]^{2+}$ > $[Mn^{IV}(O)(N4py)]^{2+}$ > $[Mn^{IV}(O)(^{DMM}N4py)]^{2+}$ for each substrate

(Table 2.2). Focusing on ethylbenzene (EtBn), $[Mn^{IV}(O)(2pyN2Q)]^{2+}$ shows rate enhancements of 14- and 133-fold compared to $[Mn^{IV}(O)(N4py)]^{2+}$ and $[Mn^{IV}(O)(^{DMM}N4py)]^{2+}$, respectively. The k_2' of 2.7× 10^{-2} $M^{-1}s^{-1}$ for $[Mn^{IV}(O)(2pyN2Q)]^{2+}$ at 298 K is larger than that of $[Mn^{IV}(O)(BnTPEN)]^{2+}$ (k_2' = 1.4 × 10^{-2} $M^{-1}s^{-1}$),[17] which is one of the most reactive nonporphyrin Mn^{IV}-oxo complexes.[17]

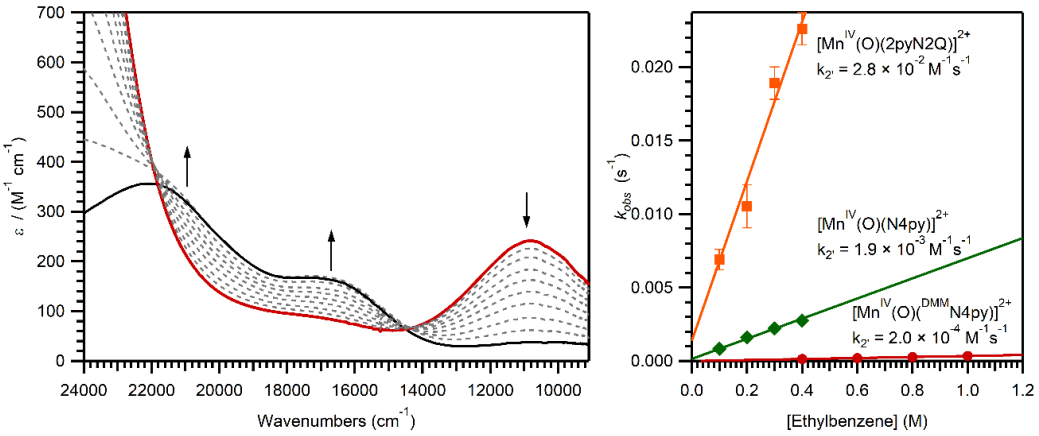

Figure 2.11. Left: UV-vis spectra showing the reaction of $[Mn^{IV}(O)(^{DMM}N4py)]^{2+}$ with ethylbenzene in CF_3CH_2OH at 298 K. Right: k_{obs} versus ethylbenzene concentration for each Mn^{IV}-oxo complex.

Table 2.2. Kinetic Parameters for Reaction of $[Mn^{IV}(O)(^{DMM}N4py)]2+$, $[Mn^{IV}(O)(N4py)]^{2+}$, and $[Mn^{IV}(O)(2pyN2Q)]^{2+}$ with Hydrocarbons.

	k_2' ($M^{-1}s^{-1}$)[a]					H/D KIE
	Xan	DHA	DPM[c]	EtBn	Tol	DHA
$[Mn^{IV}(O)(^{DMM}N4py)]^{2+}$	3.1(3) × 10^{-1}	8.6(2) × 10^{-2}	5.6(1) × 10^{-4}	2.0(1) × 10^{-4}	ND[b]	10.2
$[Mn^{IV}(O)(N4py)]^{2+}$ [c]	ND[b]	9.0(9) × 10^{-1}	9.9(6) × 10^{-3}	1.9(1) × 10^{-3}	2.1(3) × 10^{-4}	11.2
$[Mn^{IV}(O)(2pyN2Q)]^{2+}$	ND[b]	5.6(7)	8.7(5) × 10^{-2}	2.7(2) × 10^{-2}	2.7(3) × 10^{-3}	5.3

[a] Rates are corrected for the number of reactive C-H functions. Xan is xanthene, DHA is 9,10-dihydroanthracene, DPM is diphenylmethane, EtBn is ethylbenzene, and Tol is toluene. [b] Not determined. [c] From reference 19.

For each Mn^{IV}-oxo species, plots of log(k_2') versus substrate bond dissociation enthalpy (BDE) are linear (Figure 2.12), indicative of a HAT mechanism. Experiments using dihydroanthracene (DHA) and d_4-DHA yielded H/D kinetic isotope effects (KIEs) of 10.2 and 5.3 for $[Mn^{IV}(O)(^{DMM}N4py)]^{2+}$ and $[Mn^{IV}(O)(2pyN2Q)]^{2+}$, respectively. The KIE of

the former complex is very similar to that of $[Mn^{IV}(O)(N4py)]^{2+}$ (Table 2.2), consistent with a tunneling contribution.[19] The smaller KIE of $[Mn^{IV}(O)(2pyN2Q)]^{2+}$ is within the range observed for Mn^{IV}-oxo species (3.1 - 6.8).[16, 64]

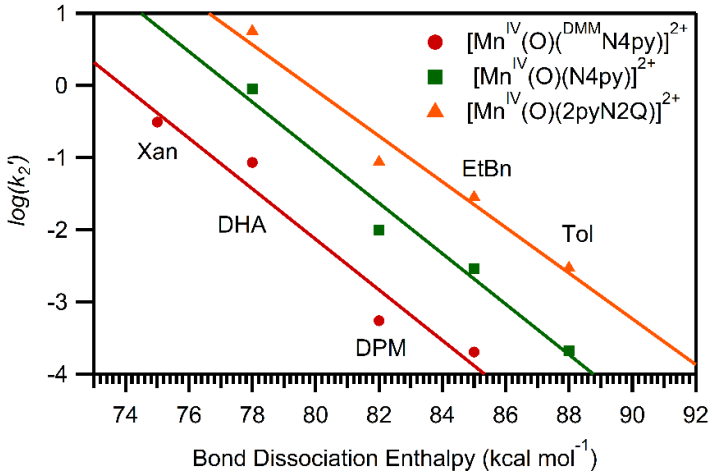

Figure 2.12. Comparison of log(k_2') versus substrate bond dissociation enthalpy (Xan = xanthene; DHA = dihydroanthracene; DPM = diphenylmethane; EtBn = ethylbenzene; and Tol = toluene).

DHA oxidation by $[Mn^{IV}(O)(^{DMM}N4py)]^{2+}$ produced 0.5 equivalents anthracene per equivalent Mn^{IV}-oxo complex, as reported for $[Mn^{IV}(O)(N4py)]^{2+}$.[19] An iodometric analysis of the solution following the reaction revealed an average Mn oxidation state of 2.8±0.1. Thus, for DHA oxidation, a radical rebound pathway, producing hydroxylated organic product and a Mn^{II} center, is not observed. The factors influencing rebound versus "non-rebound" mechanisms have been discussed by Nam and Shaik.[21, 65-66] Product analyses for reactions with $[Mn^{IV}(O)(2pyN2Q)]^{2+}$ were complicated by the excess PhIO used to generate the Mn^{IV}-oxo species.

2.4 Discussion

The available HAT and OAT kinetic data provide evidence for a correlation between the reaction rates and the energy of the ^4E state. Figure 2.13 illustrates this correlation for EtBn oxidation, and includes data for $[Mn^{IV}(O)(BnTPEN)]^{2+}$.[17] This correlation is consistent with DFT predictions that the ^4E excited state mediates HAT reactions for these Mn^{IV}-oxo complexes,[20-21] but does not prove this prediction as the ^4E energy could correlate with a separate parameter that influences the rates.

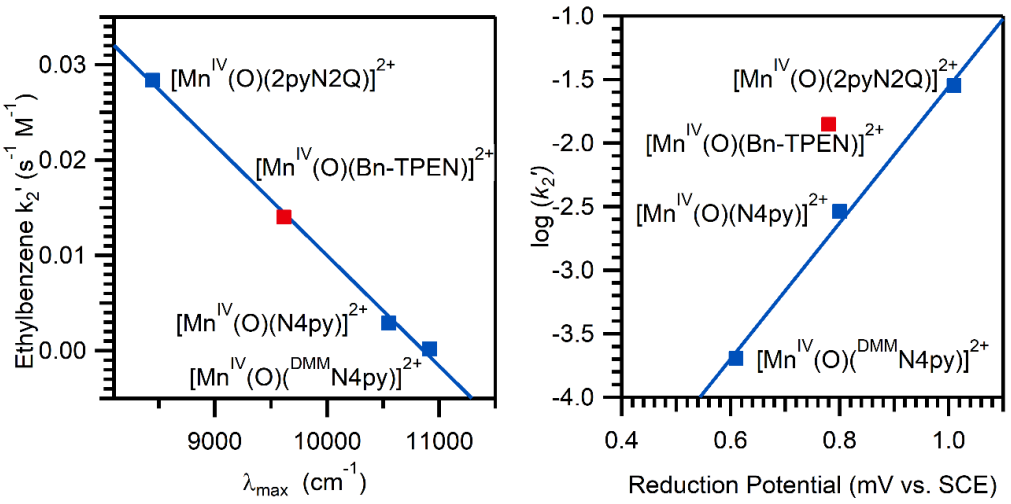

Figure 2.13 Top: Experimental k_2' value for EtBn oxidation versus near-IR absorption maxima of Mn^{IV}-oxo complexes. The fitted line shows the correlation for all complexes. Bottom: log(k_2') for EtBn oxidation versus $Mn^{III/IV}$ reduction potentials. The fitted line shows the correlation for N4py derivatives. Data for $[Mn^{IV}(O)(BnTPEN)]^{2+}$ from reference 17.

We had previously noted that $[Mn^{IV}(O)(N4py)]^{2+}$ showed a more positive $Mn^{III/IV}$ potential than other, less reactive Mn^{IV}-oxo complexes, which is in line with the known relationship between HAT rates and thermodynamic driving force.[19] For the present Mn^{IV}-oxo complexes, peak potentials ($E_{p,c}$) from cyclic voltammetry show that the most reactive complex, $[Mn^{IV}(O)(2pyN2Q)]^{2+}$, has the most positive potential (1.01 V versus SCE). In fact, the observed potentials for $[Mn^{IV}(O)(N4py)]^{2+}$ and its derivatives show a linear relationship between log(k_2') and $E_{p,c}$ (Figure 2.13). While a full thermodynamic analysis of HAT reactivity would require some knowledge of the proton affinity of the Mn^{IV}-oxo species, we have been unable to determine pK_b values for the Mn^{IV}-oxo species or pK_a values for the Mn^{III}-hydroxo products.

2.5 Conclusions

In this study we have established that both the near-IR absorption maxima and $Mn^{III/IV}$ reduction potentials of these Mn^{IV}-oxo complexes are correlated with HAT and OAT reaction rates. These observations lend experimental support for the involvement of a ^4E excited state in the reactivity of Mn^{IV}-oxo complexes, but they do not prove this model. Moreover, these correlations pertain to Mn^{IV}-oxo species in tetragonal

environments with N5 supporting ligands. Although, we have recently noted that $[Mn^{IV}(O)(OH)(Me_2EBC)]^+$, which is a more sluggish oxidant,[15, 67] has a fairly high energy ^4E excited state,[23] the applicability of these correlations to Mn^{IV}-oxo complexes with anionic ligands, O-donor ligands, and/ or trigonal coordination environments is an open question.[16, 67-70] It is also unclear what effect, if any, the steric interactions between the oxo and quinoline ligands in $[Mn^{IV}(O)(2pyN2Q)]^{2+}$ have on reactivity. One of the most reactive nonheme Fe^{IV}-oxo complexes also contains quinoline donors.[7, 71] Understanding the range and limits of these correlations within the context of the more diverse ligand spheres present in the full family of Mn^{IV}-oxo species should provide additional insight into the factors controlling Mn^{IV}-oxo reactivity.

2.6 Notes and References

1. Neu, H. M.; Baglia, R. A.; Goldberg, D. P., A Balancing Act: Stability versus Reactivity of Mn(O) Complexes. *Acc. Chem. Rev.* **2015,** *48* (10), 2754-2764.

2. Stone, K. L.; Borovik, A. S., Lessons from nature: unraveling biological CH bond activation. *Curr. Opin. Chem. Biol.* **2009,** *13* (1), 114-118.

3. Ray, K.; Pfaff, F. F.; Wang, B.; Nam, W., Status of Reactive Non-Heme Metal–Oxygen Intermediates in Chemical and Enzymatic Reactions. *Journal of the American Chemical Society* **2014,** *136* (40), 13942-13958.

4. Solomon, E. I.; Wong, S. D.; Liu, L. V.; Decker, A.; Chow, M. S., Peroxo and oxo intermediates in mononuclear nonheme iron enzymes and related active sites. *Curr. Opin. Chem. Biol.* **2009,** *13* (1), 99-113.

5. Bollinger Jr, J. M.; Chang, W.-c.; Matthews, M. L.; Martinie, R. J.; Boal, A. K.; Krebs, C., CHAPTER 3 Mechanisms of 2-Oxoglutarate-Dependent Oxygenases: The Hydroxylation Paradigm and Beyond. In *2-Oxoglutarate-Dependent Oxygenases*, The Royal Society of Chemistry: 2015; pp 95-122.

6. Krest, C. M.; Onderko, E. L.; Yosca, T. H.; Calixto, J. C.; Karp, R. F.; Livada, J.; Rittle, J.; Green, M. T., Reactive Intermediates in Cytochrome P450 Catalysis. *Journal of Biological Chemistry* **2013,** *288* (24), 17074-17081.

7. Puri, M.; Que, L., Toward the Synthesis of More Reactive S = 2 Non-Heme Oxoiron(IV) Complexes. *Acc. Chem. Rev.* **2015,** *48* (8), 2443-2452.

8. Liu, W.; Groves, J. T., Manganese Catalyzed C–H Halogenation. *Acc. Chem. Rev.* **2015,** *48* (6), 1727-1735.

9. Conde, A.; Sabenya, G.; Rodríguez, M.; Postils, V.; Luis, J. M.; Díaz-Requejo, M. M.; Costas, M.; Pérez, P. J., Iron and Manganese Catalysts for the Selective Functionalization of Arene C(sp2)−H Bonds by Carbene Insertion. *Angewandte Chemie International Edition* **2016,** *55* (22), 6530-6534.

10. Codola, Z.; Lloret-Fillol, J.; Costas, M., Aminopyridine Iron and Manganese Complexes as Molecular Catalysts for Challenging Oxidative Transformations. In *Progress in Inorganic Chemistry: Volume 59*, John Wiley & Sons, Inc.: 2014; pp 447-532.

11. Ottenbacher, R. V.; Samsonenko, D. G.; Talsi, E. P.; Bryliakov, K. P., Enantioselective Epoxidations of Olefins with Various Oxidants on Bioinspired Mn Complexes: Evidence for Different Mechanisms and Chiral Additive Amplification. *ACS Catalysis* **2016,** *6* (2), 979-988.

12. Talsi, E. P.; Ottenbacher, R. V.; Bryliakov, K. P., Bioinspired oxidations of aliphatic C–H groups with H2O2 in the presence of manganese complexes. *J. Organomet. Chem.* **2015,** *793*, 102-107.

13. Liu, W.; Huang, X.; Cheng, M.-J.; Nielsen, R. J.; Goddard, W. A.; Groves, J. T., Oxidative Aliphatic C-H Fluorination with Fluoride Ion Catalyzed by a Manganese Porphyrin. *Science* **2012,** *337* (6100), 1322-1325.

14. Smith, B. J.; Hernández Gallegos, P. A.; Butsch, K.; Stack, T. D. P., Metal complex assembly controlled by surface ligand distribution on mesoporous silica: Quantification using refractive index matching and impact on catalysis. *J. Catal.* **2016,** *335*, 197-203.

15. Yin, G.; Danby, A. M.; Kitko, D.; Carter, J. D.; Scheper, W. M.; Busch, D. H., Oxidative Reactivity Difference among the Metal Oxo and Metal Hydroxo Moieties: pH Dependent Hydrogen Abstraction by a Manganese(IV) Complex Having Two Hydroxide Ligands. *J. Am. Chem. Soc* **2008,** *130* (48), 16245-16253.

16. Garcia-Bosch, I.; Company, A.; Cady, C. W.; Styring, S.; Browne, W. R.; Ribas, X.; Costas, M., Evidence for a Precursor Complex in C□H Hydrogen Atom Transfer Reactions Mediated by a Manganese(IV) Oxo Complex. *Angew. Chem., Int. Ed. Engl.* **2011,** *123* (25), 5766-5771.

17. Wu, X.; Seo, M. S.; Davis, K. M.; Lee, Y.-M.; Chen, J.; Cho, K.-B.; Pushkar, Y. N.; Nam, W., A Highly Reactive Mononuclear Non-Heme Manganese(IV)–Oxo Complex That Can Activate the Strong C–H Bonds of Alkanes. *J. Am. Chem. Soc* **2011,** *133* (50), 20088-20091.

18. Chen, J.; Lee, Y.-M.; Davis, K. M.; Wu, X.; Seo, M. S.; Cho, K.-B.; Yoon, H.; Park, Y. J.; Fukuzumi, S.; Pushkar, Y. N.; Nam, W., A Mononuclear Non-Heme Manganese(IV)–Oxo Complex Binding Redox-Inactive Metal Ions. *J. Am. Chem. Soc* **2013,** *135* (17), 6388-6391.

19. Leto, D. F.; Ingram, R.; Day, V. W.; Jackson, T. A., Spectroscopic properties and reactivity of a mononuclear oxomanganese(iv) complex. *Chem. Commun.* **2013,** *49* (47), 5378-5380.

20. Chen, J.; Cho, K.-B.; Lee, Y.-M.; Kwon, Y. H.; Nam, W., Mononuclear nonheme iron(iv)-oxo and manganese(iv)-oxo complexes in oxidation reactions: experimental results prove theoretical prediction. *Chem. Commun.* **2015,** *51* (66), 13094-7.

21. Cho, K.-B.; Shaik, S.; Nam, W., Theoretical Investigations into C–H Bond Activation Reaction by Nonheme MnIVO Complexes: Multistate Reactivity with No Oxygen Rebound. *J. Phys. Chem. Lett.* **2012,** *3* (19), 2851-2856.

22. Kim, S.; Cho, K.-B.; Lee, Y.-M.; Chen, J.; Fukuzumi, S.; Nam, W., Factors Controlling the Chemoselectivity in the Oxidation of Olefins by Nonheme Manganese(IV)-Oxo Complexes. *Journal of the American Chemical Society* **2016,** *138* (33), 10654-10663.

23. Leto, D. F.; Massie, A. A.; Rice, D. B.; Jackson, T. A., Spectroscopic and Computational Investigations of a Mononuclear Manganese(IV)-Oxo Complex Reveal Electronic Structure Contributions to Reactivity. *J. Am. Chem. Soc* **2016,** *138* (47), 15413-15424.

24. Rana, S.; Dey, A.; Maiti, D., Mechanistic elucidation of C-H oxidation by electron rich non-heme iron(iv)-oxo at room temperature. *Chemical Communications* **2015,** *51* (77), 14469-14472.

25. Lo, W. K. C.; McAdam, C. J.; Blackman, A. G.; Crowley, J. D.; McMorran, D. A., The pentadentate ligands 2PyN2Q and N4Py, and their Cu(II) and Zn(II) complexes: A synthetic, spectroscopic and crystallographic structural study. *Inorganica Chimica Acta* **2015,** *426*, 183-194.

26. Seo, M. S.; Kim, J. Y.; Annaraj, J.; Kim, Y.; Lee, Y.-M.; Kim, S.-J.; Kim, J.; Nam, W., $[Mn(tmc)(O_2)]^+$: A Side-On Peroxide Manganese(III) Complex Bearing a Non-heme Ligand. *Angewandte Chemie International Edition* **2007,** *46*, 377-380.

27. Armarego, W. L. F.; Perrin, D. D., *Purification of Laboratory Chemicals*. Butterworth-Heinemann: Oxford, U.K., 1997.

28. Goldsmith, C. R.; Jonas, R. T.; Stack, T. D. P., C−H Bond Activation by a Ferric Methoxide Complex: Modeling the Rate-Determining Step in the Mechanism of Lipoxygenase. *J. Am. Chem. Soc* **2002,** *124* (1), 83-96.

29. Saltzman, H.; Sharefkin, J. G., Iodosobenzene. *Organic Syntheses* **1963,** *43*, 60.

30. Chang, J.; Plummer, S.; Berman, E. S. F.; Striplin, D.; Blauch, D., Synthesis and Characterization of Bis(di-2-pyridylmethanamine)ruthenium(II). *Inorg. Chem.* **2004,** *43* (5), 1735-1742.

31. Lubben, M.; Meetsma, A.; Wilkinson, E. C.; Feringa, B.; Que Jr., L., Nonheme Iron Centers in Oxygen Activation: Characterization of an Iron(III) Hydroperoxide Intermediate. *Angew. Chem., Int. Ed. Engl.* **1995,** *34* (13-14), 1512-1514.

32. Geiger, R. A.; Leto, D. F.; Chattopadhyay, S.; Dorlet, P.; Anxolabéhère-Mallart, E.; Jackson, T. A., Geometric and Electronic Structures of Peroxomanganese(III) Complexes

Supported by Pentadentate Amino-Pyridine and -Imidazole Ligands. *Inorg. Chem.* **2011,** *50* (20), 10190-10203.

33. Mitra, M.; Nimir, H.; Demeshko, S.; Bhat, S. S.; Malinkin, S. O.; Haukka, M.; Lloret-Fillol, J.; Lisensky, G. C.; Meyer, F.; Shteinman, A. A.; Browne, W. R.; Hrovat, D. A.; Richmond, M. G.; Costas, M.; Nordlander, E., Nonheme Fe(IV) Oxo Complexes of Two New Pentadentate Ligands and Their Hydrogen-Atom and Oxygen-Atom Transfer Reactions. *Inorg. Chem.* **2015,** *54* (15), 7152-7164.

34. Dohi, T.; Yamaoka, N.; Kita, Y., Fluoroalcohols: versatile solvents in hypervalent iodine chemistry and syntheses of diaryliodonium(III) salts. *Tetrahedron* **2010,** *66* (31), 5775-5785.

35. Singh, R.; Banerjee, S.; Mossain, M. K.; Nordlander, E.; Paine, T. K., *Unpublished results*.

36. Ravel, B.; Newville, M., ATHENA, ARTEMIS, HEPHAESTUS: data analysis for X-ray absorption spectroscopy using IFEFFIT. *Journal of Synchrotron Radiation* **2005,** *12* (4), 537-541.

37. Wojdyr, M., Fityk: a general-purpose peak fitting program. *Journal of Applied Crystallography* **2010,** *43* (5 Part 1), 1126-1128.

38. Neese, F. *ORCA - an ab initio, Density Functional and Semiempirical Program Package, Version 3.0, Max Planck Institute for Chemical Energy Conversion, 2013.*, 2013.

39. Neese, F., The ORCA program system. *Wiley Interdisciplinary Reviews: Computational Molecular Science* **2012,** *2* (1), 73-78.

40. Tao, J.; Perdew, J. P.; Staroverov, V. N.; Scuseria, G. E., Climbing the Density Functional Ladder: Nonempirical Meta-Generalized Gradient Approximation Designed for Molecules and Solids. *Phys. Rev. Lett.* **2003,** *91* (14), 146401.

41. Schäfer, A.; Horn, H.; Ahlrichs, R., Fully optimized contracted Gaussian basis sets for atoms Li to Kr. *J. Chem. Phys.* **1992,** *97* (4), 2571-2577.

42. Schäfer, A.; Huber, C.; Ahlrichs, R., Fully Optimized Contracted Gaussian Basis Sets of Triple Zeta Valence Quality for Atoms Li to Kr. *J. Chem. Phys.* **1994,** *100*, 5829-5835.

43. Neese, F., An Improvement of the Resolution of the Identity Approximation for the Calculation of the Coulomb Matrix. *Journal of Computational Chemistry* **2003,** *24*, 1740-1747.

44. Becke, A. D., A New Mixing of Hartree-Fock and Local-density-functional Theories. *J. Chem. Phys.* **1993,** *98* (2), 1372-1377.

45. Becke, A. D., Density-functional Thermochemistry. III. The Role of Exact Exchange. *J. Chem. Phys.* **1993,** *98* (7), 5648-5652.

46. Lee, C.; Yang, W.; Parr, R. G., Development of the Colle-Salvetti Correlation-energy Formula into a Functional of the Electron Density. *Phys. Rev. B* **1988,** *37* (2), 785-789.

47. Izsák, R.; Neese, F., An overlap fitted chain of spheres exchange method. *J. Chem. Phys.* **2011,** *135* (14), 144105.

48. Cossi, M.; Scalmani, G.; Rega, N.; Barone, V., New developments in the polarizable continuum model for quantum mechanical and classical calculations on molecules in solution. *The Journal of Chemical Physics* **2002,** *117* (1), 43-54.

49. Mennucci, B.; Tomasi, J., Continuum solvation models: A new approach to the problem of solute's charge distribution and cavity boundaries. *The Journal of Chemical Physics* **1997,** *106* (12), 5151-5158.

50. Bauernschmitt, R.; Ahlrichs, R., Treatment of electronic excitations within the adiabatic approximation of time dependent density functional theory. *Chem. Phys. Lett.* **1996,** *256*, 454-464.

51. Casida, E. M.; Jamorski, C.; Casida, K. C.; Salahub, D. R., Molecular Excitation Energies to High-lying bound States from Time-dependent Density-functional Response Theory: Characterization and Correction of the Time-dependent Local Density Approximation Ionization Threshold. *J. Chem. Phys.* **1998,** *108*, 4439-4449.

52. Hirata, S.; Head-Gordon, M., Time-dependent Density Functional Theory for Radicals: An Improved Description of Excited States with Substantial Double Excitation Character. *Chem. Phys. Lett.* **1999,** *302*, 375-382.

53. Hirata, S.; Head-Gordon, M., Time-dependent Density Functional Theory within the Tamm–Dancoff Approximation. *Chem. Phys. Lett.* **1999,** *314*, 291-299.

54. Stratman, R. E.; Scuseria, G. E.; Frisch, M. J., An Efficient Implementation of Time-dependent Density-functional Theory for the Calculation of Excitation Energies of Large Molecules. *J. Chem. Phys.* **1998,** *109*, 8218-8224.

55. Laaksonen, L., A Graphics Program for the Analysis and Display of Molecular Dynamics Trajectories. *J. Mol. Graphics* **1992,** *10*, 33-34.

56. Bergman, D. L.; Laaksonen, L.; Laaksonen, A., Visualization of Solvation Structures in Liquid Mixtures. *J. Mol. Graphics & Modelling* **1997,** *15*, 301-306.

57. Berlman, I. B., *Handbook of Fluorescence Spectra of Atomic Molecules*. Academic Press, N.Y.: 1971.

58. Perez-Benito, J. F.; Brillas, E.; Arias, C., Iodimetric determinations in organic solvents: Determination of manganese oxidation states in methylene chloride solutions. *Can. J. Chem.* **1990,** *68* (1), 79-81.

59. Goldsmith, C. R.; Cole, A. P.; Stack, T. D. P., C−H Activation by a Mononuclear Manganese(III) Hydroxide Complex: Synthesis and Characterization of a Manganese-Lipoxygenase Mimic? *Journal of the American Chemical Society* **2005,** *127* (27), 9904-9912.

60. Yin, G.; McCormick, J. M.; Buchalova, M.; Danby, A. M.; Rodgers, K.; Day, V. W.; Smith, K.; Perkins, C. M.; Kitko, D.; Carter, J. D.; Scheper, W. M.; Busch, D. H., Synthesis, Characterization, and Solution Properties of a Novel Cross-Bridged Cyclam Manganese(IV) Complex Having Two Terminal Hydroxo Ligands. *Inorg. Chem.* **2006,** *45* (20), 8052-8061.

61. Leto, D. F.; Jackson, T. A., Mn K-Edge X-ray Absorption Studies of Oxo- and Hydroxomanganese(IV) Complexes: Experimental and Theoretical Insights into Pre-Edge Properties. *Inorg. Chem.* **2014,** *53*, 6179-6194.

62. Zlatar, M.; Gruden, M.; Vassilyeva, O. Y.; Buvaylo, E. A.; Ponomarev, A. N.; Zvyagin, S. A.; Wosnitza, J.; Krzystek, J.; Garcia-Fernandez, P.; Duboc, C., Origin of the Zero-Field Splitting in Mononuclear Octahedral MnIV Complexes: A Combined Experimental and Theoretical Investigation. *Inorg. Chem.* **2016,** *55* (3), 1192-1201.

63. Leto, D. F.; Massie, A. A.; Colmer, H. E.; Jackson, T. A., X-Band Electron Paramagnetic Resonance Comparison of Mononuclear MnIV-oxo and MnIV-hydroxo Complexes and Quantum Chemical Investigation of MnIV Zero-Field Splitting. *Inorg. Chem.* **2016,** *55* (7), 3272-3282.

64. Parsell, T. H.; Yang, M.-Y.; Borovik, A. S., C−H Bond Cleavage with Reductants: Re-Investigating the Reactivity of Monomeric MnIII/IV−Oxo Complexes and the Role of Oxo Ligand Basicity. *J. Am. Chem. Soc* **2009,** *131* (8), 2762-2763.

65. Cho, K.-B.; Wu, X.; Lee, Y.-M.; Kwon, Y. H.; Shaik, S.; Nam, W., Evidence for an Alternative to the Oxygen Rebound Mechanism in C–H Bond Activation by Non-Heme FeIVO Complexes. *Journal of the American Chemical Society* **2012,** *134* (50), 20222-20225.

66. Cho, K.-B.; Hirao, H.; Shaik, S.; Nam, W., To rebound or dissociate? This is the mechanistic question in C-H hydroxylation by heme and nonheme metal-oxo complexes. *Chem. Soc. Rev.* **2016,** *45* (5), 1197-1210.

67. Shi, S., Wang, Y., Xu, A., Wang, H., Zhu, D., Roy, S.B., Jackson, T.A., Busch, D.H., Yin, G., Distinct Reactivity Differences of Metal Oxo and Its Corresponding Hydroxo Moieties in Oxidations: Implications from a Manganese(IV) Complex Having Dihydroxide Ligand. *Angew. Chem. Int. Ed.* **2011,** *50*, 7321-7324.

68. Parsell, T. H.; Behan, R. K.; Green, M. T.; Hendrich, M. P.; Borovik, A. S., Preparation and Properties of a Monomeric MnIV-Oxo Complex. *J. Am. Chem. Soc* **2006,** *128* (27), 8728-8729.

69. Wu, X.; Yang, X.; Lee, Y.-M.; Nam, W.; Sun, L., A nonheme manganese(iv)-oxo species generated in photocatalytic reaction using water as an oxygen source. *Chemical Communications* **2015,** *51* (19), 4013-4016.

70. Arunkumar, C.; Lee, Y.-M.; Lee, J. Y.; Fukuzumi, S.; Nam, W., Hydrogen-Atom Abstraction Reactions by Manganese(V)– and Manganese(IV)–Oxo Porphyrin Complexes in Aqueous Solution. *Chem. Eur. J.* **2009,** *15* (43), 11482-11489.

71. Biswas, A. N.; Puri, M.; Meier, K. K.; Oloo, W. N.; Rohde, G. T.; Bominaar, E. L.; Münck, E.; Que Jr., L., Modeling TauD-J: A High-Spin Nonheme Oxoiron(IV) Complex with High Reactivity toward C–H Bonds. *J. Am. Chem. Soc* **2015,** *137* (7), 2428-2431.

Chapter 3. Hydrogen-atom Transfer Driving Force and Rate Correlations for an Oxomanganese(IV) Species

This work has been submitted for publication in *Inorganic Chemistry* as the following: Massie, A. A.; Sinha, A.; Nordlander, E.; Jackson, T. A., *Inorganic Chemistry.*

3.1 Introduction

Hydrogen atom transfer reactions by high-valent metal-oxo species are important in both biological and synthetic settings. In nature, the Compound I intermediate of cytochrome P450 enzymes, which features an oxoiron(IV) adduct coupled to a porphyrin radical, is responsible for initiating the oxidation of strong C-H bonds under ambient conditions by a hydrogen-atom transfer (HAT) mechanism.[1-2] Several families of non-heme iron enzymes also utilize oxoiron(IV) centers to abstract hydrogen atoms from C-H bonds, leading to halogenation, hydroxylation, or desaturation reactions depending on the function of the enzyme.[3-4]

Taking inspiration from nature, a range of both heme and non-heme synthetic oxoiron(IV) and oxomanganese(IV) complexes have been prepared that show varying abilities to activate C-H bonds.[5-6] In nature, nonheme oxoiron(IV) species are found to have S = 2 (quintet) ground states, while most synthetic complexes have S = 1 (triplet) ground states. These synthetic oxoiron(IV) complexes are usually less reactive than their enzymatic counterparts.[5] To explain the lower, but, in some cases, still impressive, reactivity of S = 1 Fe^{IV}-oxo systems, a two-state reactivity (TSR) model has been proposed.[7-10] In this model, a quintet-spin excited state provides a lower transition state barrier for the hydrogen-atom transfer than the triplet-spin ground state. Over the last 14 years, advances in understanding the effects of sterics, ligand charge, coordination geometry, and spin state on the reactivity of oxoiron(IV) complexes has translated to the development of highly reactive complexes.[5, 8, 11-12] For example, some of the earliest synthetic oxoiron(IV) intermediates, $[Fe^{IV}(O)(N4py)]^{2+}$ and $[Fe^{IV}(O)(Bn\text{-}TPEN)]^{2+}$, showed HAT rates with cyclohexane of 5.5×10^{-5} M^{-1} s^{-1} and 3.9×10^{-4} M^{-1} s^{-1}, respectively, at room temperature.[13] The more recently reported oxoiron(IV) species, $[Fe^{IV}(O)(TQA)(MeCN)]^{2+}$ and $[Fe^{IV}(O)(Me_3NTB)]^{2+}$, react with cyclohexane 2-3 orders of magnitude faster at *-40 ºC*.[14-15] These rates are comparable to the rate of taurine oxidation by the oxoiron(IV) intermediate of the nonheme Fe enzyme TauD.[14, 16]

In contrast to the broad body of knowledge available for Fe^{IV}-oxo complexes, the reactivity of oxomanganese(IV) complexes towards C-H bonds has been much less

thoroughly investigated. The synthetic oxomanganese(IV) species that have been characterized feature a very wide range of ligand environments, including variations in ligand charge from -3 to neutral, and both trigonal and tetragonal Mn geometries.[17-23] Nonetheless, some general trends in reactivity have been observed. In general, oxomanganese(IV) intermediates supported by anionic ligands perform HAT reactions very slowly, even for substrates with weak C-H bonds, such as 9,10-dihydroanthracene (DHA).[18-19, 23-24] This observation could be explained, in part, by the lower reduction potentials of Mn^{IV}-oxo complexes with anionic ligands.[24-25] However, a complete description of the thermodynamic driving force of C-H bond oxidation by a metal-oxo species depends on both the reduction potential and the basicity of the oxo ligand.[24] Measuring the latter parameter has proved quite challenging. However, measurements of oxo ligand basicity have been obtained for Mn^{IV}-oxo complexes by the Busch and Borovik groups, and these results have clearly demonstrated the importance of oxo basicity on C-H bond oxidation reactions.[24, 26]

In contrast to the generally sluggish reactivity of Mn^{IV}-oxo compounds with anionic supporting ligands, there are examples of oxomanganese(IV) complexes supported by neutral, pentadentate ligands, such as N4py and Bn-TPEN (Figure 3.1), that can cleave a wide range of C-H bonds at rates approaching those of their analogous oxoiron(IV) species.[20, 27-30] These comparisons to oxoiron(IV) systems have bolstered the common conclusion that Fe^{IV}-oxo intermediates perform HAT reactions faster than their Mn^{IV}-oxo counterparts.[31]

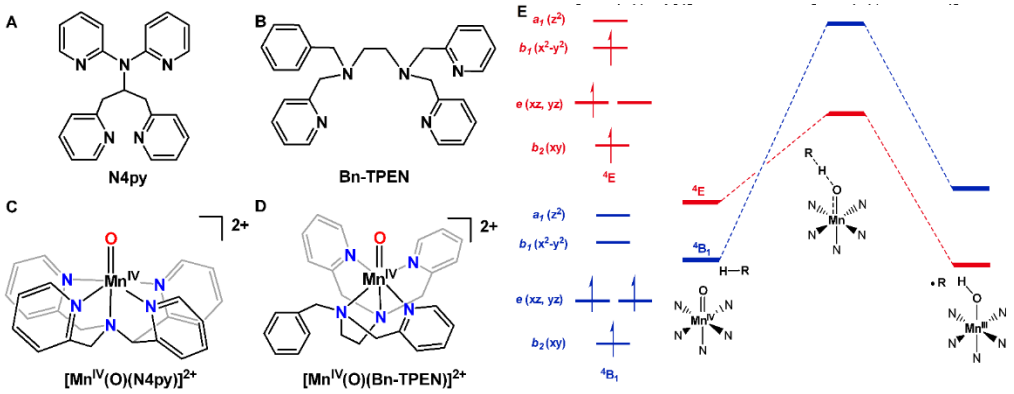

Figure 3.1. Structures of (A) N4py free ligand, (B) Bn-TPEN free ligand, (C) $[Mn^{IV}(O)(N4py)]^{2+}$, and (D) $[Mn^{IV}(O)(Bn\text{-}TPEN)]^{2+}$. (E) Electronic configurations of $^4B_1$ and ^4E states with qualitative reaction coordinates for HAT reaction from reference 10.

At present, the basis for the enhanced reactivity of $[Mn^{IV}(O)(N4py)]^{2+}$ and $[Mn^{IV}(O)(Bn\text{-}TPEN)]^{2+}$ is incompletely understood. Although no information is available on the basicity of oxo ligands in the $[Mn^{IV}(O)(N4py)]^{2+}$ and $[Mn^{IV}(O)(Bn\text{-}TPEN)]^{2+}$ complexes, these oxomanganese(IV) species exhibit $Mn^{III/IV}$ reduction potentials much higher than their less reactive counterparts.[18, 20, 24, 27] This observation suggests that a larger thermodynamic driving force could explain the enhanced C-H activation reactivity of these oxomanganese(IV) adducts.

Alternatively, density functional theory (DFT) studies by Nam and Shaik attributed the enhanced HAT reactivity of $[Mn^{IV}(O)(N4py)]^{2+}$ and $[Mn^{IV}(O)(Bn\text{-}TPEN)]^{2+}$ to a two-state reactivity model.[10] In this model, a ^4E excited state, resulting from an $e(d_{xz}, d_{yz})$ to $b_1(d_{x^2-y^2})$ one-electron excitation from the $b_2(d_{xy})^1e(d_{xz},d_{yz})^2b_1(d_{x^2-y^2})^0a_1(d_{z^2})^0$ ground configuration, provides a lower barrier for HAT than the transition-state derived from the $^4B_1$ ground state (Figure 3.1). The basis for the lower energy of the ^4E transition state derives in part from the hole in the $e(d_{xz}, d_{yz})$ orbitals that are Mn^{IV}=O π* in character. Addition of an electron from substrate to the $e(d_{xz}, d_{yz})$ hole generates a high-spin (S = 2) Mn^{III} product, which is more stable than the intermediate spin (S = 1) Mn^{III} product generated by the corresponding electron transfer on the $^4B_1$ surface. To evaluate this model, we used magnetic circular dichroism (MCD) spectroscopy to assign the near-IR feature in the electronic absorption of $[Mn^{IV}(O)(N4py)]^{2+}$ to the $^4B_1 \rightarrow {}^4E$ transition.[32] This assignment then allowed us to track the energy of the ^4E state for Mn^{IV}-oxo complexes supported by the N4py derivatives ^{DMM}N4py and 2pyN2Q, which are stronger and weaker equatorial donors, respectively.[21] Among this series of Mn^{IV}-oxo adducts, the $[Mn^{IV}(O)(2pyN2Q)]^{2+}$ complex (Figure 3.2) of HAT from hydrocarbon substrates.[21] However, the increased reactivity of $[Mn^{IV}(O)(2pyN2Q)]^{2+}$ was also correlated with a higher $Mn^{III/IV}$ reduction potential, leaving it unresolved whether a lower-energy excited state or a more positive reduction potential is responsible for the trend in HAT rates.[21]

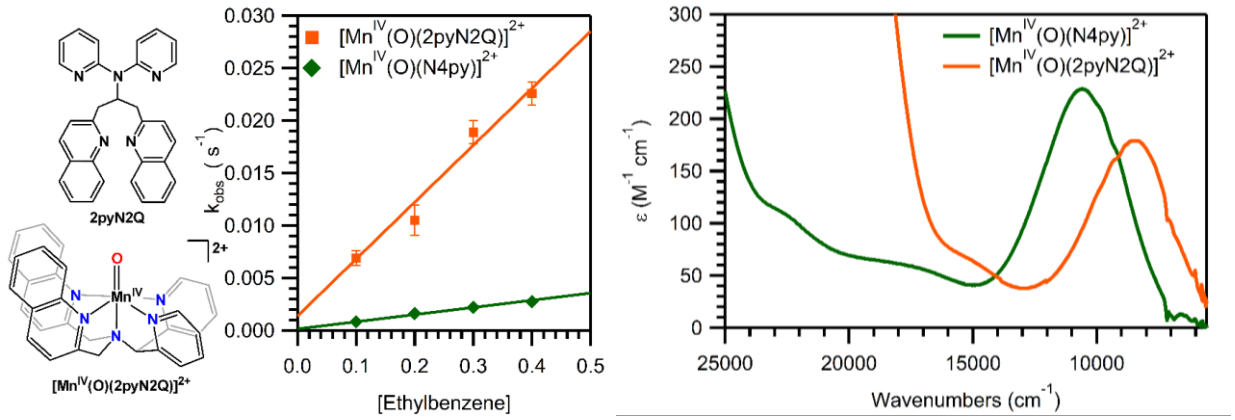

Figure 3.2. Molecular structures (left) of 2pyN2Q free ligand and $[Mn^{IV}(O)(2pyN2Q)]^{2+}$. Rate enhancement of ethylbenzene oxidation by $[Mn^{IV}(O)(2pyN2Q)]^{2+}$ compared to that of $[Mn^{IV}(O)(N4py)]^{2+}$ (center). Shift in near-IR electronic absorption feature of $[Mn^{IV}(O)(2pyN2Q)]^{2+}$ (orange) relative to $[Mn^{IV}(O)(N4py)]^{2+}$ (green) (right).

These rate enhancements observed for $[Mn^{IV}(O)(2pyN2Q)]^{2+}$ make this species the most reactive nonporphyrinic oxomanganese(IV) intermediate observed to date. This complex reacted with ethylbenzene and similar hydrocarbons roughly an order of magnitude faster than $[Mn^{IV}(O)(N4py)]^{2+}$ (Figure 3.2).[20-21] Additionally, the similarities between the rate of reaction of $[Mn^{IV}(O)(2pyN2Q)]^{2+}$ and $[Mn^{IV}(O)(Bn\text{-}TPEN)]^{2+}$ suggested that $[Mn^{IV}(O)(2pyN2Q)]^{2+}$ should be able to oxidize even stronger C-H bonds than previously investigated (in the previous work, substrates with bond dissociation enthalpies up to 88 kcal/mol were examined).[21, 27]

In this present study, we explore the HAT reactivity of $[Mn^{IV}(O)(2pyN2Q)]^{2+}$ with cyclohexane, which has a bond dissociation enthalpy near 99 kcal/mol. Complementary catalytic investigations of cyclohexane oxidation by $[Mn^{II}(2pyN2Q)](OTf)_2$:PhIO systems display modest turnover numbers. The second-order rate constant for cyclohexane oxidation by $[Mn^{IV}(O)(2pyN2Q)]^{2+}$ is much larger than that anticipated from a previous linear free energy correlation for hydrocarbon oxidation by $[Mn^{IV}(O)(2pyN2Q)]^{2+}$.[21] This unexpected result prompted us to explore the reactivity of $[Mn^{IV}(O)(2pyN2Q)]^{2+}$ with a broader range of hydrocarbon substrates and to calculate bond dissociation enthalpies for this large set of hydrocarbons using a recently validated DFT method.[33] This comprehensive set of kinetic and thermodynamic data provide new insights into Mn^{IV}-oxo reactivity, including comparisons to analogous Fe^{IV}-oxo systems.

3.2 Experimental and Computational Methods

3.2.1 Synthesis and Reactivity Studies

Materials and Instrumentation. All chemicals and solvents were ACS reagent grade or higher and purchased from commercial vendors. Iodosobenzene (PhIO) was prepared from iodosobenzene diacetate following published techniques.[34] All substrates were used as received except 9,10-dihydroanthracene, which was recrystallized from hot ethanol.[35]

Electronic absorption data were collected on an Agilent 8453 spectrometer connected to a Unisoku (USP-203-A) cryostat. Gas chromatography-mass spectrometry data were collected on a Quattro Micro GC quadrupole mass analyzer via an Agilent 6890 N gas chromatograph. A 5% phenyl methyl silicone stationary phase (HP-5 MS) 12 meter column was used with a helium carrier gas with a flow rate of 2 ml min^{-1}. The injector port was heated to 240 ºC and 1 µL of sample was injected with a split ratio of 20:1. The GC thermal gradient was an initial 50 ºC which was held for 1 minute before increasing 50 ºC min^{-1} to 300 ºC and held for two minutes.

Generation of $[Mn^{IV}(O)(2pyN2Q)]^{2+}$ and $[Fe^{IV}(O)(N4py)]^{2+}$. The free ligand, 2pyN2Q, metal complex $[Mn^{II}(OTf)(2pyN2Q)](OTf)$, and intermediate $[Mn^{IV}(O)(2pyN2Q)]^{2+}$ were prepared as described previously.[21, 36] The free ligand, N4py, was synthesized as previously published.[37] The metal complex $[Fe^{II}(OTf)(N4py)](OTf)$ was prepared in the same manner as $[Fe^{II}(CH_3CN)(N4py)](ClO_4)_2$, with the only change being the use of $Fe^{II}(OTf)_2$ instead of $Fe(ClO_4)_3$•10 H_2O.[37] The $[Fe^{IV}(O)(N4py)]^{2+}$ complex was prepared by iodosobenzene (PhIO) oxidation of $[Fe^{II}(OTf)(N4py)](OTf)$, similar to the previously published procedure.[13] However, in this study, $[Fe^{IV}(O)(N4py)]^{2+}$ was prepared in 2,2,2-trifluoroethanol (TFE) instead of MeCN. Because of the increased solubility of PhIO in TFE, there was no need to filter the excess PhIO, as all PhIO was dissolved in solution.

Kinetics Experiments. All kinetic experiments were performed at 25 ºC. The intermediate $[Mn^{IV}(O)(2pyN2Q)]^{2+}$ was prepared *in situ* by reacting 3.3 mg (0.004 mmol) $[Mn^{II}(OTf)(2pyN2Q)](OTf)$ with 8.8 mg (0.04 mmol) iodosobenzene (PhIO) in 1.7 to 1.9

mL 2,2,2-trifluoroethanol (TFE). Once the formation of $[Mn^{IV}(O)(2pyN2Q)]^{2+}$ was completed, as determined by following the appearance of the 1080 nm electronic absorption band, substrate was added to the cuvette to give a final solution volume of 2 mL. The decay of the 1080 nm feature of $[Mn^{IV}(O)(2pyN2Q)]^{2+}$ was monitored and the resulting time trace was fit to a pseudo-first order kinetic model. The observed rate constants were plotted against the substrate concentration to obtain a second order rate constant. Because of differing solubilities of the substrates employed, each substrate required slightly different injection conditions. For cyclohexane, a stock solution of cyclohexane was prepared with dichloromethane (CH_2Cl_2) and 0.3 mL of the cyclohexane solution was added to 1.7 mL $[Mn^{IV}(O)(2pyN2Q)]^{2+}$ in TFE for a final reaction volume of 2 mL. Cyclohexane concentration ranged from 50 to 200 equivalents relative to the metal, which was 2 mM. Cyclooctane reaction conditions were the same, but the concentration range of cyclooctane was only 10 to 40 equivalents relative to the metal due to the low solubility of this substrate. For reactions with tetrahydrofuran (THF), stock solutions of 0.2 mL THF diluted in TFE were added to 1.8 mL $[Mn^{IV}(O)(2pyN2Q)]^{2+}$. The THF concentration of the final reaction mixture ranged from 100 to 400 equivalents. *para*-xylene solutions were prepared in CH_2Cl_2 and 0.2 mL substrate solution was added to 1.8 mL $[Mn^{IV}(O)(2pyN2Q)]^{2+}$. Concentrations of *para*-xylene ranged from 10 to 40 equivalents relative to the metal. The same reaction conditions were used for both cumene and triphenylmethane, with concentrations ranging from 10 to 40 equivalents.

In order to evaluate if excess PhIO, or the presence of O_2, were influencing the observed reaction rate for cyclohexane oxidation by $[Mn^{IV}(O)(2pyN2Q)]^{2+}$, we performed additional experiments using a small excess of PhIO or in the absence of O_2. Reactions with only 2 equivalents of PhIO used to prepare $[Mn^{IV}(O)(2pyN2Q)]^{2+}$ resulted in the formation of the Mn^{IV}-oxo adduct in 70 – 80% yield, relative to that observed using 10 equivalents PhIO. The pseudo-first-order rate constant (k_{obs}) determined for the reaction of 100 equivalents C_6H_{12} with $[Mn^{IV}(O)(2pyN2Q)]^{2+}$ formed using 2 equivalents PhIO is essentially identical to that observed when 10 equivalents PhIO are used (k_{obs} = 3.67 × 10^{-3} s^{-1} versus 3.62 × 10^{-3} s^{-1}; see Figure A3.1). To test that the presence of O_2 was not influencing reaction rates, reactions of $[Mn^{IV}(O)(2pyN2Q)]^{2+}$, formed using 10 equivalent of PhIO, with 100 equivalents C_6H_{12} were performed under an Ar atmosphere. Under

these conditions, $[Mn^{IV}(O)(2pyN2Q)]^{2+}$ is formed in 80-85% yield, even with the 10 equivalents of PhIO. Nonetheless, the pseudo-first-order rate constant (k_{obs}) for C_6H_{12} oxidation by $[Mn^{IV}(O)(2pyN2Q)]^{2+}$ in the absence of O_2 is nearly identical to the that observed under aerobic conditions (k_{obs} = 3.63 × 10^{-3} s^{-1} versus 3.62 × 10^{-3} s^{-1}; Figure A3.1). These results provide strong support that neither the excess of PhIO used to generate $[Mn^{IV}(O)(2pyN2Q)]^{2+}$ nor the presence of O_2 influences the rate of cyclohexane oxidation by this Mn^{IV}-oxo adduct.

GC-MS Experiments. A reaction between 3.3 mg (0.004 mmol) $[Mn^{II}(OTf)(2pyN2Q)](OTf)$ and 8.8 mg (0.04 mmol) PhIO in 1.7 mL TFE led to formation of $[Mn^{IV}(O)(2pyN2Q)]^{2+}$ in 1.7 mL TFE. Following the addition of either 25 or 250 equivalents of cyclohexane in 0.3 mL CH_2Cl_2 to $[Mn^{IV}(O)(2pyN2Q)]^{2+}$, the electronic absorption bands of the Mn^{IV}-oxo complex showed pseudo-first order decay. After the reaction was complete, the solution was passed through a silica plug and eluted with ethyl acetate. The eluent was further diluted and the appropriate amount of an internal standard, naphthalene, was added. A calibration curve with known concentrations of cyclohexanol and cyclohexanone was generated using the same internal standard. The samples were analyzed by GC-MS and the amount of products produced was determined using the calibration curve.

Catalytic Reactions with Cyclohexane. For the catalytic reactions investigated, 0.328 mg (0.0004 mmol) $[Mn^{II}(OTf)(2pyN2Q)](OTf)$ were combined with 17.6 mg (0.08 mmol) PhIO in 2.0 mL TFE. To this mixture, 0.10 mL (0.925 mmol) cyclohexane was added and stirred for 5 hours. The products were eluted through a silica column with ethyl acetate and analyzed using GC-MS as previously described.

3.2.2 Electronic Structure Calculations

All density functional theory (DFT) calculations were performed using the *ORCA* 3.0.3 software package.[38] Geometry optimizations and frequency calculations of organic substrates were performed with a large integration grid (grid6 in *ORCA*). The M06-2X functional was employed along with the def2-TZVPP basis set for all atoms.[39-40] Single point energies were computed using the same functional and basis set and an even finer

integration grid (grid7 in *ORCA*). Solvent effects of 2,2,2-trifluoroethanol or acetonitrile were included in all calculations using the conductor-like screening model (COSMO). Calculation of the bond dissociation enthalpies was performed using zero-point corrected electronic energies. This approach follows that of Cramer and Que,[33] who validated this method relative to the *jun-jun* method of Truhlar *et al.*[41-42]

3.3 Results and Analysis

3.3.1 Reactivity of $[Mn^{IV}(O)(2pyN2Q)]^{2+}$ with Cyclohexane

We had previously demonstrated that the $[Mn^{IV}(O)(2pyN2Q)]^{2+}$ complex shows C-H bond oxidation rates exceeding those of all known Mn^{IV}-oxo complexes.[21] However, our exploration of the reactivity of $[Mn^{IV}(O)(2pyN2Q)]^{2+}$ was limited to substrates with C-H bond strengths below 88 kcal mol^{-1}.[43] To determine if $[Mn^{IV}(O)(2pyN2Q)]^{2+}$ is capable of attacking substrates with stronger C-H bonds, we explored the reactivity of this complex with cyclohexane, which has a bond dissociation energy near 99 kcal/mol. When a TFE solution of $[Mn^{IV}(O)(2pyN2Q)]^{2+}$ was treated with an excess of cyclohexane at 25 °C, the near-infrared (near-IR) absorption band at 1080 nm, which is characteristic of this Mn^{IV}-oxo complex, decayed over time (Figure 3.3, left and Figure A3.1). The decay of the near-IR signal showed pseudo-first order behavior to 4 half-lives. Pseudo-first order rate constants were determined for a range of cyclohexane concentrations (50 – 200 equivalents relative to the $[Mn^{IV}(O)(2pyNQ)]^{2+}$ complex). A plot of observed rate constants versus cyclohexane concentration gave a second order rate constant (k_2(cyclohexane)) of 8.2×10^{-3} M^{-1} s^{-1} (Figure 3.3, right). To the best of our knowledge, the only other Mn^{IV}-oxo adduct reported to oxidize cyclohexane is the $[Mn^{IV}(O)(Bn\text{-}TPEN)]^{2+}$ complex of Nam and co-workers.[8] The k_2(cyclohexane) value for $[Mn^{IV}(O)(Bn\text{-}TPEN)]^{2+}$ is roughly two-fold lower than that of $[Mn^{IV}(O)(2pyNQ)]^{2+}$ where k_2(cyclohexane) = 3.3×10^{-3} and 8.2×10^{-3} $M^{-1}s^{-1}$, respectively.

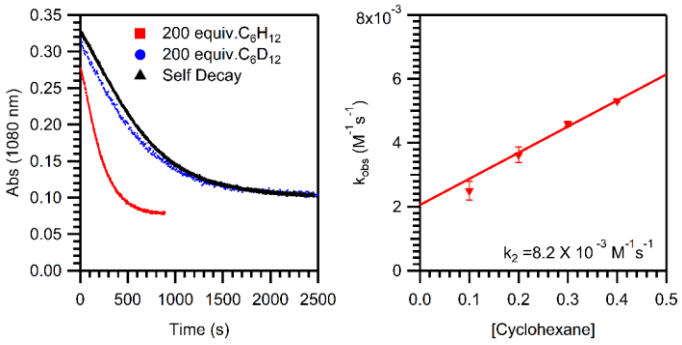

Figure 3.3. Left: Time trace of the decay of the 1080 nm feature of $[Mn^{IV}(O)(2pyN2Q)]^{2+}$ upon the addition of 200 equivalents of C_6H_{12} (red) and C_6D_{12} (blue). The time trace for the decay of $[Mn^{IV}(O)(2pyN2Q)]^{2+}$ in the absence of substrate is included for comparison (black). Right: Plot of the observed rate of the reaction of $[Mn^{IV}(O)(2pyN2Q)]^{2+}$ with cyclohexane as a function of cyclohexane concentration. The kinetic analysis assumes that k_{obs} has contributions from the self-decay rate as follows: $k_{obs} = k_{self\text{-}decay} + k_2[cyclohexane]_0$. The $k_{self\text{-}decay}$ value for $[Mn^{IV}(O)(2pyN2Q)]^{2+}$ from the y-intercept at zero substrate concentration (2×10^{-3} s^{-1}) is similar to that determined from the previously reported half-life ($t_{1/2}$ = 12 minutes; $k_{self\text{-}decay} = 1 \times 10^{-3}$ s^{-1}).

To probe the mechanism of cyclohexane oxidation by $[Mn^{IV}(O)(2pyN2Q)]^{2+}$, we performed kinetic experiments using d_{12}-cyclohexane (C_6D_{12}). While the rate of decay of the near-IR feature of $[Mn^{IV}(O)(2pyN2Q)]^{2+}$ in the presence of C_6D_{12} was significantly slower than that observed for C_6H_{12}, the observed decay rate for the reaction with C_6D_{12} is barely distinguishable from the self-decay rate of $[Mn^{IV}(O)(2pyN2Q)]^{2+}$ (Figure 3.3, left). Consequently, we cannot determine an H/D kinetic isotope effect for this reaction. However, under the reasonable assumption that the rate of reaction of $[Mn^{IV}(O)(2pyN2Q)]^{2+}$ with C_6D_{12} must be no greater than the self-decy rate, we can infer that the H/D KIE must be greater than 3.5. The inference of a KIE greater than 1 indicates that the reaction of $[Mn^{IV}(O)(2pyN2Q)]^{2+}$ with cyclohexane proceeds via a rate-limiting HAT step.

Further insight into the reaction of $[Mn^{IV}(O)(2pyN2Q)]^{2+}$ and cyclohexane was obtained through analysis of the organic products. GC-MS experiments for solutions after reaction of $[Mn^{IV}(O)(2pyN2Q)]^{2+}$ with 25 or 250 equivalents of cyclohexane showed stoichiometric, or slightly greater than stoichiometric, conversion of cyclohexane to cyclohexanol and cyclohexanone relative to the Mn^{IV}-oxo concentration (Table 3.1, entries 1 and 2). A control reaction without $[Mn^{IV}(O)(2pyN2Q)]^{2+}$ showed no evidence of

cyclohexanone or cyclohexanol production, suggesting that direct oxidation of cyclohexane by PhIO cannot account for the super-stoichiometric conversion of cyclohexane in entry 2 (Table 3.1). Instead we propose that the excess PhIO (10 equivalents relative to Mn^{II}) allows for the reformation of $[Mn^{IV}(O)(2pyN2Q)]^{2+}$, which continues to react with cyclohexane. Evidence in support of this proposal came from the analysis of a catalytic system consisting of 0.2 mM $[Mn^{II}(2pyN2Q)(OTf)](OTf)$, 40 mM PhIO, and 400 mM cyclohexane in 2 mL TFE, which was allowed to react at room temperature for 5 hours (Table 3.1, entry 3). Under these conditions, 11 equivalents of cyclohexanol and 2.7 equivalents of cyclohexanone were produced (relative to the starting $[Mn^{II}(2pyN2Q)(OTf)](OTf)$ concentration), giving a turnover number (TON) near 14. Importantly, the product yield and distribution is quite sensitive to the presence of O_2. When the catalytic reaction was performed under an atmosphere of argon rather than air, the production of cyclohexanol dropped to 4 equivalents per Mn, and only trace amounts of cyclohexanone were observed (Table 3.1, entry 4). Although the oxidant usage in these catalytic experiments is poor (see PhIO Use in Table 3.1), these results demonstrate the potential of $[Mn^{IV}(O)(2pyN2Q)]^{2+}$ to perform catalytic oxygenation of strong C-H bonds.

Table 3.1. GC-MS product analysis of reaction between $[Mn^{IV}(O)(2pyN2Q)]^{2+}$ and cyclohexane.

	Mn:PhIO:Cyclohexane[a]	Cyclohexanol/Mn	Cyclohexanone/Mn	A/K Ratio[b]	TON[c]	PhIO Use[d]
1	1:10:25	0.78(8)	0.22(2)	3.5	1.0(1)	12(1) %
2	1:10:250	0.92(7)	0.31(3)	2.9	1.2(1)	15(1) %
3	1:200:2300	11(3)	2.7(2)	4.0	14(3)	8(2) %
4	(Ar) 1:200:2300[e]	3.5(5)	Trace	-	3.5(5)	<2.5%

[a] For entries 1 and 2, [Mn] = 2×10^{-3} mol L^{-1} and [PhIO] = 2×10^{-2} mol L^{-1}. For entry 3, [Mn] = 2×10^{-4} mol L^{-1} and [PhIO] = 8×10^{-2} mol L^{-1}. [Cyclohexane] = 5×10^{-2}, 5×10^{-1}, and 4.6×10^{-1} mol L^{-1} for entries 1, 2, and 3. [b] Alcohol/Ketone Ratio [c] The turnover number is the total moles of products per mole of catalyst. [d] PhIO use is determined using the sum of the 2-electron oxidation to cyclohexanol and the 4-electron oxidation to cyclohexanone. All reactions were performed at ambient temperature and pressure. [e] Reactions performed under an argon atmosphere.

3.3.2 Linear Free Energy Relationship in C-H Bond Activation by $[Mn^{IV}(O)(2pyN2Q)]^{2+}$.

Previous studies of C-H activation by $[Mn^{IV}(O)(2pyN2Q)]^{2+}$ showed a linear correlation between the logarithm of the corrected second order rate constant (k_2', which

is k_2 divided by the number of equivalent C-H bonds) versus the bond dissociation enthalpy (BDE) of the substrate, implying a rate determining hydrogen atom transfer step following a Bell-Evans-Polanyi correlation.[21, 44-45] (We note here that this previous analysis used the base-ten log, as is common. However, as the logarithm of k_2' term represents the activation energy, or free energy of activation, an analysis using ln(k_2') is more appropriate. In practice, the plots change only slightly from log(k_2') to ln(k_2'), although the slopes are of slightly larger magnitude for the former. In this work, the listed slopes are given for the ln(k_2') relationships shown in the relevant plots, while the slope for a log(k_2') analysis is given in parentheses.) When this analysis is extended to include k_2'(cyclohexane) for $[Mn^{IV}(O)(2pyN2Q)]^{2+}$, the observed rate is over 1000-fold faster than that predicted by the trend line (Figure 3.4). There are several potential explanations for this deviation. First, there could be a change in mechanism for Mn^{IV}-oxo oxidation of substrates with strong C-H bonds. Second, the slope could be in error, due to the modest range of substrate BDEs (10 kcal mol^{-1}) used in the original analysis and/ or due to errors in the values of BDEs used in this plot (*e.g.*, because the reported values were not determined in TFE). The first potential explanation, that of a change in mechanism, can be ruled out by the observed H/D KIE for the reaction of $[Mn^{IV}(O)(2pyN2Q)]^{2+}$ with cyclohexane, which supports the conclusion that HAT is still the rate-limiting step. Thus, our efforts to explain the seemingly unexpected reactivity of $[Mn^{IV}(O)(2pyN2Q)]^{2+}$ with cyclohexane focused on extending the range of substrates used for this plot and on using DFT calculations to reinvestigate the values used for hydrocarbon BDEs.

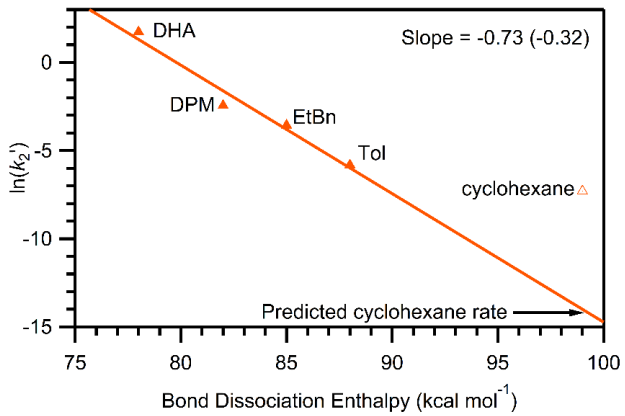

Figure 3.4. Natural log of corrected second order rate constant versus bond dissociation enthalpies of organic substrates. Trend line is the previously reported correlation from reference 20. DHA = 9,10-dihydroanthracene; DPM = diphenylmethane; EtBn = ethylbenzene; and Tol = toluene.

To extend the range of substrate BDEs under investigation, we determined second-order rate constants for the reactions of $[Mn^{IV}(O)(2pyN2Q)]^{2+}$ with triphenylmethane, cumene, *para*-xylene, tetrahydrofuran, and cyclooctane (BDEs of ca. 81 – 96 kcal/mol). When combined with our previous data, and the rate observed for cyclohexane oxidation, the range of BDEs increases to 78 – 99 kcal mol^{-1}. The results are collected in Table 3.2, which shows both the k_2 and k_2' values (Figure A3.2 in the Supporting Information shows plots of k_{obs} values versus substrate concentration, which were used to determine the second-order rate constants). When combined with our previous data, and the rate observed for cyclohexane oxidation, the range of BDEs increases to 78 – 99 kcal mol^{-1}.

Table 3.2. Second order rate constant, corrected second order rate constant, along with tabulated and calculated BDE values for each substrate investigated.

Substrate	k_2	k_2'	Mayer[25]	Luo[46]	Calculated
Dihydroanthracene	22(2)	5.6(7)	80.6[b]	76.3	78
Triphenylmethane	0.79(1)	0.79(1)	83.4[b]	81±2	78.9
Diphenylmethane	0.17(1)	0.087(5)	84.3[b]	84.5±0.5	84.1
Cumene	0.037(1)	0.037(1)	[c]	[c]	85.5
para-Xylene	0.045(2)	0.0075(4)	87.0[d]	87.7, 89.0	90.2
Ethylbenzene	0.057(4)	0.028(2)	[c]	85.4±1.5	86.4
Toluene	0.0089(7)	0.0030(3)	92[b]	89.7 ± 1.2[a]	90.5
THF	0.014(1)	0.0034(1)	[c]	92.1±1.6	93.6
Cyclooctane	0.055(4)	0.0034(3)	[c]	95.7	94
Cyclohexane	0.0082(6)	0.00068(5)	[c]	99.5	99

[a]gas phase. [b]DMSO solution. [c]not listed. [d]acetonitrile solution.

Having expanded our range of substrate BDEs from those values used for the initial Bell-Evans-Polanyi correlation, we next evaluated the BDE values available for each substrate. For the 10 organic substrates we investigated, there is no single source that includes BDEs for each substrate, let alone a single source where all BDE values have been determined using the same methods or under the same conditions. Mayer and coworkers and Luo have provided the most extensive sets of BDE values, which includes the majority of substrates under consideration here (Table 3.2).[25, 46] For some substrates, such as *p*-xylene and diphenylmethane, the sources provide similar values. However, for substrates such as DHA and toluene, the values between the two sources differ by over 2 kcal mol^{-1}. In addition, neither source contains the BDE of cumene and neither has values for substrates in TFE.

A recent study by Klein *et al.* provided a roadmap for resolving these issues.[33] In that work, the authors showed that calculated BDE values for cyclohexadiene and DHA using the M06-2X functional with the large def2-TZVPP basis set were nearly identical to those obtained using the more elaborate *jun-jun* method, which approximates the CCSD(T) method extrapolated to the complete basis set limit.[33] Thus, we applied this approach to determine the BDEs for the hydrocarbons examined in this study. The results are shown in Table 3.2. The calculated BDE values are all within ca. 2 kcal/mol of the tabulated values, which seems reasonable considering both the uncertainty in the experimental values and the influence of solvent on BDE.

Using the calculated BDE values and the k_2' values for the broader set of substrates, we re-examined the ln(k_2') versus BDE relationship (Figure 3.5). With these new data, the rate for cyclohexane oxidation by $[Mn^{IV}(O)(2pyN2Q)]^{2+}$ is no longer an outlier, and the new plot shows a much shallower slope of -0.38 (-0.17). Although ln(k_2') values for DHA and toluene now show modest deviations from the linear trend, these substrates also show the largest uncertainties in their k_2 values (Table 3.2). The change in the ln(k_2') versus BDE slope when including more substrates underscores the inherent uncertainty in the slopes of such plots when using a small set of substrates with a limited range of BDE values.

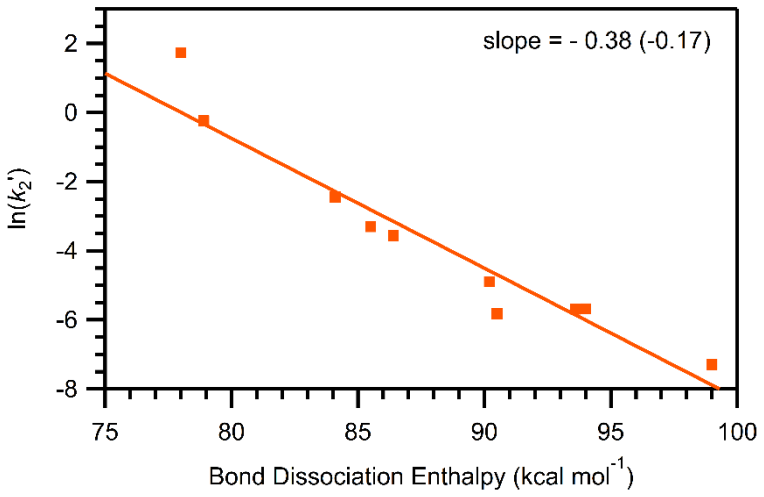

Figure 3.5. Natural log of corrected second order rate constant versus calculated bond dissociation enthalpies of organic substrates.

3.4 Discussion

Because the oxidation of cyclohexane requires the cleavage of a strong C–H bond, it is an important showcase for the reactivity of a metal-oxo complex. In addition, cyclohexane oxidation to cyclohexanol and cyclohexanone is performed on a large-scale in industry for the production of nylon-6 and nylon-6,6.[47] The industrial process is quite inefficient, occurring by a multi-step, free-radical chain reaction.[48] There is therefore substantial interest in the development of earth-abundant metal complexes for catalytic cyclohexane oxidation[47, 49] and several manganese complexes have been shown to effect such catalysis.[50-51] However, the mechanism by which these complexes operate is often not well understood. There is only one example of a Mn^{IV}-oxo complex capable of cleaving the strong C-H bonds of cyclohexane, $[Mn^{IV}(O)(Bn\text{-}TPEN)]^{2+}$.[27] Although this reaction operates stoichiometrically, a Mn^{IV}-oxo complex is clearly the active species, whereas the identity of the active oxidant in catalytic systems is often unclear. In this present work, we have shown that $[Mn^{IV}(O)(2pyN2Q)]^{2+}$ is also capable of reacting with cyclohexane at a rate slightly larger than that of $[Mn^{IV}(O)(Bn\text{-}TPEN)]^{2+}$. On the basis of a previous linear-free energy relationship for HAT reactions by $[Mn^{IV}(O)(2pyN2Q)]^{2+}$, the rate of cyclohexane oxidation by this Mn^{IV}-oxo adduct was significantly faster than anticipated. This led us to consider the rate-BDE relationship in more detail using a broader set of hydrocarbon substrates and DFT-computed BDE values. In this section, we describe the implications of the catalytic cyclohexane oxidation and compare and contrast $[Mn^{IV}(O)(2pyN2Q)]^{2+}$ with other Mn^{IV}-oxo and Fe^{IV}-oxo oxidants.

3.4.1 Catalytic Oxidation of Cyclohexane by $[Mn^{IV}(O)(2pyN2Q)]^{2+}$ - Rebound versus Substrate Dissociation.

Previous experimental and computational studies of C-H bond oxidation by Mn^{IV}-oxo complexes provided strong evidence that these reactions predominantly produce Mn^{III} products. For example, in our investigations of DHA oxidation by $[Mn^{IV}(O)(N4py)]^{2+}$, we observed ca. 0.5 equivalents anthracene product per equivalent of $[Mn^{IV}(O)(N4py)]^{2+}$.[20] Both spectroscopic data and an iodometric titration were consistent with the formation of a Mn^{III} complex as the predominant Mn-containing product. Similar

observations have been reported by Nam and Costas.[10, 19, 27, 30] In each of these cases, C-H bond oxidation is initiated by a HAT step, forming a carbon-centered substrate radical and a Mn^{III}-hydroxo adduct (Scheme 3.1). Instead of the Mn^{III}-hydroxo and carbon radical participating in a rebound step, which would give a Mn^{II} center and hydroxylated product, it has been proposed that the Mn^{III}-hydroxo and organic radical separate by a radical dissociation pathway. The organic radical could be trapped by oxygen, or oxidized further by an additional equivalent of the Mn^{IV}-oxo complex. Alternatively, the observation of Mn^{III} products could still occur by a rebound-type mechanism, if the oxidation of the final Mn^{II} product by the Mn^{IV}-oxo were sufficiently rapid compared to HAT from the C-H bond. Shaik, Nam, and co-workers have used DFT computations to discuss the relative energetics of rebound and radical dissociation process.[8, 10]

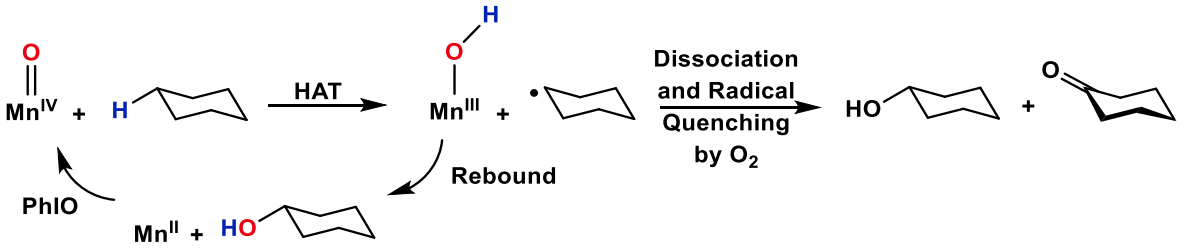

Scheme 3.1. Formation of cyclohexanol and cyclohexanone from the reaction of $[Mn^{IV}(O)(2pyN2Q)]^{2+}$ and cyclohexane. After the initial HAT step between cyclohexane and the Mn^{IV}-oxo center, the radical and Mn^{III}-hydroxo adduct can undergo a rebound process to form a Mn^{II} species and cyclohexanol (bottom path). Alternatively, radical dissociation of the Mn^{III}-hydroxo and cyclohexyl radical can lead to cyclohexanol and cyclohexanone production through O_2 quenching of the C-based radical.

Our present studies of $[Mn^{IV}(O)(2pyN2Q)]^{2+}$ provide evidence of catalytic oxidation of cyclohexane to cyclohexanol and cyclohexanone by solutions of $[Mn^{II}(2pyN2Q)(OTf)](OTf)$:PhIO, albeit with quite modest turnover numbers (Table 3.1). These results suggest that at least a portion of the Mn^{III} product, formed by the initial HAT between cyclohexane and $[Mn^{IV}(O)(2pyN2Q)]^{2+}$, is further reduced to Mn^{II}, which is then re-oxidized to Mn^{IV}-oxo by the excess PhIO in solution (Scheme 3.1). Catalytic experiments carried out under an air atmosphere show a mixture of cyclohexanol and cyclohexanone products, which is indicative of some trapping of the cyclohexyl radical by O_2. Similar experiments performed under an Ar atmosphere are suggestive of a rebound

mechanism, as cyclohexanol is the dominant product of catalysis (TON of 3). These results appear consistent with a mechanism where radical rebound and radical dissociation are of similar energy**.**

Table 3. Comparison of k_2(cyclohexane) values for Mn^{IV}-oxo and Fe^{IV}-oxo complexes supported by neutral, N5 ligands.

Complex	k_2 ($M^{-1}s^{-1}$)	solvent	ref.
$[Mn^{IV}(O)(2pyN2Q)]^{2+}$	0.0082	TFE	[a]
$[Mn^{IV}(O)(Bn\text{-}TPEN)]^{2+}$	0.0033	TFE	[27]
$[Fe^{IV}(O)(Bn\text{-}TPEN)]^{2+}$	0.00039	MeCN	[13]
$[Fe^{IV}(O)(N4py)]^{2+}$	0.000055	MeCN	[13]

[a] This work.

The lower TON observed for cyclohexane oxidation by $[Mn^{II}(2pyN2Q)(OTf)](OTf)$ under an Ar atmosphere is attributed to an increased stability of the Mn^{IV}-oxo in the presence of O_2. In support, the half-life of $[Mn^{IV}(O)(N4py)]^{2+}$ is 120 and 30 minutes under air and Ar, respectively.[20, 30, 52] Presumably, the self-decay of these Mn^{IV}-oxo adducts generates reactive radicals that can be quenched by O_2. In the absence of O_2, these radicals hasten the decay of the Mn^{IV}-oxo complex, reducing the lifetime of the catalyst.

Although the catalytic performance of $[Mn^{IV}(O)(2pyN2Q)]^{2+}$ in cyclohexane oxidation is modest, it is comparable to that porphyrinatomanganese(III) ($[Mn^{III}$(T4(-OMe)PP)(Cl)]) and chloro-5,10,15,20-tetrakis(3-bromo-4-methoxyphenyl)-2,3,7,8,12,13,17,18-octabromoporphyrinatomanganese(III) ($[Mn^{III}(Br_{12}$T4(-OMe)PP)(Cl)]) catalysts.[47, 53] With a Mn:PhIO:cyclohexane ratio of 1:10:4650 and a reaction time of 90 minutes, TONs between 2.3 and 6.6 were observed. A 5-fold increase in PhIO concentration for the $[Mn^{III}(Br_{12}$T4(-OMe)PP)(Cl)] catalyst gives a higher TON of 12.7, but this increased TON was accompanied by complete catalyst degradation by the end of the reaction.[47]

3.4.2. Comparison of Mn^{IV}-oxo and Fe^{IV}-oxo Complexes in Cyclohexane Oxidation.

In Table 3.3, we compare the reactivity of $[Mn^{IV}(O)(2pyN2Q)]^{2+}$ toward cyclohexane with similar Mn^{IV}-oxo and Fe^{IV}-oxo complexes.[13, 27] At first glance, the rate data collected in Table 3 demonstrate that the Mn^{IV}-oxo complexes perform cyclohexane

oxidation more rapidly than their most closely related Fe^{IV}-oxo analogues. While this result stands in contrast to recent reports that suggest that Fe^{IV}-oxo species are more reactive than their Mn^{IV}-oxo analogues,[31] potential complicating factors must be addressed to make a balanced comparison.[54] It may be noted tht $[Mn^{IV}(O)(Bn\text{-}TPEN)]^{2+}$ shows a 10-fold increase in k_2(cyclohexane) compared to $[Fe^{IV}(O)(Bn\text{-}TPEN)]^{2+}$ (Table 3.3),[13, 27] indicating that, at least for the Bn-TPEN ligand system, the Mn^{IV}-oxo adduct is a more rapid oxidant toward cyclohexane.

Second, the reactivity studies of the Mn^{IV}-oxo complexes were performed in TFE,[27] while the reactions for the Fe^{IV}-oxo complexes with cyclohexane were performed in MeCN.[13] Thus, solvent effects might be responsible, at least in part, for the rate enhancement observed for the Mn^{IV}-oxo complexes. In order to understand the influence of solvent on these reactions, we first assembled previously published rate data for C-H bond oxidation reactions by $[Fe^{IV}(O)(N4py)]^{2+}$ in TFE[31] and MeCN[13] (Figures 3.6 and A3.3). These data reveal that $[Fe^{IV}(O)(N4py)]^{2+}$ reacts with common substrates faster in TFE than in MeCN. For example, second-order rate constants of 0.055(3) and 0.0040 $M^{-1}s^{-1}$ were reported for the oxidation of ethylbenzene by $[Fe^{IV}(O)(N4py)]^{2+}$ in TFE[31] and MeCN,[13] respectively.

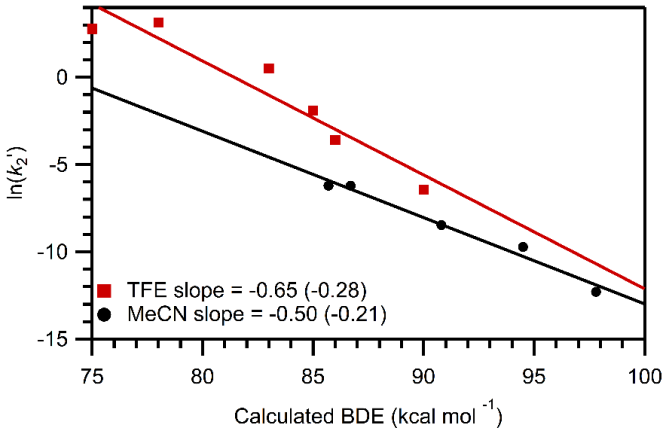

Figure 3.6. Comparison of the rate of reaction of $[Fe^{IV}(O)(N4py)]^{2+}$ and various substrates in MeCN and TFE. Data taken from references 12 (MeCN) and 30 (TFE).

Extrapolation of the ln(k_2´) versus BDE relationship for hydrocarbon oxidation in TFE suggests that the enhanced reactivity of the Fe^{IV}-oxo unit in TFE might be muted for stronger C-H bonds, such as those of cyclohexane (Figure 3.6). However, as we have

shown in this study, extrapolation of ln(k_2´) versus BDE relationships based on a limited range of BDEs is unwise. Because of this, we prepared $[Fe^{IV}(O)(N4py)]^{2+}$ in TFE and explored its reactivity with cyclohexane. These experiments were limited by both the poor solubility of cyclohexane in TFE and the slow rate of reaction. Nonetheless, we were able to determine a pseudo-first order rate constant for the reaction of 2 mM $[Fe^{IV}(O)(N4py)]^{2+}$ with 200 equivalents cyclohexane in TFE ($k_1 = 8 \times 10^{-5}$ s^{-1}). This rate constant is very similar to that reported for the reaction of 2 mM $[Fe^{IV}(O)(N4py)]^{2+}$ with 400 equivalents cyclohexane in MeCN ($k_1 = 5.5 \times 10^{-5}$ s^{-1}),[13] suggesting only a modest rate enhancement for cyclohexane oxidation by $[Fe^{IV}(O)(N4py)]^{2+}$ in TFE. (Due to the limited solubility of cyclohexane in TFE, we were unable to determine a rate for reaction with 400 equivalents of cyclohexane.) Taken together, these observations suggest that solvent effects alone cannot account for the rate enhancements of the Mn^{IV}-oxo complexes in cyclohexane oxidation relative to their Fe^{IV}-oxo analogues.

The third complicating factor in the comparison of Fe^{IV}-oxo and Mn^{IV}-oxo oxidants is that one must consider the substrate used for the comparison. For example, Table 3 shows that $[Mn^{IV}(O)(Bn\text{-}TPEN)]^{2+}$ is a more rapid agent for cyclohexane oxidation when compared to $[Fe^{IV}(O)(Bn\text{-}TPEN)]^{2+}$.[13, 27] However, this ordering of reactivity only holds true for substrates with strong C-H bonds. This conclusion is supported by the collection of previously published data shown in Figure 7.[13, 27] For substrates with weaker C-H bonds (such as cumene and ethylbenzene), $[Fe^{IV}(O)(Bn\text{-}TPEN)]^{2+}$ is the more rapid oxidant. A similar rate ordering was determined for $[Fe^{IV}(O)(N4py)]^{2+}$ and $[Mn^{IV}(O)(N4py)]^{2+}$, where the Fe^{IV}-oxo species is a more rapid oxidant towards C-H bonds of moderate strength (BDEs of 76-86 kcal/mol).[31] For $[Fe^{IV}(O)(Bn\text{-}TPEN)]^{2+}$ and $[Mn^{IV}(O)(Bn\text{-}TPEN)]^{2+}$, however, rate data collected for substrates with C-H BDEs greater than ~95 kcal/mol show a clear reversal of the reactivity trend,[13, 27] with the Mn^{IV}-oxo adduct becoming the faster oxidant. This change in ordering at higher substrate BDEs is reflected in the different slopes in the ln(k_2´) versus BDE plots (Figure 3.7). The $[Fe^{IV}(O)(Bn\text{-}TPEN)]^{2+}$ complex shows a slope near -0.6 (-0.27), while the $[Mn^{IV}(O)(Bn\text{-}TPEN)]^{2+}$ shows a notably shallower slope closer to -0.3 (-0.15). For comparison, we note that our extensive kinetic studies of $[Mn^{IV}(O)(2pyN2Q)]^{2+}$ reported here show a similarly shallow slope near -0.4 (-0.17) (Figure 3.5).

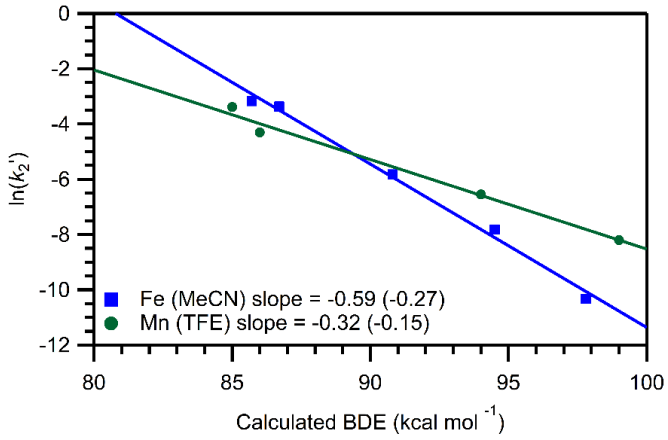

Figure 3.7. Comparison of rates of C-H bond oxidation reactions (as ln(k_2')) for $[Mn^{IV}(O)(Bn\text{-}TPEN)]^{2+}$ and $[Fe^{IV}(O)(Bn\text{-}TPEN)]^{2+}$ as a function of substrate C-H bond strength. Data from references 13 (Fe) and 27 (Mn).

In our discussion of Mn^{IV}-oxo and Fe^{IV}-oxo species in this study, we note a range of slopes from -0.3 to -0.7 (-0.15 to -0.32) (Figures 3.4-3.7). In each of these reactions, there is strong evidence for a hydrogen-atom transfer mechanism. Therefore, it appears safe to assume that there is no single slope in a ln(k_2´) versus BDE plot that is diagnostic of a hydrogen-atom transfer reaction. For the extreme example of $[Mn^{IV}(O)(2pyN2Q)]^{2+}$ (Figure 3.5), the slope of -0.38 (-0.17) marks a lower sensitivity of reaction rates to the substrate BDE than is typical for metal-oxo species. However, the basis for this low sensitivity is unclear at present. An even smaller slope of approximately -0.12 (-0.05) was noted by Goldsmith and Stack in their studies of C-H bond oxidation by a mononuclear Mn^{III}-hydroxo complex (Figure A3.5).[57] In that case, the unusually shallow slope was tentatively attributed to "imperfect synchronicity" between the hydrogen atom transfer and the reorganization of the manganese complex.[57] Reorganization energies, and their influence on hydrogen-atom transfer reactions, are a subject of significant current interest. However, other, more mundane, factors can also influence the measured slope in a ln(k_2´) versus BDE plot. These factors include the BDE values used for the plots and the influence of entropic effects. The importance of these factors in influencing the observed slope need to be understood in order to use this parameter to gain insight into hydrogen-atom transfer processes.

A comprehensive understanding of these trends in HAT reactivity should also include knowledge of the strength of the O-H bond that is formed in the metal(III)-hydroxo product.[55] The metal(III)-hydroxo O-H bond strength can be deconstructed into the one-electron reduction potential of the metal(IV)-oxo and the pK_a of the metal(III)-hydroxo.[25, 55, 58] The one-electron reduction potentials of the metal(IV)-oxo complexes in Table 3.3 have been reported. The faster rates for cyclohexane oxidation by the Mn^{IV}-oxo complexes are consistent with their higher reduction potentials (0.78 - 1.01 V versus 0.49 - 0.51 V for the Fe^{IV}-oxo complexes; all values versus SCE).[13, 20-21, 27-28, 52, 59] However, without knowledge of the basicity of the oxo ligand, this comparison is incomplete. It is also important to note that the observation that these metal(IV)-oxo complexes are capable of attacking the strong C-H bond of cyclohexane (BDE = 99 kcal/mol) does not necessarily require that the BDE of the O-H bond in the metal(III)-hydroxo product is greater than 99 kcal/mol. As discussed by Busch and co-workers,[18, 60] it is rare for metal(IV)-oxo complexes to only oxidize substrates where the cleaved C-H bond is weaker than the O-H bond formed in the metal-hydroxo product. It is commonly assumed that thermodynamically favorable follow-up reactions can pull an initially unfavorable HAT step. Whether or not this is the case for cyclohexane oxidation by $[Mn^{IV}(O)(2pyN2Q)]^{2+}$ is an unanswered question.

Finally, it is important to note that the rates of cyclohexane oxidation listed in Table 3.3 are substantially lower than those reported for the Fe^{IV}-oxo complexes $[Fe^{IV}(O)(Me_3NTB)]^{2+}$ (Me_3NTB = tris(1-methylbenzimidazol-2-ylmethyl)amine)[15] and $[Fe^{IV}(O)(TQA)(MeCN)]^{2+}$ (TQA = tris(2-quinolylmethyl)amine).[5, 14] The $[Fe^{IV}(O)(Me_3NTB)]^{2+}$ and $[Fe^{IV}(O)(TQA)(MeCN)]^{2+}$ complexes, which each contain three bulky equatorial ligands, have k_2(cyclohexane) = 0.23 and 0.37 $M^{-1}s^{-1}$ *at -40 °C.* Although these rates are the highest reported for Fe-oxo species, the basis for the high reactivity of these complexes is under debate. For these Fe^{IV}-oxo complexes, the high reactivity was postulated to arise from the high intrinsic reactivity of an S = 2 ground state (for $[Fe^{IV}(O)(TQA)(MeCN)]^{2+}$),[5, 14] or a low-lying S = 2 excited state (for $[Fe^{IV}(O)(Me_3NTB)]^{2+}$).[15] However, a recent study by Meyer, Neese, Costas, and co-workers has demonstrated that an S = 1 Fe^{IV}-oxo complex with a thermally inaccessible

S = 2 excited state is more reactive in HAT reactions than an analogous *S* = 1 complex, for which an *S* = 2 excited state has been proposed to be involved in HAT reactions.[61]

3.5 Conclusions

An oxomanganese(IV) complex was prepared that can perform HAT reactions with hydrocarbons spanning a very wide range of C-H bond strengths. Using this set of C-H containing substrates, we showed that the previously derived correlation between ln(k_2') and the bond dissociation enthalpy was not accurately describing the relationship between the barrier energy and the reaction driving force. This should serve as a reminder not to over-interpret the slopes between ln(k_2') and the BDE when a small range of BDE values is under investigation. It is also important to consider which values of BDEs are being used for such comparisons, as a range of values appear in the literature. In this study, we have used a recently validated computational approach to determine hydrocarbon BDEs.

Additionally, the $[Mn^{IV}(O)(2pyN2Q)]^{2+}$ complex can react with the strong C-H bonds of cyclohexane at a rate higher than oxoiron(IV) complexes with analogous ligands. The products of this reaction are cyclohexanol and cyclohexanone and the determined yields demonstrate the ability of $[Mn^{IV}(O)(2pyN2Q)]^{2+}$ to perform catalytic substrate oxidation. Additional work will be necessary to further evaluate the catalytic mechanism and better understand the basis for the enhanced reactivity of the $[Mn^{IV}(O)(2pyN2Q)]^{2+}$ compared to other Mn^{IV}-oxo species.

3.6 Notes and References

1. Rittle, J.; Green, M. T., Cytochrome P450 Compound I: Capture, Characterization, and C-H Bond Activation Kinetics. *Science* **2010,** *330* (6006), 933-937.

2. Huang, X.; Groves, J. T., Oxygen Activation and Radical Transformations in Heme Proteins and Metalloporphyrins. *Chem. Rev.* **2017**.

3. Wong, S. D.; Srnec, M.; Matthews, M. L.; Liu, L. V.; Kwak, Y.; Park, K.; Bell Iii, C. B.; Alp, E. E.; Zhao, J.; Yoda, Y.; Kitao, S.; Seto, M.; Krebs, C.; Bollinger, J. M.; Solomon, E. I., Elucidation of the Fe(iv)=O intermediate in the catalytic cycle of the halogenase SyrB2. *Nature* **2013,** *499*, 320.

4. Srnec, M.; Wong, S. D.; Matthews, M. L.; Krebs, C.; Bollinger, J. M.; Solomon, E. I., Electronic Structure of the Ferryl Intermediate in the α-Ketoglutarate Dependent Non-Heme Iron Halogenase SyrB2: Contributions to H Atom Abstraction Reactivity. *J. Am. Chem. Soc* **2016,** *138* (15), 5110-5122.

5. Puri, M.; Que, L., Jr., Toward the Synthesis of More Reactive S = 2 Non-Heme Oxoiron(IV) Complexes. *Acc. Chem. Res.* **2015,** *48* (Copyright (C) 2016 American Chemical Society (ACS). All Rights Reserved.), 2443-2452.

6. Rice, D. B.; Massie, A. A.; Jackson, T. A., Manganese–Oxygen Intermediates in O–O Bond Activation and Hydrogen-Atom Transfer Reactions. *Acc. Chem. Res.* **2017,** *50* (11), 2706-2717.

7. Shaik, S.; Hirao, H.; Kumar, D., Reactivity of High-Valent Iron–Oxo Species in Enzymes and Synthetic Reagents: A Tale of Many States. *Acc. Chem. Res.* **2007,** *40* (7), 532-542.

8. Cho, K.-B.; Hirao, H.; Shaik, S.; Nam, W., To rebound or dissociate? This is the mechanistic question in C-H hydroxylation by heme and nonheme metal-oxo complexes. *Chem. Soc. Rev.* **2016,** *45* (5), 1197-1210.

9. Mandal, D.; Shaik, S., Interplay of Tunneling, Two-State Reactivity, and Bell–Evans–Polanyi Effects in C–H Activation by Nonheme Fe(IV)O Oxidants. *J. Am. Chem. Soc* **2016,** *138* (7), 2094-2097.

10. Cho, K.-B.; Shaik, S.; Nam, W., Theoretical Investigations into C–H Bond Activation Reaction by Nonheme MnIVO Complexes: Multistate Reactivity with No Oxygen Rebound. *J. Phys. Chem. Lett.* **2012,** *3* (19), 2851-2856.

11. Ray, K.; Pfaff, F. F.; Wang, B.; Nam, W., Status of Reactive Non-Heme Metal–Oxygen Intermediates in Chemical and Enzymatic Reactions. *Journal of the American Chemical Society* **2014,** *136* (40), 13942-13958.

12. Nam, W., Synthetic Mononuclear Nonheme Iron–Oxygen Intermediates. *Acc. Chem. Res.* **2015,** *48* (8), 2415-2423.

13. Kaizer, J.; Klinker, E. J.; Oh, N. Y.; Rohde, J.-U.; Song, W. J.; Stubna, A.; Kim, J.; Münck, E.; Nam, W.; Que Jr., L., Nonheme FeIVO Complexes That Can Oxidize the C−H Bonds of Cyclohexane at Room Temperature. *J. Am. Chem. Soc* **2004,** *126* (2), 472-473.

14. Biswas, A. N.; Puri, M.; Meier, K. K.; Oloo, W. N.; Rohde, G. T.; Bominaar, E. L.; Münck, E.; Que Jr., L., Modeling TauD-J: A High-Spin Nonheme Oxoiron(IV) Complex with High Reactivity toward C–H Bonds. *J. Am. Chem. Soc* **2015,** *137* (7), 2428-2431.

15. Seo, M. S.; Kim, N. H.; Cho, K.-B.; So, J. E.; Park, S. K.; Clemancey, M.; Garcia-Serres, R.; Latour, J.-M.; Shaik, S.; Nam, W., A mononuclear nonheme iron(iv)-oxo complex which is

more reactive than cytochrome P450 model compound I. *Chemical Science* **2011,** *2* (6), 1039-1045.

16. Price, J. C.; Barr, E. W.; Glass, T. E.; Krebs, C.; Bollinger, J. M., Evidence for Hydrogen Abstraction from C1 of Taurine by the High-Spin Fe(IV) Intermediate Detected during Oxygen Activation by Taurine:α-Ketoglutarate Dioxygenase (TauD). *J. Am. Chem. Soc* **2003,** *125* (43), 13008-13009.

17. Bortolini, O.; Ricci, M.; Meunier, B.; Friant, P.; Ascone, I.; Goulon, J., Isolation, characterization and structural investigation by EXAFS/XANES of high valent manganese porphyrin complexes as active species in the NaOCl/Mn(porphyrin)X oxygenation system. *Nouv. J. Chim.* **1986,** *10* (1), 39 - 49.

18. Yin, G.; Danby, A. M.; Kitko, D.; Carter, J. D.; Scheper, W. M.; Busch, D. H., Understanding the Selectivity of a Moderate Oxidation Catalyst: Hydrogen Abstraction by a Fully Characterized, Activated Catalyst, the Robust Dihydroxo Manganese(IV) Complex of a Bridged Cyclam. *J. Am. Chem. Soc* **2007,** *129* (6), 1512-1513.

19. Garcia-Bosch, I.; Company, A.; Cady, C. W.; Styring, S.; Browne, W. R.; Ribas, X.; Costas, M., Evidence for a Precursor Complex in C□H Hydrogen Atom Transfer Reactions Mediated by a Manganese(IV) Oxo Complex. *Angew. Chem., Int. Ed. Engl.* **2011,** *123* (25), 5766-5771.

20. Leto, D. F.; Ingram, R.; Day, V. W.; Jackson, T. A., Spectroscopic properties and reactivity of a mononuclear oxomanganese(iv) complex. *Chem. Commun.* **2013,** *49* (47), 5378-5380.

21. Massie, A. A.; Denler, M. C.; Cardoso, L. T.; Walker, A. N.; Hossain, M. K.; Day, V. W.; Nordlander, E.; Jackson, T. A., Equatorial Ligand Perturbations Influence the Reactivity of Manganese(IV)-Oxo Complexes. *Angew. Chem., Int. Ed. Engl.* **2017,** *56* (15), 4178-4182.

22. Parsell, T. H.; Behan, R. K.; Green, M. T.; Hendrich, M. P.; Borovik, A. S., Preparation and Properties of a Monomeric MnIV-Oxo Complex. *J. Am. Chem. Soc* **2006,** *128* (27), 8728-8729.

23. Sawant, S. C.; Wu, X.; Cho, J.; Cho, K.-B.; Kim, S. H.; Seo, M. S.; Lee, Y.-M.; Kubo, M.; Ogura, T.; Shaik, S.; Nam, W., Water as an Oxygen Source: Synthesis, Characterization, and Reactivity Studies of a Mononuclear Nonheme Manganese(IV) Oxo Complex. *Angew. Chem., Int. Ed. Engl.* **2010,** *49* (44), 8190-8194.

24. Parsell, T. H.; Yang, M.-Y.; Borovik, A. S., C−H Bond Cleavage with Reductants: Re-Investigating the Reactivity of Monomeric MnIII/IV−Oxo Complexes and the Role of Oxo Ligand Basicity. *J. Am. Chem. Soc* **2009,** *131* (8), 2762-2763.

25. Warren, J. J.; Tronic, T. A.; Mayer, J. M., Thermochemistry of Proton-Coupled Electron Transfer Reagents and its Implications. *Chem. Rev.* **2010,** *110* (12), 6961-7001.

26. Yin, G.; Danby, A. M.; Kitko, D.; Carter, J. D.; Scheper, W. M.; Busch, D. H., Oxidative Reactivity Difference among the Metal Oxo and Metal Hydroxo Moieties: pH Dependent Hydrogen

Abstraction by a Manganese(IV) Complex Having Two Hydroxide Ligands. *J. Am. Chem. Soc* **2008,** *130* (48), 16245-16253.

27. Wu, X.; Seo, M. S.; Davis, K. M.; Lee, Y.-M.; Chen, J.; Cho, K.-B.; Pushkar, Y. N.; Nam, W., A Highly Reactive Mononuclear Non-Heme Manganese(IV)–Oxo Complex That Can Activate the Strong C–H Bonds of Alkanes. *J. Am. Chem. Soc* **2011,** *133* (50), 20088-20091.

28. Yoon, H.; Morimoto, Y.; Lee, Y.-M.; Nam, W.; Fukuzumi, S., Electron-transfer properties of a nonheme manganese(iv)-oxo complex acting as a stronger one-electron oxidant than the iron(iv)-oxo analogue. *Chem. Commun.* **2012,** *48* (91), 11187-11189.

29. Yoon, H.; Lee, Y.-M.; Wu, X.; Cho, K.-B.; Sarangi, R.; Nam, W.; Fukuzumi, S., Enhanced Electron-Transfer Reactivity of Nonheme Manganese(IV)–Oxo Complexes by Binding Scandium Ions. *J. Am. Chem. Soc* **2013,** *135* (24), 9186-9194.

30. Chen, J.; Lee, Y.-M.; Davis, K. M.; Wu, X.; Seo, M. S.; Cho, K.-B.; Yoon, H.; Park, Y. J.; Fukuzumi, S.; Pushkar, Y. N.; Nam, W., A Mononuclear Non-Heme Manganese(IV)–Oxo Complex Binding Redox-Inactive Metal Ions. *J. Am. Chem. Soc* **2013,** *135* (17), 6388-6391.

31. Chen, J.; Cho, K.-B.; Lee, Y.-M.; Kwon, Y. H.; Nam, W., Mononuclear nonheme iron(iv)-oxo and manganese(iv)-oxo complexes in oxidation reactions: experimental results prove theoretical prediction. *Chem. Commun.* **2015,** *51* (66), 13094-7.

32. Leto, D. F.; Massie, A. A.; Rice, D. B.; Jackson, T. A., Spectroscopic and Computational Investigations of a Mononuclear Manganese(IV)-Oxo Complex Reveal Electronic Structure Contributions to Reactivity. *J. Am. Chem. Soc* **2016,** *138* (47), 15413-15424.

33. Klein, J. E. M. N.; Dereli, B.; Que Jr., L.; Cramer, C. J., Why metal-oxos react with dihydroanthracene and cyclohexadiene at comparable rates, despite having different C-H bond strengths. A computational study. *Chem. Commun.* **2016,** *52* (69), 10509-10512.

34. Saltzman, H.; Sharefkin, J. G., Iodosobenzene. *Organic Syntheses* **1963,** *43*, 60.

35. Armarego, W. L. F.; Perrin, D. D., *Purification of Laboratory Chemicals*. Butterworth-Heinemann: Oxford, U.K., 1997.

36. Lo, W. K. C.; McAdam, C. J.; Blackman, A. G.; Crowley, J. D.; McMorran, D. A., The pentadentate ligands 2PyN2Q and N4Py, and their Cu(II) and Zn(II) complexes: A synthetic, spectroscopic and crystallographic structural study. *Inorganica Chimica Acta* **2015,** *426*, 183-194.

37. Lubben, M.; Meetsma, A.; Wilkinson, E. C.; Feringa, B.; Que Jr., L., Nonheme Iron Centers in Oxygen Activation: Characterization of an Iron(III) Hydroperoxide Intermediate. *Angew. Chem., Int. Ed. Engl.* **1995,** *34* (13-14), 1512-1514.

38. Neese, F., The ORCA program system. *Wiley Interdisciplinary Reviews: Computational Molecular Science* **2012,** *2* (1), 73-78.

39. Zhao, Y.; Truhlar, D. G., The M06 suite of density functionals for main group thermochemistry, thermochemical kinetics, noncovalent interactions, excited states, and transition elements: two new functionals and systematic testing of four M06-class functionals and 12 other functionals. *Theor. Chem. Acc.* **2008,** *120* (1), 215-241.

40. Weigend, F.; Ahlrichs, R., Balanced basis sets of split valence, triple zeta valence and quadruple zeta valence quality for H to Rn: Design and assessment of accuracy. *Phys. Chem. Chem. Phys.* **2005,** *7* (18), 3297-3305.

41. Papajak, E.; Truhlar, D. G., What are the most efficient basis set strategies for correlated wave function calculations of reaction energies and barrier heights? *J. Chem. Phys.* **2012,** *137* (6), 064110.

42. Zheng, J.; Seal, P.; Truhlar, D. G., Role of conformational structures and torsional anharmonicity in controlling chemical reaction rates and relative yields: butanal + HO2 reactions. *Chem. Sci.* **2013,** *4* (1), 200-212.

43. Goldsmith, C. R.; Jonas, R. T.; Stack, T. D. P., C−H Bond Activation by a Ferric Methoxide Complex: Modeling the Rate-Determining Step in the Mechanism of Lipoxygenase. *J. Am. Chem. Soc* **2002,** *124* (1), 83-96.

44. Evans, M. G.; Polanyi, M., Inertia and driving force of chemical reactions. *Trans. Faraday Soc.* **1938,** *34* (1), 0011-0023.

45. Bell, R. P., The Theory of Reactions Involving Proton Transfers. *Proc. R. Soc. A* **1936,** *154* (882), 414-429.

46. Luo, Y.-R., BDEs of C-H bonds. In *Comprehensive Handbook of Chemical Bond Energies*, CRC Press: 2007; pp 19-145.

47. da Silva, V. S.; dos Santos Vieira, W. C.; Meireles, A. M.; Ucoski, G. M.; Nakagaki, S.; Idemori, Y. M.; DeFreitas-Silva, G., Biomimetic oxidation of cyclic and linear alkanes: high alcohol selectivity promoted by a novel manganese porphyrin catalyst. *New J. Chem.* **2017,** *41* (3), 997-1006.

48. Jevtic, R.; Ramachandran, P. A.; Dudukovic, M. P., Effect of Oxygen on Cyclohexane Oxidation: A Stirred Tank Study. *Industrial & Engineering Chemistry Research* **2009,** *48* (17), 7986-7993.

49. Pinto, V. H. A.; Rebouças, J. S.; Ucoski, G. M.; de Faria, E. H.; Ferreira, B. F.; Silva San Gil, R. A.; Nakagaki, S., Mn porphyrins immobilized on non-modified and chloropropyl-functionalized mesoporous silica SBA-15 as catalysts for cyclohexane oxidation. *Applied Catalysis A: General* **2016,** *526* (Supplement C), 9-20.

50. Shul'pin, G. B.; Süss-Fink, G.; Shul'pina, L. S., Oxidations by the system "hydrogen peroxide–manganese(IV) complex–carboxylic acid": Part 3. Oxygenation of ethane, higher alkanes, alcohols, olefins and sulfides. *J. Mol. Catal. A: Chem.* **2001,** *170* (1), 17-34.

51. Romakh, V. B.; Therrien, B.; Süss-Fink, G.; Shul'pin, G. B., Dinuclear Manganese Complexes Containing Chiral 1,4,7-Triazacyclononane-Derived Ligands and Their Catalytic Potential for the Oxidation of Olefins, Alkanes, and Alcohols. *Inorg. Chem.* **2007,** *46* (4), 1315-1331.

52. Brink, C. P.; Crumbliss, A. L., Kinetics, Mechanism, and Thermodynamics of Aqueous Iron(III) Chelation and Dissociation: Influence of Carbon and Nitrogen Substituents in Hydroxamic Acid Ligands. *Inorg. Chem.* **1984,** *23* (26), 4708-4718.

53. da Silva, V. S.; Meireles, A. M.; da Silva Martins, D. C.; Rebouças, J. S.; DeFreitas-Silva, G.; Idemori, Y. M., Effect of imidazole on biomimetic cyclohexane oxidation by first-, second-, and third-generation manganese porphyrins using PhIO and PhI(OAc)2 as oxidants. *Applied Catalysis A: General* **2015,** *491*, 17-27.

54. A. Sinha, R. Singh, E. Nordlander, T.K. Paine, unpublished results. The FeIV-oxo complex of the 2pyN2Q ligand is currently under investigation, and [FeIV(O)(2pyN2Q)]2+ exhibits enhanced reactivity in both HAT and oxygen atom transfer reactions relative to the parent [FeIV(O)(N4pyN2Q)]2+. However, reactivity studies of [FeIV(O)(2pyN2Q)]2+ that are directly comparable to those described here remain to be undertaken

55. Mayer, J. M., Thermodynamic Influences on C-H Bond Oxidation. In *Biomimetic Oxidations Catalyzed by Transition Metal Complexes*, Meunier, B., Ed. Imperial College Press: London, 2000.

56. Morris, W. D.; Mayer, J. M., Separating Proton and Electron Transfer Effects in Three-Component Concerted Proton-Coupled Electron Transfer Reactions. *J. Am. Chem. Soc* **2017,** *139* (30), 10312-10319.

57. Goldsmith, C. R.; Cole, A. P.; Stack, T. D. P., C−H Activation by a Mononuclear Manganese(III) Hydroxide Complex: Synthesis and Characterization of a Manganese-Lipoxygenase Mimic? *J. Am. Chem. Soc.* **2005,** *127* (27), 9904-9912.

58. Mayer, J. M., Hydrogen Atom Abstraction by Metal−Oxo Complexes: Understanding the Analogy with Organic Radical Reactions. *Acc. Chem. Rev.* **1998,** *31* (8), 441-450.

59. Lee, Y.-M.; Kotani, H.; Suenobu, T.; Nam, W.; Fukuzumi, S., Fundamental Electron-Transfer Properties of Non-heme Oxoiron(IV) Complexes. *Journal of the American Chemical Society* **2008,** *130* (2), 434-435.

60. Yin, G., Understanding the Oxidative Relationships of the Metal Oxo, Hydroxo, and Hydroperoxide Intermediates with Manganese(IV) Complexes Having Bridged Cyclams:

Correlation of the Physicochemical Properties with Reactivity. *Acc. Chem. Rev.* **2013,** *46* (2), 483-492.

61. Kupper, C.; Mondal, B.; Serrano-Plana, J.; Klawitter, I.; Neese, F.; Costas, M.; Ye, S.; Meyer, F., Nonclassical Single-State Reactivity of an Oxo-Iron(IV) Complex Confined to Triplet Pathways. *Journal of the American Chemical Society* **2017,** *139* (26), 8939-8949.

Chapter 4. Structural Characterization of a Series of N5-Ligated Oxomanganese(IV) Species

4.1 Introduction

In nature, both heme and non-heme oxoiron(IV) adducts are responsible for many hydrogen-atom transfer (HAT) reactions to produce halogenation, hydroxylation, or desaturation products.[1-5] The use of well characterized, mononuclear oxoiron(IV) model complexes has provide reference data for understanding the reactivity of enzyme intermediates, that can be difficult to characterize.[6-7] Following the first reported crystal structure of an oxoiron(IV) species in 2003, it has become quite commonplace to obtain X-ray diffraction (XRD) information on these complexes.[6, 8] This structural information, as well as information from a wide variety of other spectroscopic techniques, has allowed for extensive characterization of oxoiron(IV) complexes. Collectively, these studies have helped to identify the influences of electronic structure on reactivity for oxoiron(IV) species. Analogously, non-heme, mononuclear oxomanganese(IV) species have been implicated as reactive intermediates in many hydrogen-atom transfer (HAT) and other oxidation reactions catalyzed by synthetic manganese complexes.[9-20] However, unlike their oxoiron(IV) counterparts no oxomanganese(IV) species have been characterized by XRD. Because of this, Mn K-edge X-ray absorption spectroscopy (XAS) has been an invaluable technique for the characterization of oxomanganese(IV) species.[17-21]

XAS allows for the determination of metal-ligand bond distances without the need for crystalline material through the use of high-intensity, tunable X-rays from synchrotron radiation. The use of XAS, alongside density functional theory (DFT) and a wide range of other spectroscopic techniques, has bolstered the formulation of many oxomanganese(IV) species.[13, 18-23] In addition to aiding in the characterization of these synthetic complexes, benchmarking of XAS data on small, well-defined model systems can be used to understand the features and trends expected for various structural motifs in large, poorly-defined systems, such as those in enzymes or materials chemistry. One particularly important example where XAS has been necessary to elucidate structural information is the oxygen-evolving complex in photosystem II, which consists of a Mn_4O_5Ca cluster that is responsible for the oxidation of H_2O to O_2 and protons.[24-27]

Metal K-edge XAS spectra are characterized by two regions, which provide different but complementary information about the sample. The first region is the X-ray absorption near edge structure (XANES), which is within 10 eV of the K-edge. The second region, beyond the K-edge, is the extended X-ray absorption fine structure (EXAFS) region. The XANES region is very sensitive to the oxidation state and coordination environment of the metal center.[28-29] Using an empirical comparison with similar, well characterized model complexes, the relative position of the K-edge gives information on the oxidation state of the metal. In most cases, a higher K-edge energy corresponds to a higher oxidation state due to the higher effective nuclear charge of the metal center. The pre-edge region, which occurs just before the K-edge, arises from excitations from the metal 1s-to-3d orbitals. The 1s-to-3d excitation is formally parity forbidden and thus is of low intrinsic intensity. However, the 1s-to-3d pre-edge features can gain intensity through mixing of metal 3d and 4p orbitals caused by low symmetry distortions and/or highly covalent ligand interactions.[30-32] The pre-edge region has been the focus of many combined experimental and theoretical studies, as an analysis of the pre-edge energies and intensities can provide unique insight into the electronic structure of the metal.[21, 33-38] Typically in these studies, time-dependent density-functional theory (TD-DFT) is performed alongside experimental fitting of the pre-edge region to further understand the basis for differences in pre-edge properties. Quantitative descriptions of the pre-edge region can come from careful benchmarking of well-defined model complexes.[31-32, 38]

Beyond the metal K-edge comes the EXAFS region, which provides structural information about the metal center. This region, characterized by its oscillatory nature, arises from the physical interaction of the photodissociated 1s electron with the electron density surrounding the metal atom. Fitting of this region can provide the number and identity of scattering atoms within a certain radial distance of the metal center. However, this technique has limitations: (1) small atoms close in atomic number, such as oxygen and nitrogen, cannot be distinguished from one another; and (2) atoms of the same (or indistinguishable) element at similar distances from the metal center are represented as an average distance of the scattering pathways. In spite of these limitations, analysis of EXAFS data provides metal-scatterer distances with an accuracy of ~ 0.02 Å, allowing for

the refinement of crystallographically characterized structures, and the ability to obtain accurate structural information for the first coordination sphere. [39]

Our group has previously reported a series of oxomanganese(IV) species supported by modified ligands based on the N4py ligand framework (Scheme 4.1).[13] This includes the ^{DMM}N4py and 2pyN2Q ligands, which respectively feature more electron-rich di-methyl-methoxy-pyridine groups and quinoline groups. These ligand perturbations serve to increase (for ^{DMM}N4py) and decrease (for 2pyN2Q) the equatorial ligand field of the Mn center relative to the parent N4py ligand, resulting in variations in properties of the manganese(II) and oxomanganese(IV) complexes supported by these ligands. The effects of this systematic ligand perturbation were most apparent by the (1) modulation of the Mn-N_{eq} bond distances of the manganese(II) complexes, (2) the shift in the near-IR feature of the electronic absorption spectrum of the oxomanganese(IV) species, and (3) the dramatic differences in HAT and oxygen atom transfer (OAT) reaction rates for the oxomanganese(IV) species (Figure 4.1).[13] Although the chemical reactivity of these complexes has been well characterized, structural parameters for the recently reported $[Mn^{IV}(O)(^{DMM}N4py)]^{2+}$ and $[Mn^{IV}(O)(2pyN2Q)]^{2+}$ complexes were lacking. In this study, we report metric information from analyses of Mn K-edge EXAFS data for the previously reported $[Mn^{IV}(O)(^{DMM}N4py)]^{2+}$ and $[Mn^{IV}(O)(2pyN2Q)]^{2+}$ complexes, as well as a new oxomanganese(IV) species, $[Mn^{IV}(O)(2pyN2B)]^{2+}$. This latter complex features mixed pyridine and *N*-methylbenzimidazole (BzIm) ligands in the equatorial plane. This ligand and has been previously shown to support the oxoirion(IV) complex $[Fe^{IV}(O)(2pyN2B)]^{2+}$, which is more reactive than its $[Fe^{IV}(O)(N4py)]^{2+}$ analogue at hydrogen-atom transfer reactions.[40] The Mn=O bond lengths obtained from our analysis of EXAFS data for the $[Mn^{IV}(O)(^{DMM}N4py)]^{2+}$, $[Mn^{IV}(O)(2pyN2Q)]^{2+}$, and $[Mn^{IV}(O)(2pyN2B)]^{2+}$ complexes are slightly longer than those predicted by DFT computations. Better agreement between experimental and DFT-computed Mn=O bond lengths are obtained by including explicit $HOCH_2CF_3$ solvent molecules hydrogen-bonded to the oxo ligands in the computational model. For each complex, these strong Mn=O···$HOCH_3CF_3$ hydrogen-bonding interactions lead to elongation of Mn=O bond lengths by 0.02 Å.

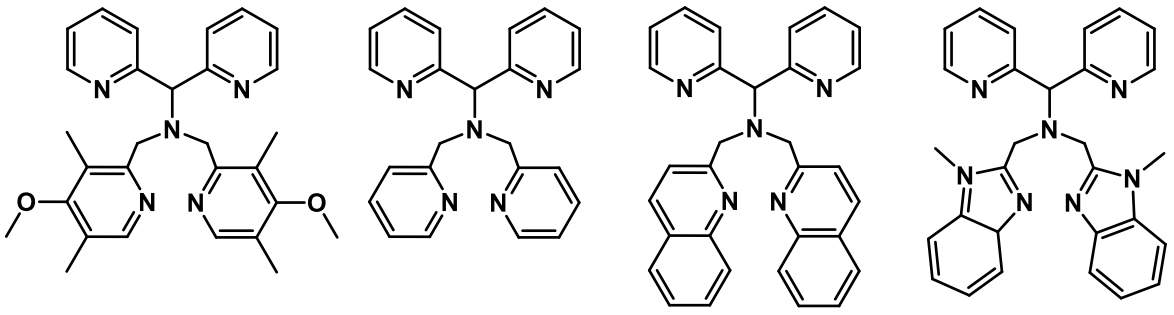

Scheme 4.1. Ligands based on the N4py framework where ^{DMM}N4py is *N*,*N*-bis(4-methoxy-3,5-dimethyl-2-pyridylmethyl)-*N*-bis(2-pyridyl)methylamine, N4py is *N*,*N*-bis(2-pyridylmethyl)-*N*-bis(2-pyridyl)methylamine, 2pyN2Q is bis(2-pyridyl)-*N*,*N*-bis(2 quinolylmethyl)methanamine, and 2pyN2B is N-bis(1-methyl-2-benzimidazolyl)methyl-N-(bis-2-pyridylmethyl)-amine.

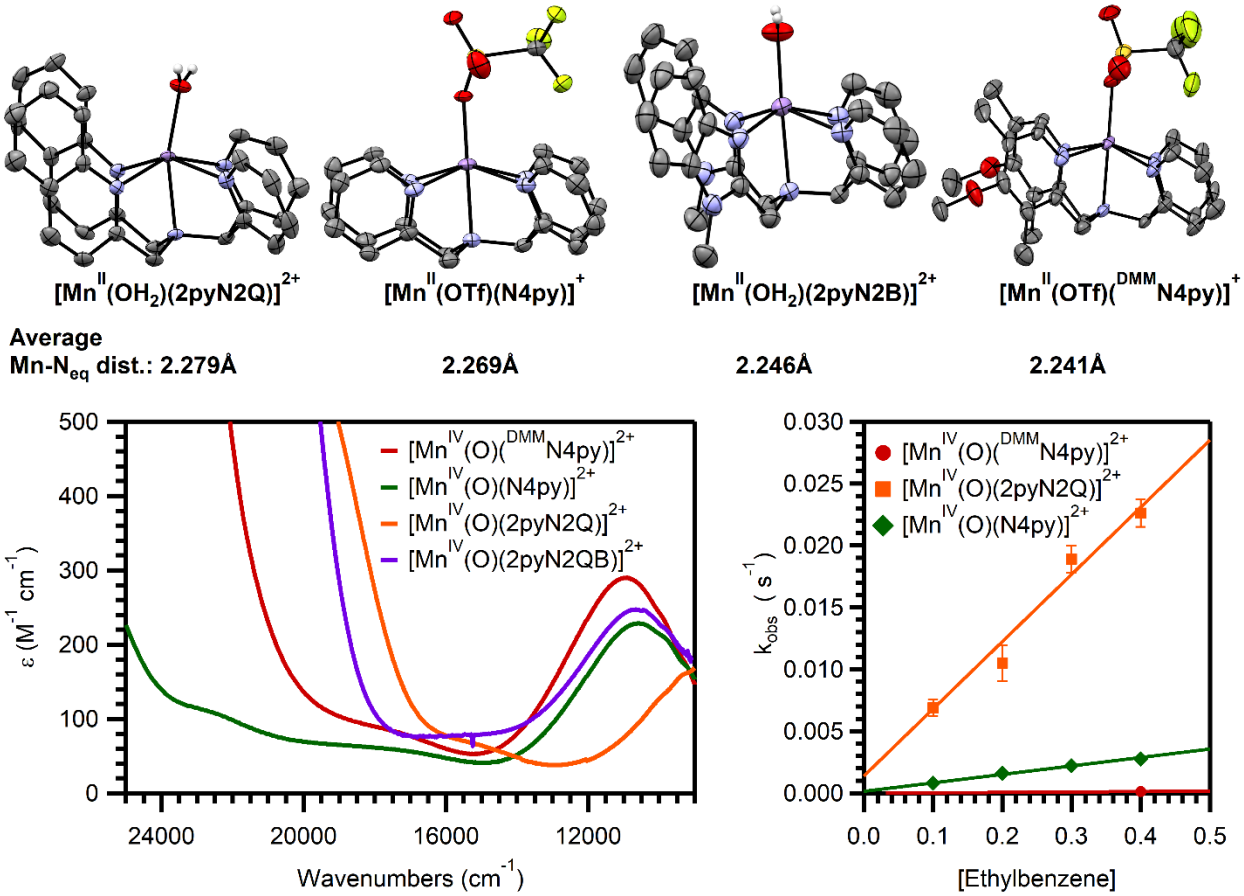

Figure 4.1. (Top) XRD structures for $[Mn^{II}(OTf)(^{DMM}N4py)](OTf)$, $[Mn^{II}(OH_2)(2pyN2B)](OTf)_2$, $[Mn^{II}(OTf)(2pyN2B)](OTf)$, and $[Mn^{II}(OH_2)(2pyN2Q)](OTf)_2$ with average Mn-N_{eq} bond distances. (Bottom Left) Shift in near-IR feature of oxomanganese(IV) electronic absorption feature. (Bottom Right) Rate enhancement for reaction between oxomanganese(IV) species and ethylbenzene.

4.2 Experimental and Computational Methods

4.2.1 Materials and Instrumentation

All chemicals and solvents were purchased from commercial vendors and were ACS reagent-grade quality or better. All chemicals were used as received. $Mn^{II}(OTf)_2$•$2CH_3CN$ used for preparation of metal complexes was synthesized according to a previously reported procedure.[41] For O_2-free reactions, solvents were dried following published procedures and degased by freeze-pump-thaw methods.[42] Iodosobenzene was prepared from iodosobenzene diacetate following a published procedure without modification.[43]

Electronic absorption spectra for formation and kinetic reactions were obtained on a Varian Cary 50 Bio or an Agilent 8453 spectrophotometer. Both spectrophotometers were interfaced with a Unisoku cryostat (USP-203-A), capable of maintaining temperatures of 298 K for all reactions. Electrospray-ionization mass spectrometry experiments were performed using an LCT Primers Mircomass electrospray time-of-flight instrument. NMR data were collected on a Bruker AVIIIHD 400 MHz NMR instrument. EPR data were collected at 5 K on a 9 GHz Bruker EMXPlus spectrometer with an Oxford ESR900 continuous-flow liquid helium cryostat controlled by an Oxford ITC503 temperature system. Perpendicular mode data were collected in a dual mode Bruker ER4116DM cavity. Recording conditions were 9.637 GHz microwave frequency, 2.0 mW microwave power, 6 G modulating amplitude, 100 kHz modulation frequency, and 141 ms time constant.

4.3.2 Synthesis and Characterization

The free ligands, 2pyN2Q, ^{DMM}N4py, and 2pyN2B, were prepared as described previously without any further modification.[13, 40] The metal complexes $[Mn^{II}(OTf)(2pyN2Q)](OTf)$ and $[Mn^{II}(OTf)(^{DMM}N4py)](OTf)$ and intermediates $[Mn^{IV}(O)(2pyN2Q)]^{2+}$ and $[Mn^{IV}(O)(^{DMM}N4py)]^{2+}$ were prepared as previously described.[13] The metal complex $[Mn^{II}(OH_2)(2pyN2B)](OTf)_2$ was prepared by reacting equimolar amounts of the 2pyN2B free ligand and $Mn^{II}(OTf)_2$•$2CH_3CN$ in CH_3CN and stirred for 30

minutes to an hour. Solid $[Mn^{II}(OH_2)(2pyN2B)](OTf)_2$ was obtained by slow diffusion of diethyl ether into the $[Mn^{II}(OH_2)(2pyN2B)](OTf)_2$ acetonitrile solution. Repeated recrystallizations were necessary to obtain pure samples of $[Mn^{II}(OH_2)(2pyN2B)](OTf)_2$ for further studies.

X-ray Crystallography of $[Mn^{II}(2pyN2B)(OH_2)](OTf)_2$ A full hemisphere of diffracted intensities (1850 10-second frames with an w scan width of 0.30°) was measured for a single-domain specimen using graphite-monochromated MoKα radiation (l= 0.71073 Å) on a Bruker SMART APEX CCD Single Crystal Diffraction System.[44] The integrated data[45] were corrected empirically for variable absorption effects using equivalent reflections. The Bruker software package SHELXTL was used to solve the structure using "direct methods" techniques. All stages of weighted full-matrix least-squares refinement were conducted using F_o^2 data with the SHELXTL XL v2014 software package.[46]

Preparation of XAS Samples. A 10 mM XAS sample of $[Mn^{II}(OTf)(2pyN2Q)](OTf)$ was prepared by dissolving 4.9 mg (0.006 mmol) $[Mn^{II}(OTf)(2pyN2Q)](OTf)$ in 0.6 mL TFE. An XAS sample holder was filled with this solution and flash-frozen in liquid nitrogen. A 10 mM XAS sample of $[Mn^{IV}(O)(2pyN2Q)]^{2+}$ was prepared by dissolving 12.3 mg (0.015 mmol) $[Mn^{II}(OTf)(2pyN2Q)](OTf)$ in 0.5 mL TFE and 24.8 mg (0.11 mmol) PhIO in 1 mL TFE, which was mixed using a vortex mixer for 15 seconds. Two separate XAS samples were immediately prepared and flash frozen. For this sample, only 7.5 equivalents of PhIO were used instead of the usual 10 equivalents because of the limited solubility of PhIO in TFE.

A 10 mM XAS sample of $[Mn^{II}(OTf)(^{DMM}N4py)](OTf)$ was prepared by dissolving 5.0 mg (mmol) $[Mn^{II}(OTf)(^{DMM}N4py)](OTf)$ in 0.6 mL TFE. An XAS sample holder was filled with this solution and flash-frozen in liquid nitrogen. A 10 mM XAS sample of $[Mn^{IV}(O)(^{DMM}N4py)]^{2+}$ was prepared by dissolving 12.5 mg (0.015 mmol) $[Mn^{II}(OTf)(^{DMM}N4py)](OTf)$ in 0.5 mL TFE and combining it with 6.6 mg (0.027 mmol) PhIO in 1 mL TFE and placing the reaction mixture into a 0.2 cm cuvette, where the formation of $[Mn^{IV}(O)(^{DMM}N4py)]^{2+}$ was monitored by UV/vis spectroscopy. At maximum formation, two XAS samples were prepared and flash frozen in liquid nitrogen.

A 10 mM XAS sample of $[Mn^{IV}(O)(2pyN2B)]^{2+}$ was prepared by dissolving 13.3 mg (0.016 mmol) $[Mn^{II}(OTf)(2pyN2B)](OTf)$ in 1.6 mL of a TFE solution containing 35.2 mg PhIO (0.16 mmol). The reaction mixture was placed into a 0.2 cm cuvette, where the formation of $[Mn^{IV}(O)(2pyN2B)]^{2+}$ was monitored by UV/vis spectroscopy. At maximum formation, two XAS samples were prepared and flash frozen in liquid nitrogen. A 15 mM sample of $[Mn^{II}(OH_2)(2pyN2B)](OTf)_2$ was prepared by dissolving 9.3 mg (0.012 mmol) $[Mn^{II}(OTf)(2pyN2B)](OTf)$ in 0.8 mL of ethanol, transferring the solution to an XAS sample holder, and flash freezing the solution in liquid nitrogen.

XAS Data Collection. XAS data for all samples, except $[Mn^{II}(OH_2)(2pyN2B)](OTf)_2$, were collected at beamline 9-3 at Stanford Synchrotron Radiation Light Source (SSRL). Mn K-edge X-ray absorption spectra were collected over an energy range of 6.3 to 7.4 keV (Si(220) monochromator). The frozen samples were maintained at 7 K during data collection by an Oxford liquid He cryostat. XAS spectra were obtained as fluorescence excitation spectra using a Canberra 100-element Ge array. A reference spectra of a manganese foil was collected for each scan and an internal calibration was performed by setting the zero crossing of the second derivative of the K-edge energy of the reference spectra to 6539.0 keV. The high flux at Beamline 9-3 lead to photo-reduction for the oxomanganese(IV) samples. When multiple scans were collected on a single spot of the frozen sample, there was a noticeable shift of the edge to a lower energy. To reduce the effects of photoreduction, the beam was moved to different spots on the sample and only one scan was collected per spot. 4 scans were collected for $[Mn^{IV}(O)(^{DMM}N4py)]^{2+}$, while 9 scans with a smaller horizontal gap were collected for $[Mn^{IV}(O)(2pyN2Q)]^{2+}$. 3 scans were collected for $[Mn^{IV}(O)(2pyN2B)]^{2+}$.

Mn K-edge XAS data for $[Mn^{II}(OTf)(2pyN2B)](OTf)$ were collected Beamline 2-2 at SSRL. Compared to conditions at Beamline 9-3, the main difference was the use of a Si(111) monochromator and a 13-element Ge array. There was also no evidence of photoreduction. The lower flux and the number of detectors at this beamline required the signal averaging of 18 scans.

XAS Data Analysis. XAS data analysis was performed using the Demeter software package.[47] Individual scans of raw data were analyzed and combined using Athena and extended X-ray absorption fine-structure (EXAFS) data were fit using Artemis. X-ray diffraction (XRD) coordinates for the Mn^{II} samples and density functional theory (DFT) optimized coordinates for the oxomanganese(IV) samples were used for fitting of the $k^3\chi(k)$ data, using *FEFF6* and DFT models (*vide infra*) for phase and amplitude functions.[48] For each fit, the parameters R, which describes the average scattering pathway distance, and σ^2 (Debye-Waller factor) were optimized individually for each path and E_0 (k = 0) was a common variable for all paths. The parameter describing the degeneracy of the scattering atom, N, was fixed for each fit and systematically varied between fits in order to achieve better goodness of fit. The goodness of fit was evaluated using the R-factor (Equation 4.1).

$$R = \sum_{i=1}^{N}(\chi_i^{data} - \chi_i^{fit})^2 \,/\, \sum_{i=1}^{N}(\chi_i^{data})^2 \qquad (4.1)$$

Fits of the pre-edge areas were performed using the FityK software.[49]

EPR Sample Preparation. A 10 mM EPR sample of $[Mn^{IV}(O)(2pyN2B)]^{2+}$ was prepared by thawing a previously described XAS sample and then immediately transferred 200 µL of this solution into a 4 mm quartz EPR tube and flash frozen in liquid nitrogen.

Electronic Structure Computations. All computations were performed using the *ORCA* 3.0.3 software package.[50] DFT geometry optimizations employed the TPSS functional[51] with D3 corrections,[52-53] def2-TZVP (Mn, O, and N) and def2-SVP (C, F, and H) basis sets,[54-56] an SMD solvation model (for 2,2,2-trifluoroethanol).[57] and a dense integration grid (Grid6 in *ORCA*). Tight optimization and SCF criteria were invoked using the TightOpt and TightSCF keywords in *ORCA*. The RI approximation, with def2-TZVP/J and def2-SVP/J auxiliary basis sets, were used. Structures of Mn^{II} and Mn^{IV} complexes were converged to the *S* = 5/2 and 3/2 spin states, respectively. Frequency calculations for all Mn^{II} species, all Mn^{IV}-oxo species lacking second-sphere TFE molecules, and $[Mn^{IV}(O)(2pyN2Q)]^{2+}\cdot(TFE)_2$ showed no imaginary frequencies, ensuring that these

structures represent true minimum. The $[Mn^{IV}(O)(N4py)]^{2+}\cdot(TFE)_2$ and $[Mn^{IV}(O)(^{DMM}N4py)]^{2+}\cdot(TFE)_2$ structures each showed one small imaginary mode (-7.30 and -25.18 cm^{-1}, respectively) associated with rotational modes of the methyl groups of TFE and the *para*-methoxy-pyridyl moieties, respectively. Attempts to eliminate these imaginary modes through the use of a denser integration grid or tighter convergence criteria were unsuccessful.

4.3 Results and Discussion

4.3.1 Formation and characterization of $[Mn^{IV}(O)(2pyN2B)]^{2+}$

Previous work showed that structural perturbations caused by the changes to the supporting ligand can be seen in the X-ray diffraction (XRD) crystal structure of the manganese(II) complexes, $[Mn^{II}(OTf)(N4py)](OTf)$, $[Mn^{II}(OTf)(^{DMM}N4py)](OTf)$, and $[Mn^{II}(OH_2)(2pyN2Q)](OTf)_2$.[13, 40] For example, the average Mn–$N_{equatorial}$ distances systematically decreased from 2.279 to 2.241 Å, reflecting the increase in equatorial ligand-field strength from 2pyN2Q to ^{DMM}N4py (Figure 4.1, top). In addition, the axial water ligand in $[Mn^{II}(OH_2)(2pyN2Q)](OTf)_2$ was distorted from an idealized octahedral position, further reflecting the influence of the steric bulk of the quinoline moieties. (An X-ray crystal structure of the $[Mn^{II}(OTf)(2pyN2Q)](OTf)$ species, although of lower resolution than the $[Mn^{II}(OH_2)(2pyN2Q)](OTf)_2$ structure, showed very similar metric parameters.)

Crystals of $[Mn^{II}(OH_2)(2pyN2B)](OTf)_2$ suitable for characterization by XRD (Figure 4.2) provided metric parameters that can be used to determine the effects of the 2pyN2B ligand on the Mn coordination sphere relative to the related manganese(II) complexes of $[Mn^{II}(OTf)(N4py)](OTf)$ and its derivatives (Table 4.1). The XRD structure of $[Mn^{II}(OH_2)(2pyN2B)](OTf)_2$ shows a mononuclear Mn^{II} center in a distorted octahedral environment with an axial water ligand and the 2pyN2B ligand bound in its expected pentadentate mode. The axial Mn-OH_2 distance of 2.087(3) Å is quite comparable to that observed for $[Mn^{II}(OH_2)(2pyN2Q)](OTf)_2$ (2.091(2) Å).[13] However, in the case of $[Mn^{II}(OH_2)(2pyN2B)](OTf)_2$, the position of the water ligand is not as distorted from the idealized octahedral position (N_{axial}-Mn-OH_2 angles of 177.9 ° and 163.8 ° for $[Mn^{II}(OH_2)(2pyN2B)](OTf)_2$ and $[Mn^{II}(OH_2)(2pyN2Q)](OTf)_2$, respectively).[13] For

$[Mn^{II}(OH_2)(2pyN2B)](OTf)_2$, the two Mn-$N_{BzIm}$ distances are 2.193(2) Å, which are ca. 0.6 – 0.8 Å shorter than the corresponding Mn-$N_{pyridine}$ distances of $[Mn^{II}(OTf)(N4py)]^{2+}$ but similar to those observed for the $[Mn^{II}(OTf)(^{DMM}N4py)]^{2+}$ complex (Table 4.1). [17] The Mn-$N_{pyridine}$ distances of $[Mn^{II}(OH_2)(2pyN2B)](OTf)_2$ (2.298(2) Å) are comparable to those observed for $[Mn^{II}(OTf)(^{DMM}N4py)]^{2+}$ and $[Mn^{II}(OH_2)(2pyN2Q)]^{2+}$ (Table 4.1). Overall, the average Mn-$N_{equatorial}$ distance for $[Mn^{II}(OH_2)(2pyN2B)](OTf)_2$ is 2.246 Å, which is quite similar to that of $[Mn^{II}(OTf)(^{DMM}N4py)]^{2+}$ (Figure 4.1, top). The largest Mn-ligand bond deviation observed for $[Mn^{II}(OH_2)(2pyN2B)](OTf)_2$ is in the Mn-N_{axial} bond distance (2.375(3) Å), which is nearly 0.09 Å than the corresponding distances for the other Mn^{II} structures (Table 4.1). The basis for this axial bond elongation is unclear.

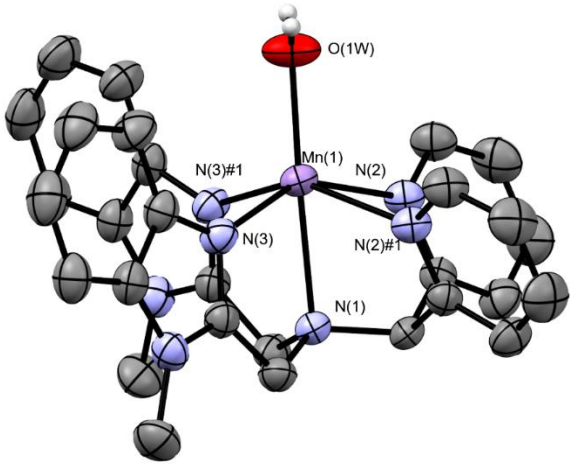

Figure 4.2. Molecular structure of $[Mn^{II}(OH_2)(2pyN2B)]^{2+}$ cation.

Table 4.1. XRD Determined bond distances (Å) for N4py based manganese(II) complexes

	$[Mn^{II}(OH_2)(2pyN2B)]^{2+}$	$[Mn^{II}(OTf)(N4py)]^{+}$ [a]	$[Mn^{II}(OTf)(^{DMM}N4py)]^{+}$ [b]	$[Mn^{II}(OH_2)(2pyN2Q)]^{2+}$ [b]
Mn-O	2.087(3)	2.125(3)	2.114(3)	2.091(2)
Mn-N(3)	2.193(2)	2.255(4)	2.189(4)	2.250(2)
Mn-N(3)	2.193(2)	2.271(4)	2.225(3)	2.265(2)
Mn-N(2)	2.298(2)	2.271(4)	2.296(4)	2.297(2)
Mn-N(2)	2.298(2)	2.278(4)	2.293(3)	2.303(2)
Mn-N(1)	2.375(3)	2.289(4)	2.278(4)	2.279(2)

[a] From reference 17. [b] From reference 13.

The trends in Mn-$N_{equatorial}$ bond length observed for the manganese(II) complexes with the 2pyN2B, N4py, and ^{DMM}N4py ligands stand are distinct from those observed for the corresponding iron(II) complexes. In that case, the $[Fe^{II}(MeCN)(2pyN2B)](ClO_4)_2$ and

$[Fe^{II}(MeCN)(N4py)](HClO_4)_2$ complexes showed the strongest similarities with average Fe-$N_{equatorial}$ distances of 1.972 Å and 1.978 Å.[40, 58] The average Fe-$N_{equatorial}$ distances for $[Fe^{II}(MeCN)(^{DMM}N4py)](OTf)_2$ are 1.971 Å.[59] Because all of these complexes are low spin, it is expected that the Fe-$N_{equatorial}$ distances should be less sensitive to minor perturbations in the equatorial ligand field, which is why there is only very subtle changes in bond distance for the iron(II) complexes.

Following the procedure previously used to prepare oxomanganese(IV) species, $[Mn^{IV}(O)(2pyN2B)]^{2+}$ was formed by the addition of a solution of iodosobenzene (PhIO) in 2,2,2-trifluoroethanol (TFE) to $[Mn^{II}(OH_2)(2pyN2B)](OTf)_2$.[13, 17] This reaction was monitored by electronic absorption spectroscopy, and the formation of $[Mn^{IV}(O)(2pyN2B)]^{2+}$ was characterized by the growth of a chromophore with a λ_{max} at 940 nm (ε = 250 $M^{-1}cm^{-1}$) and another higher intensity feature between 400 and 500 nm (Figure 4.3). A titration of monitoring absorption intensity as a function of PhIO concentration revealed that the maximum formation of $[Mn^{IV}(O)(2pyN2B)]^{2+}$ occurred with 10 equivalents of PhIO (Figure 4.3). The rate of formation of $[Mn^{IV}(O)(2pyN2B)]^{2+}$ was relatively slow, taking about 20 minutes to reach completion. This rate of formation is about 10 minutes slower than observed for$[Mn^{IV}(O)(^{DMM}N4py)]^{2+}$ and $[Mn^{IV}(O)(N4py)]^{2+}$, both of which can be formed more quickly with only 1.2 - 2.5 equivalents of PhIO.[13, 17, 19] A larger excess of PhIO may have allowed for a more rapid formation of $[Mn^{IV}(O)(2pyN2B)]^{2+}$; however, the amount of PhIO able to be used is limited by its poor solubility in TFE.

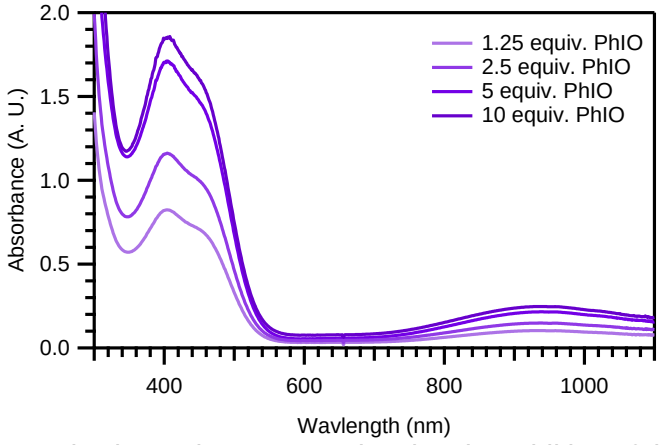

Figure 4.3. Electronic absorption spectra showing the addition of different amounts of PhIO to $[Mn^{II}(OH_2)(2pyN2B)](OTf)_2$ (1.0 mM in TFE) to maximally form $[Mn^{IV}(O)(2pyN2B)]^{2+}$.

The EPR spectrum for $[Mn^{IV}(O)(2pyN2B)]^{2+}$ (Figure 4.4) is characterized by a broad, positive feature centered at g = 5.8, a weak derivative signal near g = 2.9, and a multiline signal around g = 2. The signal at g = 5.8 shows a six-line hyperfine splitting with a = 71 mT. The multiline signal at g = 2 likely derives from a multi-nuclear Mn species. The EPR spectrum of $[Mn^{IV}(O)(2pyN2B)]^{2+}$ is significantly perturbed compared to those observed for the other N4py-based oxomanganese(IV) species (Figure 4.4). The EPR spectra for $[Mn^{IV}(O)(N4py)]^{2+}$, $[Mn^{IV}(O)(^{DMM}N4py)]^{2+}$, and $[Mn^{IV}(O)(2pyN2Q)]^{2+}$ show a feature around g = 5.8 with a six-line hyperfine splitting between 72-77 mT, a broad positive signal near g = 4.3, and a pronounced negative feature around g = 2.[13, 17] The down-field shift of the g = 5.9 signal for $[Mn^{IV}(O)(2pyN2B)]^{2+}$ and the appearance of the weak signal at g = 2.9 suggests that this oxomanganese(IV) complex is more rhombic. The rhombicity of an S = 3/2 system, such as these oxomanganese(IV) complexes, is determined by the ration of the axial (D) and rhombic (E) zero field splitting parameters (*E/D*). In a perfectly axial system, E/D is 0, and EPR signals are expected at g = 4.0 and 2.0. For systems with non-zero rhombicity *(E/*D > 0) the signal at g = 4.0 splits into two components, as observed for $[Mn^{IV}(O)(2pyN2B)]^{2+}$. The EPR spectrum of $[Mn^{IV}(O)(2pyN2B)]^{2+}$ is reminiscent of that observed for $[Mn^{IV}(O)(OH)(Me_2EBC)]^{+}$, which was reported to have two overlapping six-line hyperfine features at g = 5.95 and g = 4.99 and derivative signal at g = 2.62.[60] The multiline signal around g = 2 observed for $[Mn^{IV}(O)(2pyN2B)]^{2+}$ and, to a lesser extent, $[Mn^{IV}(O)(2pyN2Q)]^{2+}$, are likely due to the presence of a small amount of dinuclear species. For $[Mn^{IV}(O)(2pyN2B)]^{2+}$, this may be due to the preparation of the EPR sample, which was thawed from an XAS sample. Further EPR studies will be performed on this complex to understand the origin of the multiline signal.

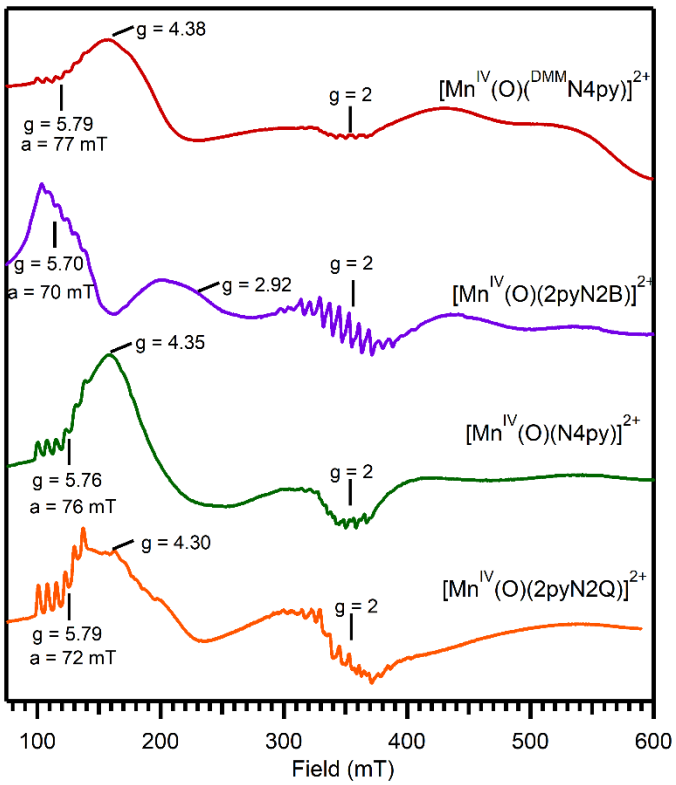

Figure 4.4. Perpendicular X-band EPR spectra of $[Mn^{IV}(O)(^{DMM}N4py)]^{2+}$, $[Mn^{IV}(O)(2pyN2B)]^{2+}$, $[Mn^{IV}(O)(N4py)]^{2+}$, and $[Mn^{IV}(O)(2pyN2Q)]^{2+}$. All experiments were carried out at 5 K, except that of $[Mn^{IV}(O)(2pyN2B)]^{2+}$, which was collected at 10 K. Previous data are from references 13 and 17.

4.3.2 Analysis of X-ray Absorption Data

Mn K-edge X-ray absorption data for the manganese(II) and oxomanganese(IV) complexes of the N4py, ^{DMM}N4py, and 2pyN2Q complexes were previously reported.[13, 17] ***For the*** $[Mn^{II}(OTf)(N4py)](OTf)$ and $[Mn^{IV}(O)(N4py)]^{2+}$ complexes, we reported analysis of both the pre-edge an EXAFS regions, and these data are included here for comparison.[17] For the manganese(II) and oxomanganese(IV) complexes of the ^{DMM}N4py and 2pyN2Q ligands, our previous report only included analysis of the edge and pre-edge regions.[13] Here we describe the collection and interpretation of EXAFS data for these complexes as well. In addition, new pre-edge data collected for these complexes shows enhanced resolution compared to the previously published data; this is also described below.

Edge Energies. The Mn K-edge energies of the $[Mn^{II}(OTf)(N4py)](OTf)$, $[Mn^{II}(OTf)(^{DMM}N4py)](OTf)$, $[Mn^{II}(OH_2)(2pyN2B)](OTf)_2$ and $[Mn^{II}(OH_2)(2pyN2Q)](OTf)_2$

are all very similar, ranging from 6547.1 to 6547.5 eV (Table 4.2 and Figure 4.5). These values are generally quite similar to those previously reported for manganese(II) complexes. For example, the edge energy of $[Mn^{II}(Cl)_2(Me_2EBC)]$ (6547.1 eV) falls within this range, while the edge energies for manganese(II) complexes supported by the anionic, N_5 dpaq and $dpaq^{2Me}$ are only slightly higher 6548 eV.[21, 61] For the manganese(II) complexes of N4py and its derivatives (Table 4.2), the position of the manganese(II) K-edge does not appear to be particularly sensitive to the identity of supporting ligand nor the solvent (Table 4.2). XAS data for $[Mn^{II}(OTf)(N4py)](OTf)$ were collected for a sample in water, whereas data for $[Mn^{II}(OTf)(^{DMM}N4py)](OTf)$ and $[Mn^{II}(OH_2)(2pyN2Q)](OTf)_2$ were of TFE solutions.[17] Data for $[Mn^{II}(OH_2)(2pyN2Q)](OTf)_2$ were collected for a sample in in ethanol, because the low flux at beamline 2-2 did not allow for the collection of EXAFS data in triflouroethanol due to very low fluorescence intensity.

Table 4.2. Summary of edge energies and other parameters for manganese(II) XAS data.

complex	edge (eV)	pre-edge (eV)	solvent	concentration
$[Mn^{II}(OTf)(^{DMM}N4py)](OTf)$	6547.5	6540.1	TFE	10 mM
$[Mn^{II}(OH_2)(2pyN2B)](OTf)_2$	6547.1	6540.3	Ethanol	15 mM
$[Mn^{II}(OTf)(N4py)](OTf)$ [a]	6547.3	6540.6	Water	10 mM
$[Mn^{II}(OH_2)(2pyN2Q)](OTf)_2$	6547.4	6540.1	TFE	10 mM

[a] From reference 17.

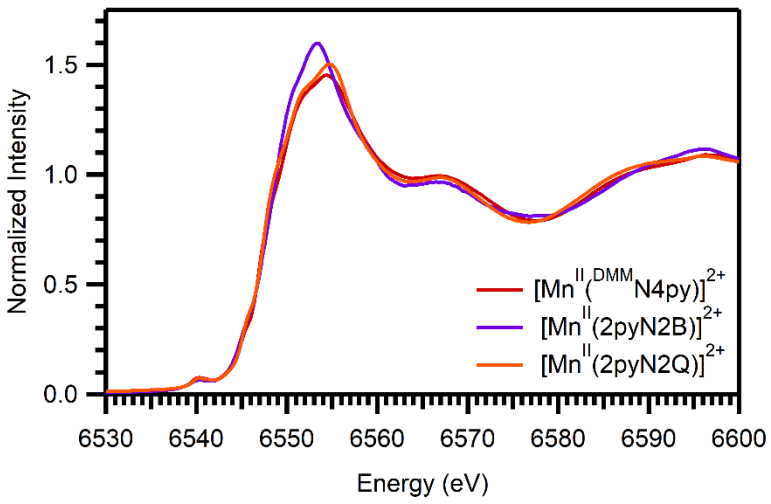

Figure 4.5. Experimental XANES of the manganese(II) complexes.

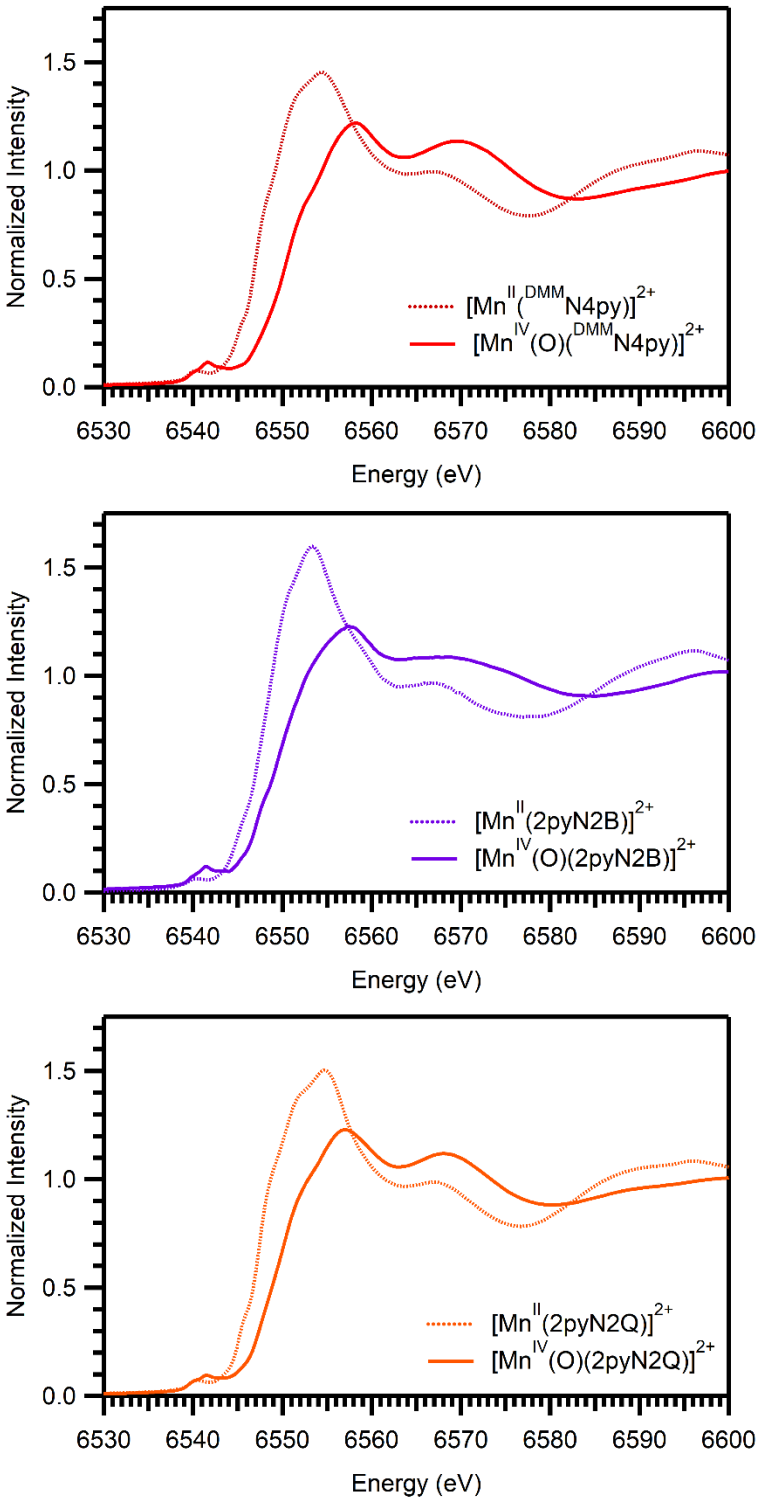

Figure 4.6. Experimental XANES data for manganese(II) complexes (dashed) and oxomanganese(IV) species (solid) showing the shift in edge energy to a higher energy upon formation of the oxomanganese(IV) species.

Upon oxidation of these manganese(II) complexes by PhIO to form the corresponding oxomanganese(IV) species, there is noticeable shift in the edge energy, as well as an increase in the intensity of the pre-edge peak (Figure 4.6). The Mn K-edge energies of $[Mn^{IV}(O)(N4py)]^{2+}$, $[Mn^{IV}(O)(^{DMM}N4py)]^{2+}$, $[Mn^{IV}(O)(2pyN2Q)]^{2+}$, and $[Mn^{IV}(O)(2pyN2B)]^{2+}$ range from 6549.6 to 6550.8 eV (Table 4.3). These energies are increased by 2 – 3 eV compared to the manganese(II) complexes (cf. Tables 4.3 and 4.2), consistent with the expected increase in Mn oxidation state. The Mn K-edges of $[Mn^{IV}(O)(2pyN2Q)]^{2+}$ or $[Mn^{IV}(O)(2pyN2B)]^{2+}$ are ca. 1 eV lower than those of $[Mn^{IV}(O)(N4py)]^{2+}$ and $[Mn^{IV}(O)(^{DMM}N4py)]^{2+}$. This difference can be appreciated in Figure 4.7 where the edge energy of $[Mn^{IV}(O)(^{DMM}N4py)]^{2+}$ is clearly higher than that of either $[Mn^{IV}(O)(2pyN2Q)]^{2+}$ or $[Mn^{IV}(O)(2pyN2B)]^{2+}$. Because the EPR spectra of $[Mn^{IV}(O)(2pyN2B)]^{2+}$ and $[Mn^{IV}(O)(2pyN2Q)]^{2+}$ each show a multiline signal (Figure 4.4) due to the presence of some multi-nuclear species (potentially a $Mn^{III}Mn^{IV}$ dimer), the lower edge energies of these complexes are most likely due to the presence of these species. We note that the previously reported Mn K-edge energy for $[Mn^{IV}(O)(2pyN2Q)]^{2+}$, which was collected for a different sample, is 0.8 eV lower than that reported here.[13] This variation in edge energy based on sample preparation further supports that reduced sample homogeneity for $[Mn^{IV}(O)(2pyN2Q)]^{2+}$, and by inference $[Mn^{IV}(O)(2pyN2B)]^{2+}$, can account for the lower edges of these samples.

Table 4.3. Summary of edge and pre-edge energies as well as pre-edge area for the series of oxomanganese(IV) complexes.

Complex	edge (eV)	pre-edge (eV)	pre-edge area
$[Mn^{IV}(O)(^{DMM}N4py)]^{2+}$	6550.5	6539.9, 6541.6, 6543.2	20.1
$[Mn^{IV}(O)(2pyN2B)]^{2+}$	6549.6	6540.1, 6541.4, 6543.1	14.6
$[Mn^{IV}(O)(N4py)]^{2+}$	6550.8[a]	6541.6[a]	18.9[b]
$[Mn^{IV}(O)(2pyN2Q)]^{2+}$	6550.0	6539.9, 6541.5[c]	15.1[c]

[a] From references 17 and 19. [b] Pre-edge area from reference 13. $[Mn^{IV}(O)(2pyN2Q)]^{2+}$ can also be fit with 3 *pseudo*-Voigt functions, however it might be an over-analysis of the data. The alternative fit and a brief discussion can be found in Appendix 4.

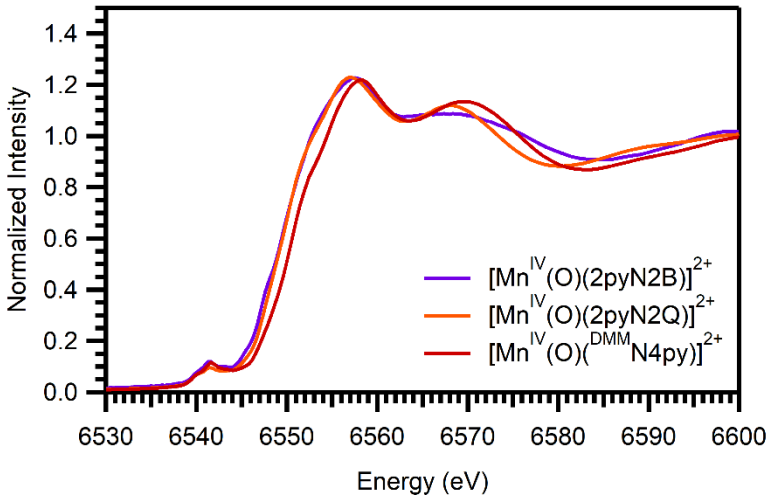

Figure 4.7. Experimental XANES of the oxomanganese(IV) species.

Pre-edge Areas. Each of the oxomanganese(IV) complexes shows a prominent pre-edge features centered at ca. 6541 eV (Figure 4.7). The The pre-edge areas of $[Mn^{IV}(O)(\ N4py)]^{2+}$, $[Mn^{IV}(O)(^{DMM}N4py)]^{2+}$, and $[Mn^{IV}(O)(2pyN2Q)]^{2+}$ were previously fit with only one *pseudo*-Voigt function.[13] However, higher quality data collected at beamline 9-3 allowed for better resolution of the XANES region, revealing additional features (Table 4.3, Figure 4.8). The newly collected data were fit with either two or three *pseudo*-Voigt functions; however, the calculated pre-edge areas did not change significantly from that previously reported.[13] As shown in Figure 4.8, the pre-edge region for $[Mn^{IV}(O)(2pyN2Q)]^{2+}$ was fit with only two *pseudo*-Voigt functions, whereas the fits for $[Mn^{IV}(O)(^{DMM}N4py)]^{2+}$ and $[Mn^{IV}(O)(2pyN2B)]^{2+}$ employed three functions. Analysis of the derivative and second derivative of the pre-edge region for $[Mn^{IV}(O)(2pyN2Q)]^{2+}$ provided inconclusive evidence as to whether or not there should be an additional function included in the pre-edge fit. Time-dependent density functional theory (TD-DFT) calculations will be necessary to understand the origin of three pre-edge transitions. Previous calculations for $[Mn^{IV}(O)(N4py)]^{2+}$ predicted two transitions in this region; however, the modulation of the equatorial ligand field caused by the ^{DMM}N4py and 2pyN2B ligands may allow for more transitions to become visible.[21]

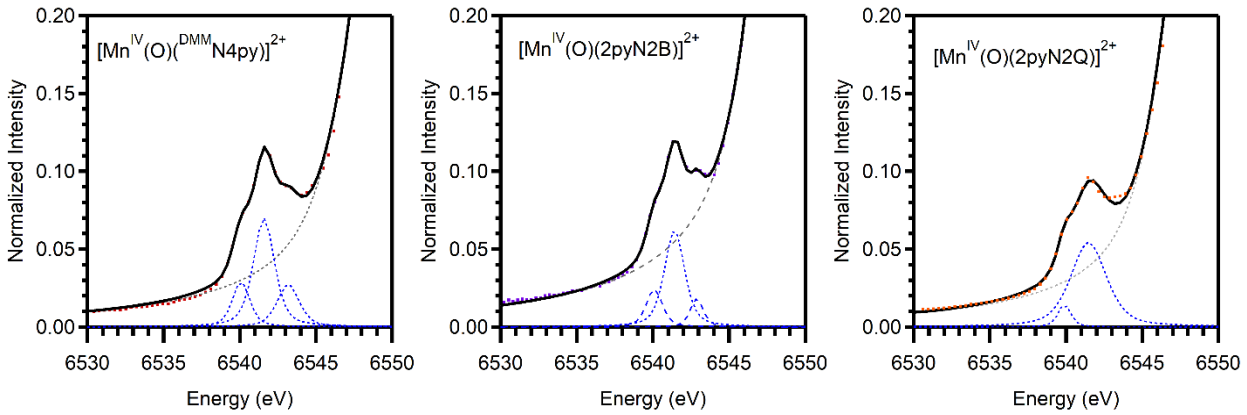

Figure 4.8. Comparison of the normalized XAS Pre-edge data (dotted line) and fits (solid line) for the oxomanganese(IV) complexes. Dashed traces represent the fit of the background and fits to the pre-edge peak.

The pre-edge areas of $[Mn^{IV}(O)(2pyN2Q)]^{2+}$ and $[Mn^{IV}(O)(^{DMM}N4py)]^{2+}$ are quite similar to what was previously reported, with areas of 15.1 and 20.1, respectively. For $[Mn^{IV}(O)(^{DMM}N4py)]^{2+}$, this represents an increase of 0.5 while $[Mn^{IV}(O)(2pyN2Q)]^{2+}$ shows a decrease of 1.9.[13] It is somewhat unexpected that the pre-edge area of $[Mn^{IV}(O)(2pyN2Q)]^{2+}$ would decrease upon a likely more homogeneous sample, but it is unclear what influence of the impurity would have on the pre-edge area. Similarly, $[Mn^{IV}(O)(2pyN2B)]^{2+}$ shows a lower pre-edge area of 14.6, the lowest of all oxomanganese(IV) species based on the N4py framework. Previously, it was demonstrated that there was a correlation between pre-edge area and the sum of Mn 4p character in the acceptor molecular orbitals (MO).[21] Thus the trend we see, where the complex with the strongest donor ligand, $[Mn^{IV}(O)(^{DMM}N4py)]^{2+}$, has the highest pre-edge area agrees with what is expected based on the previously observed correlation. Although, it is important to note that the lower pre-edge areas observed for $[Mn^{IV}(O)(2pyN2Q)]^{2+}$ and $[Mn^{IV}(O)(2pyN2B)]^{2+}$ may simply be a result of the incomplete oxomanganese(IV) formation.

The pre-edge areas determined from these fits can be compared to values reported previously for $[Mn^{IV}(O)(N4py)]^{2+}$ and $[Mn^{IV}(O)(OH)(Me_2EBC)]^{2+}$, although this comparison must be performed with some caution as the pre-edge data were normalized differently.[21] The pre-edge intensities for $[Mn^{IV}(O)(N4py)]^{2+}$ and $[Mn^{IV}(O)(OH)(Me_2EBC)]^{2+}$ were normalized relative to the most intense fluorescence

peak, whereas the tail of the EXAFS region was used to normalize data collected for $[Mn^{IV}(O)(^{DMM}N4py)]^{2+}$, $[Mn^{IV}(O)(2pyN2B)]^{2+}$, and $[Mn^{IV}(O)(2pyN2Q)]^{2+}$.[13, 17, 21] To assess the effects of this different normalization proceed on the pre-edge area, we applied the latter normalization proceed to XAS data previously reported for $[Mn^{IV}(O)(N4py)]^{2+}$. Normalization to the tail of the EXAFS region resulted in a pre-edge area of 18.9, a significant increase compared to that determined when normalizing relative to the most intense fluorescence peak (from 12.7 units).[13, 21] $[Mn^{IV}(O)(OH)(Me_2EBC)]^{2+}$ had a pre-edge area higher than $[Mn^{IV}(O)(N4py)]^{2+}$ (14.2 versus 12.7), so, if the pre-edge region for $[Mn^{IV}(O)(OH)(Me_2EBC)]^{2+}$ were normalized to the EXAFS tail, it would likely have the highest pre-edge area.

EXAFS Analysis of Manganese(II) Complexes. Although the triflate salts of $[Mn^{II}(OTf)(^{DMM}N4py)](OTf)$, $[Mn^{II}(OH_2)(2pyN2B)](OTf)_2$ and $[Mn^{II}(OH_2)(2pyN2Q)](OTf)_2$ have been characterized by XRD, analysis of EXAFS data provides information on the solution phase structure of these complexes. Further, good agreement between DFT optimized structures, XRD structures, and bond distances determined from EXAFS fitting provide support that DFT optimized structures are reliable for fitting EXAFS when XRD coordinates are unavailable. The Fourier transform (FT) spectra and raw EXAFS data for the manganese(II) complexes can be seen in Figure 4.9. The FT spectra of these manganese(II) complexes are all characterized by a large peak at R´ = 1.8 Å with a shoulder near 1.4 Å that is less prominent for $[Mn^{II}(OH_2)(2pyN2B)](OTf)_2$. Additional peaks near 2.2 Å, with some variation, are also observed in each FT spectrum.

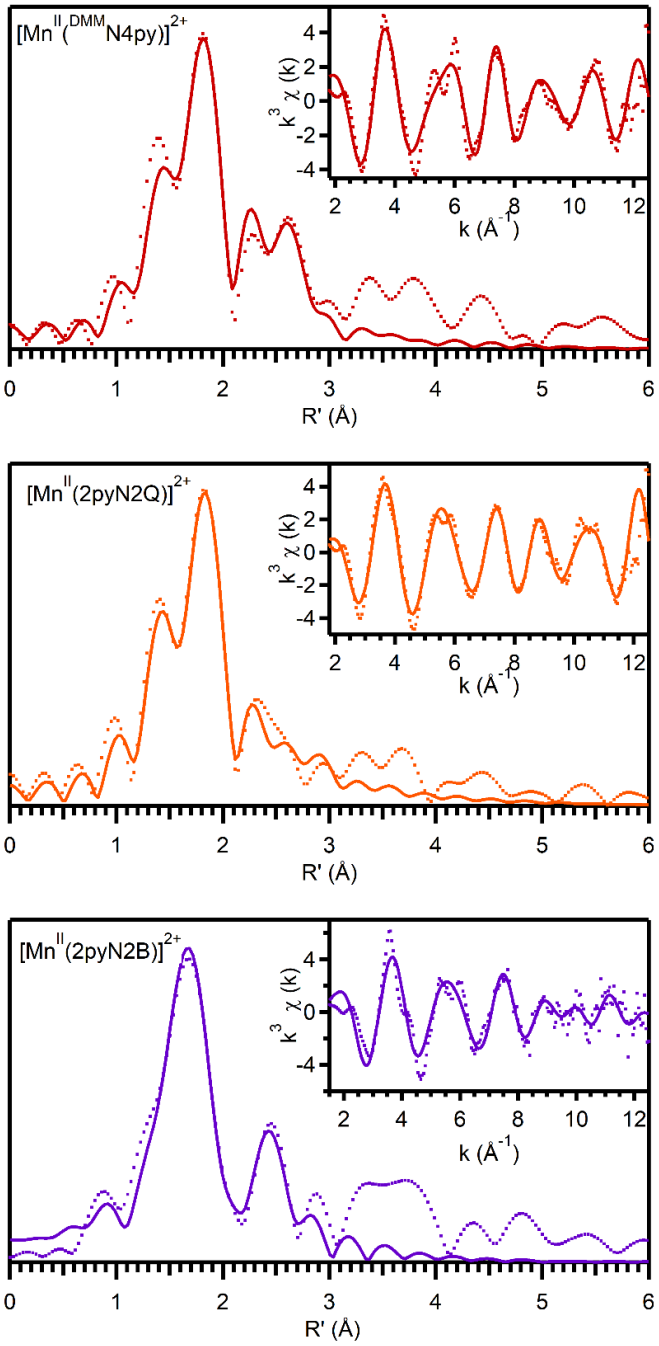

Figure 4.9. Fourier transforms of Mn K-edge EXAFS data and raw k^3 weighted EXAFS curves (insets) for the manganese(II) complexes. Experimental data is represented by dotted lines whereas fits are solid lines.

The best fits to the EXAFS data for each of these complexes are provided in Table 4.4, whereas information for other possible fits can be found in Table A4.2. The EXAFS spectra for $[Mn^{II}(OTf)(^{DMM}N4py)](OTf)$, and $[Mn^{II}(OH_2)(2pyN2Q)](OTf)_2$ are both best fit with two separate O/N shells with *n* (number of scatterers in a shell) equal to 1 and 5,

respectively, and two C shells (*n* between 3 and 6) with Mn-scatterer distances greater than 3.0 Å. The innermost Mn-O/N shell (*n*=1) occurs at 2.03 and 2.04 Å for $[Mn^{II}(OTf)(^{DMM}N4py)](OTf)$ and $[Mn^{II}(OH_2)(2pyN2Q)](OTf)_2$, respectively, while the shell of five N scatterers occurs at 2.23 and 2.25 Å, respectively. The shell of five scatterers can be readily attributed to the five N donors of the ^{DMM}N4py and 2pyN2Q ligands. The average Mn-N bond lengths in the solid-state XRD structures of $[Mn^{II}(OTf)(^{DMM}N4py)](OTf)$ and $[Mn^{II}(OH_2)(2pyN2Q)](OTf)_2$ (2.25 and 2.28 Å, respectively) are in excellent agreement with the corresponding EXAFS distances (2.23 and 2.25 Å; see Table 4.5).

Table 4.4 Parameters derived from the best EXAFS fit for each manganese(II) complex [a]

	Mn-O/N			Mn-N			Mn-C				
complex	*n*	r(Å)	σ^{2} [b]	*n*	r(Å)	σ^{2} [b]	*n*	r(Å)	σ^{2} [b]	E_0	R
$[Mn^{II}(OTf)(^{DMM}N4py)](OTf)$	1	2.03	1.23	5	2.23	3.19	3	3.53	7.37	6.702	0.1181
							5	3.07	6.20		
$[Mn^{II}(OH_2)(2pyN2B)](OTf)_2$	3	2.28	3.44	3	2.14	2.14	3	3.01	1.91	1.715	0.2148
							3	3.21	14.71		
$[Mn^{II}(OH_2)(2pyN2Q)](OTf)_2$	1	2.04	1.49	5	2.25	2.96	6	3.02	11.41	2.034	0.0867
							4	4.06	13.52		

[a] Fourier Transform range was 2-12 $Å^{-1}$ for all manganese(II) complexes [b] σ^2 is in units of 10^3 $Å^2$.

Table 4.5. Comparison of XRD, DFT, and EXAFS determined bond distances (Å) for manganese(II) complexes.

complex		XRD	DFT (OCH_2CF_3)	DFT ($HOCH_2CF_3$)	EXAFS
$[Mn^{II}(OTf)(^{DMM}N4py)](OTf)$	Mn-O (1)	2.12	1.93	2.20	2.03
	Mn-N (5)	2.25	2.31	2.26	2.23
$[Mn^{II}(OH_2)(2pyN2B)](OTf)_2$	Mn-O/N (3)	2.15	2.11	2.22	2.14
	Mn-N (3)	2.32	2.40	2.30	2.28
$[Mn^{II}(OH_2)(2pyN2Q)](OTf)_2$	Mn-O (1)	2.09	N/D	2.23	2.04
	Mn-N (5)	2.28	N/D	2.32	2.25

The innermost O/N shell for $[Mn^{II}(OTf)(^{DMM}N4py)](OTf)$ and $[Mn^{II}(OH_2)(2pyN2Q)](OTf)_2$ is attributed to the axial ligands, which are OTf^- and OH_2 in the solid-state XRD structures (Figure 4.1). However, we deem it likely that the OTf^- ligand

would be replaced by solvent (TFE) for the solution-phase sample. In support, the XRD structure of $[Mn^{II}(OTf)(^{DMM}N4py)](OTf)$ shows a Mn-OTf bond distance of 2.12 Å, significantly longer than the EXAFS distance of 2.03 Å (Table 4.5). For $[Mn^{II}(OH_2)(2pyN2Q)](OTf)_2$, the EXAFS distance of 2.04 Å is slightly shorter, but still compatible, with the Mn-OH_2 distance of 2.09 Å observed by XRD. Nonetheless, the discrepancy between XRD and EXAFS distances could indicate that the water ligand in $[Mn^{II}(OH_2)(2pyN2Q)](OTf)_2$ is also replaced by solvent for the solution-phase EXAFS sample.

The EXAFS data for $[Mn^{II}(OH_2)(2pyN2B)](OTf)_2$ are best fit with 2 O/N shells, at 2.14 and 2.28 Å, each with *n*=3. This change in EXAFS fitting relative to $[Mn^{II}(OTf)(^{DMM}N4py)](OTf)$ and $[Mn^{II}(OH_2)(2pyN2Q)](OTf)_2$ is likely due to the two shortened Mn-N_{BzIm} bond distances, which XRD shows to at 2.19 Å. Under this assumption, the inner EXAFS shell of $[Mn^{II}(OH_2)(2pyN2B)](OTf)_2$ contains contributions from the N_{BzIm} groups and the axial OTf^- (TFE) ligand. Using the Mn-OTf distance observed by XRD, these three Mn-ligand distances gives an average Mn-N/O distance of 2.15 Å, very close to the 2.14 Å determined from EXAFS fitting (Table 4.5). Similarly, the elongated Mn-N_{py} bond distances of 2.30 Å in $[Mn^{II}(OH_2)(2pyN2B)](OTf)_2$ places these scatterers closer to the Mn-N_{ax} bond distance of 2.38 Å, to give an average distance of 2.28 Å. This average from the XRD structure is just slightly longer than the EXAFS calculated distance of 2.25 Å.

Structures for the hypothetical $[Mn^{II}(HOCH_2CF_3)(^{DMM}N4py)]^{2+}$ and $[Mn^{II}(HOCH_2CF_3)(2pyN2Q)]^{2+}$ complexes were determined using DFT computations. These computations employed the meta-GGA TPSS functional with dispersion corrections and an SMD solvation model. The energy-minimized structures are shown in Figure 4.10, and relevant metric parameters are compared with EXAFS and XRD distances in Table 4.5. Each of the DFT-optimized manganese(II) structures shows significant intra-ligand π-stacking interactions that are absent in the solid-state XRD structures (Figure 4.10). Current dispersion treatments for DFT computations have been known to over-correct for π-π interactions, and this could be the case for these complexes. At present, it is unclear if the strong dispersion interactions in the

manganese(II) structures have any influence on the Mn-ligand distances. In general, the bond distances determined from DFT optimized structures agree well with those from XRD (Table 4.5), although the computations are not able to reproduce the Mn-N/O distances of 2.03 and 2.04 Å observed for $[Mn^{II}(OTf)(^{DMM}N4py)](OTf)$ and $[Mn^{II}(OH_2)(2pyN2Q)](OTf)_2$. Additional calculations lacking the dispersion correction will need to be performed to further examine these issues.

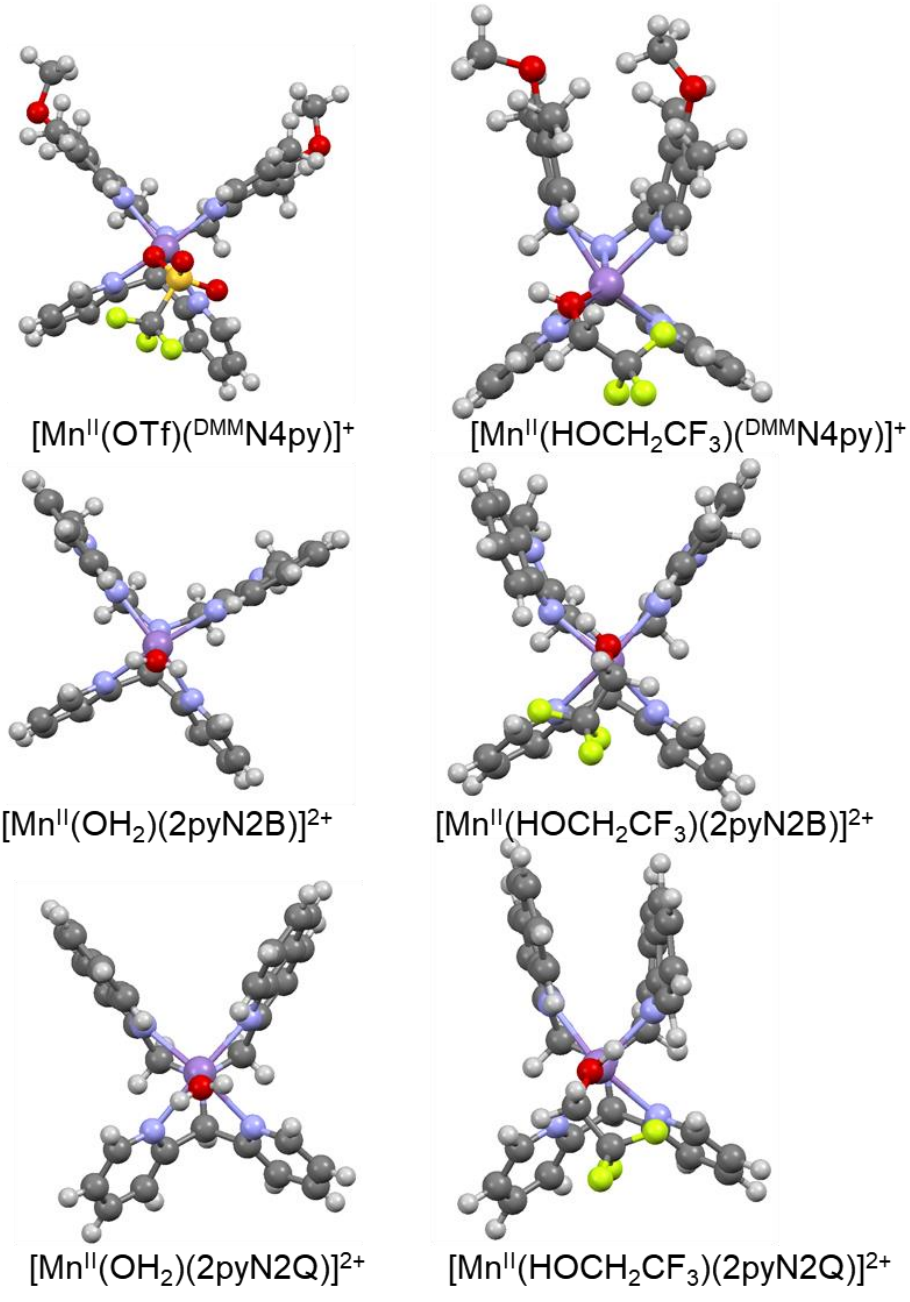

Figure 4.10. Comparison of XRD (left) and DFT optimized (right) structures, showing the distortions due to pi-stacking in the DFT structures.

EXAFS Analysis of Oxomanganese(IV) Species. The FT and raw EXAFS data for the $[Mn^{IV}(O)(^{DMM}N4py)]^{2+}$, $[Mn^{IV}(O)(2pyN2Q)]^{2+}$, and $[Mn^{IV}(O)(2pyN2B)]^{2+}$ complexes are shown in Figure 4.11, and best fits to these date are collected in Table 4.6. More complete fitting information can be found in Table A4.3. The FT spectrum of each Mn^{IV}-oxo complex is characterized by peaks at ca. 1.2, 1.6, and 1.9 Å that vary in intensity between the different complexes (Figure 4.11). In general, there is a larger variation in the appearance of the FT EXAFS data for the Mn^{IV}-oxo complexes than for their Mn^{II} analogues. Nonetheless, fits of the EXAFS data for this set of Mn^{IV}-oxo adducts reveals comparable metric parameters (Table 4.6). In particular, the set of FT EXAFS features from 1.2 – 1.9 Å are well fit with features correspond mainly to the Mn=O and Mn-N first coordination sphere. In each case, the features are well fit with an O shell (*n* = 1) near 1.70 Å, and two N shells (*n* = 4 and 1) near 2.00 and 2.20 Å, respectively. In addition, FT EXAFS features beyond 2.0 Å can be accounted for with two shells of C scatterers near 2.7 and 2.9 Å.

Table 4.6. Parameters derived from the best EXAFS fit for each oxmanganese(IV) species along with selected distances determined by DFT in parentheses.

	Mn-O/N			Mn-N			Mn-C				
complex	*n*	r(Å)	σ^2	*n*	r(Å)	σ^2	*n*	r(Å)	σ^2	E_0	R
$[Mn^{IV}(O)(^{DMM}N4py)]^{2+}$	1	1.71	1.37	4	1.99	6.9	5	2.9	4.99	-2.36	0.212
				1	2.16	1.15	3	2.7	5.78		
$[Mn^{IV}(O)(2pyN2B)]^{2+}$	1	1.70	7.34	4	2.00	14.1	3	2.68	4.77	-4.35	0.362
				1	2.21	1.52	6	2.91	15.5		
$[Mn^{IV}(O)(2pyN2Q)]^{2+}$	1	1.75	6.39	4	2.07	7.59	5	2.9	5.18	-1.58	0.271
				1	2.27	5.18	3	2.69	8.84		

[a] Fourier Transform ranges are as follows: $[Mn^{IV}(O)(^{DMM}N4py)]^{2+}$: 2-14 $Å^{-1}$, $[Mn^{IV}(O)(2pyN2B)]^{2+}$: 2-13 $Å^{-1}$, $[Mn^{IV}(O)(2pyN2Q)]^{2+}$: 2-14 $Å^{-1}$. [b] σ^2 is in units of 10^3 $Å^2$.

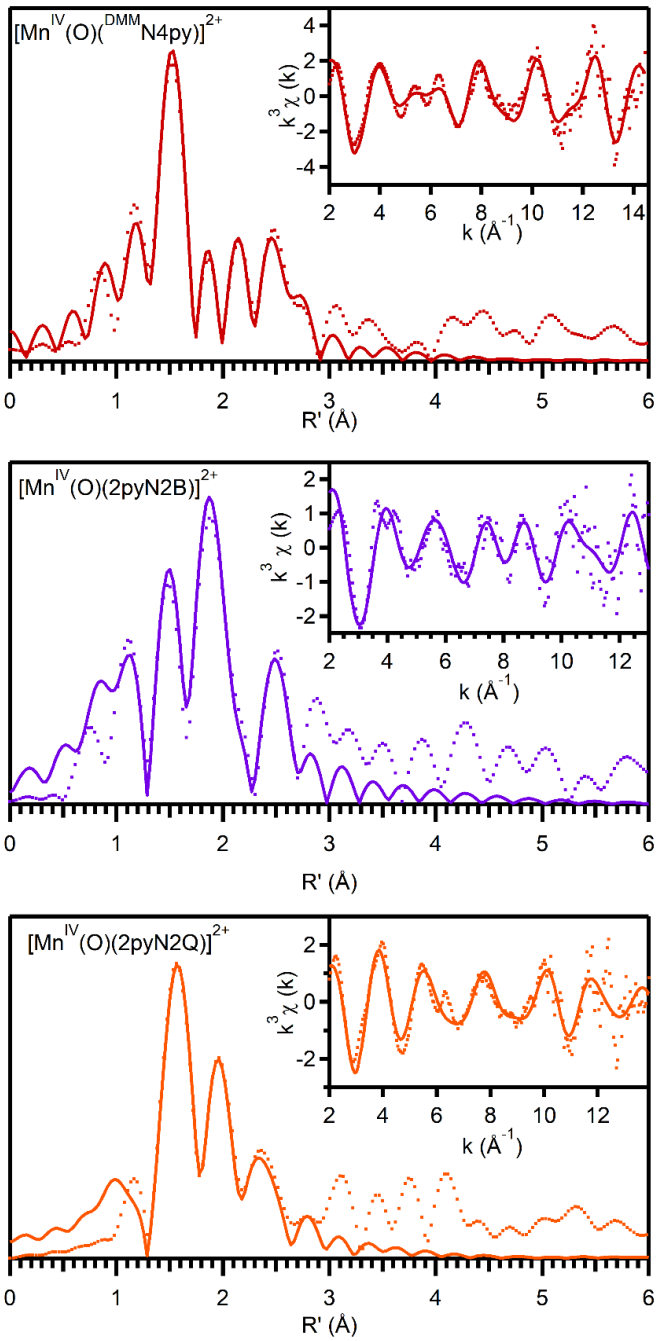

Figure 4.11. Fourier transforms of Mn K-edge EXAFS data and raw k^3 weighted EXAFS curves (insets) for the oxomanganese(IV) species. Experimental data is represented by dotted lines whereas fits are solid lines.

The Mn-O scatterer distances for $[Mn^{IV}(O)(^{DMM}N4py)]^{2+}$ and $[Mn^{IV}(O)(2pyN2B)]^{2+}$, which 1.71 and 1.70 Å, respectively, are in excellent agreement with Mn-O distances previously reported from EXAFS analysis of Mn^{IV}-oxo complexes in a pseudo-octahedral

environment.[17-19, 21, 23] The O shell for $[Mn^{IV}(O)(2pyN2B)]^{2+}$ displays a relatively large Debye-Waller (σ^2) parameter for a scatterer at this short distance (Table 4.6). The presence of multi-nuclear Mn species in this sample, as indicated by the EPR data and Mn K-edge value (*vide supra*) could account for this larger than expected σ^2 value. Similarly, sample heterogeneity could also account for the Mn-O distance for the $[Mn^{IV}(O)(2pyN2Q)]^{2+}$ complex (1.75 Å), which is longer than expected for a Mn^{IV}-oxo adduct.

For $[Mn^{IV}(O)(^{DMM}N4py)]^{2+}$, $[Mn^{IV}(O)(2pyN2B)]^{2+}$ and $[Mn^{IV}(O)(2pyN2Q)]^{2+}$, the Mn-$N_{eq}$ bond distances determined by EXAFS can be compared to DFT optimized structures (Table 4.7). Before making these comparisons, it is important to note that the structural distortions observed for the manganese(II) DFT structure were not observed for any of the DFT structures of $[Mn^{IV}(O)(^{DMM}N4py)]^{2+}$, $[Mn^{IV}(O)(2pyN2B)]^{2+}$ and $[Mn^{IV}(O)(2pyN2Q)]^{2+}$. For $[Mn^{IV}(O)(^{DMM}N4py)]^{2+}$, the EXAFS Mn-$N_{eq}$ bond distances are within 0.01 Å of the DFT calculated bond distances. The EXAFS of $[Mn^{IV}(O)(2pyN2Q)]^{2+}$ on the other hand, shows an elongation of the Mn-N_{eq} bonds of 0.04 Å, which is once again likely a result of some inhomogeneity of the sample or photoreduction. Unexpectedly, the EXAFS Mn-N_{eq} bond distance for $[Mn^{IV}(O)(2pyN2B)]^{2+}$ is much shorter than DFT calculates (2.00 Å versus 2.05 Å). This may be a result of the very elongated Mn-N_{ax} bond that is calculated for $[Mn^{IV}(O)(2pyN2B)]^{2+}$.

The metric parameters from analysis of EXAFS data for $[Mn^{IV}(O)(^{DMM}N4py)]^{2+}$, $[Mn^{IV}(O)(2pyN2B)]^{2+}$ and $[Mn^{IV}(O)(2pyN2Q)]^{2+}$ can be further compared to those obtained for DFT-optimized structures (Table 4.7). Before making these comparisons, it is important to note that the structural distortions, presumably caused by an over-correction for dispersion interactions, observed for the DFT-optimized structures of the manganese(II) were not observed for any of the DFT structures of the Mn^{IV}-oxo complexes.

Table 4.7. Comparison of DFT and EXAFS determined bond distances (Å) for manganese(IV) complexes.

complex		DFT	DFT (H-bonding)	EXAFS
$[Mn^{IV}(O)(^{DMM}N4py)]^{2+}$	Mn-O (1)	1.66	1.70	1.71
	Mn-N (4)	2.00	2.00	1.99
	Mn-N (1)	2.09	2.07	2.16
$[Mn^{IV}(O)(2pyN2B)]^{2+}$	Mn-O (1)	1.66	1.68	1.70
	Mn-N (4)	2.05	2.00	2.00
	Mn-N (1)	2.03	2.16	2.21
$[Mn^{II}(OH_2)(2pyN2Q)]^{2+}$	Mn-O (1)	1.68	1.70	1.75
	Mn-N (4)	2.03	2.03	2.07
	Mn-N (1)	2.09	2.07	2.27

4.3.3 Comparison of DFT and EXAFS Structures of Oxomanganese(IV) Species

We had previously reported DFT-derived structures for the $[Mn^{IV}(O)(N4py)]^{2+}$, $[Mn^{IV}(O)(^{DMM}N4py)]^{2+}$, and $[Mn^{IV}(O)(2pyN2Q)]^{2+}$ complexes.[13, 17] The DFT-predicted Mn-oxo distances for these structures are near 1.66 to 1.68 Å, ca. 0.04-0.07 Å shorter than those determined by analysis of EXAFS data. This discrepancy between experimental and computed distances could suggest some degree of photoreduction of the oxomanganese(IV) complexes during data collection and/or sample heterogeneity. Alternatively, hydrogen-bonding interactions between the oxomanganese(IV) complexes and TFE solvent molecules could also account for the longer oxomanganese(IV) distances observed experimentally. To evaluate this latter possibility, we performed DFT geometry optimizations for models of $[Mn^{IV}(O)(N4py)]^{2+}$, $[Mn^{IV}(O)(^{DMM}N4py)]^{2+}$, $[Mn^{IV}(O)(2pyN2Q)]^{2+}$, and $[Mn^{IV}(O)(2pyN2B)]^{2+}$ that included two TFE molecules. These structures are referred to as $[Mn^{IV}(O)(N4py)]^{2+}\cdot(TFE)_2$, $[Mn^{IV}(O)(^{DMM}N4py)]^{2+}\cdot(TFE)_2$, $[Mn^{IV}(O)(2pyN2Q)]^{2+}\cdot(TFE)_2$, and $[Mn^{IV}(O)(2pyN2B)]^{2+}\cdot(TFE)_2$. These optimizations employed the meta-GGA TPSS functional,[51] with dispersion corrections.[52-53] (Importantly, the structural distortions, presumably caused by an over-correction for dispersion interactions, observed for the DFT-optimized structures of the manganese(II) were not observed for any of the DFT structures of the Mn^{IV}-oxo complexes.) To provide a balanced comparison, we also re-optimized the structures of the oxomanganese(IV)

complexes in the absence of added TFE using the same level of theory. (Previous optimization of $[Mn^{IV}(O)(N4py)]^{2+}$ employed the BP functional, and all previous optimizations lacked treatment of dispersion effects.) The results are summarized in Table 4.8, and molecular structures of the complexes with hydrogen-bonded TFE molecules are shown in Figure 4.12.

Table 4.8 Selected Bond Lengths (Å), Bond Angles (°), and Hydrogen-Bonding Distances (Å) for Oxomanganese(IV) Complexes $[Mn^{IV}(O)(N4py)]^{2+}$, $[Mn^{IV}(O)(^{DMM}N4py)]^{2+}$, and $[Mn^{IV}(O)(2pyN2Q)]^{2+}$ from DFT Computations.

	Mn–O	Mn–N_{eq}[a]	Mn–N_{ax}[b]	O–Mn–N_{ax}	O···H[c]
$[Mn^{IV}(O)(N4py)]^{2+}$	1.681	2.000	2.097	179.65	NA[d]
$[Mn^{IV}(O)(^{DMM}N4py)]^{2+}$	1.682	1.997	2.089	179.28	NA[d]
$[Mn^{IV}(O)(2pyN2Q)]^{2+}$	1.684	2.032	2.088	170.14	NA[d]
$[Mn^{IV}(O)(2pyN2B)]^{2+}$	1.661	2.054	2.335	176.03	NA[d]
$[Mn^{IV}(O)(N4py)]^{2+}\cdot(TFE)_2$	1.699	2.000	2.077	178.27	1.641, 1.651
$[Mn^{IV}(O)(^{DMM}N4py)]^{2+}\cdot(TFE)_2$	1.702	1.996	2.069	177.97	1.622, 1.653
$[Mn^{IV}(O)(2pyN2Q)]^{2+}\cdot(TFE)_2$	1.703	2.030	2.070	170.44	1.678, 1.703
$[Mn^{IV}(O)(2pyN2B)]^{2+}\cdot(TFE)_2$	1.680	1.999	2.155	178.24	1.739, 1.749

[a] The average of the four equatorial Mn–N bond lengths. [b] N_{ax} refers to the axial nitrogen donor *trans* to the oxo ligand. [c] Distances between the oxo ligand the alcohol hydrogen atoms of the TFE ligands. [d] Not applicable.

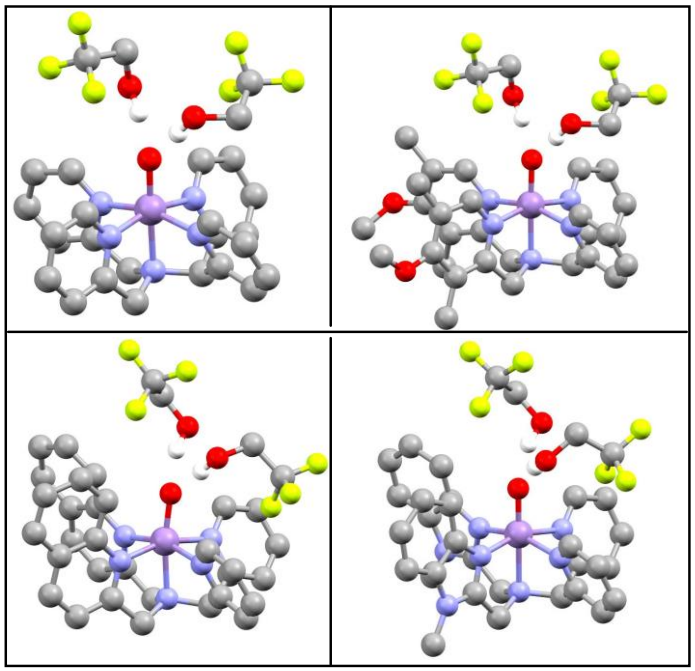

Figure 4.12. Molecular structures of Mn^{IV}-oxo complexes, $[Mn^{IV}(O)(N4py)]^{2+}\cdot(TFE)_2$ (top-left), $[Mn^{IV}(O)(^{DMM}N4py)]^{2+}\cdot(TFE)_2$ (top-right), $[Mn^{IV}(O)(2pyN2Q)]^{2+}\cdot(TFE)_2$ (bottom-left), and $[Mn^{IV}(O)(2pyN2B)]^{2+}\cdot(TFE)_2$ (bottom-right).

The structures of the Mn^{IV}-oxo complexes lacking the explicit TFE molecules are essentially identical to those previously reported. In each case, the Mn=O distance is near 1.68 Å, and the Mn–N_{eq} distances (which were obtained by averaging the equatorial Mn–N bond lengths), steadily increase from $[Mn^{IV}(O)(^{DMM}N4py)]^{2+}$ to $[Mn^{IV}(O)(N4py)]^{2+}$ to $[Mn^{IV}(O)(2pyN2Q)]^{2+}$ (Table 4.8). In addition, the oxo ligand in $[Mn^{IV}(O)(2pyN2Q)]^{2+}$ is shifted away from the quinoline groups, giving a O–Mn–N_{ax} angle of 170 °.

The optimized structures of the $[Mn^{IV}(O)(N4py)]^{2+}\cdot(TFE)_2$, $[Mn^{IV}(O)(^{DMM}N4py)]^{2+}\cdot(TFE)_2$, $[Mn^{IV}(O)(2pyN2Q)]^{2+}\cdot(TFE)_2$, and $[Mn^{IV}(O)(2pyN2B)]^{2+}\cdot(TFE)_2$ complexes each show two TFE groups with strong hydrogen-bonding interactions with the oxo ligand (Figure 4.12). The distances between the oxo ligand the alcohol hydrogen atom of the TFE molecules varies from 1.622 – 1.749 Å. The longer oxo···$HOCH_2CF_3$ distances come from the $[Mn^{IV}(O)(2pyN2Q)]^{2+}\cdot(TFE)_2$ and $[Mn^{IV}(O)(2pyN2B)]^{2+}\cdot(TFE)_2$ structures (Table 4.8). Presumably, the steric bulk of the quinoline and benzimidazole groups prevent the TFE molecules from forming shorter hydrogen bonds with the oxo ligand.

We will comment in more detail here on the DFT-optimized structure of $[Mn^{IV}(O)(2pyN2B)]^{2+}$, as this species has not been previously described. The $[Mn^{IV}(O)(2pyN2B)]^{2+}$ complex has the shortest Mn=O bond lengths of the series, irrespective of whether or not H-bonding is included, at 1.661 and 1.680 Å, for the complexes with and without explicit TFE molecules, respectively. The complex lacking H-bonding, the Mn–N_{eq} distances are the longest of the series, while the distances for $[Mn^{IV}(O)(2pyN2B)]^{2+}\cdot(TFE)_2$ are in between those observed for $[Mn^{IV}(O)(^{DMM}N4py)]^{2+}\cdot(TFE)_2$ and $[Mn^{IV}(O)(N4py)]^{2+}\cdot(TFE)_2$. This elongation reflects longer Mn–N_{py} distances, which are 2.138 and 2.140 Å. The EXAFS Mn-N_{eq} distance of 2.00 Å is in excellent agreement with that calculated for $[Mn^{IV}(O)(2pyN2B)]^{2+}\cdot(TFE)_2$. We also note that the 2pyN2B ligand provides significantly less steric crowding of the oxo compared to the 2pyN2Q ligand. In the $[Mn^{IV}(O)(2pyN2Q)]^{2+}\cdot(TFE)_2$ structure, the closest C–H functions from the quinoline moieties have H···oxo distances of 2.046 Å, whereas the corresponding distances for the closest C–H functions from the benzamidazole

moieties of $[Mn^{IV}(O)(2pyN2B)]^{2+}\cdot(TFE)_2$ are 2.539 Å. In addition, the O–Mn–N_{ax} angle in $[Mn^{IV}(O)(2pyN2B)]^{2+}\cdot(TFE)_2$ is 178 °, which is less distorted than in $[Mn^{IV}(O)(2pyN2Q)]^{2+}\cdot(TFE)_2$.

For each oxomanganese(IV) complex, the strong oxo···$HOCH_2CF_3$ interaction causes an elongation in the Mn=O distance of ca. 0.02 Å (Table 4.8). For $[Mn^{IV}(O)(N4py)]^{2+}\cdot(TFE)_2$ and $[Mn^{IV}(O)(^{DMM}N4py)]^{2+}\cdot(TFE)_2$ this leads to DFT-derived Mn=O bond lengths nearly identical to those determined from fitting EXAFS data[17] (Table 4.8). The DFT-computed Mn=O distance for $[Mn^{IV}(O)(2pyN2B)]^{2+}\cdot(TFE)_2$ is also in acceptable agreement with that observed by EXAFS (1.68 versus 1.70 Å, respectively). Therefore, we propose that the relatively long Mn=O distances determined in our EXAFS fits derive from hydrogen-bonding interactions between solvent and the oxo ligands. While it would be helpful to test this prediction by collecting EXAFS data for these oxomanganese(IV) species in an aprotic solvent, to date, we have been unable to form these complexes in high yields in solvents other than TFE. In contrast, the DFT models of $[Mn^{IV}(O)(2pyN2Q)]^{2+}\cdot(TFE)_2$ shows a Mn=O distance notable shorter than that observed from EXAFS (1.70 versus 1.75 Å, respectively). This results provides further support for our proposal that the longer Mn=O distance of $[Mn^{IV}(O)(2pyN2Q)]^{2+}$ derives from sample heterogeneity and is not evidence of an intrinsically long Mn=O bond.

4.5 Conclusions

The preparation and preliminary reactivity of a novel oxomanganese(IV) species, $[Mn^{IV}(O)(2pyN2B)]^{2+}$, have shown that replacing two pyridines of the N4py ligand framework with benzamidazole groups causes a stronger Mn-N_{eq} bond and decreases reactivity towards C-H bonds. Additionally the structural information of a series of oxomanganese(IV) species supported by modified versions of N4py have been reported for the first time. The Mn-N_{eq} bond distances determined from the analysis of EXAFS data agree well with the expected strength of the equatorial ligand field. Additionally, DFT calculated hydrogen bonding adducts between trifluoroethanol solvent molecules and the Mn=O bond provide excellent agreement between DFT-calculated Mn=O bond distances and those observed by EXAFS in trifluorethanol solution.

4.6 Notes and References

1. Rittle, J.; Green, M. T., Cytochrome P450 Compound I: Capture, Characterization, and C-H Bond Activation Kinetics. *Science* **2010,** *330* (6006), 933-937.

2. Huang, X.; Groves, J. T., Oxygen Activation and Radical Transformations in Heme Proteins and Metalloporphyrins. *Chem. Rev.* **2017**.

3. Wong, S. D.; Srnec, M.; Matthews, M. L.; Liu, L. V.; Kwak, Y.; Park, K.; Bell Iii, C. B.; Alp, E. E.; Zhao, J.; Yoda, Y.; Kitao, S.; Seto, M.; Krebs, C.; Bollinger, J. M.; Solomon, E. I., Elucidation of the Fe(iv)=O intermediate in the catalytic cycle of the halogenase SyrB2. *Nature* **2013,** *499*, 320.

4. Srnec, M.; Wong, S. D.; Matthews, M. L.; Krebs, C.; Bollinger, J. M.; Solomon, E. I., Electronic Structure of the Ferryl Intermediate in the α-Ketoglutarate Dependent Non-Heme Iron Halogenase SyrB2: Contributions to H Atom Abstraction Reactivity. *J. Am. Chem. Soc* **2016,** *138* (15), 5110-5122.

5. Price, J. C.; Barr, E. W.; Glass, T. E.; Krebs, C.; Bollinger, J. M., Evidence for Hydrogen Abstraction from C1 of Taurine by the High-Spin Fe(IV) Intermediate Detected during Oxygen Activation by Taurine:α-Ketoglutarate Dioxygenase (TauD). *J. Am. Chem. Soc* **2003,** *125* (43), 13008-13009.

6. Puri, M.; Que, L., Toward the Synthesis of More Reactive S = 2 Non-Heme Oxoiron(IV) Complexes. *Acc. Chem. Rev.* **2015,** *48* (8), 2443-2452.

7. Nam, W., Synthetic Mononuclear Nonheme Iron–Oxygen Intermediates. *Acc. Chem. Res.* **2015,** *48* (8), 2415-2423.

8. Rohde, J.-U.; In, J.-H.; Lim, M. H.; Brennessel, W. W.; Bukowski, M. R.; Stubna, A.; Münck, E.; Nam, W.; Que, L., Crystallographic and Spectroscopic Characterization of a Nonheme Fe(IV)=O Complex. *Science* **2003,** *299* (5609), 1037-1039.

9. Rice, D. B.; Massie, A. A.; Jackson, T. A., Manganese–Oxygen Intermediates in O–O Bond Activation and Hydrogen-Atom Transfer Reactions. *Acc. Chem. Res.* **2017,** *50* (11), 2706-2717.

10. Yin, G.; Danby, A. M.; Kitko, D.; Carter, J. D.; Scheper, W. M.; Busch, D. H., Understanding the Selectivity of a Moderate Oxidation Catalyst: Hydrogen Abstraction by a Fully Characterized, Activated Catalyst, the Robust Dihydroxo Manganese(IV) Complex of a Bridged Cyclam. *J. Am. Chem. Soc* **2007,** *129* (6), 1512-1513.

11. Parsell, T. H.; Behan, R. K.; Green, M. T.; Hendrich, M. P.; Borovik, A. S., Preparation and Properties of a Monomeric MnIV-Oxo Complex. *J. Am. Chem. Soc* **2006,** *128* (27), 8728-8729.

12. Parsell, T. H.; Yang, M.-Y.; Borovik, A. S., C−H Bond Cleavage with Reductants: Re-Investigating the Reactivity of Monomeric MnIII/IV−Oxo Complexes and the Role of Oxo Ligand Basicity. *J. Am. Chem. Soc* **2009,** *131* (8), 2762-2763.

13. Massie, A. A.; Denler, M. C.; Cardoso, L. T.; Walker, A. N.; Hossain, M. K.; Day, V. W.; Nordlander, E.; Jackson, T. A., Equatorial Ligand Perturbations Influence the Reactivity of Manganese(IV)-Oxo Complexes. *Angew. Chem., Int. Ed. Engl.* **2017,** *56* (15), 4178-4182.

14. Sawant, S. C.; Wu, X.; Cho, J.; Cho, K.-B.; Kim, S. H.; Seo, M. S.; Lee, Y.-M.; Kubo, M.; Ogura, T.; Shaik, S.; Nam, W., Water as an Oxygen Source: Synthesis, Characterization, and Reactivity Studies of a Mononuclear Nonheme Manganese(IV) Oxo Complex. *Angew. Chem., Int. Ed. Engl.* **2010,** *49* (44), 8190-8194.

15. Garcia-Bosch, I.; Company, A.; Cady, C. W.; Styring, S.; Browne, W. R.; Ribas, X.; Costas, M., Evidence for a Precursor Complex in C□H Hydrogen Atom Transfer Reactions Mediated by a Manganese(IV) Oxo Complex. *Angew. Chem., Int. Ed. Engl.* **2011,** *123* (25), 5766-5771.

16. Yoon, H.; Lee, Y.-M.; Wu, X.; Cho, K.-B.; Sarangi, R.; Nam, W.; Fukuzumi, S., Enhanced Electron-Transfer Reactivity of Nonheme Manganese(IV)–Oxo Complexes by Binding Scandium Ions. *J. Am. Chem. Soc* **2013,** *135* (24), 9186-9194.

17. Leto, D. F.; Ingram, R.; Day, V. W.; Jackson, T. A., Spectroscopic properties and reactivity of a mononuclear oxomanganese(iv) complex. *Chem. Commun.* **2013,** *49* (47), 5378-5380.

18. Wu, X.; Seo, M. S.; Davis, K. M.; Lee, Y.-M.; Chen, J.; Cho, K.-B.; Pushkar, Y. N.; Nam, W., A Highly Reactive Mononuclear Non-Heme Manganese(IV)–Oxo Complex That Can Activate the Strong C–H Bonds of Alkanes. *J. Am. Chem. Soc* **2011,** *133* (50), 20088-20091.

19. Chen, J.; Lee, Y.-M.; Davis, K. M.; Wu, X.; Seo, M. S.; Cho, K.-B.; Yoon, H.; Park, Y. J.; Fukuzumi, S.; Pushkar, Y. N.; Nam, W., A Mononuclear Non-Heme Manganese(IV)–Oxo Complex Binding Redox-Inactive Metal Ions. *J. Am. Chem. Soc* **2013,** *135* (17), 6388-6391.

20. Kurahashi, T.; Kikuchi, A.; Tosha, T.; Shiro, Y.; Kitagawa, T.; Fujii, H., Transient Intermediates from Mn(salen) with Sterically Hindered Mesityl Groups: Interconversion

between MnIV-Phenolate and MnIII-Phenoxyl Radicals as an Origin for Unique Reactivity. *Inorg. Chem.* **2008,** *47* (5), 1674-1686.

21. Leto, D. F.; Jackson, T. A., Mn K-Edge X-ray Absorption Studies of Oxo- and Hydroxomanganese(IV) Complexes: Experimental and Theoretical Insights into Pre-Edge Properties. *Inorg. Chem.* **2014,** *53*, 6179-6194.

22. Leto, D. F.; Massie, A. A.; Rice, D. B.; Jackson, T. A., Spectroscopic and Computational Investigations of a Mononuclear Manganese(IV)-Oxo Complex Reveal Electronic Structure Contributions to Reactivity. *J. Am. Chem. Soc* **2016,** *138* (47), 15413-15424.

23. Brink, C. P.; Crumbliss, A. L., Kinetics, Mechanism, and Thermodynamics of Aqueous Iron(III) Chelation and Dissociation: Influence of Carbon and Nitrogen Substituents in Hydroxamic Acid Ligands. *Inorg. Chem.* **1984,** *23* (26), 4708-4718.

24. Pecoraro, V. L.; Hsieh, W.-Y., In Search of Elusive High-Valent Manganese Species That Evaluate Mechanisms of Photosynthetic Water Oxidation. *Inorg. Chem.* **2008,** *47* (6), 1765-1778.

25. McEvoy, J. P.; Brudvig, G. W., Water-Splitting Chemistry of Photosystem II. *Chem. Rev.* **2006,** *106* (11), 4455-4483.

26. Glöckner, C.; Kern, J.; Broser, M.; Zouni, A.; Yachandra, V.; Yano, J., Structural Changes of the Oxygen-evolving Complex in Photosystem II during the Catalytic Cycle. *Journal of Biological Chemistry* **2013,** *288* (31), 22607-22620.

27. Yano, J.; Yachandra, V., Mn4Ca Cluster in Photosynthesis: Where and How Water is Oxidized to Dioxygen. *Chem. Rev.* **2014,** *114* (8), 4175-4205.

28. Frank, P.; Benfatto, M.; Qayyam, M.; Hedman, B.; Hodgson, K. O., A high-resolution XAS study of aqueous Cu(II) in liquid and frozen solutions: Pyramidal, polymorphic, and non-centrosymmetric. *The Journal of Chemical Physics* **2015,** *142* (8), 084310.

29. Kau, L. S.; Spira-Solomon, D. J.; Penner-Hahn, J. E.; Hodgson, K. O.; Solomon, E. I., X-ray absorption edge determination of the oxidation state and coordination number of copper. Application to the type 3 site in Rhus vernicifera laccase and its reaction with oxygen. *Journal of the American Chemical Society* **1987,** *109* (21), 6433-6442.

30. Westre, T. E.; Kennepohl, P.; DeWitt, J. G.; Hedman, B.; Hodgson, K. O.; Solomon, E. I., A Multiplet Analysis of Fe K-Edge 1s → 3d Pre-Edge Features of Iron Complexes. *Journal of the American Chemical Society* **1997,** *119* (27), 6297-6314.

31. DeBeer George, S.; Petrenko, T.; Neese, F., Prediction of Iron K-Edge Absorption Spectra Using Time-Dependent Density Functional Theory†. *Journal of Physical Chemistry A* **2008,** *112* (50), 12936-12943.

32. DeBeer George, S.; Brant, P.; Solomon, E. I., Metal and Ligand K-Edge XAS of Organotitanium Complexes: Metal 4p and 3d Contributions to Pre-edge Intensity and Their Contributions to Bonding. *J. Am. Chem. Soc* **2005,** *127*, 667-674.

33. England, J.; Martinho, M.; Farquhar, E. R.; Frisch, J. R.; Bominaar, E. L.; Münck, E.; Que, L., A Synthetic High-Spin Oxoiron(IV) Complex: Generation, Spectroscopic Characterization, and Reactivity. *Angewandte Chemie International Edition* **2009,** *48* (20), 3622-3626.

34. Jackson, T. A.; Rohde, J.-U.; Seo, M. S.; Sastri, C. V.; DeHont, R.; Ohta, T.; Stubna, A.; Kitagawa, T.; Münck, E.; Nam, W.; Que, L., Jr., Axial Ligand Effects on the Geometric and Electronic Structures of Nonheme Oxoiron(IV) Complexes. *J. Am. Chem. Soc* **2008,** *130* (37), 12394-12407.

35. Rohde, J.-U.; Torelli, S.; Shan, X.; Lim, M. H.; Klinker, E. J.; Kaizer, J.; Chen, K.; Nam, W.; Que, L., Jr., Structural Insights into Nonheme Alkylperoxoiron(III) and Oxoiron(IV) Intermediates by X-ray Absorption Spectroscopy. *J. Am. Chem. Soc* **2004,** *126* (51), 16750-16761.

36. Krewald, V.; Lassalle-Kaiser, B.; Boron, T. T.; Pollock, C. J.; Kern, J.; Beckwith, M. A.; Yachandra, V. K.; Pecoraro, V. L.; Yano, J.; Neese, F.; DeBeer, S., The Protonation States of Oxo-Bridged MnIV Dimers Resolved by Experimental and Computational Mn K Pre-Edge X-ray Absorption Spectroscopy. *Inorg. Chem.* **2013,** *52* (22), 12904-12914.

37. Rees, J. A.; Martin-Diaconescu, V.; Kovacs, J. A.; DeBeer, S., X-ray Absorption and Emission Study of Dioxygen Activation by a Small-Molecule Manganese Complex. *Inorg. Chem.* **2015,** *54* (13), 6410-6422.

38. Roemelt, M.; Beckwith, M. A.; Duboc, C.; Collomb, M.-N.; Neese, F.; DeBeer, S., Manganese K-Edge X-Ray Absorption Spectroscopy as a Probe of the Metal–Ligand Interactions in Coordination Compounds. *Inorg. Chem.* **2011,** *51* (1), 680-687.

39. Yano, J.; Kern, J.; Irrgang, K.-D.; Latimer, M. J.; Bergmann, U.; Glatzel, P.; Pushkar, Y.; Biesiadka, J.; Loll, B.; Sauer, K.; Messinger, J.; Zouni, A.; Yachandra, V. K., X-ray damage to the Mn4Ca complex in single crystals of photosystem II: A case study for metalloprotein crystallography. *Proceedings of the National Academy of Sciences of the United States of America* **2005,** *102* (34), 12047-12052.

40. Mitra, M.; Nimir, H.; Demeshko, S.; Bhat, S. S.; Malinkin, S. O.; Haukka, M.; Lloret-Fillol, J.; Lisensky, G. C.; Meyer, F.; Shteinman, A. A.; Browne, W. R.; Hrovat, D. A.;

Richmond, M. G.; Costas, M.; Nordlander, E., Nonheme Fe(IV) Oxo Complexes of Two New Pentadentate Ligands and Their Hydrogen-Atom and Oxygen-Atom Transfer Reactions. *Inorg. Chem.* **2015,** *54* (15), 7152-7164.

41. Seo, M. S.; Kim, J. Y.; Annaraj, J.; Kim, Y.; Lee, Y.-M.; Kim, S.-J.; Kim, J.; Nam, W., $[Mn(tmc)(O_2)]^+$: A Side-On Peroxide Manganese(III) Complex Bearing a Non-heme Ligand. *Angewandte Chemie International Edition* **2007,** *46*, 377-380.

42. Armarego, W. L. F.; Perrin, D. D., *Purification of Laboratory Chemicals*. Butterworth-Heinemann: Oxford, U.K., 1997.

43. Saltzman, H.; Sharefkin, J. G., Iodosobenzene. *Organic Syntheses* **1963,** *43*, 60.

44. *Data Collection: SMART Software in APEX2 v2014.11-0 Suite*. Bruker-AXS. 5465 E. Cheryl Parkway, Madison, WI 53711-5373 USA, 1998.

45. *Data Reduction: SAINT Software in APEX2 v2014.11-0 Suite*. Bruker-AXS, 5465 E. Cheryl Parkway, Madison, WI 53711-5373 USA.

46. *Refinement: SHELXTL Software in APEX2 v2014.11-0 Suite*. Bruker-AXS, 5465 E. Cheryl Parkway, Madison, WI 53711-5373 USA.

47. Ravel, B.; Newville, M., ATHENA, ARTEMIS, HEPHAESTUS: data analysis for X-ray absorption spectroscopy using IFEFFIT. *Journal of Synchrotron Radiation* **2005,** *12* (4), 537-541.

48. Rehr, J. J.; Mustre de Leon, J.; Zabinsky, S. I.; Albers, R. C., Theoretical x-ray absorption fine structure standards. *Journal of the American Chemical Society* **1991,** *113* (14), 5135-5140.

49. Wojdyr, M., Fityk: a general-purpose peak fitting program. *Journal of Applied Crystallography* **2010,** *43* (5 Part 1), 1126-1128.

50. Neese, F., The ORCA program system. *Wiley Interdisciplinary Reviews: Computational Molecular Science* **2012,** *2* (1), 73-78.

51. Tao, J.; Perdew, J. P.; Staroverov, V. N.; Scuseria, G. E., Climbing the Density Functional Ladder: Nonempirical Meta\char21{}Generalized Gradient Approximation Designed for Molecules and Solids. *Phys. Rev. Lett.* **2003,** *91* (14), 146401.

52. Grimme, S.; Antony, J.; Ehrlich, S.; Krieg, H., A consistent and accurate ab initio parametrization of density functional dispersion correction (DFT-D) for the 94 elements H-Pu. *J. Chem. Phys.* **2010,** *132* (15), 154104.

53. Grimme, S.; Ehrlich, S.; Goerigk, L., Effect of the damping function in dispersion corrected density functional theory. *Journal of Computational Chemistry* **2011,** *32* (7), 1456-1465.

54. Schäfer, A.; Horn, H.; Ahlrichs, R., Fully optimized contracted Gaussian basis sets for atoms Li to Kr. *J. Chem. Phys.* **1992,** *97* (4), 2571-2577.

55. Schäfer, A.; Huber, C.; Ahlrichs, R., Fully Optimized Contracted Gaussian Basis Sets of Triple Zeta Valence Quality for Atoms Li to Kr. *J. Chem. Phys.* **1994,** *100*, 5829-5835.

56. Weigend, F.; Ahlrichs, R., Balanced basis sets of split valence, triple zeta valence and quadruple zeta valence quality for H to Rn: Design and assessment of accuracy. *Phys. Chem. Chem. Phys.* **2005,** *7* (18), 3297-3305.

57. Marenich, A. V.; Cramer, C. J.; Truhlar, D. G., Universal Solvation Model Based on Solute Electron Density and on a Continuum Model of the Solvent Defined by the Bulk Dielectric Constant and Atomic Surface Tensions. *The Journal of Physical Chemistry B* **2009,** *113* (18), 6378-6396.

58. Lubben, M.; Meetsma, A.; Wilkinson, E. C.; Feringa, B.; Que Jr., L., Nonheme Iron Centers in Oxygen Activation: Characterization of an Iron(III) Hydroperoxide Intermediate. *Angew. Chem., Int. Ed. Engl.* **1995,** *34* (13-14), 1512-1514.

59. Rana, S.; Dey, A.; Maiti, D., Mechanistic elucidation of C-H oxidation by electron rich non-heme iron(iv)-oxo at room temperature. *Chemical Communications* **2015,** *51* (77), 14469-14472.

60. Leto, D. F.; Massie, A. A.; Colmer, H. E.; Jackson, T. A., X-Band Electron Paramagnetic Resonance Comparison of Mononuclear MnIV-oxo and MnIV-hydroxo Complexes and Quantum Chemical Investigation of MnIV Zero-Field Splitting. *Inorg. Chem.* **2016,** *55* (7), 3272-3282.

61. Rice, D. B.; Wijeratne, G. B.; Jackson, T. A., Mn K-edge X-ray absorption studies of mononuclear Mn(III)–hydroxo complexes. *JBIC Journal of Biological Inorganic Chemistry* **2017,** *22* (8), 1281-1293.

Chapter 5. Electrochemical Formation of a Peroxomanganese(III) Species Supported by a Pentadentate Ligand with an Amide trans to the Peroxo

These experiments were performed at the Laboratoire d'Electrochemie Moléculaire during a collaboration with Dr. Elodie Anxolabéhère-Mallart. Manganese complex used in these experiments was provided by Gayan B. Wijeratne and Derek B. Rice.

5.1 Introduction

In nature, many manganese enzymes react with dioxygen and its reduced species ($O_2^{\bullet-}$, H_2O_2, H_2O) for a wide range of biological functions.[1-2] Peroxomanganese(III) species have often been invoked as an important intermediate in many of these processes, bolstered by the structural characterization of a peroxomanganese(III) adduct in a crystal structure of Mn superoxide dismutase (MnSOD) adduct soaked in H_2O_2.[3] Important in the protection against reactive oxygen species, MnSOD catalyzes the disproportionation of superoxide to produce dioxygen and hydrogen peroxide.[4] In MnSOD, it is proposed that acid aids to cleave the Mn-O bond of the peroxomanganese intermediate to give H_2O_2 and a Mn^{III} center.[2] The reactivity of a wide variety of synthetic peroxomanganese(III) complexes has been characterized by many groups. Many mononuclear peroxomanganese(III) species have shown the ability to perform the deformylation of aldehydes.[5-12] However, studies focusing on the factors that influence the cleavage of either the Mn-O or O-O bond remain scarce.[10, 13-19] This rarity is likely due to the difficulties involved in forming peroxomanganese(III) intermediate, often including formation only in low yield, high reactivity of intermediates, or unwanted side products. Further, there are additional challenges to the use of superoxide to form peroxomanganese(III) species. Superoxide is often used in the form of potassium superoxide, which has a limited solubility in many organic solvents and often requires the use of 18-crown-6 ether to go into solution.[18-21] One way to circumvent these problems is to form the peroxomanganese(III) species superoxide generated in situ from electrochemical dioxygen reduction.[15-16]

Previous work from our groups first showed the formation and characterization of three peroxomanganese(III) species using electrochemically generated superoxide.[16] This technique was further used for the formation and characterization of a peroxomanganese(III) species, $[Mn^{III}L(O_2)]$, where L is the deprotonated form of the N_4OH ligand, *N*-(2-hydroxybenzyl)-*N,N'*-bis[2-*N*-methylimidazolyl)methyl]ethane-1,2-diamine) (Scheme 5.1).[15] $[Mn^{III}L(O_2)]$, was prepared by the reaction of the Mn^{II} salt upon the electrochemically generatedsuperoxide in an O_2-saturated DMF solution. Upon the addition of a strong acid, $HClO_4$, formation of $[Mn^{III}L(O_2)]$ resulted in the cleavage of the

Mn-O bond is observed with the release of H_2O_2. However, the addition of a weak acid, H_2O, formation of $[Mn^{III}L(O_2)]$ produced the cleavage of the O-O bond in a concerted dissociative two-electron transfer. From the electrochemical studies, the cleavage of the O-O bond was determined to be a two-electron reduction, which was further supported by a range of theoretical calculations. While $[Mn^{III}L(O_2)]$ offered very interesting insights into the factors that influence O-O versus Mn-O cleavage, the phenolate-containing ligand is redox active, complicating mechanistic studies. Additionally, the Mn-based products of the bond cleavage events, in particular the O-O bond cleavage are very unstable, which prevented their characterization. To offer broader conclusions regarding the factors that influence the Mn-O versus O-O bond cleavage, similar studies to those carried out on $[Mn^{III}L(O_2)]$ need to be performed with a different ligand system.

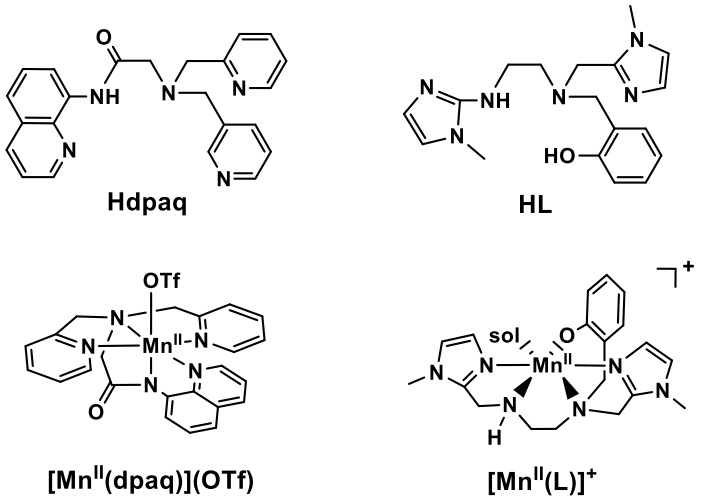

Scheme 5.1. Molecular structures of ligands and Mn^{II} complexes.

$[Mn^{II}(dpaq)](OTf)$ (dpaq =2-[bis(pyridin-2-ylmethyl)]amino-*N*-quinolin-8-yl-acetamidate) (Scheme 5.1) has previously been well characterized and can activate dioxygen to form $[Mn^{III}(OH)(dpaq)]^+$.[22] The anionic ligand, dpaq, which has an amide group *trans* to the open coordination site, which is expected to weaken the manganese-peroxo bond(s), offered a good platform for investigating the factors that influence the cleavage of the O-O versus Mn-O bond. Following the electrocatalytic generation of superoxide in the presence of $[Mn^{II}(dpaq)](OTf)$, we are able to show the formation of a new species that we propose as $[Mn^{III}(O_2)(dpaq)]$. This assignment is further supported mainly by UV-visible spectroscopy and time-dependent density functional theory (TD-

DFT) calculations. Electron paramagnetic resonance (EPR) spectroscopy shows consumption of the [Mn^{II}(dpaq)](OTf), but a lack of a signal suggests either a mononuclear Mn^{III} species or a *S*=0 spin coupled system. The mechanism by which [Mn^{II}(dpaq)](OTf) is able to activate oxygen is not currently well understood. Looking specifically at the reduction of the [$Mn^{III}(O_2)$(dpaq)] is of great interest, as this could provide insight into the reduction of dioxygen by [Mn^{II}(dpaq)](OTf). The other examples of Mn^{II} species that can activate dioxygen involve high-valent manganese intermediates.[10, 23-25] A high valent manganese species was also postulated in the as the O-O bond cleavage product in the reduction of [$Mn^{III}L(O_2)$], but it was unable to be isolated.[15] The information gained from studying the reduction of [$Mn^{III}(O_2)$(dpaq)] provides information about the stability of the formed peroxo species.

5.2 Experimental and Computational Methods

5.2.1 Materials

The free ligand, Hdpaq, and metal complexes [Mn^{II}(dpaq)](OTf) and [Mn^{III}(OH)(dpaq)](OTf) were made as previously described.[22, 26] Anhydrous *N,N'*-dimethylformamide (DMF, >99.8%, stored on molecular sieves), and other chemicals were purchased from commercial vendors and used as received. Air was passed through a $CaCl_2$ column for moisture removal before coming into contact with the reaction solution.

5.2.2 Experimental Methods and Instrumentation

Cyclic Voltammetry. Cyclic voltammetry experiments were performed under either argon atmosphere or dehumidified air. A Metrohm potentiostat (AUTOLAB model) was used to record cyclic voltammograms and to compensate for the ohmic drop. For cyclic voltammetry experiments, the counter electrode was a Pt wire and the working electrode was a glassy carbon disk. The working electrode was carefully polished between each scan with a 1 μm diamond paste, sonicated in an ethanol bath, rinsed with ethanol, and air dried. A saturated calomel electrode (SCE) isolated from the bulk solution by a fritted bridge was the reference electrode.

UV-Vis Spectroelectrochemistry. UV-visible spectroelectrochemical experiments were performed using a 50 mm x 10 mm x 2 mm quartz UV-Vis-NIR cell fused to a glass compartment that could be sealed, allowing for control over the environment. The working electrode was a 30 mm x 7 mm x 0.3 mm Pt mesh grid, covered in Teflon except for the working electrode area to avoid electrolysis outside of the cuvette path length. The reference (AgCl) and counter (Au wire) were both separated from the reaction solution by fritted glass and placed into the top of the cell. The entire solution was saturated with Ar or air (1 mM O_2 in DMF), and the temperature was held constant by the use of a Julabo circulation cryostat. Spectra were recorded on a Varian Cary 5E spectrophotometer.

Bulk Electrolysis Experiments. Bulk electrolysis experiments for UV-visible data and EPR sample preparation were performed in a conventional spectroscopic cuvette (optical length = 10 mm) in a Specord S600 (Analytik Jena) spectrophotometer. The working electrode was a vitreous carbon plate (50 mm x 10 mm x 0.18 mm). The reference (AgCl) and counter electrode (Au wire) were separated by a fritted glass bridge and placed near the top of the cell. This set-up has been described previously.[16] Measurements were performed at 273 K, which was maintained by a Julabo circulation cryostat.

X-Band EPR Collection. EPR samples were taken from the reaction solution of spectroelectrolysis measurements, transferred into a 4 mm quartz EPR tube, and flash frozen in liquid nitrogen. EPR spectra were collected at 5 K on a 9 GHz Bruker EMXPlus spectrometer with an Oxford ESR900 continuous-flow liquid helium cryostat controlled by an Oxford ITC503 temperature system. Parallel and perpendicular mode data were collected in a dual mode Bruker ER4116DM cavity. Recording conditions were 9.639 GHz microwave frequency, 0.1262 mW microwave power, 4 G modulating amplitude, 100 kHz modulation frequency, and 120.6 ms time constant.

5.2.3 Electronic Structure Computations

Need All computations were performed using *ORCA*, version 3.03.[27] DFT geometry optimizations employed the TPSS functional[28] with D3 corrections,[29-30] def2-

TZVP (Mn, O, and N) and def2-SVP (C, F, and H) basis sets,[31-33] an SMD solvation model (for DMF), and a dense integration grid (Grid6 and, for B3LYP calculations, GridX6 in *ORCA*). Additional calculations were performed using the B3LYP functional with the same dispersion correction, basis sets, and solvation model. Tight SCF criteria were invoked using the TightSCF keyword in *ORCA*. The RI approximation, with def2-TZVP/J and def2-SVP/J auxiliary basis sets, were used. Structures were converged to the S = 2 and 3/2 spin state. Frequency calculations for all showed no imaginary frequencies, ensuring that these structure represent true minimum. Total energies were determined using the TPSSh (for TPSS-optimized structures) and B3LYP (for B3LYP-optimized structures) functionals with D3 corrections, def2-TZVPP basis set, an SMD solvation model (for DMF), and a denser integration grid (Grid7 and GridX7 in *ORCA*).

5.3 Results and Analysis

5.3.1 Formation and Characterization of $[Mn^{III}(O_2)(dpaq)]$

A cyclic voltammetry (CV) experiment fan air-saturated *N,N*-dimethylformamide (DMF) solution (1.0 mM O_2) shows a reversible one-electron wave at -0.87 V versus the saturated calomel electrode (SCE), as shown in the black trace of Figure 5.1. This wave can be attributed to the $O_2/O_2^{\bullet-}$ couple. In the presence of 1.0 mM $[Mn^{II}(dpaq)]^+$, the reduction of O_2 is no longer reversible, which can be seen in the red trace of Figure 5.1. The irreversibility of the $O_2/O_2^{\bullet-}$ couple in the presence of $[Mn^{II}(dpaq)]^+$ can be attributed to the $O_2^{\bullet-}$ trapping by the Mn^{II} complex, as previously observed.[15-16] Figure 5.2 shows the $O_2/O_2^{\bullet-}$ couple with 0.1 to 1.1 mM $[Mn^{II}(dpaq)]^+$ in the DMF solution. An increasing concentration $[Mn^{II}(dpaq)]^+$ shows a lower intensity of the $O_2^{\bullet-}$ oxidation as well as the growth of the pre-edge peak, visible before the O_2 reduction wave. With concentrations of $[Mn^{II}(dpaq)]^+$ up to 1.0 mM, there is evidence of superoxide oxidation, but at 1.0 mM $[Mn^{II}(dpaq)]^+$ there is no longer any superoxide oxidation observed. These observations corroborate the proposal that $[Mn^{II}(dpaq)]^+$ is trapping $O_2^{\bullet-}$. These data also appear very similar to those reported for $[Mn^{III}L(O_2)]$, with the only difference being the slightly less pronounced pre-edge peak. The pre-edge peak, along with the loss of reversibility of the $O_2/O_2^{\bullet-}$ couple implies an EC (electrochemical step, chemical step) mechanism. The

electrochemical process is the reduction of O_2 by one electron which is followed by a chemical reaction between $O_2^{\bullet-}$ and $[Mn^{II}(dpaq)]^+$ to form $[Mn^{III}(O_2)(dpaq)]$. Simulations of the data in Figure 5.2 are needed to definitively clarify that the formation of $[Mn^{III}(O_2)(dpaq)]$ follows an EC mechanism.

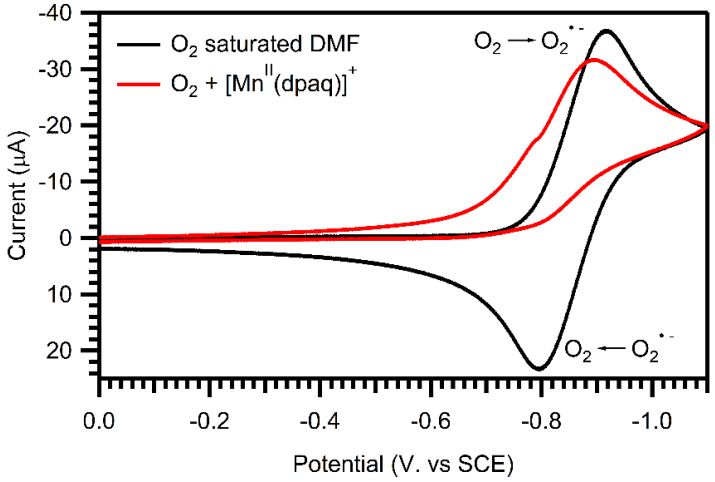

Figure 5.6. CV of 1.0 mM $[Mn^{II}(dpaq)]^+$ and O_2 (1.0 mM, air saturated) in DMF + 0.1 M Bu_4NPF_6 at 0.1 V/s at a glassy carbon disk electrode (T = 293 K) scanning toward cathodic potentials.

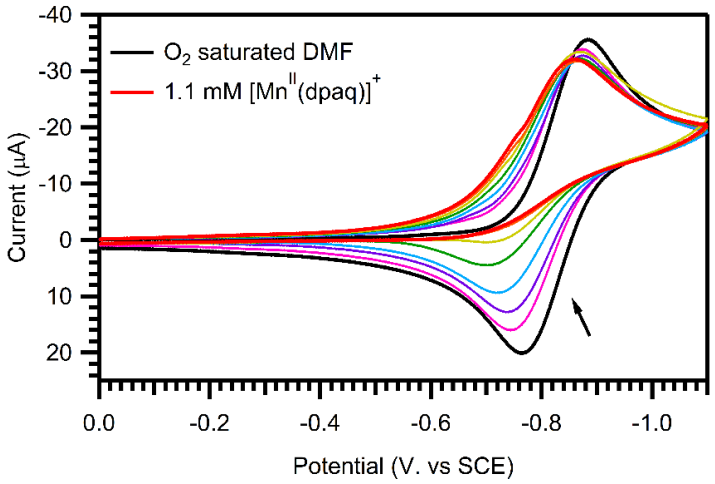

Figure 5.7. CV of $[Mn^{II}(dpaq)]^+$ and O_2 (1.0 mM, air saturated) in DMF + 0.1 M Bu_4NPF_6 at 0.1 V/s at a glassy carbon disk electrode (T = 293 K) scanning toward cathodic potentials. Increasing amounts of the manganese complex were added to show the consumption of the generated superoxide. $[Mn^{II}(dpaq)]^+$ concentrations are as follows: 0.1 mM (pink), 0.2 mM (purple), 0.3 mM (blue), 0.5 mM (green), 0.75 mM (yellow) and 1.0 mM (orange).

To further investigate the species formed upon $O_2^{\bullet-}$ trapping by $[Mn^{II}(dpaq)]^+$, spectroelectrical experiments were performed at -20 °C (Figure 5.3). After taking a blank

with the DMF and 0.2 M Bu_2NPF_6, 2 mL 1.0 mM $[Mn^{II}(dpaq)]^+$ was placed into the cuvette. The spectrum of the Mn^{II} under argon is featureless at wavelengths longer than 450 nm (Figure 5.3, black). The addition of air by bubbling through the solution for 15 minutes, causes no changes in the electronic absorption spectrum of $[Mn^{II}(dpaq)]^+$ (Figure 5.3, blue). Following the addition of air, a potential of -1.0 V (vs. AgCl) was applied to the solution. A new species is apparent from the rise in absorbance from about 700 to 450 nm. However, the resulting absorption spectrum is not well-defined (Figure 5.3, red) and the formation of the new intermediate is quite slow (60 minutes for maximum absorbance increase). This is in stark contrast to the 300 seconds required to form previously reported peroxomanganese(III) species supported by neutral, pentadentate ligands.[16] The low formation made further characterization of the decay products difficult.

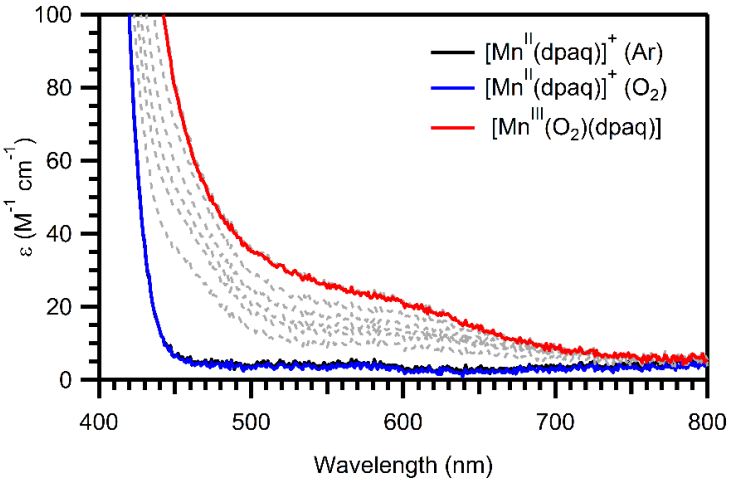

Figure 5.3. Reaction of $[Mn^{II}(dpaq)](OTf)$ (1.0 mM) in air saturated DMF (blue) (+ 0.2M Bu_4NPF_6) while applying a potential of -1.0 V to form the peroxo species (red) at 253 K. Dashed gray traces represent 10 minutes of reaction time.

To further investigate the product of the reaction between $O_2^{\bullet-}$ and $[Mn^{II}(dpaq)]^+$, bulk electrolysis experiments were performed. This method allows for a larger quantity of the product to be formed, allowing for further characterization by other spectroscopic methods. Bulk electrolysis experiments were carried out in a 1 cm pathlength cuvette with a carbon electrode plate, an Ag/Cl working electrode, and a gold counter electrode submersed in the reaction solution that was held at 0 °C for the duration of the experiment. The initial volume of sample in the cell was 2 mL, although aliquots of 0.2 mL were removed to make samples for analysis by electron paramagnetic resonance (EPR)

spectroscopy. After taking a blank with the DMF and 0.2 M Bu_2NPF_6, 2 mL 1.0 mM $[Mn^{II}(dpaq)]^+$ was placed into the cuvette. The featureless spectra of $[Mn^{II}(dpaq)]^+$ under argon, and after 15 minutes of bubbling air through the solution, can be seen in the black and blue traces, respectively, in Figure 5.4. Thus, no changes were noticed upon the addition of 1.0 mM O_2.

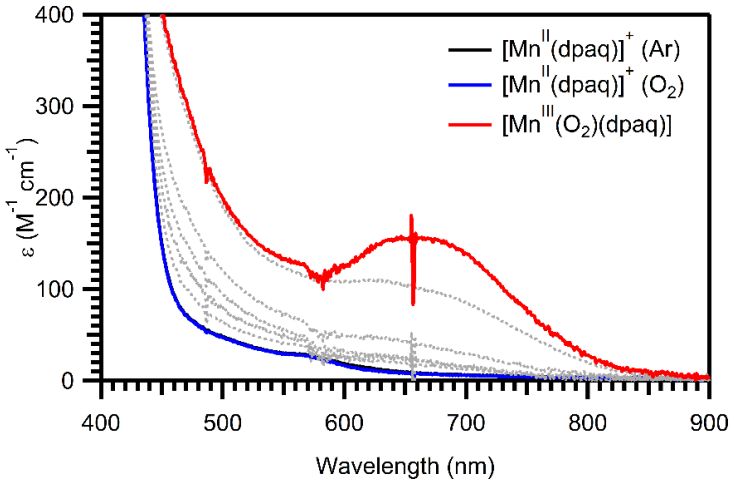

Figure 5.4. Reaction of 1.0 mM $[Mn^{II}(dpaq)]^+$ in air saturated DMF (blue) (1.0 mM O_2) + 0.2 M Bu_2NPF_6 while applying a potential of -1.0 V vs. AgCl at a carbon electrode and a temperature of 273 K.

As a potential of -1.0 V was applied to the air-saturated solution of $[Mn^{II}(dpaq)]^+$, a broad band with a maximum at about 660 nm began to form after about 5 minutes. The red trace (Figure 5.4) shows the maximum formation of this species after about 18 minutes. For the peak at 630 nm, the ε would be 154 M^{-1} cm^{-1} if this represents complete formation of the intermediate species. This feature is distinctly different from that of the $[Mn^{III}(OH)(dpaq)]^+$, which features two absorption features at 550 nm (ε = 320 M^{-1} cm^{-1}) and 780 nm (ε = 130 M^{-1} cm^{-1}) in acetonitrile.[22] Many reported side-on peroxomanganese(III) show absorbance features ranging from 415 to 670 nm that are often quite weak with ε ranging from 60 to 490 M^{-1} cm^{-1}.[13] The absorbance spectrum shown in Figure 5.4 agrees well with the expected absorbance of peroxomanganese(III) species.

During the bulk electrolysis experiment, an EPR samples was prepared of the species represented by the red trace of Figure 5.4. While many other

peroxomanganese(III) species have exhibited a six-line signal at approximately 80 mT in parallel mode EPR,[15-18, 20-21] the intermediate formed was EPR silent in both parallel and perpendicular mode. This does not rule out a mononuclear Mn^{III} species with large zero-field splitting or a *S*=0 spin-coupled system, both of which would also be EPR silent. In the perpendicular mode EPR spectrum (Figure 5.5), there is a large Mn^{II} signal (black) that disappears with the formation of the intermediate (red). The perpendicular mode data indicates the consumption of the starting $[Mn^{II}(dpaq)]^+$ and confirms that there are no new signals corresponding to a perpendicular mode EPR active species. However, a peroxomanganese(III) is still the most likely product due to the similar CV behavior as $[Mn^{III}L(O_2)]$.[18] Additionally, the reaction stoichiometry observed in Figure 5.2 further suggest the formation of $[Mn^{III}(O_2)(dpaq)]$.

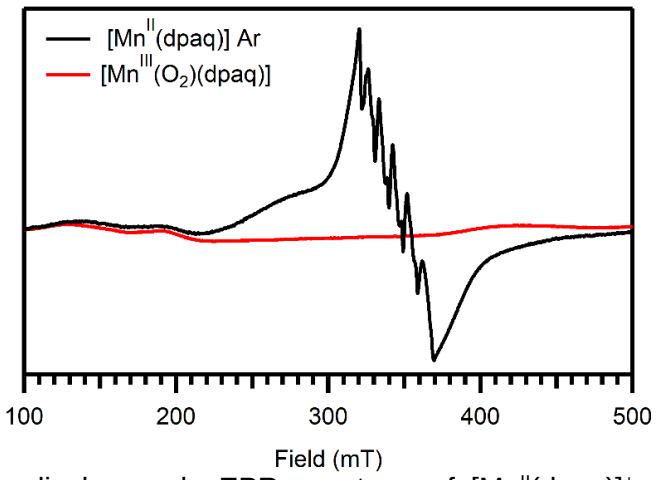

Figure 5.5. Perpendicular mode EPR spectrum of $[Mn^{II}(dpaq)]^+$ under Argon (black) and after 10 minutes exposure to O_2 and an applied potential of -1.0 V vs. SCE for 18 minutes (red). The red species corresponds to the EPR sample prepared corresponding to the red trace in Figure 5.4.

5.3.2 Hypothetical Structures for [MnIII(O2)(dpaq)] from DFT Computations

Because of the lack of structural data for $[Mn^{III}(O_2)(dpaq)]$ from experiment, we used DFT computations to compare several hypothetical structures for this Mn^{III}-peroxo species. This approach was employed previously to postulate structures for the Mn^{III}-peroxo adducts of the mL_5^2, imL_5^2, and N4py ligands (Figure 1).[34] We will briefly discuss the results of those computations to provide context for our evaluation of the DFT-computed structures for $[Mn^{III}(O_2)(dpaq)]$. The results for $[Mn^{III}(O_2)(mL_5^2)]^+$ and

$[Mn^{III}(O_2)(imL_5^2)]^+$ are particularly relevant, given the similar topologies of these ligands (Scheme 5.2).

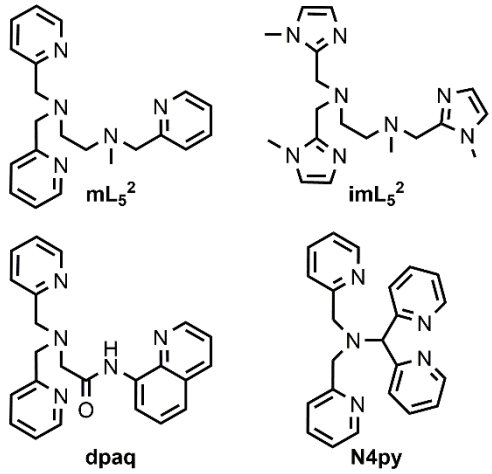

Scheme 5.2. Comparison of pentadentate ligands used to support Mn^{III}-peroxo complexes.

Our analysis of experimental electronic absorption and magnetic circular dichroism (MCD) data for the $[Mn^{III}(O_2)(mL_5^2)]^+$, $[Mn^{III}(O_2)(imL_5^2)]^+$, and $[Mn^{III}(O_2)(N4py)]^+$ complexes strongly supported a six-coordinate geometry about the Mn^{III} center. Nonetheless, in our computational evaluation of these structures, we considered both six- and seven-coordinate geometries. From the computational work, we derived two central conclusions. First, the η^2-Mn^{III}-peroxo binding mode is highly favored over the η^1-Mn^{III}-peroxo structure. Second, the Mn^{III} centers in these complexes prefer a six-coordinate geometry. Three hypothetical structures considered for $[Mn^{III}(O_2)(mL_5^2)]^+$, along with their relative electronic energies, are shown in Figure 5.6. The top structure features the mL_5^2 ligand in its commonly observed pentadentate binding mode, while the other two structures feature dissociated pyridine ligands (Figure 5.6, center and bottom). As shown in Figure 5.62 (top), even when we attempted to retain the mL_5^2 ligand in its pentadentate binding mode, the amine *trans* to the peroxo moiety was observed to have a weak interaction with the Mn^{III} center (Mn–N(1) distance of 2.610 Å). Thus, we were unable to obtain any *bona fide* structures of a seven-coordinate η^2-Mn^{III}-peroxo adduct. Notably, the structures with the dissociated amine ligand were considerably higher in energy than the structures with dissociated pyridine ligands (Figure 5.6). This trend was also observed

for the the $[Mn^{III}(O_2)(imL_5^2)]^+$ and $[Mn^{III}(O_2)(N4py)]^+$ complexes. On the basis of these result, we postulated that each of these Mn^{III}-peroxo complexes feature the N_5 supporting ligand bound in an unusual κ^4 coordination mode with a dissociated pyridine (or imidazole for imL_5^2) ligand.[34] Importantly, an X-ray crystal structure for the $[Mn^{III}Mn^{IV}(\mu\text{-}O)_2(\kappa^4\text{-}N4py)_2]^{3+}$ complex revealed κ^4-N4py ligation with a dissociated pyridine ligand.[19]

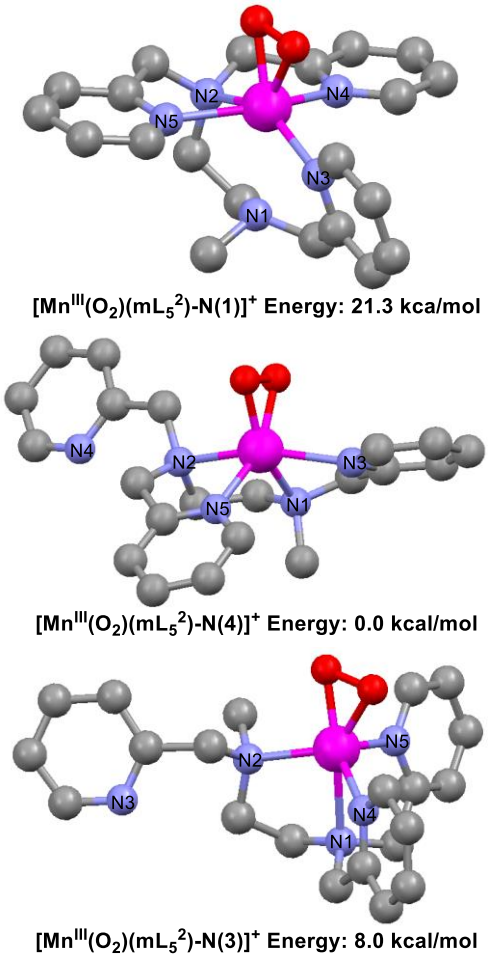

Figure 5.6. Hypothetical structures of $[Mn^{III}(O_2)(mL_5^2)]^+$ from DFT computations from reference 34.

A similar computational approach yielded three hypothetical structures for $[Mn^{III}(O_2)(dpaq)]$. In this case, however, we performed optimizations using two density functionals (the meta-GGA TPSS functional and the hybrid functional B3LYP), both of which included dispersion corrections. The structures optimized at the TPSS-D3 level are

shown in Figure 5.7, while manganese-ligand separations and relative enthalpies and free energies for all structures are collected in Table 5.1. The structures and energies obtained using the TPSS-D3 and B3LYP-D3 functionals are quite similar. Of the optimized structures, one features the dpaq bound to the Mn^{III} center in the commonly observed pentadentate binding mode (Figure 5.7A), while the other two structures have dissociated pyridine and quinoline arms (Figure 5.7, B and C, respectively). The lowest-energy structure is $[Mn^{III}(O_2)(dpaq\text{-}py)]$, where the pyridine ligand is dissociated (Figure 5.7B). This structure features Mn–O distances of 1.864 and 1.844 Å and an O–O bond length of 1.458 Å, which are in good agreement with corresponding values obtained for structurally characterized Mn^{III}-peroxo adducts.[6, 8, 21, 35-37] Unexpectedly, we also obtained a low-energy structure, $[Mn^{III}(O_2)(dpaq)]$, which features an η^2-Mn^{III}-peroxo unit with the dpaq ligand bound in a pentadentate fashion. This structure is only ca. 2 kcal/mol higher than $[Mn^{III}(O_2)(dpaq\text{-}py)]$ (Table 1). Unlike that observed for the $[Mn^{III}(O_2)(mL_5^2)]^+$ complex where the ligand *trans* to the peroxo was essentially dissociated (see Figure 5.6, top), the nitrogen ligand *trans* to the peroxo group in the structure of $[Mn^{III}(O_2)(dpaq)]$ shows a short Mn–N distance of 2.173 Å (Figure 5.7A). Although one of the Mn–O(peroxo) distances in $[Mn^{III}(O_2)(dpaq)]$ is slightly elongated compared to commonly observed values (1.945 Å versus 1.838 – 1.901 Å),[38] the $[Mn^{III}(O_2)(dpaq)]$ structure clearly reveals a seven-coordinate Mn^{III} center. We tentatively attribute this unexpected change in binding preference relative to $[Mn^{III}(O_2)(mL_5^2)]^+$ to the presence of the strongly donating amidate function in dpaq. The third structure considered, $[Mn^{III}(O_2)(dpaq\text{-}qn)]$, which features a dissociated quinoline, is only ca. 5 kcal/mol higher in energy than $[Mn^{III}(O_2)(dpaq\text{-}py)]$. Given the accepted error of DFT energies for transition metal complexes,[39] we are unable to conclude which complex is most reasonable given the small energy differences. Nonetheless, these computations demonstrate that the $[Mn^{III}(O_2)(dpaq)]$ complex could potentially have a seven-coordinate structure, distinct from those of previously reported Mn^{III}-peroxo adducts.

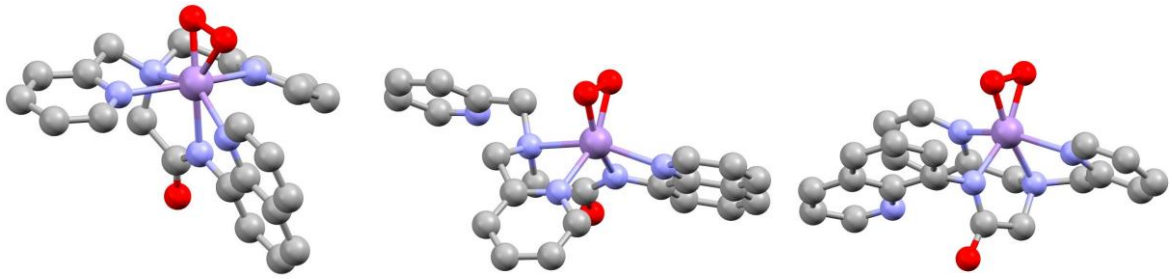

A) $[Mn^{III}(O_2)(dpaq)]$ B) $[Mn^{III}(O_2)(dpaq\text{-}py)]$ C) $[Mn^{III}(O_2)(dpaq\text{-}qn)]$

Figure 5.7. Hypothetical structures of $[Mn^{III}(O_2)(dpaq)]$ from DFT computations.

Table 5.1. Relative Enthalpies (kcal/mol, Relative Free Energies (kcal/mol), and Mn–Ligand Bond Lengths (Å) for Hypothetical Models of $[Mn^{III}(O_2)(dpaq)]$

	enthalpy[a]	free energy[b]	Mn–O	O–O	Mn–N_{qn}	Mn–N_{py}	Mn–N_{amide}	Mn–N_{amine}
TPSS-D3/TPSSh-D3[c]								
$[Mn^{III}(O_2)(dpaq)]$	2.52	2.92	1.838 1.945	1.43 7	2.345	2.258 2.328	2.173	2.213
$[Mn^{III}(O_2)(dpaq\text{-}py)]$	0.00	0.00	1.844 1.864	1.45 8	2.228	2.104 5.309	2.029	2.305
$[Mn^{III}(O_2)(dpaq\text{-}qn)]$	6.11	4.53	1.852 1.857	1.46 0	4.197	2.245 2.277	1.987	2.216
B3LYP-D3[d]								
$[Mn^{III}(O_2)(dpaq)]$	1.53	1.75	1.875 1.974	1.39 9	2.153	2.299 2.322	2.271	2.402
$[Mn^{III}(O_2)(dpaq\text{-}py)]$	0.00	0.00	1.853 1.875	1.43 7	2.247	2.125 5.339	2.043	2.325
$[Mn^{III}(O_2)(dpaq\text{-}qn)]$	5.84	4.15	1.859 1.882	1.43 9	4.164	2.269 2.296	1.995	2.239

[a] Enthalpies from the electronic energy with zero-point correction. [b] Free energies from the enthalpies and entropic contributions at 298 K. [c] Geometry optimization performed with the TPSS-D3 functional with def2-TZVP (Mn, O, and N) and def2-SVP (C and H) basis sets. Single point energy determined with the hybrid TPSSh-D3 functional with def2-TZVPP basis set on all atoms. [d] Geometry optimization performed with the B3LYP-D3 functional with def2-TZVP (Mn, O, and N) and def2-SVP (C and H) basis sets. Single point energy determined with the B3LYP-D3 functional with def2-TZVPP basis set on all atoms.

5.3.3 Electrochemical Reduction of $[Mn^{III}(O_2)(dpaq)]$

To further probe the electrochemical properties of the putative $[Mn^{III}(O_2)(dpaq)]$ species, CV experiments were performed over a wider sweep width. This analysis revealed that the reduction of the generated $[Mn^{III}(O_2)(dpaq)]$ (red trace, Figure 5.8) occurs at -1.4 V. This is quite different than the reduction of $[Mn^{III}L(O_2)]$, which was reduced at -1.65 V.[18] $[Mn^{III}(O_2)(dpaq)]$ is clearly more easily reduced than $[Mn^{III}L(O_2)]$. Further, the reduction of the $[Mn^{III}(O_2)(dpaq)]$ complex occurs at a potential nearly 1 V above that required for the reduction of superoxide, which occurs in DMF at *ca.* -2.3 V (Figure 5.8, black). Additionally, the CV experiments with the wider sweep width show the

appearance of a peak around -0.1 V that is not present when the peroxomanganese(III) species is generated but not reduced. This peak could arise from the oxidation of the reduced peroxo. More insight into this reduction process comes from Figure 5.9, where three different CV scans show (1) the oxidation of $[Mn^{II}(dpaq)](OTf)$ (black); (2) formation and then oxidation of $[Mn^{III}(O_2)(dpaq)]$ (red); and (3) formation of $[Mn^{III}(O_2)(dpaq)]$, along with its reduction and finally the oxidation of that species (blue).

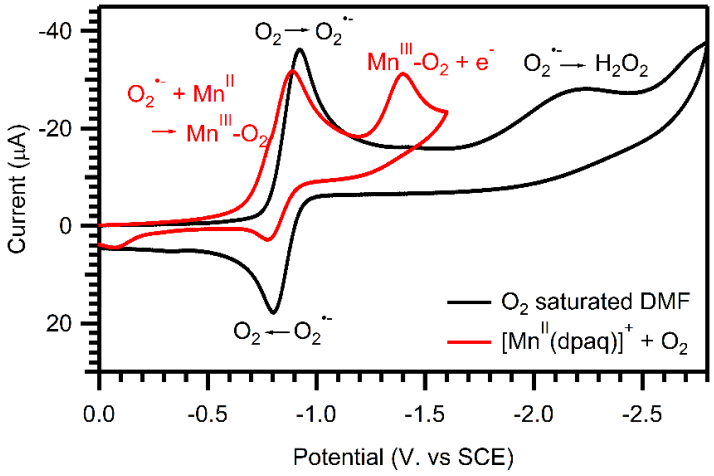

Figure 5.8. CV of 1.0 mM $[Mn^{II}(dpaq)]^+$ and O_2 (1.0 mM, air saturated) in DMF + 0.1 M Bu_4NPF_6 at 0.1 V/s at a glassy carbon disk electrode (T = 293 K) scanning toward a more negative potential to show the reduction of the formed peroxo species. This is a comparison of the reduction of O_2 in the presence (red) and absence (black) of $[Mn^{II}(dpaq)]^+$.

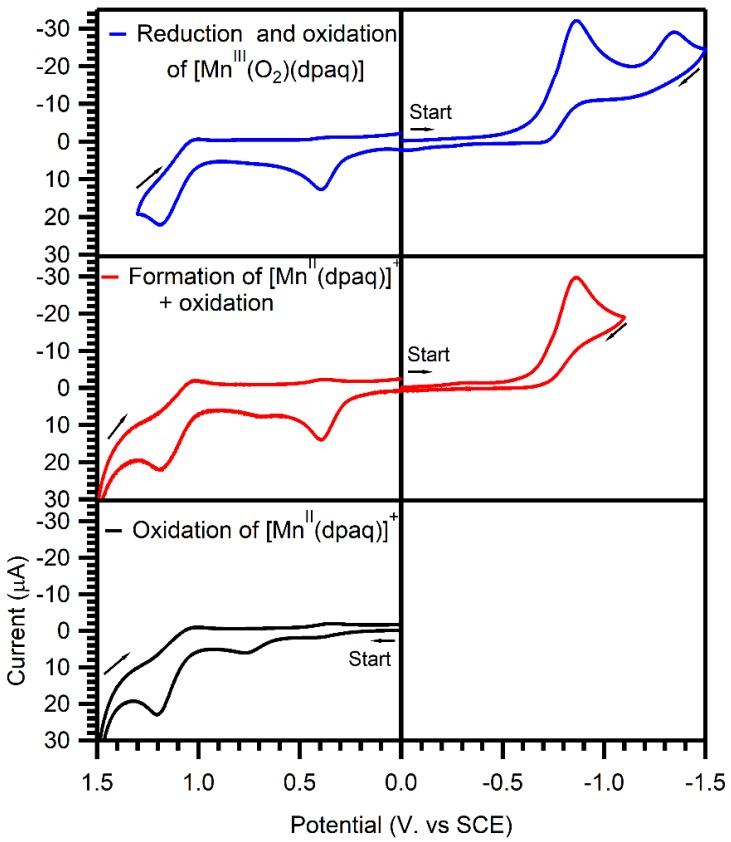

Figure 5.9. CV of $[Mn^{II}(dpaq)](OTf)$ (1mM) and O_2 (1.0 mM, air saturated) in DMF + 0.1 M Bu_4NPF_6 at 0.1 V/s at a glassy carbon disk electrode (T = 293 K), scanning towards cathodic (blue and red traces) and anodic (black trace) potentials.

Figure 5.9 shows three separate CV scans of 1.0 mM $[Mn^{II}(dpaq)]^+$ in DMF. In black, there is a scan from 0 to 1.5 back to 0 V. where there the oxidation and subsequent reduction of $[Mn^{II}(dpaq)]^+$ is probed. This CV trace shows two small oxidation peaks near 0.4 V and 0.8 V. The signal at 0.4 V appears to be reversible, but the one at 0.8V is irreversible. One of these peaks corresponds to the Mn^{II}/Mn^{III} oxidation, but both peaks are lower in intensity than expected. This CV trace also shows a very intense oxidation signal at about 1.2V that is irreversible, which is attributed to an oxidation of the dpaq ligand. This assignment is confirmed by CV investigations of the free ligand, Hdpaq (Figure 5.10). The red trace, shows the reduction of O_2 to superoxide which is irreversible because the formed superoxide is reacting with $[Mn^{II}(dpaq)](OTf)$ to form $[Mn^{III}(O_2)(dpaq)]$. When potential is reversed, and scanned towards anodic potentials, there appears a large signal at 0.4V. This is likely the oxidation of the species formed by

the reaction of Mn and superoxide. Lastly, in blue, [$Mn^{III}(O_2)$(dpaq)] is formed, reduced and then scanned to anodic potentials. The notable feature here is the appearance of a very small signal at -0.1 V and the slightly reduced intensity of the peak at 0.4 V. In similar experiments with [$Mn^{III}L(O_2)$], there was a small signal around 0.1 V but it was attributed to oxidation of the phenolato moiety of the ligand. CV studies of the Hdpaq ligand did not show any ligand oxidation peaks in this region (Figure 5.10), suggesting that the signal observed at -0.1 V could correspond to the oxidation of the reduced peroxo species. Because it is small and the peak at 0.4 V is still very large, it is likely that the reduced peroxo species is very unstable, so there is very little of it left to be oxidized.

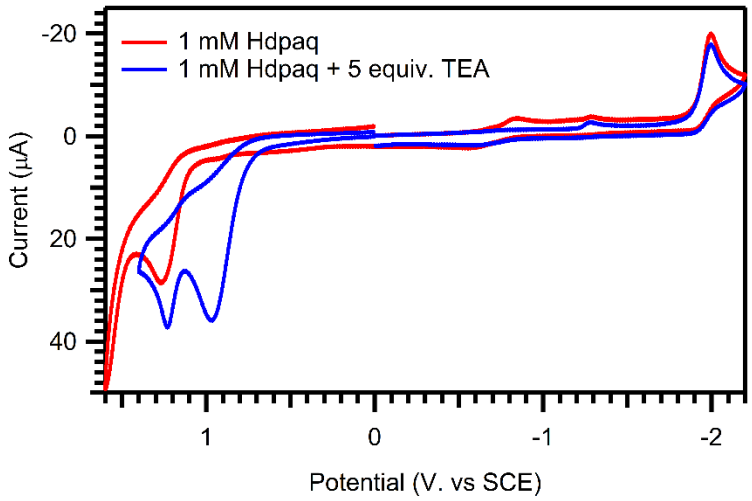

Figure 5.10. CV of Hdpaq (1mM, red) and 5 equivalents of triethylamine (blue) in DMF + 0.1 M Bu_4NPF_6 at 0.1 V/s at a glassy carbon disk electrode (T = 293 K), scanning towards anodic and cathodic potentials.

The CV data in Figure 5.9 shows an oxidation event near +1.2 V which corresponds to a dpaq ligand based oxidation. This oxidation occurs at the same potential as the oxidation events seen in Figure 5.9, thus confirming that the oxidation process at +1.2 V is a ligand based oxidation. Triethylamine was added to the reaction mixture to deprotonate the free ligand. This would highlight the effects of the ligand partially dissociating from the metal complex during CV investigations. Upon deprotonation, a large oxidation feature shows up at +0.95 V, likely an oxidation of the amide nitrogen. This oxidation event is not observed in any other oxidation processes that are relevant to the current studies. This implies that the amide nitrogen is not de-coordinating from the

Mn center, which is unsurprising given that it is the strongest Mn-N bond.[22] This also confirms that the feature we have labeled as the reduction of the peroxo, the reduction at -1.4 V, is not a dpaq centered reduction.

Although it is clear that [$Mn^{III}(O_2)$(dpaq)] is more easily reduced than [$Mn^{III}L(O_2)$], further insight is gained from studying the reduction at varying scan rates. To specifically study the peroxo reduction, a 20 second pre-electrolysis at -1.1 V is performed to give a constant concentration of [$Mn^{III}(O_2)$(dpaq)] at the surface of the electrode. Then the reduction of this peroxo was scanned at a variety of scan rates while carefully adjusting for ohmic drop. The normalized results of these experiments can be seen in Figure 5.11.

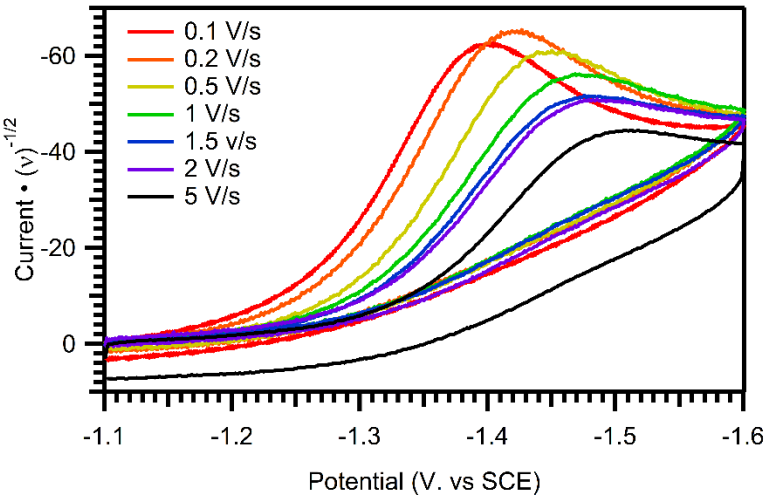

Figure 5.11. Normalized CV of 1.0 mM $[Mn^{II}(dpaq)]^+$ and O_2 (1.0 mM, air saturated) in DMF + 0.1 M Bu_4NPF_6 at a 3mm diameter glassy carbon disk electrode (T = 293 K) after a 20 second pre-electrolysis at -1.1 V.

The variation of the peak position, E_p, with the log of the scan rate, v, can be used to determine the number of electrons involved in a reduction (or oxidation). When E_p is plotted versus log(v) (Figure 5.12, left), the slope is -63 mV per decade for [$Mn^{III}(O_2)$(dpaq)]. This means that the reduction of [$Mn^{III}(O_2)$(dpaq)] is a one-electron event. This is in contrast to the two-electron reduction of [$Mn^{III}L(O_2)$], which had a slope of -110 mV per decade.[15]

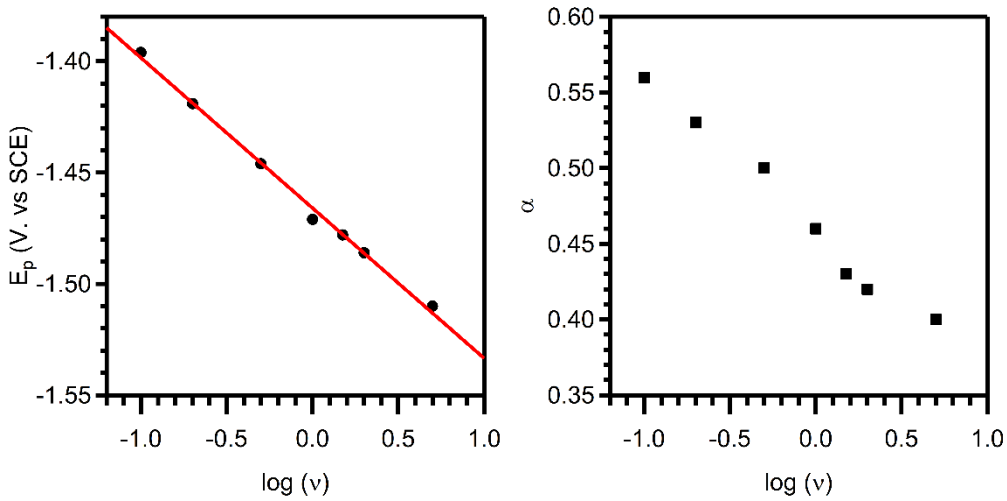

Figure 5.12. Left. Peak potential of the peroxo reduction wave as a function of log(v) with a slope of -0.06210. Right. Transfer coefficient (α) values, determined from the peak width values from Figure 5, as a function of log(v).

In addition to the number of electrons this reduction corresponds to, further details can be gained from these data. The transfer coefficient, α, can be calculated from the width of the peaks in Figure 5.11 using equation 5.1, where R is the gas constant,

$$\alpha = 1.856(RT/F)(E_{p/2}-E_p) \qquad (5.1)$$

T is the temperature in Kelvin, F is Faraday's constant, E_p is the peak potential, and $E_{p/2}$ is the potential at half of the peak height.[40] The variation of α with the log of the scan rate can be seen in Figure 5.12. In general, the values of α of are higher for $[Mn^{III}(O_2)(dpaq)]$ than those for $[Mn^{III}L(O_2)]$. For example, at a scan rate of 100 mV/s, α is calculated to be 0.53 for $[Mn^{III}(O_2)(dpaq)]$, which is much higher than the value of 0.35 observed for $[Mn^{III}L(O_2)]$. The calculated α can be used to further calculate the free energy of activation, $\Delta G^{\ddagger}_{peak}$, using equation 5.2, where D is the diffusion coefficient of the substrate, Z is the collision frequency determined from $Z = (RT/2\pi M)^{1/2}$ where M is the molar mass, and v is

$$\Delta G^{\ddagger}_{peak} = (RT/F)\ \ln\ [Z(RT/\alpha F v D)^{1/2} - 0.78] \qquad (5.2)$$

the experimental scan rate.[40] The value of the D, 4 x 10^{-6} cm^2 s^{-1}, was determined for $[Mn^{III}L(O_2)]$, based on simulated CV data. Though the exact value of D has not yet been determined for $[Mn^{III}(O_2)(dpaq)]$, the calculations involving D are insensitive to the exact

value of D. Thus we can assume that 4 x 10^{-6} cm^2 s^{-1} is a good estimate for [$Mn^{III}(O_2)$(dpaq)], especially considering the diffusion of the two manganese complexes would be expected to be on the same order of magnitude. For [$Mn^{III}(O_2)$(dpaq)], $\Delta G^{\ddagger}_{peak}$, was equal to 0.35 eV, which is identical of that for [$Mn^{III}L(O_2)$].[15] Lastly, using the $\Delta G^{\ddagger}_{peak}$ and α, the reorganization energy, λ, can be determined using equation 5.3.[40]

$$\lambda = \Delta G^{\ddagger}_{peak} / \alpha^2 \qquad (5.3)$$

The reduction of [$Mn^{III}(O_2)$(dpaq)] has a much lower reorganization energy than that of [$Mn^{III}L(O_2)$], with values of λ being 1.12 eV and 2.93 eV, respectively.[15] The large λ of [$Mn^{III}L(O_2)$] was attributed to the dissociation of the phenolato group of the ligand and the pendant imidizolyl moiety re-coordinating to the metal.[15] The lower λ for [$Mn^{III}(O_2)$(dpaq)] suggests there is much less ligand rearrangement. If the heptacoordinate DFT structure is correct, this could explain the lower λ for [$Mn^{III}(O_2)$(dpaq)]. It had previously been proposed that the large λ for [$Mn^{III}L(O_2)$] may have been ligand rearrangement involving both the phenolato and imidazolyl moieties.[15] These events are possibly less likely to occur with the more rigidly bound dpaq ligand. The difference in λ may also stem from the difference in the number of electrons transferred in the reduction process.

This reduction can be further probed in the presence of either a weak acid (H_2O) or a strong acid ($HClO_4$). For [$Mn^{III}L(O_2)$], in the presence of a large excess of H_2O, the reduction of [$Mn^{III}L(O_2)$] was largely unchanged, indicating that the protonation of the peroxo was not the rate limiting step in the reduction of [$Mn^{III}L(O_2)$].[15] The reduction of [$Mn^{III}(O_2)$(dpaq)] behaves very similarly (Figure 5.13), indicating that the rate limiting step for the one electron reduction is not a protonation step. Further, the reduction of O_2 does not increase to a two-electron reduction, which is expected if the peroxo is protonated leading to the release of H_2O_2.[15] However, the behavior of [$Mn^{III}(O_2)$(dpaq)] in a strong acid does differ from that of [$Mn^{III}L(O_2)$], giving further information on the differences between the two complexes.

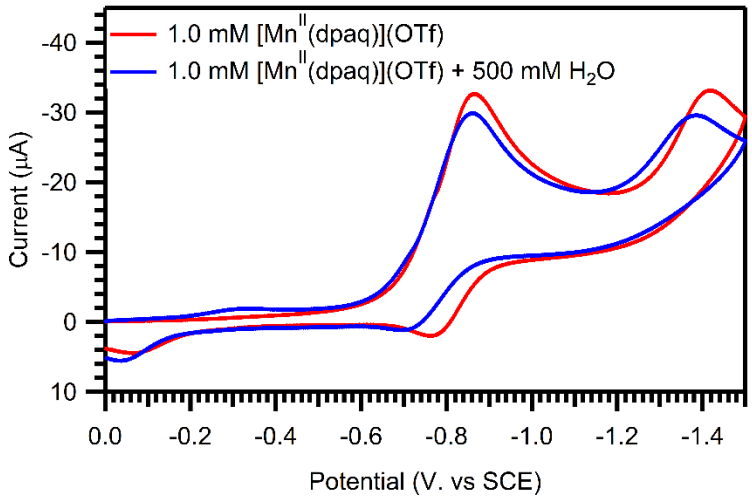

Figure 5.13. CV of the reduction of O_2 (1.0 mM, air saturated) in DMF (plus 0.1 M Bu_4NPF_6) as well as the reduction of the peroxo species formed in the presence of 1.0 mM $[Mn^{II}(dpaq)]^+$ with (red) and without 500 mM water (blue). CV collected at 0.1 V/s at a glassy carbon disk electrode (T = 293 K) scanning toward cathodic potentials.

The oxidation of $[Mn^{II}(dpaq)](OTf)$ in the presence of increasing $HClO_4$ shows that the peak for the oxidation at +0.8 V decreases with increasing acid concentration (Figure 5.14, arrow). This is similar to that of $[Mn^{III}L(O_2)]$, and was attributed to the protonation and loss of the ligand from the metal, to form the acid LH.[15] The decrease and then disappearance of the oxidation peak at +0.8 V confirms that $[Mn^{II}(dpaq)](OTf)$ is also decomposing upon the addition of the acid. When $HClO_4$ decomposes $[Mn^{II}(dpaq)](OTf)$, it is likely to form Hdpaq, which acts as an acid as had LH.[15] A confirmation of this process using UV-visible spectroscopy may be necessary to further support this. After confirming the oxidative behavior of $[Mn^{II}(dpaq)](OTf)$ in the presence of $HClO_4$, the effects of the $HClO_4$ on the peroxo formation were investigated (Figure 5.15).

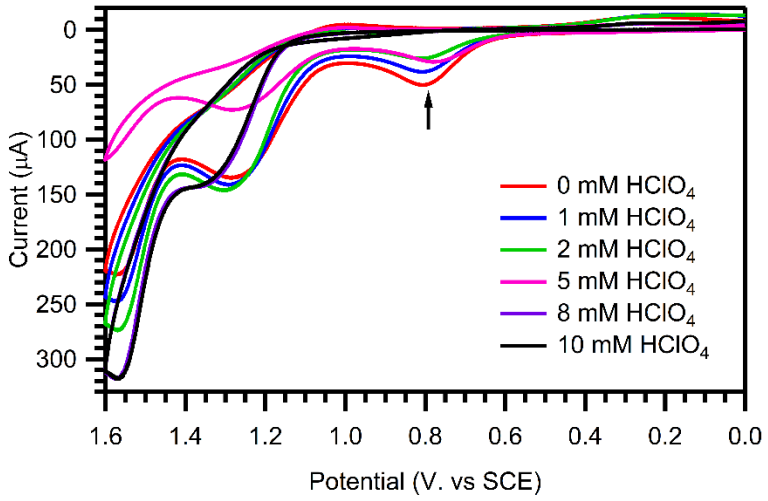

Figure 5.14. CV of [Mn^{II}(dpaq)](OTf) (10mM, red) and O_2 (1.0 mM, air saturated) in DMF + 0.1 M Bu_4NPF_6 at 0.1 V/s at a glassy carbon disk electrode (T = 293 K), scanning towards anodic potentials. The effects of the addition of $HClO_4$ can be seen in the additional traces.

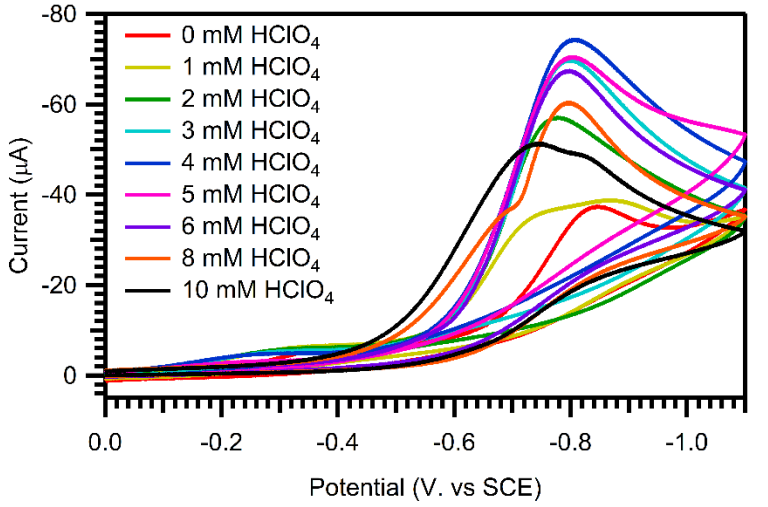

Figure 5.15. CV of [Mn^{II}(dpaq)](OTf) (10mM) and O_2 (1.0 mM, air saturated, Red) in DMF + 0.1 M Bu_4NPF_6 at 0.1 V/s at a glassy carbon disk electrode (T = 293 K), scanning towards cathodic potentials to show the O_2 reduction wave in the presence of 10 mM [Mn^{II}(dpaq)](OTf) and increasing equivalents of $HClO_4$.

The behavior of the formation of [$Mn^{III}(O_2)$(dpaq)] has some important differences from that of [$Mn^{III}L(O_2)$], but it also has some similarities. Unlike the addition of water, the addition of $HClO_4$ causes the peak for O_2 reduction to increase to a two-electron process. For [$Mn^{III}L(O_2)$], this peak was shown to decrease proportionally with $HClO_4$ concentration

and showed a crossing of trace on the reverse scan, which indicated the appearance of a reduction process. However, with $[Mn^{III}(O_2)(dpaq)]$, the peak increased until 4 equivalents of $HClO_4$ were added and then began to decrease. Additionally, the backwards scan did not cross the forward scan. To determine the significance of these differences, it is important to consider the processes that might be going on at the electrode surface.

There are two competing reaction pathways that can be occurring at the electrode surface that would lead to a two-electron reduction peak (Schemes 2 and 3). First, the formed superoxide can be protonated by the Hdpaq in solution to give $HOO^{\bullet}$ and $dpaq^-$ (Scheme 2, reaction 2). The molecule of $HOO^{\bullet}$ can react with a second electron to give HOO^- (Scheme 2, reaction 3), or in a reaction with a second molecule of $O_2^{\bullet-}$ to give HOO^- and O_2 (Scheme 2, reaction 4). Lastly the formation of H_2O_2 results from the protonation of the formed HOO^- by a second equivalent of Hdpaq (Scheme 2, reaction 5). The competing reaction pathway is the normal peroxo formation. Once formed, the peroxo is protonated by Hdpaq, cleaving the Mn-O bond to release HOO^- and $[Mn^{III}(dpaq)]^{2+}$ (Scheme 3, reaction 3).The $[Mn^{III}(dpaq)]^{2+}$ is expected to be very unstable since it is formed well below the $[Mn^{III}(dpaq)]^{2+}/[Mn^{II}(dpaq)]^+$ standard potential. $[Mn^{III}(dpaq)]^{2+}$ is expected to react with an electron to give $[Mn^{II}(dpaq)]^+$ (Scheme 3, reaction 4) or superoxide to give $[Mn^{II}(dpaq)]^+$ and O_2 (Scheme 3, reaction 5). Lastly, the formed HOO^- should be protonated by Hdpaq to give H_2O_2 in the same way described in Scheme 2, reaction 5. For $[Mn^{III}L(O_2)]$, it was shown that the route described by Scheme 3 was the more prominent reaction, which was further supported by simulations, DFT calculations, and the fact that the reduction process was observed with the crossing of the traces on the reverse scan. Without simulations of the data and supporting DFT calculations, it is only speculation that there is a change in mechanism from the Mn based process (Scheme 1) to the acid protonation process (Scheme 2). It is also entirely possible that there could be a mechanism that involves the unreacted $[Mn^{II}(dpaq)]^+$ could react with the peroxo to provide another reaction pathway.

$$O_2 + e^- \leftrightharpoons O_2^{\cdot-} \quad (1)$$

$$Hdpaq + O_2^{\cdot-} \rightarrow HOO^{\cdot} + dpaq^- \quad (2)$$

$$HOO^{\cdot} + e^- \leftrightharpoons HOO^- \quad (3)$$

$$HOO^{\cdot} + O_2^{\cdot-} \rightarrow HOO^- \quad (4)$$

$$HOO^- + Hdpaq \rightarrow H_2O_2 \quad (5)$$

Scheme 2. Reaction pathway leading to the production of H_2O_2 without involving the manganese center.[15, 40]

$$O_2 + e^- \rightleftharpoons O_2^{\cdot-} \quad (1)$$

$$[Mn^{II}(dpaq)]^+ + O_2^{\cdot-} \rightarrow [Mn^{II}(O_2)(dpaq)] \quad (2)$$

$$[Mn^{II}(O_2)(dpaq)] + Hdpaq \rightarrow [Mn^{III}(dpaq)]^{2+} + HOO^- \quad (3)$$

$$[Mn^{III}(dpaq)]^{2+} + e^- \rightleftharpoons [Mn^{II}(dpaq)]^+ \quad (4)$$

$$[Mn^{III}(dpaq)]^{2+} + O_2^{\cdot-} \rightarrow [Mn^{II}(dpaq)]^+ + O_2 \quad (5)$$

$$HOO^- + Hdpaq \rightarrow H_2O_2 \quad (6)$$

Scheme 3. Formation of H_2O_2 from the cleavage of the Mn-O bond of $[Mn^{III}(O_2)(dpaq)]$.[15, 40]

5.5 Conclusions

The formation of $[Mn^{III}(O_2)(dpaq)]$ by the reaction of electrochemically generated superoxide and $[Mn^{II}(dpaq)]^+$ has been characterized by cyclic voltammetry and UV-visible spectroscopy with further support coming from DFT calculations and EPR spectroscopy. This putative peroxomanganese(III) species is reduced by one-electron near -1.4 V in a reaction that exhibits a low organization energy. This species is less stable then the previously studied phenlato ligand-supported peroxomanganese(III)

species, $[Mn^{III}L(O_2)]$. This is supported by the difficulty in forming the peroxo in the spectroelectrochemical experiments and the fact that its reduction occurs at a less negative potential. In contrast to $[Mn^{III}L(O_2)]$, $[Mn^{III}(O_2)(dpaq)]$ exhibits a one-electron reduction, which occurs at a less negative potential and has a lower reorganization energy. The exact mechanistic implications of these differences still need to be determined. Simulations of the CV data as well as DFT calculations will be necessary to rule out plausible intermediates. It may also be necessary to perform further experiments to try to further characterize both $[Mn^{III}(O_2)(dpaq)]$ and its one-electron reduced intermediate. This would help to fully shed light on the influences of the amide group *trans* to the peroxo ligand.

5.6 Notes and References

1. Pecoraro, V. L.; Baldwin, M. J.; Gelasco, A., Interaction of Manganese with Dioxygen and Its Reduced Derivatives. *Chem. Rev.* **1994,** *94* (3), 807-826.

2. Sheng, Y.; Abreu, I. A.; Cabelli, D. E.; Maroney, M. J.; Miller, A.-F.; Teixeira, M.; Valentine, J. S., Superoxide Dismutases and Superoxide Reductases. *Chem. Rev.* **2014,** *114* (7), 3854-3918.

3. Porta, J.; Vahedi-Faridi, A.; Borgstahl, G. E. O., Structural Analysis of Peroxide-Soaked MnSOD Crystals Reveals Side-On Binding of Peroxide to Active-Site Manganese. *J. Mol. Biol.* **2010,** *399* (3), 377-384.

4. Miller, A.-F., Superoxide dismutases: active sites that save, but a protein that kills. *Curr. Opin. Chem. Biol.* **2004,** *8* (2), 162-168.

5. Geiger, R. A.; Chattopadhyay, S.; Day, V. W.; Jackson, T. A., Nucleophilic reactivity of a series of peroxomanganese(iii) complexes supported by tetradentate aminopyridyl ligands. *Dalton Transactions* **2011,** *40* (8), 1707-1715.

6. Annaraj, J.; Cho, J.; Lee, Y.-M.; Kim, S. Y.; Latifi, R.; de Visser, S. P.; Nam, W., Structural Characterization and Remarkable Axial Ligand Effect on the Nucleophilic Reactivity of a Nonheme Manganese(III)-Peroxo Complex. *Angew. Chem. Int. Ed.* **2009,** *48* (23), 4150-4153.

7. Kang, H.; Cho, J.; Cho, K.-B.; Nomura, T.; Ogura, T.; Nam, W., Mononuclear Manganese–Peroxo and Bis(μ-oxo)dimanganese Complexes Bearing a Common N-Methylated Macrocyclic Ligand. *Chem. Eur* **2013,** *19* (14119-14125).

8. Seo, M. S.; Kim, J. Y.; Annaraj, J.; Kim, Y.; Lee, Y.-M.; Kim, S.-J.; Kim, J.; Nam, W., $[Mn(tmc)(O_2)]^+$: A Side-On Peroxide Manganese(III) Complex Bearing a Non-heme Ligand. *Angewandte Chemie International Edition* **2007,** *46*, 377-380.

9. Shook, R. L.; Gunderson, W. A.; Greaves, J.; Ziller, J. W.; Hendrich, M. P.; Borovik, A. S., A Monomeric Mn^{III}-Peroxo Complex Derived Directly from Dioxygen. *Journal of the American Chemical Society* **2008,** *130* (28), 8888-8889.

10. Shook, R. L.; Peterson, S. M.; Greaves, J.; Moore, C.; Rheingold, A. L.; Borovik, A. S., Catalytic Reduction of Dioxygen to Water with a Monomeric Manganese Complex at Room Temperature. *Journal of the American Chemical Society* **2011,** *133* (15), 5810-5817.

11. Shook, R. L.; Borovik, A. S., Role of the Secondary Coordination Sphere in Metal-Mediated Dioxygen Activation. *Inorg. Chem.* **2010,** *49* (8), 3646-3660.

12. Barman, P.; Upadhyay, P.; Faponle, A. S.; Kumar, J.; Nag, S. S.; Kumar, D.; Sastri, C. V.; Visser, S. P. d., Deformylation Reaction by a Nonheme Manganese(III)–Peroxo Complex via Initial Hydrogen-Atom Abstraction. *Angewandte Chemie* **2016,** *128* (37), 11257-11261.

13. Leto, D. F.; Jackson, T. A., Peroxomanganese complexes as an aid to understanding redox-active manganese enzymes. *J. Biol. Inorg. Chem.* **2014,** *19*, 1-15.

14. Rice, D. B.; Massie, A. A.; Jackson, T. A., Manganese–Oxygen Intermediates in O–O Bond Activation and Hydrogen-Atom Transfer Reactions. *Acc. Chem. Res.* **2017,** *50* (11), 2706-2717.

15. Ching, H. Y. V.; Anxolabéhère-Mallart, E.; Colmer, H. E.; Costentin, C.; Dorlet, P.; Jackson, T. A.; Policar, C.; Robert, M., Electrochemical Formation and Reactivity of a Manganese Peroxo Complex: Acid Driven H2O2 Generation vs. O-O Bond Cleavage. *Chemical Science* **2014,** *5* (2304-2310).

16. El Ghachtouli, S.; Vincent Ching, H. Y.; Lassalle-Kaiser, B.; Guillot, R.; Leto, D. F.; Chattopadhyay, S.; Jackson, T. A.; Dorlet, P.; Anxolabehere-Mallart, E., Electrochemical formation of MnIII-peroxo complexes supported by pentadentate amino pyridine and imidazole ligands. *Chemical Communications* **2013,** *49* (50), 5696-5698.

17. Groni, S.; Dorlet, P.; Blain, G.; Bourcier, S.; Guillot, R.; Anxolabéhère-Mallart, E., Reactivity of an Aminopyridine $[LMn^{II}]^{2+}$ Complex with H_2O_2. Detection of Intermediates at Low Temperature. *Inorg. Chem.* **2008,** *47* (8), 3166-3172.

18. Colmer, H. E.; Howcroft, A. W.; Jackson, T. A., Formation, Characterization, and O–O Bond Activation of a Peroxomanganese(III) Complex Supported by a Cross-Clamped Cyclam Ligand. *Inorg. Chem.* **2016,** *55* (5), 2055-2069.

19. Leto, D. F.; Chattopadhyay, S.; Day, V. W.; Jackson, T. A., Reaction landscape of a pentadentate N5-ligated MnII complex with $O2^{\cdot-}$ and H2O2 includes conversion of a

peroxomanganese(III) adduct to a bis(μ-oxo)-dimanganese(III,IV) species. *Dalton Trans.* **2013,** *42*, 13014.

20. Groni, S.; Blain, G.; Guillot, R.; Policar, C.; Anxolabéhère-Mallart, E., Reactivity of Mn^{II} with Superoxide. Evidence for a $[Mn^{III}OO]^{+}$ Unit by Low-Temperature Spectroscopies. *Inorg. Chem.* **2007,** *46* (6), 1951-1953.

21. Colmer, H. E.; Geiger, R. A.; Leto, D. F.; Wijeratne, G. B.; Day, V. W.; Jackson, T. A., Geometric and electronic structure of a peroxomanganese(iii) complex supported by a scorpionate ligand. *Dalton Transactions* **2014,** *43* (48), 17949-17963.

22. Wijeratne, G. B.; Corzine, B.; Day, V. W.; Jackson, T. A., Saturation Kinetics in Phenolic O–H Bond Oxidation by a Mononuclear Mn(III)–OH Complex Derived from Dioxygen. *Inorg. Chem.* **2014,** *53* (14), 7622-7634.

23. Coggins, M. K.; Toledo, S.; Shaffer, E.; Kaminsky, W.; Shearer, J.; Kovacs, J. A., Characterization and Dioxygen Reactivity of a New Series of Coordinatively Unsaturated Thiolate-Ligated Manganese(II) Complexes. *Inorg. Chem.* **2012,** *51* (12), 6633-6644.

24. Gennari, M.; Brazzolotto, D.; Pécaut, J.; Cherrier, M. V.; Pollock, C. J.; DeBeer, S.; Retegan, M.; Pantazis, D. A.; Neese, F.; Rouzières, M.; Clérac, R.; Duboc, C., Dioxygen Activation and Catalytic Reduction to Hydrogen Peroxide by a Thiolate-Bridged Dimanganese(II) Complex with a Pendant Thiol. *Journal of the American Chemical Society* **2015,** *137* (26), 8644-8653.

25. Brazzolotto, D.; Reinhard, F. G. C.; Smith-Jones, J.; Retegan, M.; Amidani, L.; Faponle, A. S.; Ray, K.; Philouze, C.; Visser, S. P. d.; Gennari, M.; Duboc, C., A High-Valent Non-Heme μ-Oxo Manganese(IV) Dimer Generated from a Thiolate-Bound Manganese(II) Complex and Dioxygen. *Angewandte Chemie International Edition* **2017,** *56* (28), 8211-8215.

26. Hitomi, Y.; Arakawa, K.; Funabiki, T.; Kodera, M., An Iron(III)–Monoamidate Complex Catalyst for Selective Hydroxylation of Alkane C-H Bonds with Hydrogen Peroxide. *Angewandte Chemie International Edition* **2012,** *51* (14), 3448-3452.

27. Neese, F., The ORCA program system. *Wiley Interdisciplinary Reviews: Computational Molecular Science* **2012,** *2* (1), 73-78.

28. Tao, J.; Perdew, J. P.; Staroverov, V. N.; Scuseria, G. E., Climbing the Density Functional Ladder: Nonempirical Meta-Generalized Gradient Approximation Designed for Molecules and Solids. *Phys. Rev. Lett.* **2003,** *91* (14), 146401.

29. Grimme, S.; Antony, J.; Ehrlich, S.; Krieg, H., A consistent and accurate ab initio parametrization of density functional dispersion correction (DFT-D) for the 94 elements H-Pu. *J. Chem. Phys.* **2010,** *132* (15), 154104.

30. Grimme, S.; Ehrlich, S.; Goerigk, L., Effect of the damping function in dispersion corrected density functional theory. *Journal of Computational Chemistry* **2011,** *32* (7), 1456-1465.

31. Schäfer, A.; Horn, H.; Ahlrichs, R., Fully optimized contracted Gaussian basis sets for atoms Li to Kr. *J. Chem. Phys.* **1992,** *97* (4), 2571-2577.

32. Schäfer, A.; Huber, C.; Ahlrichs, R., Fully Optimized Contracted Gaussian Basis Sets of Triple Zeta Valence Quality for Atoms Li to Kr. *J. Chem. Phys.* **1994,** *100*, 5829-5835.

33. Weigend, F.; Ahlrichs, R., Balanced basis sets of split valence, triple zeta valence and quadruple zeta valence quality for H to Rn: Design and assessment of accuracy. *PCCP* **2005,** *7* (18), 3297-3305.

34. Geiger, R. A.; Leto, D. F.; Chattopadhyay, S.; Dorlet, P.; Anxolabéhère-Mallart, E.; Jackson, T. A., Geometric and Electronic Structures of Peroxomanganese(III) Complexes Supported by Pentadentate Amino-Pyridine and -Imidazole Ligands. *Inorg. Chem.* **2011,** *50* (20), 10190-10203.

35. VanAtta, R. B.; Strouse, C. E.; Hanson, L. K.; Valentine, J. S., [Peroxotetraphenylporphinato]manganese(III) and [Chlorotetraphenylporphinato]manganese(II) Anions. Synthesis, Crystal Structures, and Electronic Structures. *Journal of the American Chemical Society* **1987,** *109*, 1425-1434.

36. Kitajima, N.; Komatsuzaki, H.; Hikichi, S.; Osawa, M.; Moro-oka, Y., A Monomeric Side-On Peroxo Manganese(III) Complex: $Mn(O_2)(3,5\text{-}iPr_2pzH)(HB(3,5\text{-}iPr_2pz)_3)$. *J. Am. Chem. Soc* **1994,** *116*, 11596-11597.

37. Singh, U. P.; Sharma, A. K.; Hikichi, S.; Komatsuzaki, H.; Moro-oka, Y.; Akita, M., Hydrogen bonding interaction between imidazolyl N-H group and peroxide: Stabilization of Mn(III)-peroxo complex $Tp^{iPr2}Mn(\eta^2\text{-}O_2)(im^{Me}H)$ ($im^{Me}H$ = 2-methylimidazole). *Inorganica Chimica Acta* **2006,** *359*, 4407-4411.

38. Leto, D. F.; Jackson, T. A., Peroxomanganese complexes as an aid to understanding redox-active manganese enzymes. *J. Biol. Inorg. Chem.* **2014,** *19* (1), 1-15.

39. Neese, F., A critical evaluation of DFT, including time-dependent DFT, applied to bioinorganic chemistry. *Journal of Biological Inorganic Chemistry* **2006,** *11*, 702-711.

40. Savéant, J.-M., *Elements of molecular and biomolecular electrochemistry: an electrochemical approach to electron transfer chemistry*. John Wiley & Sons, Inc.: Hoboken, NJ., 2006.

Chapter 6. Summary and Open Questions

6.1 Summary

The majority of this dissertation (Chapters 2-4) has focused on the synthesis, characterization, and hydrogen-atom transfer (HAT) reactivity of a series of oxomanganese(IV) species supported by neutral, pentadentate ligands. Previously, $[Mn^{IV}(O)(N4py)]^{2+}$ was prepared from the reaction of the starting $[Mn^{II}(N4py)](OTf)_2$ and the oxygen-atom transfer agent, iodosobenzene (PhIO) in 2,2,2-trifluoroethanol (TFE).[1] The impressive reactivity of $[Mn^{IV}(O)(N4py)]^{2+}$ towards C-H bonds led to open questions regarding the basis for the rate enhancement compared to other oxomanganese(IV) species. Previously our group postulated that the increased reactivity of $[Mn^{IV}(O)(N4py)]^{2+}$ stemmed from its high one-electron reduction potential, which could imply a high thermodynamic driving force for HAT.[1] Conversely, based on density functional theory (DFT) calculations, Nam and Shaik suggested that a one electron excited-state involving an $e(d_{xz},d_{yz})\rightarrow b_1(d_{x^2-y^2})$ excitation provides a lower barrier to HAT to explain the enhanced reactivity.[2] To further elucidate the factors responsible for this enhanced reactivity, a series of oxomanganese(IV) species supported by systematically modified versions of the N4py ligand were prepared, spectroscopically characterized, and kinetically interrogated.[3]

New ligands were based on a modified version of the synthesis of N4py, where two of the pyridines were replaced with different groups to specifically modulate the equatorial ligand field. To probe the excited-state mechanism, tuning the equatorial ligand field would raise (or lower) the energy of the manganese(IV) $d_{x^2-y^2}$ orbital, making it more (or less) costly to access the one-electron excited state, thus decreasing (or enhancing) reactivity. Two different derivatives of N4py were initially prepared, ^{DMM}N4py and 2pyN2Q. For ^{DMM}N4py, the two pyridines were substituted with methoxy (electron-donating group) *para* to the nitrogen that coordinates to the Mn center as well as two methyl groups. This was expected to destabilize the manganese(IV) $d_{x^2-y^2}$ orbital, which is Mn-N σ^* with the equatorial ligands, due to the increased σ-bonding abilities of this substituted pyridine. Conversely, 2pyNQ, where two of the donating pyridines have been replaced by bulky quinoline groups, is expected to lower the energy of the manganese(IV) $d_{x^2-y^2}$ orbital. While ^{DMM}N4py is modulated by electronic effects, the steric effects of 2pyN2Q were responsible

for weakening the σ bond between the ligand and the metal center, thus stabilizing the manganese(IV) $d_{x^2-y^2}$ orbital. When the Mn^{II} complexes were prepared with these new ligands, confirmation of these expected modulations came from the shorter Mn-N_{eq} bond distances for $[Mn^{II}(^{DMM}N4py)](OTf)_2$ and longer Mn-N_{eq} bond distances for $[Mn^{II}(2pyN2Q)](OTf)_2$, which was determined from solid state X-ray diffraction measurements.[3]

After the preparation of the new Mn^{II} complexes, the formation of the corresponding oxomanganese(IV) complexes using PhIO was monitored by UV-visible spectroscopy. Once formed, the HAT reactivity of the new oxomanganese(IV) complexes was investigated with several substrates containing C-H bonds strengths spanning roughly 10 kcal mol^{-1}. Across all substrates, it was observed that $[Mn^{IV}(O)(2pyN2Q)]^{2+}$ performed HAT reactions an order of magnitude faster than $[Mn^{IV}(O)(N4py)]^{2+}$ while $[Mn^{IV}(O)(^{DMM}N4py)]^{2+}$ reacted an order of magnitude slower than $[Mn^{IV}(O)(N4py)]^{2+}$.[3] While this reactivity trend does support the involvement of the excited-state in HAT reactivity, the ligand perturbations also caused a change in the one-electron reduction potential of the oxomanganese(IV) complexes. $[Mn^{IV}(O)(2pyN2Q)]^{2+}$ exhibits a more positive reduction potential than $[Mn^{IV}(O)(N4py)]^{2+}$, while $[Mn^{IV}(O)(^{DMM}N4py)]^{2+}$ exhibits a lower reduction potential. The one-electron reduction potentials correlate well with the $\log(k_2')$, thus suggesting that changes in the thermodynamic driving force are responsible for the increased reactivity. However, it must be noted that a complete description requires information on both the one-electron reduction potential, as well as the pK_a data of the product of HAT, the Mn^{III}-OH adduct. Although the correlation between reduction potential and rate suggests that a larger thermodynamic driving force is responsible for increased reactivity, without the pK_a information, the influence of the thermodynamic driving force remains incomplete.

The HAT rate enhancements observed for $[Mn^{IV}(O)(2pyN2Q)]^{2+}$ make this species the most reactive nonporphyrinic oxomanganese(IV) intermediate observed to date. $[Mn^{IV}(O)(2pyN2Q)]^{2+}$ performed the oxidation of ethylbenzene faster than a related oxomanganese(IV) complex, $[Mn^{IV}(O)(Bn\text{-}TPEN)]^{2+}$, which has previously been

characterized to cleave the strong C-H bonds of cyclohexane.[4] This suggested that $[Mn^{IV}(O)(2pyN2Q)]^{2+}$ should be capable of oxidizing even stronger C-H bonds than previously investigated. When probed, HAT reactivity of $[Mn^{IV}(O)(2pyN2Q)]^{2+}$ with cyclohexane showed surprising results. The second-order rate constant for cyclohexane oxidation by $[Mn^{IV}(O)(2pyN2Q)]^{2+}$ was much larger than anticipated by the previously determined linear free energy correlation for hydrocarbon oxidation by $[Mn^{IV}(O)(2pyN2Q)]^{2+}$.[3] The explanation of this enhanced reactivity required both the exploration of the reactivity of $[Mn^{IV}(O)(2pyN2Q)]^{2+}$ with a broader range of hydrocarbon substrates and the calculation of bond dissociation enthalpies for this large set of hydrocarbons using a recently validated DFT method.[5] This approach allowed for the more accurate description of the relationship between the barrier energy and the reaction driving force. Further, complementary catalytic investigations of cyclohexane oxidation by $[Mn^{II}(2pyN2Q)](OTf)_2$:PhIO systems display modest turnover numbers.

$[Mn^{IV}(O)(2pyN2Q)]^{2+}$ and $[Mn^{IV}(O)(Bn\text{-}TPEN)]^{2+}$ are the only reported examples of oxomanganese(IV) species capable of reacting with cyclohexane. While the corresponding $[Fe^{IV}(O)(2pyN2Q)]^{2+}$ complex has not been reported, $[Mn^{IV}(O)(2pyN2Q)]^{2+}$ reacted with cyclohexane roughly 150-times faster than the related $[Fe^{IV}(O)(N4py)]^{2+}$.[6] Further, the reactivity with cyclohexane of both $[Mn^{IV}(O)(Bn\text{-}TPEN)]^{2+}$ and its oxoiron(IV) analogue have been reported, with the oxomanganese(IV) species reacting roughly an order of magnitude faster.[4, 6] It had previously been reported that oxoiron(IV) species reacted more rapidly with C-H bonds than their oxomanganese(IV) counterparts.[7] However, this study only investigated weaker C-H bonds (below ~90 kcal mol^{-1}). The enhanced reactivity of $[Mn^{IV}(O)(2pyN2Q)]^{2+}$ and $[Mn^{IV}(O)(Bn\text{-}TPEN)]^{2+}$ suggests that, for stronger C-H bonds, oxomanganese(IV) species perform HAT faster than related oxoiron(IV) species.

To offer further comparison with oxoiron species, an additional oxomanganese(IV) species, $[Mn^{IV}(O)(2pyN2B)]^{2+}$ was prepared. In this ligand, which was prepared by the group of our collaborator, Dr. Ebbe Nordlander, two pyridine groups have been replaced with (*N*-methyl)benzimidazole groups. When the corresponding $[Fe^{IV}(O)(2pyN2B)]^{2+}$ was

characterized by XRD, the benzimidazole (BzIm) groups were shown to elongate the Fe-N_{BzIm} bonds relative to those of the Fe-N_{py}.[8] Further, the replacement of two pyridines with benzimidazole groups allowed for $[Fe^{IV}(O)(2pyN2B)]^{2+}$ to react with C-H bonds roughly two orders of magnitude faster than $[Fe^{IV}(O)(N4py)]^{2+}$.[8] In contrast, XRD of $[Mn^{II}(2pyN2B)](OTf)_2$ revealed that the Mn-N_{BzIm} bond distances were shortened relative to those of $[Mn^{II}(N4py)](OTf)_2$ while the Mn-N_{py} bond distances were slightly elongated. Overall, the average Mn-N_{eq} bond distances of $[Mn^{II}(2pyN2B)](OTf)_2$ were shorter than observed for $[Mn^{II}(N4py)](OTf)_2$.

As the kinetic behavior of these new oxomanganese(IV) species had been well investigated, further insight into the electronic structure properties of the complexes was necessary to gain a better understanding of the influences on reactivity. In the absence of structural characterization by X-ray diffraction (XRD), other spectroscopic techniques were necessary to probe the electronic structure. Electronic paramagnetic resonance (EPR) spectroscopy provided evidence that the environment around the metal center was nearly unchanged for $[Mn^{IV}(O)(N4py)]^{2+}$, $[Mn^{IV}(O)(^{DMM}N4py)]^{2+}$, and $[Mn^{IV}(O)(2pyN2Q)]^{2+}$.[3] However, the more rhombic signal observed for $[Mn^{IV}(O)(2pyN2B)]^{2+}$ may indicate a slightly more perturbed first coordination sphere. Further, the shift in the λ_{max} of the near-IR electronic absorption feature showed a correlation with the reaction rate, with higher-energy maximum associated with slower HAT reactivity. Lastly, the use of X-ray absorption spectroscopy (XAS) was necessary to gain structural insights into these complexes. XAS confirmed the very minor ligand perturbations resulted in very small changes to the Mn-N_{eq} bond distances. Additionally, the use of DFT calculations in which trifluoroethanol molecules were hydrogen bonding with the Mn=oxo helped explain why the long Mn=O bonds determined from EXAFS from EXAFS fitting were longer than what is predicted by DFT.

Lastly, in collaboration with Dr. Elodie Anxolabéhère-Mallart, we described the formation of $[Mn^{III}(O_2)(dpaq)]$ by the reaction of electrochemically generated superoxide and $[Mn^{II}(dpaq)]^+$. This species was characterized by cyclic voltammetry, UV-visible spectroscopy, and EPR spectroscopy. This putative peroxomanganese(III) species was

reduced by one-electron near -1.4 V in a reaction that exhibits a low reorganization energy. This species was less stable then the previously studied phenlato ligand-supported peroxomanganese(III) species, $[Mn^{III}L(O_2)]$.[9] In further contrast to $[Mn^{III}L(O_2)]$, $[Mn^{III}(O_2)(dpaq)]$ exhibited a one-electron reduction rather than a two-electron reduction, which also occurs at a less negative potential with a lower reorganization energy. The exact mechanistic implications of these differences still need to be determined, through the use of simulations of the CV data and DFT calculations to rule out plausible intermediates. This would help to fully shed light on the influences of the amide group *trans* to the peroxo ligand.

6.2 Perspectives and Open Questions

Through this work, the effects of systematic ligand perturbations on the reactivity of oxomanganese(IV) species supported by neutral, pentadentate ligands has been well established. However, there are still some open questions regarding the reactivity of oxomanganese(IV) species. First and foremost is the solvent necessary for these reactions, 2,2,2-trifluoroethanol (TFE). These oxomanganese(IV) species will only form in the presence of TFE. Currently, it is unknown if TFE is necessary for the stability of the oxomanganese(IV) species or if it stabilizes the oxygen atom transfer agent, PhIO. The use of different oxidants to form oxomanganese(IV) seems like the obvious next step in trying to eliminate the use of TFE. We had some early success with the use of *tert*-butyl hydrogen peroxide in acetonitrile. At low temperatures, the near-IR feature indicative of $[Mn^{IV}(O)(N4py)]^{2+}$ became visible, but only briefly. Attempts at optimizing reaction conditions still did not result in a stable, isolable species. However, there are several other oxidants that may be able to form the oxomanganese(IV) species that could lend to more favorable reaction conditions.

Another huge open question is the thermodynamic driving force. Our knowledge on the thermodynamic driving force can currently only be inferred from the one-electron reduction potential of the oxomanganese(IV) species, where a more positive reduction potential correlates well with faster HAT reactivity. A complete description of the thermodynamic driving force could be obtained if the pK_a of the Mn^{III}-OH could be

determined experimentally. This has so far been hampered by the inability to isolate the Mn^{III}-OH that results from HAT from the C-H containing substrate. A ligand exchange with the solvent results in a Mn^{III}-trifluoroethoxy species visible by mass spectrometry. Further, attempts to isolate the Mn^{III}-OH by removing solvent from the reaction mixture has only resulted in the formation of a dinuclear decay product. Moving away from the use of TFE as mentioned above could help in the isolation of the Mn^{III}-OH product as well.

Lastly, the involvement of the one-electron excited state proposed by Nam and Shaik remains unclear.[2] We saw that tuning the equatorial ligand field to make the $d_{x^2-y^2}$ more accessible did enhance reactivity. However, that this also correlated with a change in the one-electron reduction potential of the oxomanganese(IV) species thus making it difficult to describe what is causing the observed rate enhancement. Work at circumventing the excited state reactivity through the use of changing the geometry around the metal center from *pseudo*-octahedral to trigonal-bipyramidal may shed light on this open question.

In spite of these open questions, the knowledge gained from these systematic ligand perturbation studies has helped highlight the potential use of oxomanganese(IV) species in catalytic C-H activation reactions. Before this work, there was only one example of an oxomanganese(IV) species that could react stoichiometrically with the strong bonds of cyclohexane, now there are two. Further, a broader understanding of the differences between oxomanganese(IV) and oxoiron(IV) species has been gained through this work. We have highlighted the conditions in which oxomanganese(IV) species can even outperform their iron counterparts- in the cleavage of strong C-H bonds. Although the basis for this observation is not currently well understood, it shows that there is a lot more to understand about HAT reactivity by oxometal species.

6.3 References

1. Leto, D. F.; Ingram, R.; Day, V. W.; Jackson, T. A., Spectroscopic properties and reactivity of a mononuclear oxomanganese(iv) complex. *Chem. Commun.* **2013,** *49* (47), 5378-5380.

2. Cho, K.-B.; Shaik, S.; Nam, W., Theoretical Investigations into C–H Bond Activation Reaction by Nonheme MnIVO Complexes: Multistate Reactivity with No Oxygen Rebound. *J. Phys. Chem. Lett.* **2012,** *3* (19), 2851-2856.

3. Massie, A. A.; Denler, M. C.; Cardoso, L. T.; Walker, A. N.; Hossain, M. K.; Day, V. W.; Nordlander, E.; Jackson, T. A., Equatorial Ligand Perturbations Influence the Reactivity of Manganese(IV)-Oxo Complexes. *Angew. Chem., Int. Ed. Engl.* **2017,** *56* (15), 4178-4182.

4. Wu, X.; Seo, M. S.; Davis, K. M.; Lee, Y.-M.; Chen, J.; Cho, K.-B.; Pushkar, Y. N.; Nam, W., A Highly Reactive Mononuclear Non-Heme Manganese(IV)–Oxo Complex That Can Activate the Strong C–H Bonds of Alkanes. *J. Am. Chem. Soc* **2011,** *133* (50), 20088-20091.

5. Klein, J. E. M. N.; Dereli, B.; Que Jr., L.; Cramer, C. J., Why metal-oxos react with dihydroanthracene and cyclohexadiene at comparable rates, despite having different C-H bond strengths. A computational study. *Chem. Commun.* **2016,** *52* (69), 10509-10512.

6. Kaizer, J.; Klinker, E. J.; Oh, N. Y.; Rohde, J.-U.; Song, W. J.; Stubna, A.; Kim, J.; Münck, E.; Nam, W.; Que Jr., L., Nonheme FeIVO Complexes That Can Oxidize the C−H Bonds of Cyclohexane at Room Temperature. *J. Am. Chem. Soc* **2004,** *126* (2), 472-473.

7. Chen, J.; Cho, K.-B.; Lee, Y.-M.; Kwon, Y. H.; Nam, W., Mononuclear nonheme iron(iv)-oxo and manganese(iv)-oxo complexes in oxidation reactions: experimental results prove theoretical prediction. *Chem. Commun.* **2015,** *51* (66), 13094-7.

8. Mitra, M.; Nimir, H.; Demeshko, S.; Bhat, S. S.; Malinkin, S. O.; Haukka, M.; Lloret-Fillol, J.; Lisensky, G. C.; Meyer, F.; Shteinman, A. A.; Browne, W. R.; Hrovat, D. A.; Richmond, M. G.; Costas, M.; Nordlander, E., Nonheme Fe(IV) Oxo Complexes of Two New Pentadentate Ligands and Their Hydrogen-Atom and Oxygen-Atom Transfer Reactions. *Inorg. Chem.* **2015,** *54* (15), 7152-7164.

9. Ching, H. Y. V.; Anxolabéhère-Mallart, E.; Colmer, H. E.; Costentin, C.; Dorlet, P.; Jackson, T. A.; Policar, C.; Robert, M., Electrochemical Formation and Reactivity of a Manganese Peroxo Complex: Acid Driven H2O2 Generation vs. O-O Bond Cleavage. *Chemical Science* **2014,** *5* (2304-2310).

Appendix 2

A2.1 X-ray Crystallography of [Mn^{II}(^{DMM}N4py)(OTf)](OTf)$_{0.5}$(ClO_4)$_{0.5}$(CH_3CN)$_{0.25}$ ([Mn^{II}(^{DMM}N4py)(OTf)](OTf)), [Mn^{II}(2pyN2Q)(OH_2)](OTf)$_2$(OH_2)$_2$ ([Mn^{II}(2pyN2Q)(OH_2)](OTf)$_2$) and [Mn^{II}(2pyN2Q)(OTf)](OTf)($C_2H_5OC_2H_5$) ([Mn^{II}(2pyN2Q)(OTf)](OTf)).

Sets of unique diffraction data [4431 ([Mn^{II}(^{DMM}N4py)(OTf)](OTf)), 3908 ([Mn^{II}(2pyN2Q)(OH_2)](OTf)$_2$) and 5243 ([Mn^{II}(2pyN2Q)(OTf)](OTf)) 0.5º([Mn^{II}(^{DMM}N4py)(OTf)](OTf))- or 1.0º([Mn^{II}(2pyN2Q)(OH_2)](OTf)$_2$ and [Mn^{II}(2pyN2Q)(OTf)](OTf))-wide ω- or ϕ-scan frames with scan times of 3-20 seconds] were collected[1] for single-domain ([Mn^{II}(^{DMM}N4py)(OTf)](OTf) and [Mn^{II}(2pyN2Q)(OH_2)](OTf)$_2$) or two-domain ([Mn^{II}(2pyN2Q)(OTf)](OTf)) crystals using monochromated CuKα radiation (λ= 1.54178 Å) on a Bruker Proteum Single Crystal Diffraction System equipped with dual CCD area detectors. Data collection for [Mn^{II}(^{DMM}N4py)(OTf)](OTf) utilized a Platinum 135 CCD detector and Helios high-brilliance multilayer optics and data collection for [Mn^{II}(2pyN2Q)(OH_2)](OTf)$_2$ and [Mn^{II}(2pyN2Q)(OTf)](OTf) utilized a Bruker Apex2 CCD detector and Helios multilayer optics. X-rays were provided with a Bruker MicroSTAR microfocus Cu rotating anode x-ray source operating at 45kV and 60mA. The integrated data[2] were corrected empirically for variable absorption effects using equivalent reflections. The Bruker software package SHELXTL was used to solve all three structures using “direct methods” techniques. All stages of weighted full-matrix least-squares refinement were conducted using F_o^2 data with the SHELXTL XL v2014 software package.[3]

The asymmetric unit of [Mn^{II}(^{DMM}N4py)(OTf)](OTf) contains one ordered [Mn(^{DMM}N4py)(O_3SCF_3)]$^+$ cation and a second [Mn(^{DMM}N4py)(O_3SCF_3)]$^+$ cation with a coordinated triflate ligand that is 52/48 disordered with two slightly different orientations about the Mn-O bond. The asymmetric unit also contains an ordered triflate counterion and a ClO_4^- anion that is 79/21 disordered with two slightly different orientations in the lattice (the perchlorate anion was introduced during the ligand synthesis procedure). An acetonitrile solvent molecule of crystallization is also statistically disordered about the crystallographic inversion center at (1, ½, 1) in the unit cell. Both orientations for the disordered triflate in the second cation were restrained to have bond lengths and angles

similar to those of the ordered triflate in the first cation and the bond lengths and angles for the minor occupancy perchlorate were restrained to have values similar to those of the major occupancy perchlorate.

The monoclinic unit cell of $[Mn^{II}(2pyN2Q)(OTf)](OTf)$ is metrically pseudo-orthorhombic with β = 90.011° and the asymmetric unit contains four crystallographically-independent cation/anion/solvent moieties that are related by non-crystallographic pseudosymmetry. There are four $[Mn(2pyN2Q)(O_3SCF_3)]^+$ cations, four $[O_3SCF_3]^-$ anions and four $C_2H_5OC_2H_5$ solvent molecules of crystallization. The crystal is 93/7 pseudomerohedrally twinned with the two domains related by a 180° rotation about the **c**-axis of the unit cell.

The positional parameters for all nonhydrogen atoms were allowed to vary in least-squares refinement cycles. Nonhydrogen atoms in all three structures, except those of the minor-occupancy perchlorate in $[Mn^{II}(^{DMM}N4py)(OTf)](OTf)$, were included in their respective structural models with anisotropic thermal parameters. Hydrogen atoms in all three structures and the nonhydrogen atoms of the minor-occupancy perchlorate in $[Mn^{II}(^{DMM}N4py)(OTf)](OTf)$ were included in their respective structural models with isotropic thermal parameters. All hydrogen atoms for $[Mn^{II}(2pyN2Q)(OH_2)](OTf)_2$ were located from a difference Fourier and refined in least square refinement cycles as independent isotropic atoms, as were the Cl and O atoms for the minor-occupancy perchlorate in $[Mn^{II}(^{DMM}N4py)(OTf)](OTf)$. Methyl groups for $[Mn^{II}(^{DMM}N4py)(OTf)](OTf)$ and $[Mn^{II}(2pyN2Q)(OTf)](OTf)$ were incorporated into the structural models as an idealized rigid group (using sp^3-hybridized geometry and a C-H bond length of 0.98 Å) with “staggered” geometry. The remaining nonmethyl hydrogen atoms for $[Mn^{II}(^{DMM}N4py)(OTf)](OTf)$ and $[Mn^{II}(2pyN2Q)(OTf)](OTf)$ were included in the structural model as idealized atoms (assuming sp^2- or sp^3-hybridization of the carbon atoms with C-H bond lengths of 0.95 - 1.00 Å). The isotropic thermal parameters of all idealized hydrogen atoms in both structures were fixed at values 1.2 (nonmethyl) or 1.5 (methyl) times the equivalent isotropic thermal parameter of the carbon atom to which they are covalently bonded.

Crystal data and structure refinement details are collected in Tables A2.1 – A2.3, with selected metric parameters for high-precision structures in Tables A2.4 – A2.5. Molecular structures of the Mn^{II} complexes are displayed in Figures 2.3-2.4 and A2.1-A2.2.

The refined structure for $[Mn^{II}(2pyN2Q)(OTf)](OTf)$ is of too low a resolution to provide precise bond lengths and angles (Table A2.3), because of the issues associated with the structure that are described above (*i.e.*, the pseudomerohedral twinning, with the asymmetric unit containing four virtually indistinquishable cations related by noncrystallographic pseudosymmetry). This results in high correlation between metric parameters, which leads to the low precision of this structure. Nonetheless, the molecular composition of the cationic species in this sample can be reliably determined from the available crystallographic data (Figure A2.2); it is $[Mn^{II}(2pyN2Q)(OTf)]^{+}$. The structure of $[Mn^{II}(2pyN2Q)(OH_2)](OTf)_2(OH_2)_2$ is virtually identical to that of $[Mn^{II}(2pyN2Q)(OTf)](OTf)$ (Figure S4) and is of significantly higher precision.

All X-ray structures reported in this work were submitted to the Cambridge Crystallographic Data Center (CCDC) and can be accessed free of charge. The reference numbers are 1522813, 1522814, and 1522815.

Table A2.1. Crystal Data and Structure Refinement for $[Mn^{II}(^{DMM}N4py)(OTf)](OTf)$ ($[Mn(C_{29}H_{33}N_5O_2)(O_3SCF_3)][O_3SCF_3]$)

Identification code	v17c4	
Empirical formula	C31 H33.75 Cl0.50 F4.50 Mn N5.25 O8.50 S1.50	
Formula weight	822.14	
Temperature	100(2) K	
Wavelength	1.54178 Å	
Crystal system	Triclinic	
Space group	P -1	
Unit cell dimensions	a = 12.6301(10) Å	α = 73.6228(19)°.
	b = 17.6284(14) Å	β = 73.4911(19)°.
	c = 17.9078(14) Å	γ = 75.0828(19)°.
Volume	3598.9(5) $Å^3$	
Z	4	
Density (calculated)	1.517 Mg/m^3	
Absorption coefficient	4.859 mm^{-1}	
F(000)	1690	
Crystal size	0.280 x 0.200 x 0.160 mm^3	
Theta range for data collection		3.301 to 68.106°.
Index ranges	-14<=h<=14, -20<=k<=20, -19<=l<=21	
Reflections collected	12930	
Independent reflections	11846 [R(int) = 0.0428]	
Completeness to theta = 66.000°		93.5 %
Absorption correction	Multi-scan	
Max. and min. transmission	1.000 and 0.258	
Refinement method	Full-matrix least-squares on F^2	
Data / restraints / parameters	11846 / 85 / 1049	
Goodness-of-fit on F^2	1.041	
Final R indices [I>2sigma(I)]	R1 = 0.0721, wR2 = 0.2051	
R indices (all data)	R1 = 0.0745, wR2 = 0.2070	
Extinction coefficient	n/a	
Largest diff. peak and hole	0.752 and -0.874 $e.Å^{-3}$	

$R_1 = \Sigma \, ||F_o| - |F_c|| \, / \, \Sigma \, |F_o|$

$wR_2 = \{ \Sigma \, [w(F_o^2 - F_c^2)^2] \, / \, \Sigma \, [w(F_o^2)^2] \}^{1/2}$

Table A2.2. Crystal Data and Structure Refinement for $[Mn^{II}(2pyN2Q)(OH_2)](OTf)_2(OH_2)$ $([Mn(C_{31}H_{25}N_5)(H_2O)][O_3SCF_3]_2\text{-}(H_2O)_2)$.

Identification code	q63f	
Empirical formula	C33 H31 F6 Mn N5 O9 S2	
Formula weight	874.69	
Temperature	200(2) K	
Wavelength	1.54178 Å	
Crystal system	Monoclinic	
Space group	$P2_1/c$	
Unit cell dimensions	a = 13.1591(6) Å	α = 90°.
	b = 13.2877(6) Å	β = 94.185(2)°.
	c = 21.3597(10) Å	γ = 90°.
Volume	3724.9(3) $Å^3$	
Z	4	
Density (calculated)	1.560 Mg/m^3	
Absorption coefficient	4.737 mm^{-1}	
F(000)	1788	
Crystal size	0.430 x 0.220 x 0.125 mm^3	
Theta range for data collection	3.367 to 69.963°.	
Index ranges	-15<=h<=15, -13<=k<=16, -25<=l<=18	
Reflections collected	39872	
Independent reflections	6901 [R(int) = 0.0583]	
Completeness to theta = 66.000°	99.5 %	
Absorption correction	Multi-scan	
Max. and min. transmission	1.000 and 0.490	
Refinement method	Full-matrix least-squares on F^2	
Data / restraints / parameters	6901 / 0 / 629	
Goodness-of-fit on F^2	1.044	
Final R indices [I>2sigma(I)]	R1 = 0.0538, wR2 = 0.1321	
R indices (all data)	R1 = 0.0608, wR2 = 0.1388	
Extinction coefficient	n/a	
Largest diff. peak and hole	0.782 and -0.809 $e.Å^{-3}$	

$R_1 = \Sigma \, ||F_o| - |F_c|| \, / \, \Sigma \, |F_o|$

$wR_2 = \{ \Sigma \, [w(F_o^2 - F_c^2)^2] \, / \, \Sigma \, [w(F_o^2)^2] \}^{1/2}$

Table A2.3. Crystal Data and Structure Refinement for $[Mn^{II}(2pyN2Q)(OTf)](OTf)$ ($[Mn(C_{31}H_{25}N_5)(O_3SCF_3)][O_3SCF_3]$).

Identification code	q32f	
Empirical formula	C37 H35 F6 Mn N5 O7 S2	
Formula weight	894.76	
Temperature	200(2) K	
Wavelength	1.54178 Å	
Crystal system	Monoclinic	
Space group	$P2_1$	
Unit cell dimensions	a = 11.5990(6) Å	α = 90°.
	b = 38.620(2) Å	β = 90.011(3)°.
	c = 17.9612(9) Å	γ = 90°.
Volume	8045.9(7) $Å^3$	
Z	8	
Density (calculated)	1.477 Mg/m^3	
Absorption coefficient	4.362 mm^{-1}	
F(000)	3672	
Crystal size	0.230 x 0.150 x 0.020 mm^3	
Theta range for data collection	1.144 to 70.142°.	
Index ranges	-12<=h<=13, -42<=k<=46, -21<=l<=21	
Reflections collected	123910	
Independent reflections	26457 [R(int) = 0.0797]	
Completeness to theta = 66.000°	99.9 %	
Absorption correction	Multi-scan	
Max. and min. transmission	1.000 and 0.677	
Refinement method	Full-matrix least-squares on F^2	
Data / restraints / parameters	26457 / 1 / 2090	
Goodness-of-fit on F^2	1.019	
Final R indices [I>2sigma(I)]	R1 = 0.0761, wR2 = 0.1886	
R indices (all data)	R1 = 0.0953, wR2 = 0.2069	
Absolute structure parameter	0.196(3)	
Extinction coefficient	n/a	
Largest diff. peak and hole	1.561 and -1.238 $e.Å^{-3}$	

$R_1 = \Sigma \, ||F_o| - |F_c|| \, / \, \Sigma \, |F_o|$

$wR_2 = \{ \Sigma \, [w(F_o^2 - F_c^2)^2] \, / \, \Sigma \, [w(F_o^2)^2] \}^{1/2}$

Table A2.4. Selected Bond Lengths (Å) and Angles (°) for $[Mn^{II}(^{DMM}N4py)(OTf)](OTf)$.

bond	distance	bonds	angles	bonds	angles
Mn(1)–O(11)	2.114(3)	O(11)–Mn–N(11)	168.28(13)	N(11)–Mn–N(15)	74.36(13)
Mn(1)–N(11)	2.278(4)	O(11)–Mn–N(12)	113.07(13)	N(12)–Mn–N(13)	90.29(13)
Mn(1)–N(12)	2.296(4)	O(11)–Mn–N(13)	110.47(14)	N(12)–Mn–N(14)	150.76(13)
Mn(1)–N(13)	2.189(4)	O(11)–Mn–N(14)	95.30(13)	N(12)–Mn–N(15)	81.19(12)
Mn(1)–N(14)	2.225(3)	O(11)–Mn–N(15)	97.83(13)	N(13)–Mn–N(14)	86.05(13)
Mn(1)–N(15)	2.293(3)	N(11)–Mn–N(12)	74.87(13)	N(13)–Mn–N(15)	151.53(13)
		N(11)–Mn–N(13)	77.20(13)	N(14)–Mn–N(15)	88.33(12)
		N(11)–Mn–N(14)	76.02(13)	S(1)-O(11)-Mn(1)	126.8(2)
Mn(2)–O(21)[a]	2.118(6)	O(21)[a]–Mn–N(21)	170.6(2)	N(21)–Mn–N(25)	75.91(13)
Mn(2)–N(21)	2.276(3)	O(21)[a]–Mn–N(22)	112.96(19)	N(22)–Mn–N(23)	93.62(13)
Mn(2)–N(22)	2.326(3)	O(21)[a]–Mn–N(23)	109.1(2)	N(22)–Mn–N(24)	148.49(12)
Mn(2)–N(23)	2.181(4)	O(21)[a]–Mn–N(24)	95.3(2)	N(22)–Mn–N(25)	80.12(12)
Mn(2)–N(24)	2.219(4)	O(21)[a]–Mn–N(25)	98.2(2)	N(23)–Mn–N(24)	89.73(13)
Mn(2)–N(25)	2.240(3)	N(21)–Mn–N(22)	73.63(12)	N(23)–Mn–N(25)	152.22(13)
		N(21)–Mn–N(23)	76.36(13)	N(24)–Mn–N(25)	82.43(12)
		N(21)–Mn–N(24)	76.78(12)	S(2)–O(21)[a]–Mn(2)	125.8(5)

[a] The triflate molecule in the second fragment is disordered over two positions; we include metric parameters for one of these.

Table A2.5. Selected Bond Lengths (Å) and Angles (°) for $[Mn^{II}(2pyN2Q)(OH_2)](OTf)_2(OH_2)_2$.

bond	distance	bonds	angles	bonds	angles
Mn–O(1W)	2.091(2)	O(1W)–Mn–N(1)	163.83(10)	N(1)–Mn–N(5)	77.27(8)
Mn–N(1)	2.279(2)	O(1W)–Mn–N(2)	95.51(9)	N(2)–Mn–N(3)	80.72(8)
Mn–N(2)	2.297(2)	O(1W)–Mn–N(3)	92.99(9)	N(2)–Mn–N(4)	150.04(9)
Mn–N(3)	2.303(2)	O(1W)–Mn–N(4)	113.59(10)	N(2)–Mn–N(5)	86.79(9)
Mn–N(4)	2.250(2)	O(1W)–Mn–N(5)	114.54(9)	N(3)–Mn–N(4)	90.36(8)
Mn–N(5)	2.265(2)	N(1)–Mn–N(2)	73.42(8)	N(3)–Mn–N(5)	150.78(9)
		N(1)–Mn–N(3)	73.88(9)	N(4)–Mn–N(5)	87.43(8)
		N(1)–Mn–N(4)	76.63(9)		

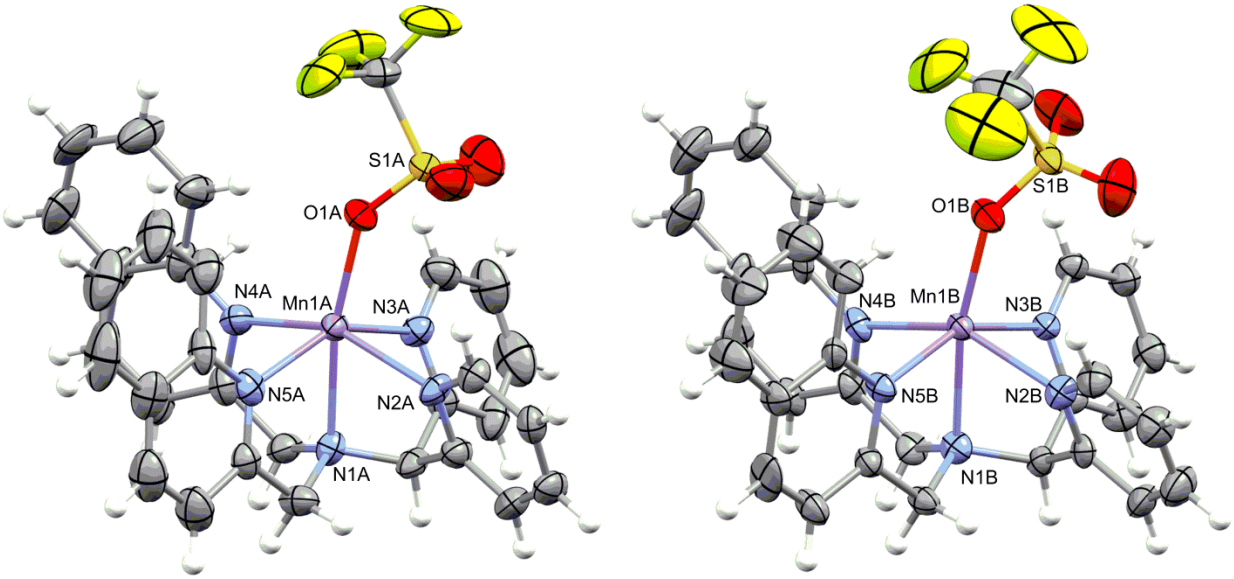

Figure A2.1. Molecular structures of the two $[Mn^{II}(2pyN2Q)(OTf)]^{+}$ cations found in the asymmetric unit of $[Mn^{II}(2pyN2Q)(OTf)](OTf)$.

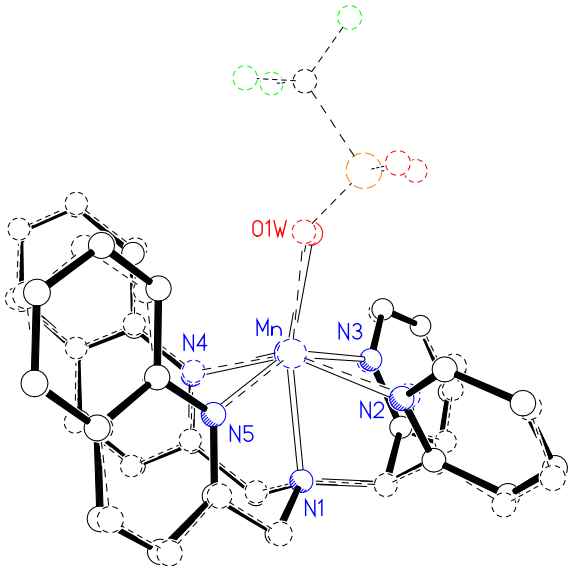

Figure A2.2. Overlay of molecular structures of cationic portions of $[Mn^{II}(2pyN2Q)(OH_2)]^{+}$ (solid lines) and $[Mn^{II}(2pyN2Q)(OTf)]^{+}$ (dashed lines).

A2.2. Supporting Figures

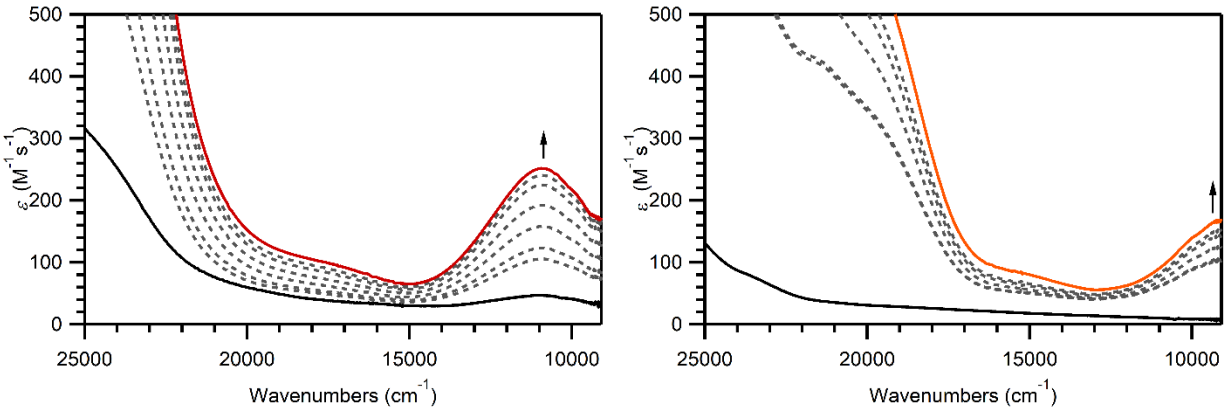

Figure A2.3. UV-Vis electronic absorption of the formation of $[Mn^{IV}(O)(^{DMM}N4py)]^{2+}$ (left) and $[Mn^{IV}(O)(2pyN2Q)]^{2+}$(right).

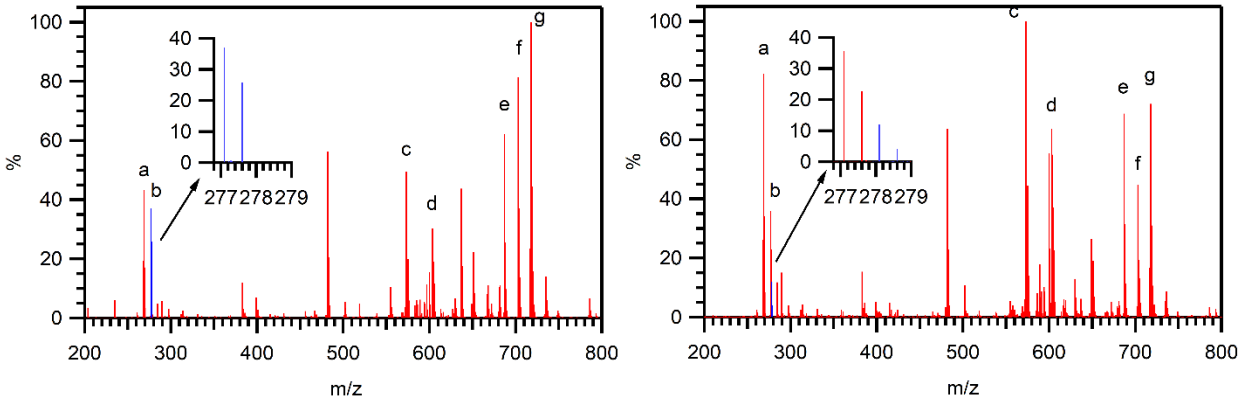

Figure A2.4. ESI-MS spectra of $[Mn^{IV}(O)(^{DMM}N4py)]^{2+}$ (left) and $[Mn^{IV}(^{18}O)(^{DMM}N4py)]^{2+}$ (right). Peak assignments are as follows:
a) $[Mn^{II}(^{DMM}N4py)]^{2+}$ b) $[Mn^{IV}(O)(^{DMM}N4py)]^{2+}$ (left), $[Mn^{IV}(^{18}O)(^{DMM}N4py)]^{2+}$ (right), c) $[Mn^{II}(^{DMM}N4py)](Cl)^{+}$, d) contaminant observed in blank scan, e) $[Mn^{II}(^{DMM}N4py)](OTf)^{+}$, f) $[Mn^{IV}(O)(^{DMM}N4py)](OTf)^{2+}$ (left), $[Mn^{IV}(^{18}O)(^{DMM}N4py)](OTf)^{2+}$ (right), g) $[Mn^{II}(^{DMM}N4py)](CH_3OH)(OTf)^{+}$.

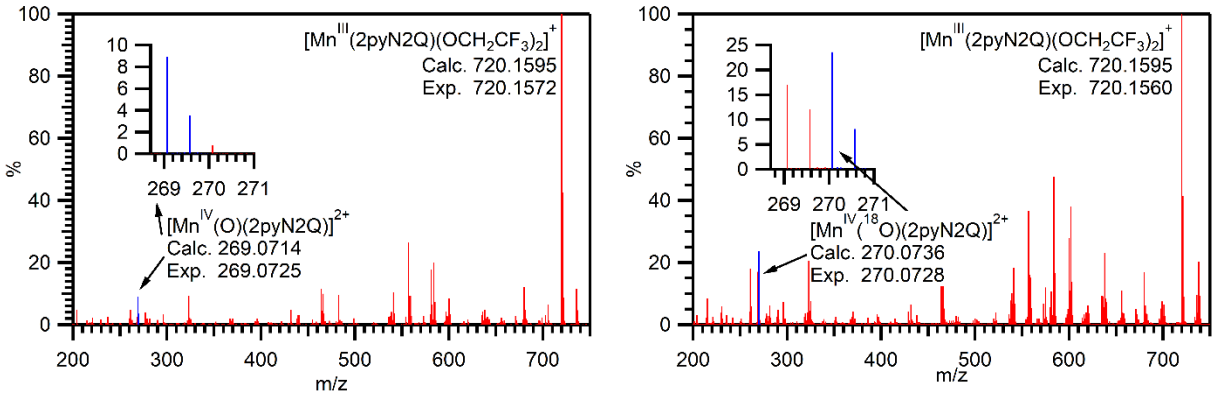

Figure A2.5. ESI-MS spectra of $[Mn^{IV}(O)(2pyN2Q)]^{2+}$ (left) and $[Mn^{IV}(^{18}O)(2pyN2Q)]^{2+}$ (right).

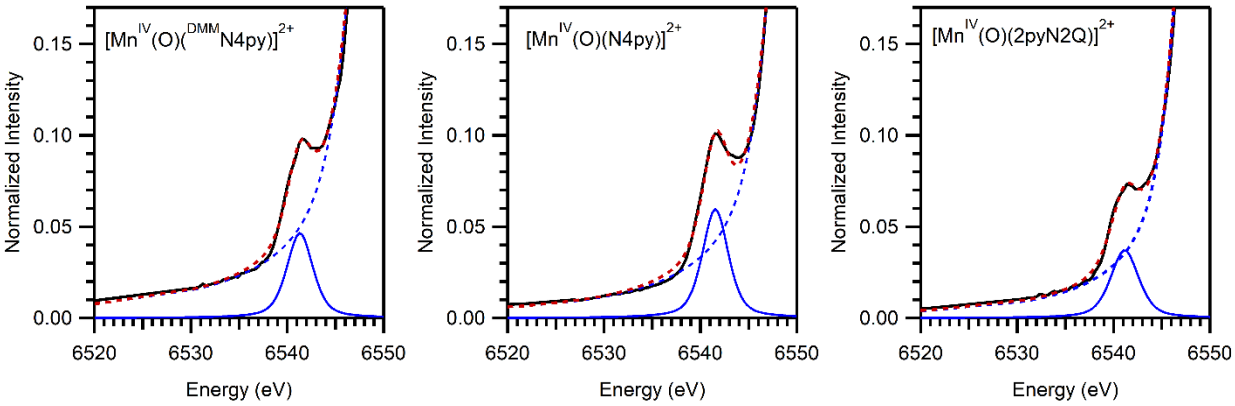

Figure A2.6. Pre-edge data (solid black trace) and fits (dashed red trace) for $[Mn^{IV}(O)(^{DMM}N4py)]^{2+}$ (left), $[Mn^{IV}(O)(N4py)]^{2+}$ (middle), and $[Mn^{IV}(O)(2pyN2Q)]^{2+}$ (right). Dashed blue traces represent the fit of the background and solid blue traces represent fits to the pre-edge peak.

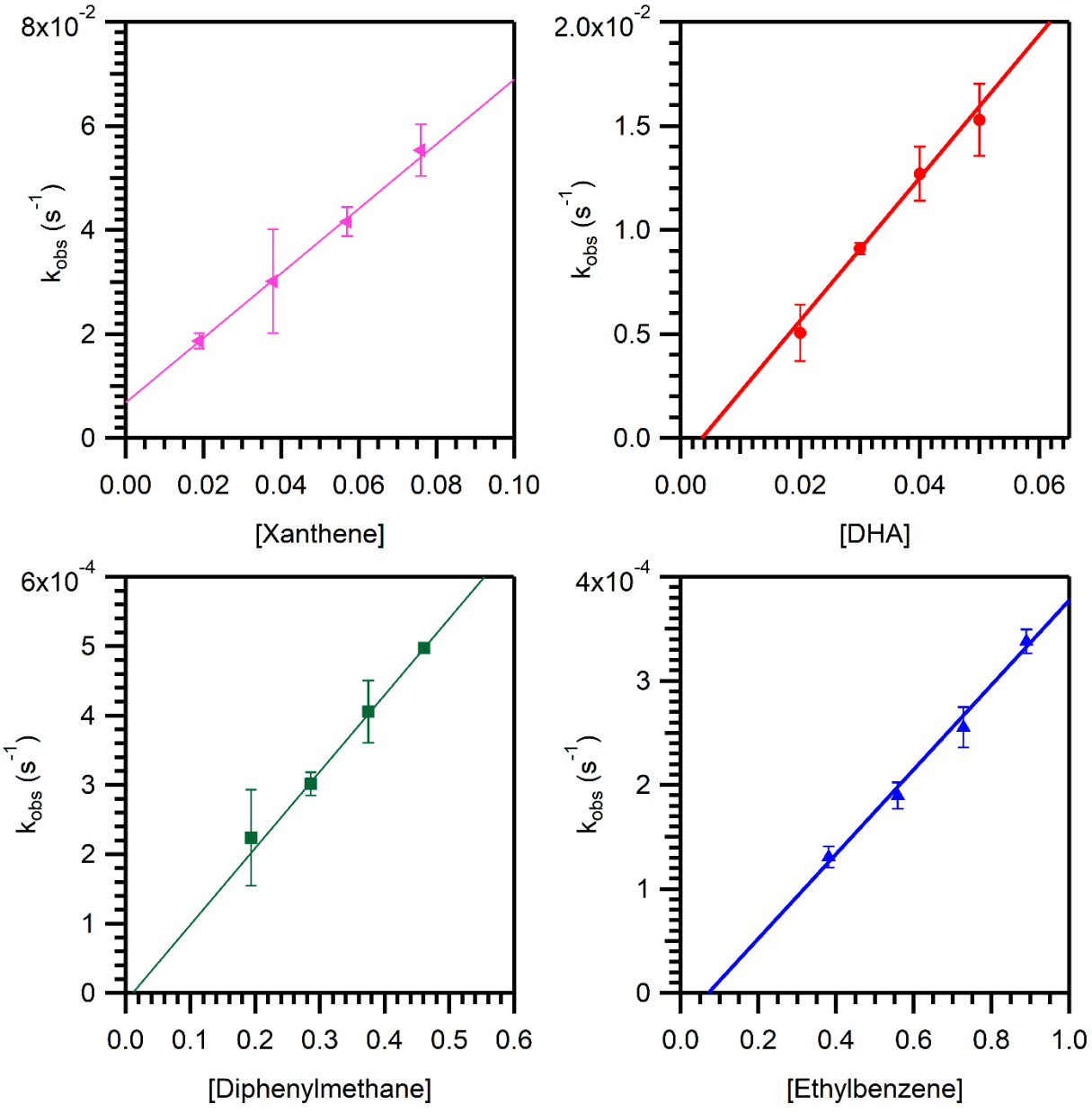

Figure A2.7. Plots of pseudo-first order rate constants (k_{obs}) versus substrate concentration for reaction of 2.0 mM $[Mn^{IV}(O)(^{DMM}N4py)]^{2+}$ and xanthene (top left) 9,10-dihydroanthracene (top right), diphenylmethane (bottom left), and ethylbenzene (bottom right) at 298 K.

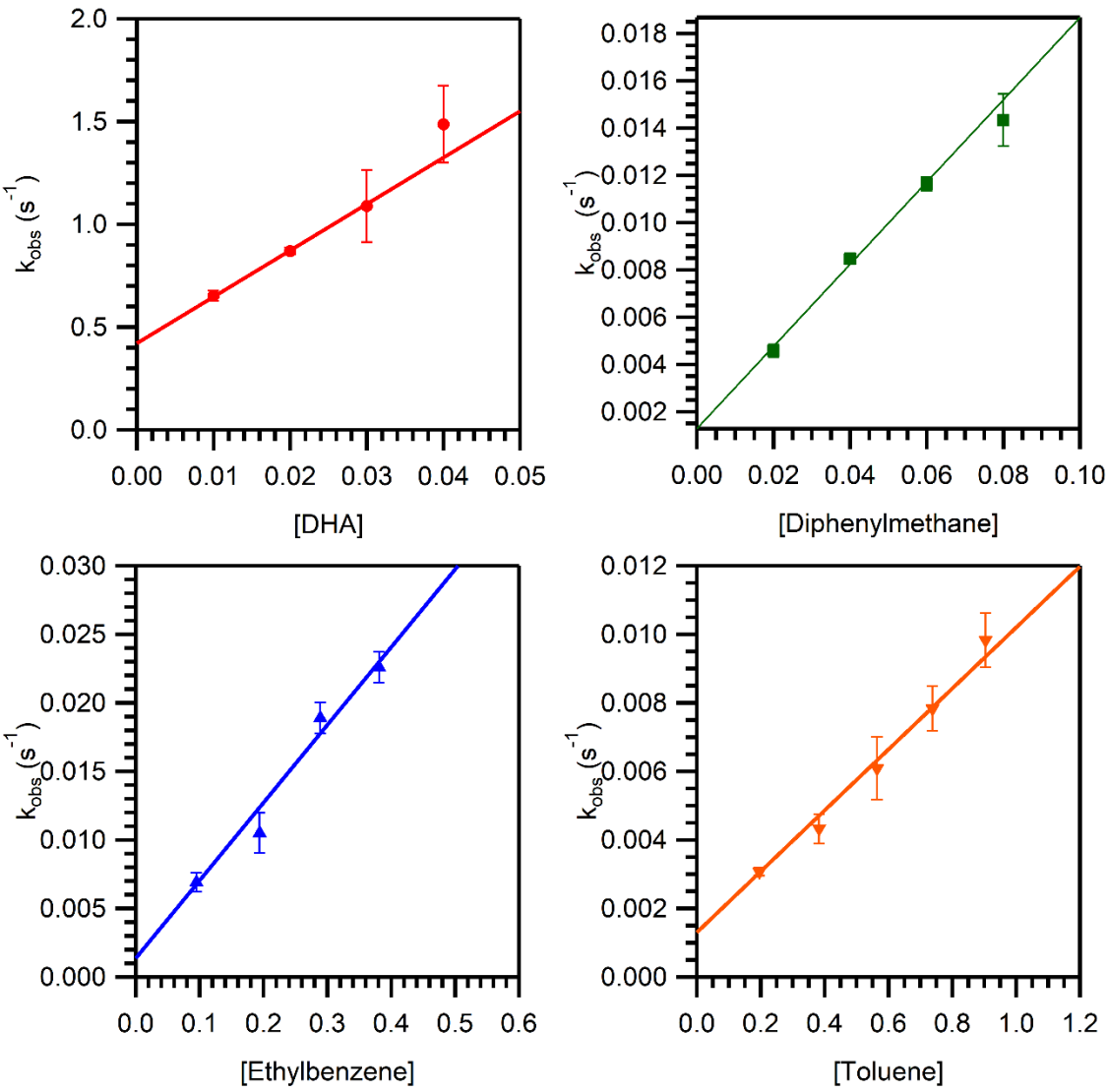

Figure A2.8. Plots of pseudo-first order rate constants (k_{obs}) versus substrate concentration for reaction of 2.0 mM $[Mn^{IV}(O)(2pyN2Q)]^{2+}$ and 9,10-dihydroanthracene (top left), diphenylmethane (top right), ethylbenzene (bottom left), and toluene (bottom right) at 298 K.

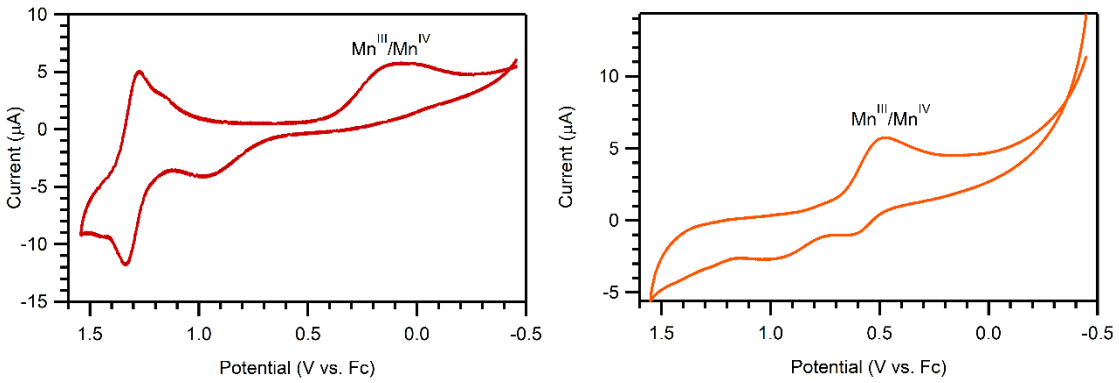

Figure A2.9. Cyclic voltammograms of $[Mn^{IV}(O)(^{DMM}N4py)]^{2+}$ (left) and $[Mn^{IV}(O)(2pyN2Q)]^{2+}$ (right) recorded in TFE with 0.1 M Bu_4NPF_6 electrolyte solution at 50 mV s^{-1}.

A2.3 Electronic Structure Coordinates

Table A2.6. Cartesian Coordinates for $[Mn^{IV}(O)(^{DMM}N4py)]^{2+}$ Optimized by DFT Computations.

Atom	x	y	z
Mn	-0.191220	0.556681	0.932623
O	0.240110	2.118671	1.363413
N	0.440561	-0.353565	2.583713
N	1.486848	0.075582	-0.019886
N	-2.106292	0.559202	1.637982
N	-1.102995	0.967411	-0.846190
C	0.169367	-1.687575	2.703587
C	-2.870680	-0.383752	1.024327
C	1.519669	-1.134296	-0.654156
N	-0.741415	-1.404002	0.388886
C	-1.966643	-0.018495	-1.209605
C	-0.913927	2.038143	-1.641853
C	-2.629720	1.343547	2.600319
C	0.625783	-2.426784	3.794755
C	-4.756977	0.221456	2.389088
C	2.671072	-1.585730	-1.299201
C	-0.728826	-2.266944	1.621185
C	0.200266	-1.891152	-0.678782
C	2.587943	0.858029	-0.017325
C	1.161684	0.269883	3.540631
C	1.672662	-0.358758	4.679984
C	-2.131985	-1.075259	-0.119514
C	3.836659	-0.748210	-1.280602
C	-2.467348	1.140359	-3.257386
C	1.398755	-1.753456	4.799516
C	-1.587381	2.156705	-2.863238
C	3.799559	0.519006	-0.626862
C	-3.963060	1.199998	3.001360

C	-4.205411	-0.585317	1.378408
C	-2.666677	0.031961	-2.415801
C	0.330893	-3.894796	3.985603
C	2.749278	-2.901397	-2.034958
C	2.451493	0.501547	5.656515
O	4.863716	-1.315086	-1.936905
O	1.768571	-2.591739	5.783286
C	4.927977	1.528373	-0.536590
C	2.568865	-2.247135	6.949421
C	6.191885	-0.744890	-2.110972
H	-0.220737	2.794331	-1.263634
H	-1.953271	2.090836	3.023836
H	-5.801137	0.087715	2.688407
H	-0.427252	-3.291869	1.352461
H	-1.761278	-2.327751	2.007643
H	0.356165	-2.976040	-0.567441
H	-0.283023	-1.736176	-1.659337
H	2.467159	1.809919	0.508440
H	1.323929	1.337328	3.363544
H	-2.681179	-1.959461	-0.486350
H	-3.001949	1.208483	-4.209930
H	-1.423445	3.038450	-3.488746
H	-4.368024	1.853319	3.779016
H	-4.805185	-1.350198	0.876473
H	-3.355182	-0.771319	-2.694045
H	1.268432	-4.468020	4.081212
H	-0.259212	-4.321560	3.162069
H	-0.225141	-4.054503	4.925332
H	3.562033	-3.525104	-1.626018
H	2.995865	-2.731958	-3.097147
H	1.811024	-3.472333	-1.988121
H	3.493725	0.163788	5.771247
H	1.986733	0.521415	6.655058
H	2.479606	1.538334	5.287467
H	5.809763	1.124537	-0.014287
H	4.585363	2.409226	0.027838
H	5.250576	1.879969	-1.529555
H	2.663038	-3.195513	7.494108
H	2.047254	-1.508089	7.573712
H	3.563090	-1.889677	6.646240
H	6.732452	-1.507036	-2.687079
H	6.680559	-0.595388	-1.137799
H	6.140502	0.190891	-2.685089

Table A2.7. Cartesian Coordinates for $[Mn^{IV}(O)(2pyN2Q)]^{2+}$ Optimized by DFT Computations.

Aatom	x	y	z
Mn	8.102715	2.812005	9.156300
O	8.301902	2.584991	10.806986
N	10.056915	2.395412	8.734568
N	8.148169	3.273268	7.098977
N	8.767574	4.742739	9.225082
N	7.544715	0.941976	8.476986
N	6.141325	3.440734	9.000692
C	10.871351	1.579164	9.432139
C	12.189484	1.353659	9.019469
C	12.662587	1.993186	7.866691
C	11.811186	2.856883	7.155783
C	10.509591	3.036884	7.624362
C	8.135488	1.987817	6.336689
C	9.474434	4.004266	7.061851
C	9.360696	5.142729	8.068625
C	9.869372	6.432530	7.915627
C	9.762450	7.324603	8.997165
C	9.162557	6.895097	10.188044
C	8.673281	5.586509	10.272040
C	6.965683	4.135587	6.797509
C	7.494068	0.869136	7.128466
C	6.963356	-0.240139	6.437064
C	6.489606	-1.323796	7.156648
C	6.565478	-1.315541	8.570732
C	7.111794	-0.151243	9.232199
C	7.220319	-0.159279	10.644765
C	6.243286	-2.404036	10.728976
C	6.800116	-1.267517	11.369441
C	5.828054	3.880514	7.761621
C	4.511442	4.195427	7.366419
C	3.481012	4.068393	8.281821
C	3.762388	3.644766	9.603006
C	5.129158	3.332213	9.957910
C	5.413258	2.937383	11.288349
C	4.389032	2.847500	12.221882
C	3.043907	3.134299	11.876182
C	6.128733	-2.425263	9.350449
C	2.737937	3.527988	10.585958
H	10.439289	1.127633	10.328266
H	12.832168	0.688886	9.603433
H	13.688518	1.828971	7.523418
H	12.156904	3.378397	6.258627
H	7.637062	2.116398	5.360805
H	9.181160	1.700482	6.127563
H	9.746441	4.363406	6.055187
H	10.341743	6.736232	6.976937
H	10.151532	8.343421	8.908195
H	9.076050	7.560224	11.051791
H	8.209387	5.177434	11.172846
H	6.636613	3.998818	5.753115
H	7.273949	5.191140	6.901311

H	6.938268	-0.231103	5.343377
H	6.066469	-2.193228	6.642645
H	7.653831	0.712266	11.142051
H	5.914287	-3.261059	11.324223
H	6.905440	-1.262738	12.459287
H	4.323630	4.538843	6.345408
H	2.449862	4.300608	7.995899
H	6.449264	2.722858	11.561094
H	4.628095	2.550874	13.248162
H	2.255943	3.050647	12.630699
H	5.711568	-3.296026	8.834211
H	1.708612	3.765057	10.298849

Table A2.8. Selected Metric Parameters for DFT-derived Structures of $[Mn^{IV}(O)(^{DMM}N4py)]^{2+}$ and **2-2pyN2Q**.

$[Mn^{IV}(O)(^{DMM}N4py)]^{2+}$ [a]					
bond	distances	bonds	angles	bonds	angles
Mn–O(1)	1.678	O(1)–Mn–N(1)	179.76	N(1)–Mn–N(5)	82.63
Mn–N(1)	2.108	O(1)–Mn–N(2)	98.71	N(2)–Mn–N(3)	83.21
Mn–N(2)	2.041	O(1)–Mn–N(3)	98.71	N(2)–Mn–N(4)	163.32
Mn–N(3)	2.041	O(1)–Mn–N(4)	97.55	N(2)–Mn–N(5)	90.47
Mn–N(4)	1.988	O(1)–Mn–N(5)	97.55	N(3)–Mn–N(4)	90.67
Mn–N(5)	1.989	N(1)–Mn–N(2)	81.13	N(3)–Mn–N(5)	163.27
		N(1)–Mn–N(3)	81.10	N(4)–Mn–N(5)	91.08
		N(1)–Mn–N(4)	82.61		
2-2pyN2Q[a]					
bond	distances	bonds	angles	bonds	angles
Mn–O(1)	1.678	O(1)–Mn–N(1)	170.63	N(1)–Mn–N(5)	83.28
Mn–N(1)	2.109	O(1)–Mn–N(2)	93.55	N(2)–Mn–N(3)	83.59
Mn–N(2)	2.042	O(1)–Mn–N(3)	93.22	N(2)–Mn–N(4)	162.79
Mn–N(3)	2.043	O(1)–Mn–N(4)	103.18	N(2)–Mn–N(5)	90.34
Mn–N(4)	2.066	O(1)–Mn–N(5)	103.47	N(3)–Mn–N(4)	91.37
Mn–N(5)	2.066	N(1)–Mn–N(2)	79.78	N(3)–Mn–N(5)	162.58
		N(1)–Mn–N(3)	79.58	N(4)–Mn–N(5)	89.67
		N(1)–Mn–N(4)	83.13		

[a] The atom numbering scheme refers to that used in Figures 2.3 and 2.4.

Table A2.9. Energies (eV) and Compositions (%) of the Mn 3d-, O 2p-, and N 2p-Based MOs from Spin-Unrestricted B3LYP DFT Computations for $[Mn^{IV}(O)(^{DMM}N4py)]^{2+}$.

orbital	description	occupancy	spin	energy	Mn 3d	O 2p	N 2p[a]
130 α	Mn d_{xy} / ^{DMM}N4py σ	1.0	↑	-10.212	21.0	4.5	12.4
132 α	Mn d_{xy} / ^{DMM}N4py σ	1.0	↑	-9.828	15.2	4.2	13.3
135 α	Mn d_{xy} / ^{DMM}N4py σ	1.0	↑	-9.170	16.3	3.4	17.9
141 α	^{DMM}N4py π	1.0	↑	-7.707	0.0	0.0	0.2
144 α	Mn d_{yz}	1.0	↑	-7.295	31.3	59.0	4.1
145 α	Mn d_{xz}	1.0	↑	-7.291	31.8	59.0	4.3
146 α	Mn $d_{x^2-y^2}$	0.0	↑	-3.025	63.2	0.0	19.7
150 α	Mn d_{z^2}	0.0	↑	-1.971	52.2	20.5	6.1
141 β	^{DMM}N4py π	1.0	↓	-7.651	2.8	0.1	19.8
142 β	^{DMM}N4py π	1.0	↓	-7.399	0.4	1.1	16.7
143 β	Mn d_{xy}	0.0	↓	-3.760	54.5	1.1	16.7
145 β	Mn d_{yz}	0.0	↓	-2.555	47.3	23.4	6.0
146 β	Mn d_{xz}	0.0	↓	-2.417	52.6	23.4	4.7
149 β	Mn $d_{x^2-y^2}$	0.0	↓	-1.780	30.0	0.0	15.7
155 β	Mn d_{z^2}	0.0	↓	-0.671	60.4	15.5	4.5

[a] Contributions include the coordinating N atoms of the ^{DMM}N4py ligand.

Table A2.10. Energies (eV) and Compositions (%) of the Mn 3d-, O 2p-, and N 2p-Based MOs from Spin-Unrestricted B3LYP DFT Computations for $[Mn^{IV}(O)(2pyN2Q)]^{2+}$.

orbital	description	occupancy	spin	energy	Mn 3d	O 2p	N 2p[a]
123 α	Mn d_{xy}	1.0	↑	-10.236	18.5	0.1	6.8
129 α	Mn d_{xy}	1.0	↑	-9.265	17.5	2.5	19.4
134 α	2pyN2Q π	1.0	↑	-7.939	0.0	0.4	0.3
136 α	Mn d_{yz}	1.0	↑	-7.531	28.3	54.6	5.3
137 α	Mn d_{xz}	1.0	↑	-7.484	27.4	55.3	5.5
138 α	2pyN2Q π	1.0	↑	-7.426	2.4	1.3	8.6
139 α	2pyN2Q π	1.0	↑	-7.233	0.5	1.0	9.4
140 α	Mn $d_{x^2-y^2}$	0.0	↑	-3.631	62.5	0.3	20.1
141 α	2pyN2Q π	0.0	↑	-3.104	0.1	0.0	30.0
143 α	2pyN2Q π	0.0	↑	-2.755	1.2	0.0	17.7
144 α	Mn d_{z^2}	0.0	↑	-2.398	53.9	20.2	9.8
135 β	2pyN2Q π	1.0	↓	-7.478	0.1	1.5	7.7
136 β	2pyN2Q π	1.0	↓	-7.232	0.0	0.0	9.6
137 β	Mn d_{xy}	0.0	↓	-4.041	58.6	0.0	2.3
138 β	2pyN2Q π	0.0	↓	-3.082	0.7	0.8	21.1
139 β	Mn d_{yz}	0.0	↓	-2.878	38.5	19.8	7.9
140 β	Mn d_{xz}	0.0	↓	-2.802	58.3	28.2	3.1
143 β	Mn $d_{x^2-y^2}$	0.0	↓	-2.248	49.8	0.3	15.5
149 β	Mn d_{z^2}	0.0	↓	-1.090	59.7	14.6	8.7

[a] Contributions include the coordinating N atoms of the 2pyN2Q ligand.

Table A2.11. TD-DFT Calculated Energies (cm^{-1}), Oscillator Strengths, and Contributions from Dominant One-Electron Excitations for the Major Electronic Transitions of $[Mn^{IV}(O)(^{DMM}N4py)]^{2+}$ and $[Mn^{IV}(O)(2pyN2Q)]^{2+}$.

band	state	energy	$f_{osc} \times 10^3$	transition[a]	%	donor MO	acceptor MO	comments
$[Mn^{IV}(O)(^{DMM}N4py)]^{2+}$								
i	1	14 601	4.77	145 α→146 α	82	Mn d_{xz}	Mn $d_{x^2-y^2}$	Mn^{IV} d→d
	2	14 659	4.17	144 α →146 α	81	Mn d_{yz}	Mn $d_{x^2-y^2}$	Mn^{IV} d→d
ii	5	21 748		145 α →150 α	76	Mn d_{xz}	Mn d_{z^2}	Mn^{IV} d→d
	6	21 774		144 α →150 α	79	Mn d_{yz}	Mn d_{z^2}	Mn^{IV} d→d
	8	22 942	51.80	142 β→143 β	85	^{DMM}N4py π	Mn d_{xy}	^{DMM}N4py→Mn^{IV} CT
	7	23 258		144 α →146 α	43	Mn d_{yz}	Mn $d_{x^2-y^2}$	Mn^{IV} d→d
				135 α →146 α	18	Mn d_{xy}	Mn $d_{x^2-y^2}$	
				130 α →146 α	11	Mn d_{xy}	Mn $d_{x^2-y^2}$	
				132 α →146 α	11	Mn d_{xy}	Mn $d_{x^2-y^2}$	
	12	24 714	53.34	141 β →143 β	88	^{DMM}N4py π	Mn d_{xy}	^{DMM}N4py→Mn^{IV} CT
iii	22	31 341	9.79	141 α →146 α	95	^{DMM}N4py π	Mn $d_{x^2-y^2}$	^{DMM}N4py→Mn^{IV} CT
$[Mn^{IV}(O)(2pyN2Q)]^{2+}$								
i	1	12 021	3.545	137 α →140 α	82	Mn d_{xz}	Mn $d_{x^2-y^2}$	Mn^{IV} d→d
	2	12 315	5.061	136 α →140 α	83	Mn d_{yz}	Mn $d_{x^2-y^2}$	Mn^{IV} d→d
ii	5	19 120	12.40	136 β →137 β	80	2pyN2Q π	Mn d_{xy}	
	6	20 427	0.044	137 α →144 α	81	Mn d_{xz}	Mn d_{z^2}	Mn^{IV} d→d
	7	20 748	0.463	136 α →144 α	76	Mn d_{yz}	Mn d_{z^2}	Mn^{IV} d→d
	8	21 526	0.199	138 α →140 α	42	2pyN2Q π	Mn $d_{x^2-y^2}$	Mn^{IV} d→d
				129 α →140 α	20	Mn d_{xy}	Mn $d_{x^2-y^2}$	
	9	21 222	12.02	135 β →137 β	58	2pyN2Q π	Mn d_{xy}	2pyN2Q→Mn^{IV} CT
	10	21 590	6.869	139 α →140 α	89	2pyN2Q π	Mn $d_{x^2-y^2}$	2pyN2Q→Mn^{IV} CT
	15	24 023	11.99	135 β →137 β	22	2pyN2Q π	Mn d_{xy}	2pyN2Q→Mn^{IV} CT
				139 α →143 α	16	2pyN2Q π	2pyN2Q π	
				138 α →141 α	15	2pyN2Q π	2pyN2Q π	
iii	24	28 640	6.023	136 α →141 α	40	Mn d_{yz}	2pyN2Q π	2pyN2Q→Mn^{IV} CT
				139 α →141 α	22	2pyN2Q π	2pyN2Q π	
				136 α →138 α	17	2pyN2Q π	2pyN2Q π	
	27	28 898	8.699	136 β →138 β	37	2pyN2Q π	2pyN2Q π	2pyN2Q→Mn^{IV} CT
				136 α →141 α	26	Mn d_{yz}	2pyN2Q π	
				136 β →140 β	18	2pyN2Q π	Mn d_{yz}	

[a] α and β refer to spin-up and spin-down MOs, respectively. MO compositions are collected in Tables A2.9 and A2.10.

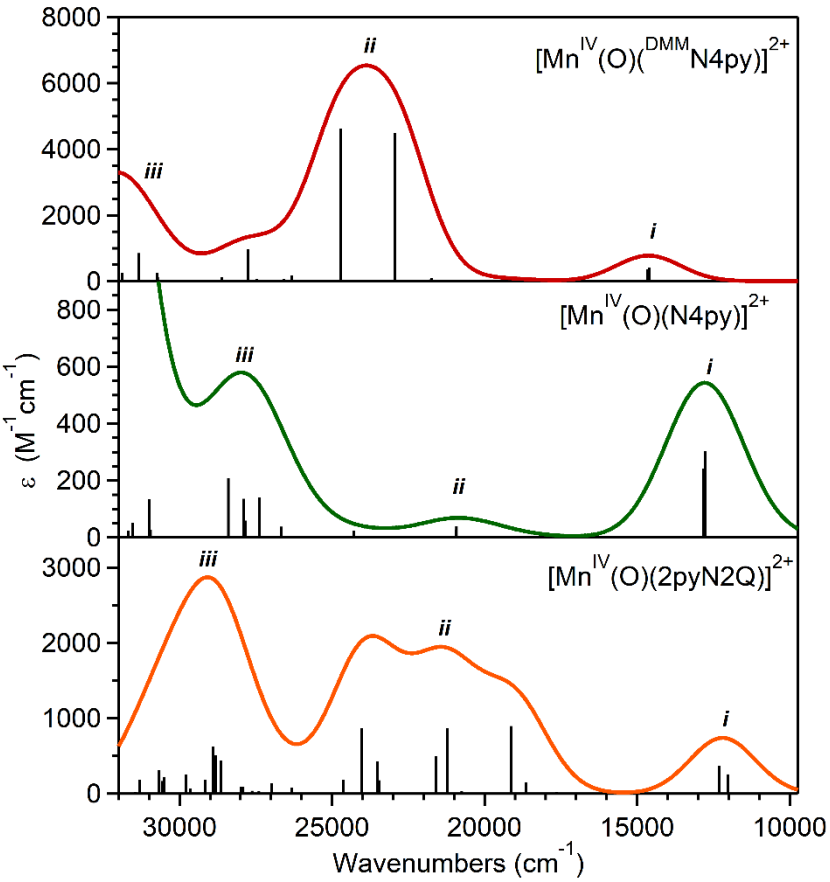

Figure A2.10 TD-DFT-computed electronic absorption spectra of $[Mn^{IV}(O)(N4py)]^{2+}$ (top), $[Mn^{IV}(O)(^{DMM}N4py)]^{2+}$ (center), and $[Mn^{IV}(O)(2pyN2Q)]^{2+}$ (bottom).

A2.4. References

(1) *Data Collection: SMART Software in APEX2 v2014.11-0 Suite* Bruker-AXS. 5465 E. Cheryl Parkway, Madison, WI 53711-5373 USA, 1998.

(2) *Data Reduction: SAINT Software in APEX2 v2014.11-0 Suite* Bruker-AXS, 5465 E. Cheryl Parkway, Madison, WI 53711-5373 USA.

(3) *Refinement: SHELXTL Software in APEX2 v2014.11-0 Suite* Bruker-AXS, 5465 E. Cheryl Parkway, Madison, WI 53711-5373 USA.

Appendix 3

A3.1 Supporting Figures and Tables

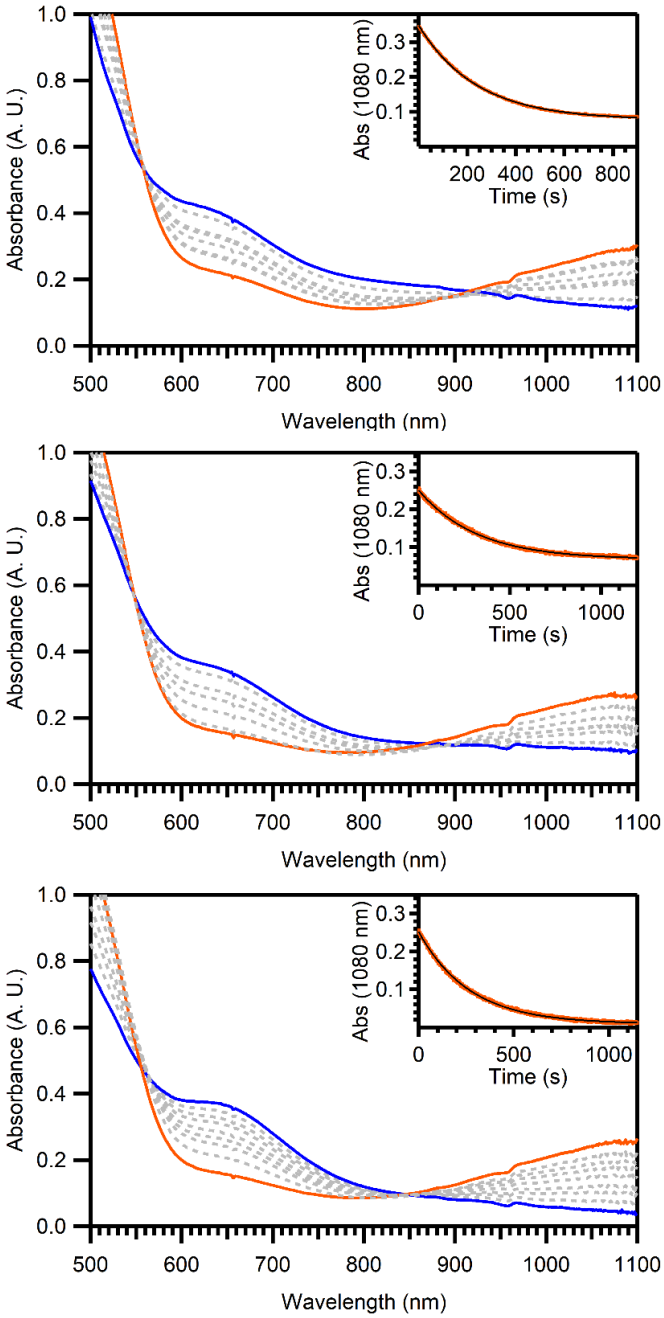

Figure A3.1. Electronic absorption spectra show the reactions of $[Mn^{IV}(O)(2pyN2Q)]^{2+}$ (orange trace) formed with 10 equivalents PhIO in the presence of O_2 (top), 2 equivalents PhIO in the presence of O_2 (middle), and 10 equivalents PhIO under an Ar atmosphere (bottom) with 100 equivalents of cyclohexane in CF_3CH_2OH at 298 K. The decay of the electronic absorption feature at 1080 nm (inset) shows the absorbance versus time (orange dots) along with pseudo-first order fits (black line).

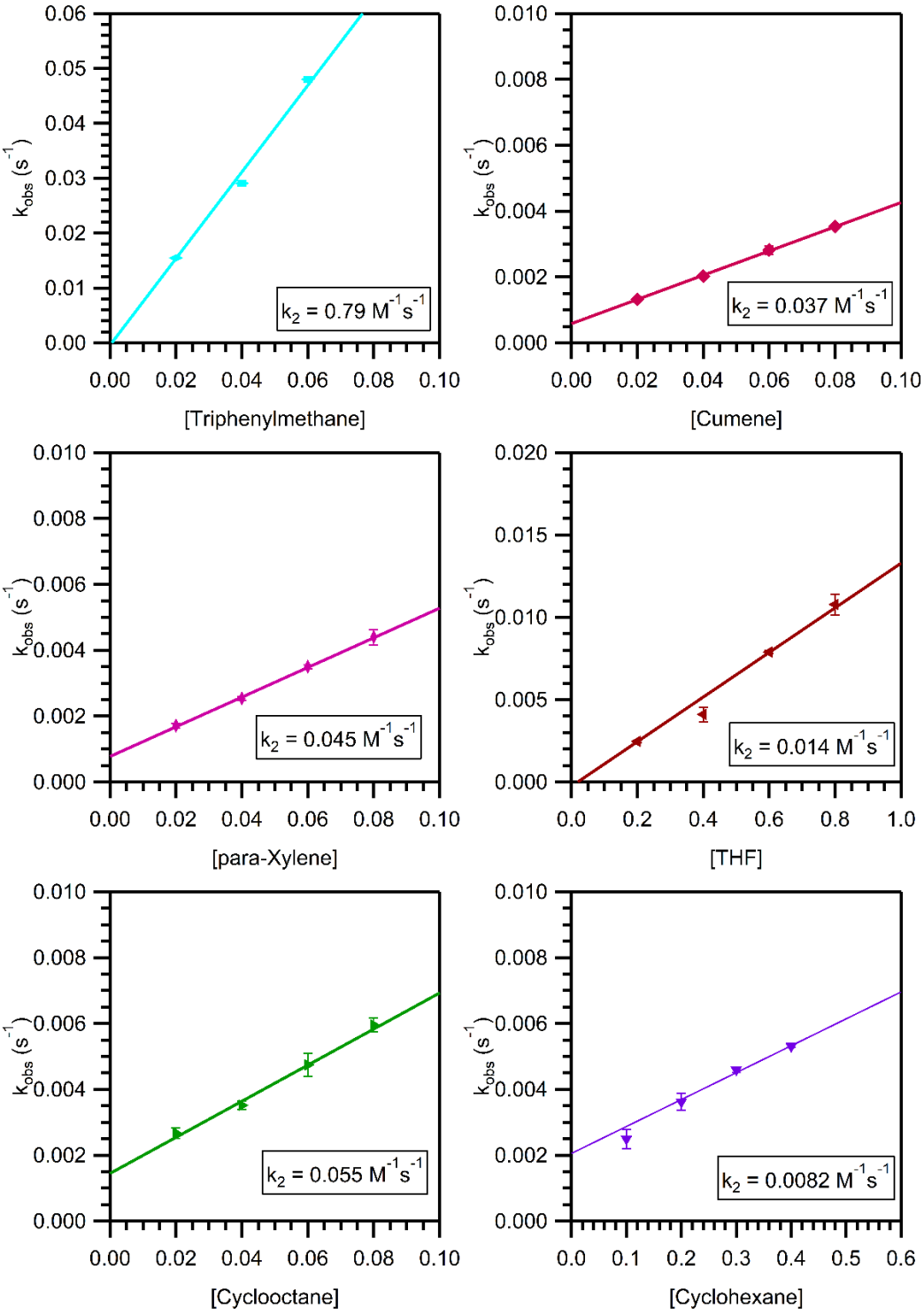

Figure A3.2. Plots of pseudo-first order rate constants (k_{obs}) versus substrate concentration for reactions of triphenylmethane (top-left), cumene (top-right), *para*-xylene (center-left), tetrahydrofuran (center-right), cyclooctane (bottom-left) and cyclohexane (bottom-right) with 2.0 mM $[Mn^{IV}(O)(2pyN2Q)]^{2+}$ at 298 K in CF_3CH_2OH. The non-zero intercepts are within error of the self-decay rate of $[Mn^{IV}(O)(2pyN2Q)]^{2+}$ at 298 K in CF_3CH_2OH.

Table A3.1. Comparison of Tabulated and Calculated Bond Dissociation Enthalpy Values (kcal mol^{-1}).

Substrate	Mayer[1]	Luo[2]	Calculated (TFE)[a]	Calculated (MeCN)[b]
Cyclohexadiene	76.0[c]	76±1.2	75.4	[g]
Xanthene	77.9[d]	74, 75.5, 75.2, 80.7	76.7	[g]
Dihydroanthracene	80.6[d]	76.3	78	[g]
Fluorene	82.0[d]	82.0±2	82.5	[g]
Triphenylmethane	83.4[d]	81±2	78.9	[g]
Diphenylmethane	84.3[d]	84.5±0.5	84.1	[g]
Cumene	[e]	[e]	85.5	85.7
para-Xylene	87.0[f]	87.7, 89.0	90.2	[g]
Ethylbenzene	[e]	85.4±1.5	86.4	86.7
Toluene	92[d]	89.7 ± 1.2[c]	90.5	90.0
THF	[e]	92.1±1.6	93.6	[g]
Cyclooctane	[e]	95.7	94	[g]
2,3-dimethylbutane	[e]	95.4	[g]	94.5
Cyclohexane	[e]	99.5	99	97.8

[a]DFT values calculated with M06-2X functional with the large def2-TZVPP basis set using a continuum dielectric for TFE. [b]DFT values calculated with same parameters using a continuum dielectric for MeCN. [c]Gas phase. [d]DMSO solution. [e]Not listed. [f]Acetonitrile solution. [g]Not determined.

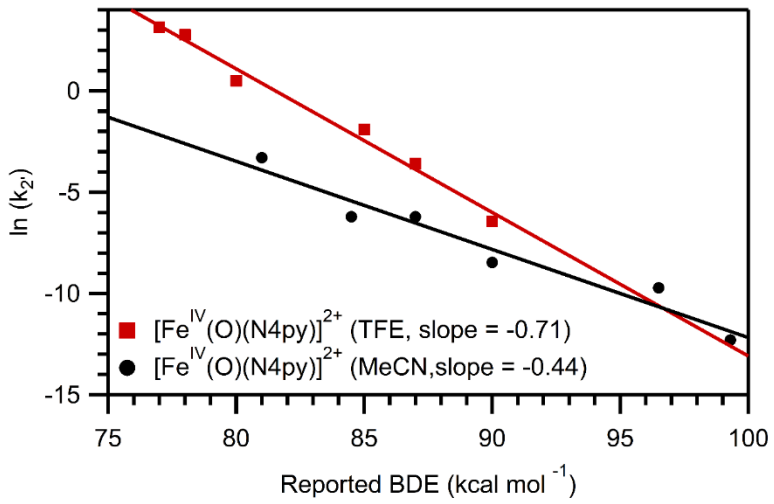

Figure A3.3. Comparison of the second-order rate constants for reactions of $[Fe^{IV}(O)(N4py)]^{2+}$ with various hydrocarbon substrates in acetonitrile and 2,2,2-trifluoroethanol. Rate data and BDE values used are from references 3 and 4.

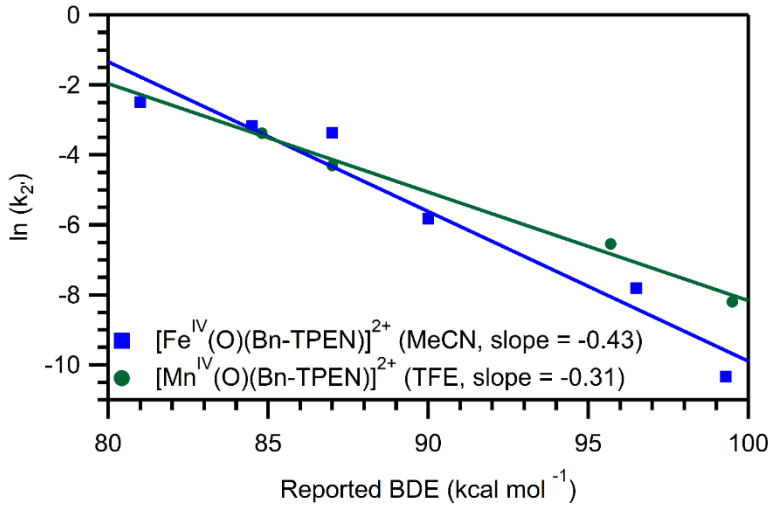

Figure A3.4. Comparison of the second-order rate constants for reactions of $[Mn^{IV}(O)(Bn\text{-}TPEN)]^{2+}$ and $[Fe^{IV}(O)(Bn\text{-}TPEN)]^{2+}$ with various hydrocarbon substrates. Rate data and BDE values used are from references 3 ($[Fe^{IV}(O)(Bn\text{-}TPEN)]^{2+}$) and 5 ($[Mn^{IV}(O)(Bn\text{-}TPEN)]^{2+}$).

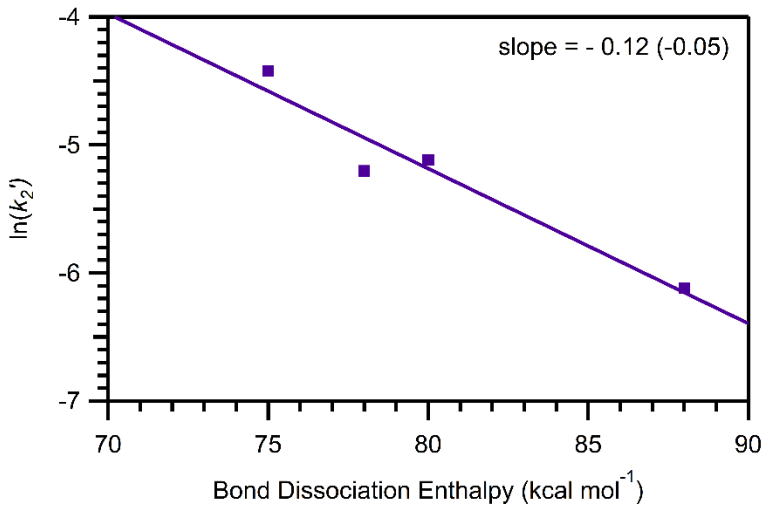

Figure A3.5. Plot of ln(k_2') versus BDE for the reaction of [Mn^{III}(**PY5**)(OH)](CF_3SO_3)$_2$ with hydrocarbon substrates. Rate data and BDE from reference 6.

A3.2 Coordinates for Substrates Optimized by DFT Computations with the M06-2X Functional with the def2-TZVPP Basis Set Using a Continuum Dielectric for 2,2,2-Trifluoroethanol

Xanthene			
C	-3.60023448300128	0.63902875254682	0.51545619359289
C	-3.58588398761475	-0.75272135795453	0.50922537758636
C	-2.39118886350855	-1.42989363768112	0.34394051427855
C	-1.21213060602371	-0.71056688555793	0.18305114235836
C	-1.19850165570355	0.67724787320802	0.18265256058878
C	-2.41420805439903	1.33662362455281	0.35330233964817
O	-0.07964633394249	-1.45953330289782	0.02681759096970
C	1.12614868262783	-0.84495656042088	-0.15716918211007
C	1.26813503303370	0.53548144520181	-0.18231594949828
C	0.08329946047082	1.44100336665309	0.00466846683657
C	2.21497276380685	-1.69512218167477	-0.31671797747167
C	3.47627424912354	-1.16075401503871	-0.50778211186558
C	3.64653205891364	0.22034426503073	-0.54330830396978
C	2.54817594249196	1.04962350416129	-0.38048773672607
H	-4.53096439954375	1.17394077100718	0.64441227046247
H	-4.50481361315922	-1.30962369157782	0.63202727419986
H	-2.34856121804001	-2.51083925413807	0.33543523207279
H	-2.41926924863371	2.41998428857029	0.35762241294726
H	-0.00678138746605	2.11043653225530	-0.85419048231587
H	0.24992129567976	2.08552622571956	0.87143555343683
H	2.05063849055529	-2.76405750767132	-0.28729704674193
H	4.32376979722848	-1.82116376890991	-0.63024644412471
H	4.62902244830555	0.64478325949379	-0.69563075414025
H	2.67529262879870	2.12520825512219	-0.40490394001438

[Xanthene-H]$^{\bullet}$			
C	-3.58557860826522	0.64955373521319	0.45147093835044
C	-3.58321592239298	-0.74553002021240	0.50947127379875
C	-2.39312087654112	-1.44630793322689	0.37484666457022
C	-1.21618992546976	-0.74768563588509	0.17773787055679
C	-1.18234838014570	0.65876284394942	0.10827816226394
C	-2.40725864927731	1.33976353734366	0.25464784180080
O	-0.07751600864375	-1.48270324322081	0.05239664716661
C	1.12410354072001	-0.88261151996351	-0.16331745829296
C	1.22978806888056	0.51949521801478	-0.24675732519005
C	0.05949289815677	1.30171211592727	-0.10485486524516
C	2.22324919857658	-1.71232171619376	-0.29090678278621
C	3.47415012364927	-1.15298699201038	-0.50891759608638
C	3.61555640904859	0.23331439285983	-0.59883815091102
C	2.51407971800949	1.05462674952665	-0.47023965307771
H	-4.51539212575968	1.19090405803053	0.55958765624859
H	-4.50777921734902	-1.28553160142228	0.65869713300390
H	-2.36274440269991	-2.52659988816703	0.41773076863721
H	-2.40466429282600	2.42116776370647	0.20911839404946
H	0.11318751523484	2.37996411501682	-0.16200574235586
H	2.08518764991968	-2.78265404311746	-0.21866118402504
H	4.33680054139319	-1.79659871735029	-0.60926999471545
H	4.59230070456704	0.66454149814009	-0.76935327698825
H	2.61938704121440	2.12964628304118	-0.53920832077260

Fluorene			
C	-3.85440365092302	0.77361230011383	-1.56314003544537
C	-2.94571214109136	0.43396732206828	-0.41138684023216
C	-1.58349144236434	0.64037003250893	-0.27407923923621
C	-0.95786745400173	0.24125147264323	0.90430439366833
C	-1.68545239645780	-0.36128478679822	1.92852388524901
C	-3.05258540749392	-0.57315500130968	1.79541959230258
C	-3.67679317234791	-0.16887934970276	0.62195963679456
C	-5.08093096660161	-0.25205068991742	0.20814373335399
C	-6.19203076779091	-0.75508405276342	0.87249189479992
C	-7.42626689551214	-0.70927016564484	0.23526261659794
C	-7.54501036807908	-0.16659112313571	-1.04230143532463
C	-6.43129411100290	0.34266155911671	-1.70595105411054
C	-5.19843788518289	0.29766420579542	-1.07649164058100
H	-3.85433766695185	1.84504229109547	-1.77622607606364
H	-3.55267018519334	0.26919112101557	-2.48392073898121
H	-1.00885001922943	1.10326112958387	-1.06641075392170
H	0.10605644754406	0.39601287576129	1.02465657916695
H	-1.18012260524462	-0.66701890876598	2.83483780561371
H	-3.61516153280187	-1.04260555235340	2.59248059214699
H	-6.10394574307256	-1.17508431996072	1.86637688635602
H	-8.30341852054439	-1.09811077462661	0.73528108758449
H	-8.51398252670597	-0.14036444591841	-1.52263779240435
H	-6.53298398895041	0.76646686119457	-2.69718809733368

[Fluorene-H]•			
C	-3.86111582847199	0.59832468498999	-1.50412145823396
C	-2.95599198581003	0.34298336410494	-0.42747415796492
C	-1.58004579164865	0.54916734927259	-0.31399501760881
C	-0.94919608123765	0.20331882486351	0.87387447951415
C	-1.67040889743878	-0.34662491249549	1.93471273780305
C	-3.04654127574966	-0.55850260238451	1.83435522551199
C	-3.68639998252870	-0.21113389624687	0.66035396511151
C	-5.08821639657058	-0.29504884489599	0.24663847073598
C	-6.21993843050576	-0.73817318581193	0.90268014231763
C	-7.44401760787727	-0.69271111380120	0.23326890464414
C	-7.53103310190957	-0.20614751038212	-1.07171961094593
C	-6.40106997959934	0.24762351461226	-1.74003072058861
C	-5.16975789236518	0.20547059739562	-1.08272465908610
H	-3.60186163052564	1.01736447212324	-2.46425289776723
H	-1.01460183223722	0.96986776144832	-1.13527173103822
H	0.11640778666331	0.35651000567023	0.97837671290804
H	-1.15537398819577	-0.61332930748211	2.84766672240154
H	-3.59366828895108	-0.98666992968409	2.66476019485208
H	-6.16796780801788	-1.11565101682460	1.91598524137324
H	-8.33820072217001	-1.03878183589673	0.73411566282876
H	-8.49243910629030	-0.18224446195225	-1.56667172867079
H	-6.47435515856228	0.62831804337719	-2.75050447809753

Cyclohexadiene			
C	-1.40311441395349	-0.57429558483754	0.18653027749718
C	-0.04432719708823	-1.20581114954415	0.18675524488082
C	1.06246890961230	-0.19607868603907	0.18647258475870
C	0.86147242214006	1.11693072235005	0.18615154517242
C	-0.49729217418491	1.74844719860897	0.18589999351114
C	-1.60406604364089	0.73872072366120	0.18612529563796
H	-2.25512705617815	-1.24507718607597	0.18671352799397
H	2.07606064210765	-0.58181964806606	0.18657676399279
H	1.71346651593572	1.78773523164195	0.18597510672402
H	-2.61764418884989	1.12449541583455	0.18599464490063
H	-0.59911798491798	2.41101921457361	-0.68051276723270
H	-0.59923958039119	2.41152618877446	1.05190731120492
H	0.05752893251806	-1.86836345663494	1.05317990549563
H	0.05757931689094	-1.86891058424706	-0.67924073453750

[CHD-H]•			
C	-1.37873319035360	-0.56527055893483	0.32132915832181
C	-0.06309101797148	-1.08464504525180	0.38563073360314
C	1.03692469836367	-0.19477952105680	0.32198323867823
C	0.85664843197091	1.14542940153483	0.20738248262403
C	-0.49964141237273	1.76432375345945	0.14136203175867
C	-1.60809806117383	0.76769691779694	0.20870576400648
H	-2.21661449129241	-1.25015252813902	0.36409530254745
H	2.04158560004876	-0.59697996290388	0.36538106822214
H	1.71297489136770	1.80597524781758	0.16059134346450
H	-2.62294601550884	1.14192161526951	0.16271740809636
H	-0.59332869916369	2.36932475032084	-0.77308016943741
H	-0.61317785696249	2.50930140400602	0.94281445621948
H	0.09934012304804	-2.14833507391884	0.48080908189511

Dihydroanthracene			
C	-1.28286043877293	0.69603947747536	-0.00085496727331
C	-1.28299895847463	-0.69593098735388	-0.00018570982653
C	-0.01117758442211	-1.49891033536241	0.00188086576731
C	1.26081259667314	-0.69619547313166	-0.00020279886260
C	1.26095016874451	0.69577444415249	-0.00063551637189
C	-0.01087171601640	1.49875379502960	0.00075807502860
C	2.48171183053034	-1.37740194433524	-0.00128829451788
C	3.68583833857291	-0.69695064035161	-0.00287257675500
C	3.68598099439060	0.69604618929776	-0.00342581244755
C	2.48199007718002	1.37673137980656	-0.00236670139477
C	-2.50375617306569	1.37725146166136	-0.00279051879614
C	-3.70788445778240	0.69680151375516	-0.00386755131930
C	-3.70803075157878	-0.69619499928799	-0.00304109203951
C	-2.50404153903028	-1.37688319476907	-0.00127481878425
H	-0.01126870756557	-2.16554119630491	-0.86522168701989
H	-0.01122797453721	-2.16100414275823	0.87250866601088
H	-0.01089127212189	2.16144206429342	0.87093276950375
H	-0.01071299413158	2.16479494740127	-0.86679807260531
H	2.47563686756609	-2.46132196189572	-0.00082994445459
H	4.61936402095184	-1.24362534306911	-0.00367948635034
H	4.61958592940118	1.24258647937147	-0.00470934171350
H	2.47609599517448	2.46065781946375	-0.00283828067524
H	-2.49767569276501	2.46117084915377	-0.00336412631694
H	-4.64141397355062	1.24347175588592	-0.00531130533061
H	-4.64163500904639	-1.24273379433691	-0.00385640608726
H	-2.49815457632363	-2.46081016379116	-0.00072636736812

[DHA-H]•			
C	-3.64448835250249	-0.73399811356153	-0.13530675642751
C	-3.66651044824852	0.64386227364127	0.07483847719798
C	-2.44221741981486	-1.38252733246100	-0.31952516737895
C	-2.47525474829514	1.35747402980821	0.08994103821940
C	-1.22458892940220	-0.67381480628387	-0.29547986559182
C	-1.25657328724444	0.72434363224113	-0.09799490123532
C	0.02218799123434	-1.34481253701789	-0.42267677026621
C	0.01664335197869	1.52354592032435	-0.14492483651827
C	1.28162874022759	0.72139344993794	-0.01394107921283
C	1.25930885517651	-0.67627789186052	-0.21561587412528
C	2.48698098214628	1.35069053302073	0.25591427553170
C	2.47435059837910	-1.38780981156428	-0.16365877148091
C	3.67500674611044	0.63411245275843	0.31618417029937
C	3.66386582841473	-0.74291508652824	0.09978165596257
H	-4.56899640004314	-1.29491385760552	-0.14628205783353
H	-4.60661652841645	1.15613708424359	0.22480957052776
H	-2.41741923873646	-2.45423560714379	-0.47188037243080
H	-2.49190153163979	2.42925244420000	0.24862781373410
H	0.02668497638805	-2.41412620002792	-0.58998765167152
H	0.04923132975246	2.05410115763698	-1.10579186209702
H	-0.00774705130833	2.30569945426941	0.61710718678174
H	2.49576000806285	2.42197692865576	0.41879614191930
H	2.45659331250958	-2.45906201427456	-0.31997691800744
H	4.60422602739661	1.14377662460738	0.52965961185220
H	4.58607118787460	-1.30577672701609	0.14595794225130

Triphenylmethane			
C	-4.28613453674754	0.61824687332156	0.43157600416776
C	-5.19308316643694	-0.50615135690773	0.90512850844051
C	-4.77835453065648	-1.83316377252941	0.96634877288331
C	-5.65179084762039	-2.82985070384426	1.39091078460527
C	-6.95045435915382	-2.51227977922322	1.76059065542494
C	-7.37636580372009	-1.18979913601356	1.69839534229099
C	-6.50393440745015	-0.19940722265997	1.27144800827288
C	-2.81770274576523	0.31285548415207	0.66886722206569
C	-2.27916204550365	0.53491118797921	1.93613587310933
C	-0.95854795866205	0.21382478003868	2.21545089049323
C	-0.15353284218980	-0.34008418710912	1.22644269949801
C	-0.67791253421052	-0.55858435033144	-0.04039430412832
C	-2.00042830900529	-0.23070267452387	-0.31792538885524
C	-4.56814573116108	1.04178437897018	-0.99989846260853
C	-4.21364025693221	2.33243308060948	-1.39508469531892
C	-4.42496214877418	2.76370670771710	-2.69598829859230
C	-4.99551230916822	1.90483907585863	-3.62979721337975
C	-5.34824823384931	0.61859195085654	-3.24835095604991
C	-5.13542993067740	0.18959460275685	-1.94150619659205
H	-4.52370703522217	1.48362676215682	1.05550820619091
H	-3.76589448815331	-2.09789874106214	0.68992327405569
H	-5.31086874122796	-3.85565371912223	1.43700295975651
H	-7.62592562644026	-3.28706689606211	2.09787168468784
H	-8.38642152026092	-0.93058407206457	1.98673910126098
H	-6.84171788080641	0.82938191937536	1.22423378765720
H	-2.90376257882963	0.96268034022285	2.71177207418630
H	-0.55753245075969	0.39745164130595	3.20338522693192
H	0.87632759925852	-0.59204591224712	1.44086460495524
H	-0.05654025120003	-0.98265858974740	-0.81800821438448
H	-2.39620866130484	-0.40345534873427	-1.31102159366744
H	-3.77080922313422	3.00707316483455	-0.67128960038287
H	-4.15094530037937	3.77102196121507	-2.98043287972518
H	-5.16739784063229	2.24004851937759	-4.64376497456881
H	-5.79405068504866	-0.05684614293470	-3.96649348226832
H	-5.42034561817440	-0.81583782563135	-1.65864142041239

[TPM-H]•			
C	-4.11411932497908	-0.05050641378076	-0.04242152269404
C	-5.14344199312817	-0.78624875130803	0.67971574842502
C	-4.84641176822148	-1.98969381452449	1.34314053645667
C	-5.82433327127765	-2.68796682860132	2.03127686032477
C	-7.12639164277467	-2.20234801141273	2.08898560310269
C	-7.44037352494058	-1.01182668355294	1.44193999746815
C	-6.46738754037289	-0.31740472811331	0.74239651588017
C	-2.73970050922580	-0.05557292933002	0.44163154852818
C	-2.45046619131784	-0.10618010143889	1.81647429285807
C	-1.14362701416003	-0.10757456807095	2.27419862801763
C	-0.08429665422334	-0.07006860556381	1.37380685088174
C	-0.34881590255340	-0.02407075071457	0.00913524003211
C	-1.65440038157697	-0.01006083899060	-0.45107662928193
C	-4.45492904179795	0.69729615928829	-1.24571108324335
C	-3.79723306152877	1.89893751013053	-1.56164987466573
C	-4.11783333507074	2.61290506662142	-2.70370185880189
C	-5.09374612319170	2.14216852468224	-3.57556492912283
C	-5.75580036900000	0.95510207239652	-3.28181945013980
C	-5.44659450533164	0.24521627423806	-2.13325447308946
H	-3.84158903160817	-2.38761162171565	1.29539474460453
H	-5.57080543719870	-3.61811749484038	2.52227970538673
H	-7.88742802645874	-2.74647350204198	2.63183779499870
H	-8.44764114414712	-0.61974814712091	1.48814424436475
H	-6.72421675771032	0.61434321987973	0.25633037743625
H	-3.26416584313015	-0.11908155935081	2.52924494246759
H	-0.95039762148254	-0.13198439573494	3.33836915055174
H	0.93630189855525	-0.07551717910881	1.73149240155520
H	0.46737363035708	-0.00440885850381	-0.70075161044162
H	-1.84295887865360	0.01177131380040	-1.51607754282377
H	-3.04343930006717	2.28353059049315	-0.88789408235359
H	-3.60582324755722	3.54248042588376	-2.91370290894727
H	-5.33794019348655	2.69507467841704	-4.47241159628284
H	-6.51265153954764	0.57666734788747	-3.95594579317485
H	-5.96025435319170	-0.68458639989891	-1.92746182827773

Diphenylmethane			
C	-4.26089896090912	1.44658883110651	-0.02014293877637
C	-5.20206476939799	0.28532624527391	0.19697781192644
C	-5.13592748838138	-0.46063871937375	1.37423407633023
C	-5.97912632412210	-1.54236620614058	1.57916948728201
C	-6.90789045474103	-1.89775744096617	0.60615286581760
C	-6.98262958516553	-1.16249851283272	-0.56844450801894
C	-6.13470507664056	-0.07809749665047	-0.76991787160664
C	-2.83412913947372	0.99371654794107	-0.21648916031126
C	-1.91191230364095	1.05590468785138	0.82479263587545
C	-0.60572151017858	0.61336316810199	0.64581138345096
C	-0.20478121097397	0.10431169506260	-0.58188756156133
C	-1.11839561190231	0.03664454279803	-1.62828700900019
C	-2.42202459865713	0.47676460185999	-1.44454167795647
H	-4.58664762352464	2.01592961867049	-0.89133111544901
H	-4.30796807678643	2.11600644880037	0.83997367075269
H	-4.41683778597303	-0.18906372544328	2.13822923321824
H	-5.91438512014474	-2.10734791054878	2.49975856640385
H	-7.56884968382058	-2.73890329273513	0.76667969215600
H	-7.70228069789818	-1.42934401907845	-1.33096375504492
H	-6.20324844090807	0.49236702695807	-1.68823864264452
H	-2.21478405145221	1.46385051039423	1.78165343513667
H	0.09900962360121	0.67367669764599	1.46450937199177
H	0.81243578265539	-0.23471000821546	-0.72447331767524
H	-0.81316929412560	-0.35706391136349	-2.58884581364486
H	-3.12901459743874	0.42334362088362	-2.26437585865216

[DPM-H]•			
C	-4.11219513903122	0.95387297259901	0.33037618433394
C	-5.16128533487912	-0.02301609382205	0.28008481675170
C	-4.95849247877151	-1.40359668440207	0.47712352179423
C	-6.01756906935495	-2.29333715824254	0.42203716839300
C	-7.30929748360145	-1.84097316297863	0.17203635001554
C	-7.53614738535465	-0.47750261309622	0.00275317796413
C	-6.48462399984404	0.41728681040363	0.06822515443510
C	-2.71190397751350	0.76820736226618	0.10384095861653
C	-1.82092681407130	1.79053727955485	0.49751096789230
C	-0.46205632603574	1.68691517882338	0.27060803120791
C	0.06012780097129	0.56565845472141	-0.37107152817126
C	-0.80186707144773	-0.44329567008382	-0.78883905316536
C	-2.16297248935596	-0.34970812570648	-0.55860794037668
H	-4.42392546688901	1.97016140549126	0.54173416533127
H	-3.97282825102992	-1.77376124897160	0.71896948822501
H	-5.83708977639218	-3.34749039462084	0.58554952932155
H	-8.13195720121483	-2.54112759302060	0.12390692995956
H	-8.53906467076432	-0.11397886097275	-0.17739276669506
H	-6.66869184386884	1.47644680618578	-0.06189260456440
H	-2.21953428768500	2.66800104592003	0.99152278143270
H	0.19649358411345	2.48367611461947	0.58993171873335
H	1.12277336712108	0.48524274438481	-0.55466943703041
H	-0.40957397596502	-1.30581324749407	-1.31103113273183
H	-2.81258370913554	-1.12415032155814	-0.93861648167280

Cumene				[Cumene-H]•			
C	-5.28827145811382	0.01278102929465	-0.09578536137270	C	-5.10259934422162	-0.14025969395540	0.08749977430662
C	-4.95458326728552	-0.96568977902057	0.84202200961472	C	-4.68522416468041	-1.49137745433164	0.00849647423753
C	-5.75550666634563	-2.08577358007000	1.01952475399373	C	-5.59595299376153	-2.52861221502954	0.08141412705265
C	-6.90753512514619	-2.25062749270215	0.25866787239779	C	-6.95604486488042	-2.27146374972158	0.24000190793630
C	-7.25076992831105	-1.28517907438480	-0.67752684916418	C	-7.39105433822118	-0.95094807039090	0.32826590681931
C	-6.44642260913654	-0.16436507530512	-0.84965269471780	C	-6.48960834837221	0.09418456640343	0.25158715334482
C	-4.40037809189784	1.21570728167711	-0.32191603950664	C	-4.17004075432805	0.93392507811522	0.00360072598711
C	-3.13145370616918	0.81147710420731	-1.07302211631365	C	-2.71090099015826	0.65240091378919	-0.13499876442419
C	-4.04816124246314	1.93495700829687	0.97740042931018	C	-4.64545018055971	2.34780806212576	0.05131563957821
H	-4.05825719560426	-0.85683585992956	1.44051045291722	H	-3.63634428193650	-1.72321206151646	-0.11420642142277
H	-5.47932701844149	-2.83269041681274	1.75219392980408	H	-5.24470865019669	-3.55024174383863	0.01573966082647
H	-7.53226404844764	-3.12280904020557	0.39723754500335	H	-7.66460393311526	-3.08626263692776	0.29541408302446
H	-8.14557583000449	-1.40191548103504	-1.27481776832575	H	-8.44432443294883	-0.73742772102807	0.45631859924908
H	-6.72183321029337	0.58489425120893	-1.58213466233837	H	-6.85709906889150	1.10864763882012	0.32097387706163
H	-4.95676201994369	1.91276102697156	-0.95253519426116	H	-2.48851802545883	0.08380550591428	-1.04393937793564
H	-3.36911540090870	0.33259298422388	-2.02390327186366	H	-2.13371537744035	1.57384930627450	-0.17294446995420
H	-2.50941853988453	1.68431958374999	-1.27799862307051	H	-2.33043386798229	0.05718796657373	0.70124347170573
H	-2.54007262865549	0.10876090307091	-0.48135789915371	H	-5.35320410640068	2.56698172307359	-0.75476233248165
H	-4.94314290857825	2.21854866612116	1.53247922949901	H	-3.81524010425046	3.04502181755293	-0.03958120098960
H	-3.47958085342863	2.84168695303406	0.76553994142091	H	-5.16564917219521	2.57367976809724	0.98786116607815
H	-3.43323025094057	1.30739900760913	1.62507431612716				
Ethylbenzene				[EtBn-H]•			
C	-5.16839800744338	0.32597991760012	-0.00187978911152	C	-5.13490282310887	0.25660182242066	-0.13485595048787
C	-4.70710878939910	-0.91452508750831	0.43364550137150	C	-4.69245827626971	-1.02182289718278	0.28044759229969
C	-5.58858623487503	-1.96936236936378	0.64986805516936	C	-5.59782952942768	-2.02474859314356	0.57534759543679
C	-6.94853286709911	-1.80123431346724	0.43271933266036	C	-6.96815845998648	-1.79660126160857	0.47118782669214
C	-7.42311520192619	-0.56740899338696	0.00022915014245	C	-7.42677068059168	-0.54000710479138	0.07253473129210
C	-6.54031409974635	0.48104337051992	-0.21318474159076	C	-6.53230674736839	0.46823775446142	-0.22243142271393
C	-4.24537557772562	1.49787505850319	-0.23352702966453	C	-4.23260207415954	1.29621352510254	-0.45818677589972
C	-2.78582031810904	1.14145492510376	-0.46942315236704	C	-2.75511996300641	1.15181462054644	-0.40751497826915
H	-3.65051319665372	-1.07134149353176	0.60489730187133	H	-3.63216901382294	-1.21893848984494	0.36806336614077
H	-5.20753505389594	-2.92486496216340	0.98580144372757	H	-5.23644247726078	-2.99546408381825	0.88885940675127
H	-7.63377434047927	-2.62204655200319	0.59576774499906	H	-7.67151682039494	-2.58536623386828	0.69952355630391
H	-8.48146134489217	-0.42370637298845	-0.17379621634258	H	-8.48988671052332	-0.35387765078713	-0.00522000681199
H	-6.91718152887554	1.43785453508355	-0.55549880274905	H	-6.89351422594842	1.44181226159978	-0.53073793682914
H	-4.31523750968886	2.17099235151316	0.62596718472451	H	-4.65183072882060	2.25148710866268	-0.74607051802340
H	-4.62308981497625	2.06784880748649	-1.08484241737352	H	-2.26137772241686	2.02405374997652	-0.83059059953994
H	-2.21504054565807	2.03799403598927	-0.71135208085256	H	-2.41335936357381	0.27084951919645	-0.95833370358349
H	-2.67578861760027	0.44021699542969	-1.29854741364835	H	-2.39248438331956	1.03397395307842	0.62012281724198
H	-2.32927395095609	0.69322814718392	0.41315492903378				
Para-Xylene				[*para*-Xylene-H]•			
C	-4.26936064429436	2.23840435588840	-0.59399046579639	C	-4.23851736325558	2.20844520966656	-0.59073192497044
C	-5.17219697423068	1.07970708745451	-0.28472523952288	C	-5.19392459069206	1.09141765572488	-0.30082056862573
C	-4.66409312489807	-0.17045857770410	0.04835833700371	C	-4.73187533028331	-0.14685724072452	0.16171902233166
C	-5.51058379831596	-1.23939122017717	0.32989136285191	C	-5.60282909161772	-1.17667110193753	0.44591959182221
C	-6.89216632267991	-1.09110006273900	0.28838315379714	C	-7.00100645608020	-1.01946438808944	0.27914806283923
C	-7.40302107770125	0.16560086960474	-0.04628703715061	C	-7.45876884673190	0.23936672125988	-0.18169293555157
C	-6.56085641544424	1.22870996780089	-0.32711952815316	C	-6.57379514879031	1.25963740345009	-0.46179839116269
C	-7.81549914592118	-2.23497426977603	0.59243312717130	C	-7.89224772443461	-2.07103622762805	0.54965121777587
H	-3.22094251174078	1.95129016211953	-0.52929623993560	H	-4.65103781119984	2.90154455361982	-1.32338498632052
H	-4.45253913109317	2.62158242906002	-1.59922848695190	H	-4.01746854256740	2.78072949156104	0.31379198709547
H	-4.43594287033337	3.06347555022336	0.10062791670623	H	-3.29111475829289	1.82786095729312	-0.97218648741272
H	-3.59130783304522	-0.31617549768632	0.08864301068702	H	-3.66693129224789	-0.29785761691470	0.29262178063592
H	-5.08489508235952	-2.20236492103611	0.58537858297184	H	-5.22076325526057	-2.12740449630247	0.79647774732490
H	-8.47673575097246	0.30919109307411	-0.08567559723069	H	-8.52204387218076	0.39336438566098	-0.31797620536160
H	-6.98456135255874	2.19294272179303	-0.58326357791063	H	-6.95222563398106	2.21040293143519	-0.81796117079080
H	-7.25934785799093	-3.13494638025427	0.85101452404553	H	-8.95659835109726	-1.94546127221006	0.41199794205467
H	-8.47562288443599	-1.99525622035094	1.42782045820736	H	-7.53155229328665	-3.02733096786477	0.90027125031612
H	-8.45259922198416	-2.46623808729465	-0.26296530079019				

Toluene			
C	-8.26725247392154	0.54855028212348	-0.15771083427454
C	-7.75360729454118	-0.67836494993819	0.26187932503615
C	-8.59591132727753	-1.74331519831050	0.55352491257688
C	-9.97248661508462	-1.59850739403524	0.42896669040391
C	-10.49691531584081	-0.38079741454347	0.01419733139400
C	-9.64971059637270	0.68173756810219	-0.27556726906929
C	-7.35357038551095	1.70199416246644	-0.45204117078413
H	-6.68113484413004	-0.80028050727686	0.35627783214570
H	-8.17668344420635	-2.68816616912493	0.87357493103037
H	-10.63064825514171	-2.42756519006204	0.65109050312385
H	-11.56727666974654	-0.25709323122042	-0.08612365118424
H	-10.06668338382459	1.62743264063735	-0.60045642491689
H	-6.41407389888903	1.35990920850020	-0.88536372425365
H	-7.81614216727748	2.40530214017534	-1.14365655379847
H	-7.11049732823494	2.24916705250663	0.46140610257034

[Tol-H]•			
C	-8.35363205612574	0.62751613326534	-0.16040079728054
C	-7.78467465216479	-0.65152261470904	0.05522206319736
C	-8.57933831619531	-1.74404762212053	0.33848974949337
C	-9.96522717579521	-1.60716990552129	0.41835232836520
C	-10.54697473995180	-0.35481437441867	0.22088466639034
C	-9.76176490430865	0.74471464755523	-0.06237187698627
C	-7.54684236081220	1.73796105307981	-0.46864573044423
H	-6.70931486918732	-0.76206378584744	-0.00635532074573
H	-8.12395113169809	-2.71259604361087	0.49749981377362
H	-10.58596662751615	-2.46601102058924	0.63338780469765
H	-11.62130110394896	-0.24407489687073	0.28737389886167
H	-10.21887656931090	1.71410051828142	-0.21704315265359
H	-6.47382306088396	1.63788694263003	-0.54569394198036
H	-7.98200143210096	2.71359296887597	-0.63022750468850

Tetrahydrofuran			
O	-6.45480499394260	0.49611197993408	-1.36061006190849
C	-5.47951774960602	-0.08778882862699	-0.50219532868551
C	-6.10391463281800	-0.07661733948873	0.88122273351051
C	-7.56882244016666	-0.34114799455687	0.54192401685632
C	-7.74060889404470	0.46413629404017	-0.73947226589062
H	-4.56153021495183	0.49385926800904	-0.57762784396192
H	-5.27153540978335	-1.11073051268372	-0.83045843656003
H	-5.66829819708923	-0.82234546462820	1.54227027603399
H	-5.98811937231621	0.90750665892553	1.33813737903901
H	-8.26253816895630	-0.03209803857343	1.32037719471789
H	-7.72048958250775	-1.40356210671075	0.34707284126809
H	-8.45773578817738	0.02239178452570	-1.43141296644780
H	-8.05203355563998	1.49028529983417	-0.52922653797145

[THF-H]•			
O	-6.57282686395888	0.06867641072880	-1.44819238018015
C	-5.57539161055425	-0.08446582688064	-0.52377889597422
C	-6.13937057878535	-0.16992363702127	0.85978783155909
C	-7.64750419811431	-0.28722896407007	0.58906106929714
C	-7.78183795629610	0.40096017161229	-0.75818016966374
H	-4.71243562270059	-0.62177666913675	-0.89046244094365
H	-5.74276519888233	-1.01542950975351	1.42174835704168
H	-5.92063962831046	0.73317185117431	1.43721432854108
H	-8.26209762980616	0.17914622634690	1.35506572299451
H	-7.93568301571310	-1.33461015281570	0.49948578878295
H	-8.61604693674061	0.05386926990262	-1.36222819089511
H	-7.84154376013785	1.48676282991303	-0.65223502055959

Cyclooctane			
C	-7.39851590703687	-0.11106598434059	-0.29120942841310
C	-6.81267382567419	-1.51841830231453	-0.31435452070976
C	-5.28474591381366	-1.64059376623408	-0.27708451152391
C	-4.52053238689469	-0.64791910729686	-1.16540566114883
C	-3.92766650429955	0.55878935229826	-0.43644412117668
C	-4.88919546769491	1.58036325622204	0.17452604953917
C	-5.74728778520381	1.06727148443684	1.34196385450091
C	-7.19049562907370	0.70018397159696	0.98273348668654
H	-8.47528677646176	-0.19710575496539	-0.45970959454519
H	-7.01752952788662	0.45430133780247	-1.14508330502371
H	-7.23724696739788	-2.09875532304915	0.51034633064192
H	-7.16332743270308	-1.99962328069356	-1.23197187845550
H	-4.91817444909051	-1.55652490241551	0.74727768202534
H	-5.04073451766035	-2.65864662397300	-0.58699215896239
H	-5.15708936281459	-0.30684275230141	-1.98734598844289
H	-3.68778270202470	-1.17261619164565	-1.63826538979877
H	-3.27611229281728	0.18555455334118	0.36179125565183
H	-3.27428556330656	1.08832445261247	-1.13497476708487
H	-5.52927395539647	1.99996948555763	-0.60758526322282
H	-4.27818715490766	2.41236823291250	0.53111115303671
H	-5.24446563364586	0.22109058195530	1.81349732613857
H	-5.79642972225089	1.83830419795871	2.11353206375940
H	-7.64261367606785	0.17054295545400	1.82703416427738
H	-7.75493384587655	1.63104312708138	0.87261322225066

[Cyclooctane-H]•			
C	-7.34928583586414	-0.25613548041591	-0.12830160295117
C	-6.46413057724979	-1.39703437632421	0.22772492603752
C	-5.28167410327613	-1.77391556453024	-0.59466953859965
C	-4.51375334295198	-0.60309096999036	-1.21776805221767
C	-3.96942535862982	0.44183405330250	-0.23939951150235
C	-4.90574714096334	1.57633505211525	0.20268085319816
C	-5.89086802394002	1.27027413256122	1.33963364157694
C	-7.30154835212587	0.87935491659504	0.90539293390425
H	-8.38964505332090	-0.58500755638701	-0.22553384578490
H	-7.06397139002083	0.14024660117454	-1.10433037585134
H	-6.72021535152025	-2.00146429903555	1.08954203518197
H	-4.59117329017928	-2.36647342530284	0.01173478621226
H	-5.58917743043078	-2.43812808981805	-1.41776125540775
H	-5.12722372441076	-0.10543318906910	-1.97337082226875
H	-3.67085088138544	-1.03305751764138	-1.76377536000580
H	-3.57601977935411	-0.06339579495982	0.64959031215659
H	-3.10784449876714	0.91221016551276	-0.71925519772527
H	-5.44802535216935	1.95663754644863	-0.66973067495939
H	-4.26464318089422	2.39759906477855	0.52941742810325
H	-5.47125407903273	0.47794440760021	1.96612779626548
H	-5.97689217403884	2.14804098766485	1.98369219386897
H	-7.86936419274159	0.58330061637653	1.79131982909894
H	-7.80815188673270	1.75376071934439	0.48730750166970

Cyclohexane				[Cyclohexane-H]•			
C	-5.70631763144646	-0.18567704506917	1.08609532325024	C	-5.50940196945039	0.07784390171426	1.25320269922294
C	-6.94351311046516	0.68805546123517	1.27485398899067	C	-6.70333922513219	1.02786294697633	1.39545641077685
C	-7.40602470127769	1.28095891821349	-0.05347388458523	C	-7.09202593601714	1.62124512734270	0.04465282156359
C	-7.65992028919485	0.18569383431587	-1.08606881720269	C	-7.41536091991592	0.52664139638843	-0.96861772813694
C	-6.42274812711112	-0.68804677993181	-1.27488349532616	C	-6.23578769130917	-0.43783193123305	-1.13529146575689
C	-5.96026331676342	-1.28090322407449	0.05347598647039	C	-5.75150957962572	-0.93108377755044	0.18430485376572
H	-5.40099842667416	-0.62337219784591	2.03863872915193	H	-5.27991562508290	-0.40296978793685	2.20494219005990
H	-4.87468272692715	0.44092120492523	0.74536846144019	H	-4.62605500367747	0.68330836540411	0.99204235295238
H	-7.75166307961718	0.07862826306359	1.69404173225150	H	-7.55542320098051	0.47267082171140	1.79989937158002
H	-6.74078758606323	1.48361705792484	1.99470960193780	H	-6.46864540799800	1.82072283512244	2.10797594975776
H	-8.30626208585200	1.88141976580892	0.09276030841433	H	-7.94769693031066	2.28922355064673	0.16123142280414
H	-6.63294840764347	1.95804213304094	-0.43278509980824	H	-6.26408066781529	2.23127639970274	-0.33309950568133
H	-8.49149296748711	-0.44096421479490	-0.74528804652244	H	-8.28745349505390	-0.03544887618401	-0.62035712383960
H	-7.96532936961962	0.62333970901425	-2.03861199805964	H	-7.68142127476450	0.96331600665464	-1.93288952081778
H	-6.62550518123369	-1.48365842395236	-1.99467044211282	H	-6.50568714468502	-1.26822068635178	-1.78909513578602
H	-5.61460845738370	-0.07867071033853	-1.69415753306673	H	-5.42207002005844	0.10519538704301	-1.64300151004638
H	-6.73340545421782	-1.95792018054932	0.43278179840031	H	-5.31304888012278	-1.91712426045066	0.26432795558166
H	-5.06009008102217	-1.88146357098582	-0.09278761362341				

A3.3 Coordinates for Substrates Optimized by DFT Computations Using a Continuum Dielectric for Acetonitrile

Cumene				[Cumene-H]•			
C	-5.28798208142377	0.01188171627168	-0.09732386584535	C	-5.10266226307507	-0.14025033134240	0.08758272759443
C	-4.95162955556621	-0.96865557456850	0.83758481521403	C	-4.68516714888680	-1.49151564543138	0.00845960736750
C	-5.75296481263619	-2.08837674960330	1.01632643555004	C	-5.59593284070054	-2.52898026788782	0.08127708043391
C	-6.90817090506286	-2.25070085838144	0.25938712293533	C	-6.95624689505889	-2.27175225717004	0.23994992032931
C	-7.25426305927755	-1.28311016520007	-0.67378287192452	C	-7.39140819077348	-0.95102883462615	0.32837535734441
C	-6.44942710285305	-0.16260047503747	-0.84699610144574	C	-6.48982491101561	0.09424022629745	0.25172765014745
C	-4.39982097650898	1.21486927348528	-0.32388009770524	C	-4.16994605038610	0.93406495419057	0.00370981514388
C	-3.12744899763812	0.81074047284568	-1.06971529585370	C	-2.71057797396691	0.65247131430749	-0.13491911376685
C	-4.05181940076426	1.93704764344259	0.97533569859415	C	-4.64529840502391	2.34823903149604	0.05125427490518
H	-4.05263869452543	-0.86086243080021	1.43217589255707	H	-3.63618842412497	-1.72256384912671	-0.11418239491292
H	-5.47481510464671	-2.83684133257326	1.74650785259059	H	-5.24470641737706	-3.55047012805827	0.01547334453659
H	-7.53310348460240	-3.12249010961497	0.39870191303441	H	-7.66471789909921	-3.08647419158334	0.29524585591794
H	-8.15145617357745	-1.39796180848421	-1.26765509804107	H	-8.44454495931996	-0.73755088010717	0.45650797867519
H	-6.72636164241758	0.58863277411751	-1.57674469127759	H	-6.85680981505077	1.10880736456654	0.32107908393985
H	-4.95500510172662	1.90980526065720	-0.95772456247150	H	-2.48863260621659	0.08342003855726	-1.04355112190555
H	-3.36071790858560	0.32892766123232	-2.02005545109044	H	-2.13385289583345	1.57407279789531	-0.17315294822046
H	-2.50676175494170	1.68455501860171	-1.27401840367746	H	-2.33044283682406	0.05724407799105	0.70131778459771
H	-2.53731736265400	0.11105186272738	-0.47341308306710	H	-5.35326699428575	2.56686584083964	-0.75463359486249
H	-4.94857217614189	2.22489717969048	1.52510037534843	H	-3.81485475011683	3.04497365795169	-0.03986924478340
H	-3.47898379969246	2.84091541360933	0.76322652234907	H	-5.16563472286401	2.57387408124026	0.98764793751837c
H	-3.44240190475718	1.30827522758230	1.62696289422660				
Ethylbenzene				[EtBn-H]•			
C	-5.16837698403182	0.32595860934697	-0.00162403305173	C	-5.13491582504860	0.25657361634483	-0.13518346933408
C	-4.70709462696739	-0.91449528439720	0.43445859992913	C	-4.69239384540475	-1.02203302263225	0.28003522147041
C	-5.58867119843410	-1.96951185618625	0.65072289446315	C	-5.59780342992088	-2.02506586389928	0.57531002449403
C	-6.94875900671274	-1.80145953463955	0.43294975494871	C	-6.96835679878477	-1.79676791756509	0.47143643045927
C	-7.42332609819754	-0.56765177570587	-0.00033838928648	C	-7.42708873621844	-0.53999920706545	0.07263373675223
C	-6.54033330266103	0.48093015950380	-0.21377916838318	C	-6.53250659677146	0.46831039998656	-0.22263977325986
C	-4.24521585955766	1.49815251042575	-0.23301281428435	C	-4.23244647385323	1.29637295151156	-0.45829842491665
C	-2.78558989612834	1.14168850083988	-0.47025269713310	C	-2.75470782146342	1.15201569370080	-0.40734132299619
H	-3.65052127624542	-1.07073461389328	0.60579634045645	H	-3.63206772878019	-1.21870510889995	0.36716033264200
H	-5.20759819773733	-2.92472169193790	0.98704755368834	H	-5.23641415467593	-2.99563529714022	0.88885173328545
H	-7.63400855320413	-2.62209570806741	0.59600272686535	H	-7.67164296498570	-2.58535722698248	0.70004973554668
H	-8.48145570590501	-0.42408298708526	-0.17497833816775	H	-8.49010067214026	-0.35389435530282	-0.00494643273875
H	-6.91657669856601	1.43756202189476	-0.55691986236634	H	-6.89331044995433	1.44195785057445	-0.53088221994154
H	-4.31434726863334	2.17022279237097	0.62719935898753	H	-4.65199434173970	2.25139953078064	-0.74627354479419
H	-4.62369353959495	2.06883194252270	-1.08335979227873	H	-2.26112014083455	2.02415019265700	-0.83051381243282
H	-2.21458048835179	2.03835834612110	-0.71052513258337	H	-2.41313570952503	2.07079022754240	-0.95765425278356
H	-2.67657376684106	0.44190579324151	-1.30061113602190	H	-2.39272430989874	1.03410553638933	0.62040103854759
H	-2.32942453223036	0.69114077564524	0.41122313421828				

Toluene			
C	-8.26723657388062	0.54859358571771	-0.15752473548853
C	-7.75345817555858	-0.67848497155550	0.26186676813280
C	-8.59585568805531	-1.74359747100779	0.55355606560897
C	-9.97260648287776	-1.59864648921981	0.42912086610959
C	-10.49716277126461	-0.38074535080298	0.01434453646047
C	-9.64983364150933	0.68187915707252	-0.27544472899767
C	-7.35339797772818	1.70225098387013	-0.45211188899239
H	-6.68099031273388	-0.79999282772459	0.35575465271421
H	-8.17663724436365	-2.68839338528885	0.87339392699018
H	-10.63075015363896	-2.42757851447258	0.65121822569194
H	-11.56742036282221	-0.25711931253901	-0.08593956474580
H	-10.06612349246443	1.62770569615759	-0.60052340945711
H	-6.41387622921460	1.35958782018330	-0.88465922809396
H	-7.81633518147895	2.40473144410946	-1.14416689797395
H	-7.11090971240893	2.24981263550040	0.46111341204124

[Tol-H]•			
C	-8.35362964009283	0.62768681929123	-0.15954001131449
C	-7.78447956765701	-0.65154366934722	0.05563765438690
C	-8.57926176001598	-1.74447596210056	0.33776565732747
C	-9.96541905702585	-1.60764984242778	0.41669257819062
C	-10.54735891365577	-0.35513134521920	0.21961378668062
C	-9.76193985458570	0.74481353258176	-0.06232666861615
C	-7.54662844931346	1.73856990575603	-0.46674401588430
H	-6.70907849689018	-0.76104984084721	-0.00542974539412
H	-8.12416367490938	-2.71306012288890	0.49654689199583
H	-10.58601619971258	-2.46670926956985	0.63069516155846
H	-11.62161411132240	-0.24449791035346	0.28537748634312
H	-10.21843027875857	1.71442810593323	-0.21671471380306
H	-6.47369276562547	1.63806538877196	-0.54302149378186
H	-7.98197623043480	2.71402621041997	-0.62808056768903

2,3-Dimethylbutane			
C	1.77396566299751	0.55577219614368	-0.59193903677004
C	0.70124897357760	-0.30921804013846	0.06644211240572
C	-0.70200510881343	0.30798578150865	-0.06660677560742
C	-1.77447525083652	-0.55526395032255	0.59437917033636
C	-0.76125100876979	1.71852752743547	0.51407995776489
C	0.76173162822142	-1.71861774557026	-0.51677569800180
H	2.74757574559563	0.06575646974454	-0.54099726842535
H	1.54029015839744	0.71862419272181	-1.64790185466032
H	1.87453722770655	1.52972460598949	-0.11426829522372
H	0.92508125924183	-0.37140045709637	1.13863762581040
H	-0.92651208714242	0.36782189836586	-1.13880441699253
H	-2.74835208920292	-0.06606387905832	0.54096777546901
H	-1.87429317835790	-1.53115264606503	0.12051054903836
H	-1.54139159635336	-0.71397684817054	1.65109590070422
H	-1.77823779621122	2.11186376756511	0.46845720359258
H	-0.11825893909330	2.41643553972472	-0.02069622777772
H	-0.45497921355713	1.71289494370571	1.56397717190019
H	0.11498373831336	-2.41686230123378	0.01301112315000
H	1.77795728386111	-2.11332430855282	-0.46620668781227
H	0.46138459042554	-1.71052674669689	-1.56836232890056

[2,3-DMB-H]•			
C	1.70502429088008	0.35875291135052	0.09837528217065
C	0.50195586996422	-0.13395288258855	-0.63424901624236
C	-0.86619312766319	0.23374287562168	-0.12987137959778
C	-1.10106736942113	-0.34148775777653	1.27362340807623
C	-1.12233766036474	1.74048250623763	-0.12878484323843
C	0.65246466303881	-1.42631531080375	-1.36282322704535
H	1.97658218948710	-0.32376824026221	0.91742334035601
H	2.57651741391951	0.40864761313381	-0.55879311146117
H	1.55694601927333	1.34503167405369	0.53899430777424
H	-1.59617081029719	-0.22847021843574	-0.80098604219235
H	-2.11186777124775	-0.12000190459411	1.62160436265980
H	-0.97140365726435	-1.42511292457491	1.28427280093489
H	-0.39899109622726	0.09262862506715	1.98908767285573
H	-2.15523559206599	1.94983007299095	0.15472277975333
H	-0.94884525258269	2.17541452479188	-1.11429271721615
H	-0.47637520810238	2.25357795573781	0.58596126552513
H	-0.17636052915993	-1.60673120774334	-2.04958323791549
H	0.68026970280355	-2.27731880418389	-0.66476614097119
H	1.58508792502999	-1.46494950802208	-1.92991550422572

Cyclohexane			
C	-5.70600034578773	-0.18540700439884	1.08590750461694
C	-6.94386576999675	0.68777853758330	1.27501602734643
C	-7.40566647083495	1.28120779457264	-0.05363061253218
C	-7.66026918824053	0.18541999481695	-1.08590057467271
C	-6.42240877910475	-0.68776376478786	-1.27501355859263
C	-5.96061214657354	-1.28118895466943	0.05363917270900
H	-5.39985914268098	-0.62255389660140	2.03827312189792
H	-4.87556294431724	0.44165317718740	0.74350743314329
H	-7.75187011237918	0.07723519182106	1.69253332265009
H	-6.74181878652044	1.48288857150700	1.99533657171063
H	-8.30530985182228	1.88237596801810	0.09227468085889
H	-6.63131036040053	1.95661649840353	-0.43295973549797
H	-8.49068235210031	-0.44168168307959	-0.74351085331879
H	-7.96645315029995	0.62254706530590	-2.03826334780350
H	-6.62445144181950	-1.48290330336531	-1.99530366694068
H	-5.61441869804785	-0.07722494364502	-1.69255843263042
H	-6.73498817734800	-1.95658340904819	0.43296178169329
H	-5.06101328172547	-1.88241583962024	-0.09230983463759

[Cyclohexane-H]•			
C	-5.50943769630978	0.07787705232610	1.25310803046891
C	-6.70378920354189	1.02773330225181	1.39556086929959
C	-7.09170972721774	1.62151161898392	0.04446452549412
C	-7.41584214379617	0.52646794414051	-0.96840175756969
C	-6.23570937407475	-0.43768543314576	-1.13520830939319
C	-5.75208083963451	-0.93169525973965	0.18462342353468
H	-5.27887692727135	-0.40218719360936	2.20481896104366
H	-4.62712612045375	0.68381776971732	0.98999208129387
H	-7.55602365124893	0.47200152248106	1.79869455899563
H	-6.46936232862266	1.82020842856229	2.10841000487427
H	-7.94658264099478	2.29036059097225	0.16066273435678
H	-6.26247939954148	2.22962610158243	-0.33332813551356
H	-8.28718010383326	-0.03572079494953	-0.61868668008955
H	-7.68244741956865	0.96259555542017	-1.93262870407068
H	-6.50458331240606	-1.26745380428467	-1.78999745872813
H	-5.42192355747270	0.10685641311923	-1.64095768390726
H	-5.31376852601155	-1.91768639482812	0.26455757791057

A3.4 Appendix Notes and References

1. Warren, J. J.; Tronic, T. A.; Mayer, J. M., Thermochemistry of Proton-Coupled Electron Transfer Reagents and its Implications. *Chem. Rev.* **2010,** *110* (12), 6961-7001.

2. Luo, Y.-R., BDEs of C-H bonds. In *Comprehensive Handbook of Chemical Bond Energies*, CRC Press: 2007; pp 19-145.

3. Kaizer, J.; Klinker, E. J.; Oh, N. Y.; Rohde, J.-U.; Song, W. J.; Stubna, A.; Kim, J.; Münck, E.; Nam, W.; Que Jr., L., Nonheme FeIVO Complexes That Can Oxidize the C−H Bonds of Cyclohexane at Room Temperature. *J. Am. Chem. Soc* **2004,** *126* (2), 472-473.

4. Chen, J.; Cho, K.-B.; Lee, Y.-M.; Kwon, Y. H.; Nam, W., Mononuclear nonheme iron(iv)-oxo and manganese(iv)-oxo complexes in oxidation reactions: experimental results prove theoretical prediction. *Chem. Commun.* **2015,** *51* (66), 13094-7.

5. Wu, X.; Seo, M. S.; Davis, K. M.; Lee, Y.-M.; Chen, J.; Cho, K.-B.; Pushkar, Y. N.; Nam, W., A Highly Reactive Mononuclear Non-Heme Manganese(IV)–Oxo Complex That Can Activate the Strong C–H Bonds of Alkanes. *J. Am. Chem. Soc* **2011,** *133* (50), 20088-20091.

6. Goldsmith, C. R.; Cole, A. P.; Stack, T. D. P., C−H Activation by a Mononuclear Manganese(III) Hydroxide Complex: Synthesis and Characterization of a Manganese-Lipoxygenase Mimic? *Journal of the American Chemical Society* **2005,** *127* (27), 9904-9912.

Appendix 4.

A4.1. X-ray Crystallographic Information

Table 4.1. Crystal data and structure refinement for $Mn^{II}(OH_2)(2pyN2B)](OTf)_2$

Identification code	k33k	
Empirical formula	C17.50 H19.50 F3 Mn0.50 N3.50 O4 S	
Formula weight	459.39	
Temperature	228(2) K	
Wavelength	0.71073 Å	
Crystal system	Orthorhombic	
Space group	Pnma	
Unit cell dimensions	a = 19.166(2) Å	α= 90°.
	b = 19.200(2) Å	β= 90°.
	c = 11.2881(12) Å	γ = 90°.
Volume	4153.9(8) $Å^3$	
Z	8	
Density (calculated)	1.469 Mg/m^3	
Absorption coefficient	0.502 mm^{-1}	
F(000)	1892	
Crystal size	0.450 x 0.180 x 0.180 mm^3	
Theta range for data collection	2.125 to 28.280°.	
Index ranges	-25<=h<=25, -25<=k<=25, -15<=l<=15	
Reflections collected	55690	
Independent reflections	5299 [R(int) = 0.0588]	
Completeness to theta = 27.500°	99.9 %	
Absorption correction	Multi-scan	
Max. and min. transmission	1.000 and 0.768	
Refinement method	Full-matrix least-squares on F^2	
Data / restraints / parameters	5299 / 0 / 331	
Goodness-of-fit on F^2	1.053	
Final R indices [I>2sigma(I)]	R1 = 0.0477, wR2 = 0.1237	
R indices (all data)	R1 = 0.0705, wR2 = 0.1445	
Extinction coefficient	n/a	
Largest diff. peak and hole	0.534 and -0.447 $e.Å^{-3}$	

A4.2 Additional EXAFS Fits

Table A4.2. EXAFS fitting results for each Mn^{II} complex.

		Mn-O/N			Mn-N			Mn-C				
complex	fit	*n*	r(Å)	σ^2	*n*	r(Å)	σ^2	*n*	r(Å)	σ^2	E_0	R
$[Mn^{II}(^{DMM}N4py)]^{2+}$	1	1	2.03	1.27	5	2.23	3.15				6.247	0.2031
	2	1	2.02	-3.7	3	2.20	-4.3				7.373	0.1795
					2	2.34	-3.9					
	3	1	2.03	1.76	5	2.24	3.33	5	3.08	6.29	7.337	0.1314
	4	**1**	**2.03**	1.23	**5**	**2.23**	3.19	**3**	**3.53**	7.37	**6.702**	**0.1181**
								5	**3.07**	6.20		
	5	1	2.02	1.11	5	2.23	3.28	3	2.88	13.97	6.005	0.1207
								4	3.07	3.66		
$[Mn^{II}(2pyN2B)]^{2+}$	1	1	2.33	-2.3	5	2.19	3.93				1.934	0.2568
	2	2	2.31	0.56	4	2.17	2.21				1.633	0.2627
	3	3	2.27	3.63	3	2.14	2.16	5	3.02	6.47	0.834	0.2222
	4	3	2.28	3.3	3	2.14	1.97	5	3.03	4.95	1.976	0.2170
								3	3.28	6.96		
	5	**3**	**2.28**	3.44	**3**	**2.14**	2.14	**3**	**3.01**	1.91	**1.715**	**0.2148**
								3	**3.21**	14.71		
$[Mn^{II}(2pyN2Q)]^{2+}$	1	1	2.26	-1.7	5	2.21	9.34				3.123	0.1401
	2	1	2.25	-2.3	5	2.20	10	6	3.05	11.43	2.286	0.1010
	3	**1**	**2.04**	**1.49**	**5**	**2.25**	**2.96**	**6**	**3.02**	**11.41**	**2.034**	**0.0867**
								4	**4.06**	**13.52**		

Table A4.3. EXAFS fitting results for each oxomanganese(IV) species.

		Mn-O/N			Mn-N			Mn-C				
complex	fit	*n*	r(Å)	σ^2	*n*	r(Å)	σ^2	*n*	r(Å)	σ^2	E_0	R
$[Mn^{IV}(O)(^{DMM}N4py)]^{2+}$	1	1	1.7	1	5	1.99	11.6				-6.42	0.408
	2	1	1.71	1.49	4	1.99	5.96				-3.37	0.341
					1	2.15	-0.1					
	3	1	1.72	1.66	4	2	6.85	4	2.92	6.00	0.255	0.26
					1	2.17	0.34					
	4	1	1.71	1.32	4	1.99	6.93	4	2.91	3.51	-2.7	0.212
					1	2.15	1.21	4	2.72	8.93		
	5	**1**	**1.71**	**1.37**	**4**	**1.99**	**6.9**	**5**	**2.9**	**4.99**	**-2.36**	**0.212**
					1	**2.16**	**1.15**	**3**	**2.7**	**5.78**		
$[Mn^{IV}(O)(2pyN2B)]^{2+}$	1	1	1.93	22.2	5	2.27	22.9				10.76	0.561
	2	1	1.96	39.7	4	2.2	35.1				9.186	0.525
				0	1	2.28	4.93					
	3	1	1.69	6.49	4	1.98	13	3	2.66	6.65	-8.73	0.42
				0	1	2.19	1.89					
	4	**1**	**1.7**	**7.34**	**4**	**2**	**14.1**	**3**	**2.68**	**4.77**	**-4.35**	**0.362**
					1	**2.21**	**1.52**	**6**	**2.91**	**15.5**		
	5	1	1.69	7.19	4	1.99	14.3	4	2.68	6.52	-4.86	0.366
					1	2.21	1.81	6	2.92	13.7		
$[Mn^{IV}(O)(2pyN2Q)]^{2+}$	1	1	1.76	24.4	5	2.27	23.7				12.95	0.503
	2	1	1.76	8.17	4	2.11	11				4.902	0.383
				0	1	2.3	1.49					
	3	1	1.76	7.19	4	2.09	10.6	4	2.9		1.982	0.306
				0	1	2.28	1.84			15.08		
	4	1	1.76	6.68	4	2.08	10	4	2.9		-0.6	0.275
				0	1	2.27	1.89	2	2.7	7.59		
	5	**1**	**1.75**	**6.39**	**4**	**2.07**	**7.59**	**5**	**2.9**	**5.18**	**-1.58**	**0.271**
					1	**2.27**	5.18	**3**	**2.69**	**8.84**		
										7.25		